ABSTRACT

Title of dissertation: ROTOR HOVER PERFORMANCE
AND SYSTEM DESIGN
OF AN EFFICIENT COAXIAL ROTARY WING
MICRO AIR VEHICLE

Felipe Bohorquez, Doctor of Philosophy, 2007

Dissertation directed by: Professor Darryll Pines
Department of Aerospace Engineering

Rotary-wing Micro air vehicles (MAVs) due to their unique hovering and low-speed flight capabilities are specially suited for missions that require operation in constrained spaces. Size restrictions force MAVs to operate in a low Reynolds number aerodynamic regime where viscous effects are dominant. This results in poor aerodynamic performance of conventional airfoils and rotor configurations. This dissertation explores the design issues that affect the hover performance of small-scale rotors and the implementation of a working coaxial MAV prototype.

A computerized hover test stand was used for the systematic testing of single and coaxial small-scale rotors. Thin circular arcs were chosen for blade manufacturing because of their good aerodynamic characteristics at low Reynolds numbers, and simplified parameterization. Influence of airfoil geometry on single rotor hover performance was studied on untwisted rectangular blades. Non rectangular blades were used to study coupled airfoil and blade parameters. Tip tapered geometries were manufactured by removing material from baseline rectangular blades producing

a coupling between blade planform, twist distribution, and spanwise airfoil shape. Performance gains were obtained by introducing large negative twist angles over short radial distances at the blade tips. A parametric study of the blade geometries resulted in maximum figures of merit of 0.65.

Coaxial rotor performance at torque equilibrium was explored for different trims and operating conditions. It was found that the upper rotor was marginally affected by the lower one at spacings larger than 35% of the rotor radius, and that it produced about 60% of the total thrust. Experiments showed that power loading was maximized when higher collectives were used at the lower rotor, resulting in sizable differences in rotational speed between rotors.

The CFD solver INS2d was used for a two-dimensional parametric aerodynamic study of circular arc airfoils. Lift, drag, and moment coefficients were explored over a range of Reynolds numbers. Validation with wind-tunnel data showed that lift predictions were satisfactory; however, drag was under-predicted at low angles of attack. The CFD database was integrated to a BEMT rotor model through a parameterization that coupled blade planform with twist distribution and airfoil shape. Thrust and maximum FM predictions were satisfactory for rectangular and non-rectangular blades with maximum cambers of 6% and below. The BEMT model was extended to the coaxial rotor case, producing good thrust and power predictions with errors within 5% of the experimental measurements. The approach validated the use of analytical and numerical tools commonly used in full-scale analysis, and proved to be a versatile system design tool.

A fully functional coaxial MAV was developed based on the aerodynamic studies performed. Transmission, rotors, and swashplate were designed from scratch. Batteries, motors, and electronics were carefully selected off-the-shelf components. The prototype has been used as a testing platform for control systems and algorithms.

ROTOR HOVER PERFORMANCE AND SYSTEM DESIGN OF AN EFFICENT COAXIAL ROTARY WING MICRO AIR VEHICLE

by

Felipe Bohorquez

Dissertation submitted to the Faculty of the Graduate School of the
University of Maryland, College Park in partial fulfillment
of the requirements for the degree of
Doctor of Philosophy
2007

Advisory Committee:

Professor Darryll Pines, Chair/Advisor
Professor Amr Baz
Professor Inderjit Chopra
Professor Norman Wereley
Professor James Baeder

ACKNOWLEDGMENTS

Several years ago I showed up at Dr. Pines office looking for an opportunity. I was just a guy from a distant place with lots of enthusiasm that had missed all the application deadlines. Somehow, he saw my potential and gave me the chance to be a grad student at the Rotorcraft Center. I owe my gratitude to him for believing in me, for his support, and for his guidance through the course of this research. I would also like to thank my committee, especially Dr. Chopra, for their advice and support.

I would like to acknowledge the invaluable help of Jayant Sirohi, he introduced me to the lab, and taught me the fundamental skills that were essential for most of the experimental aspects of this work. We shared endless hours tinkering with experimental setups and MAV prototypes, while having fun with our peers at the Smart Structures lab. My colleagues Paul Samuel, Jason Pereira, Joe Conroy, Anubav Datta, Atul Jayasimha, and Ron Couch not only helped me on various aspect of my research, but also enriched in many ways my graduate student life.

Some of the students of the CFD lab were incredibly patient and helpful answering thoroughly the many questions I had. Karthik Duraisamy, Eric Shroeder, Vinod Lakshminarayan, Falcon Rankins, and Brandon Bush, thanks for all your help.

I would also like to acknowledge some of the staff members, Becky, Julia, Debora and specially Pat Baker, who guided me through a maze of deadlines and paper work.

Grad student life would have been less enjoyable without my lunch buddies and good friends Natalia Perez, Andres Garay, Ashish Purekar, Carlos Malpica, Sandra Ugrina, and Maria Ribera. We will always cherish the memories of the culinary delicacies of suburban Maryland.

I owe my deepest gratitude to my family, my mother, father, and sister, and to Maria Francisca, Gonzalo, and Claudia. They are the foundation of who I am and have always believed in me.

Finally and most importantly, I would like to thank my wife Patricia for being the sweetest, most inspiring woman one can imagine. She calmly dealt with the stress of two Ph.Ds, hers and mine. Her constant love and support kept me going. Without her this journey would have been impossible.

TABLE OF CONTENTS

4 Sectional Airfoil Characteristics from CFD 117

LIST OF TABLES

LIST OF FIGURES

Chapter 1

Introduction

1.1 Historical Background

At the end of the 19th Century, dozens of people around the world were trying to develop the first powered heavier-than-air machine that could finally let Man experience the timeless dream of flying. On December 17 1903, the Wright brothers achieved that dream, making history at Kitty Hawk North Carolina by successfully flying their airplane for twelve seconds. However, the foundations of this challenging enterprise were layed out more than a century earlier by the sometimes called "Father of Aviation", Sir George Cayley. Cayley was the first researcher that used a scientific approach to the problem of flying. As is common in the history of science, he observed nature and tried to learn from it. He studied the cross section of bird wings and, using a rudimentary whirling arm apparatus, identified the positive effect of camber on lift generation. His 1804 experiments can be considered the first aerodynamic airfoil study in history.

The German civil engineer Otto Lilienthal also made important contributions to the development of the modern airplane. He was the first researcher to make a serious systematic effort to develop pilot controlled gliders. He built and tested eighteen different models of his gliders, achieving relative success and inspiring the Wright brothers to take on the invention of the airplane.

Cayley, Lilienthal, and specially the Wright brothers experimented with small-scale models that were used to extrapolate the characteristics of their larger scale prototypes. In a consistent way, they all converged to optimal airfoil shapes similar to those of the larger birds. The factor known as Reynolds number was a new concept, unknown to the aviation pioneers. Inadvertently, they became the first low Reynolds number aerodynamic researchers. In fact, the Wright brothers' wind tunnel was used to test wing sections at Reynolds numbers close to 100,000, as opposed to the 1.8 million chord-based Re that their flying prototype had during cruise.

The historic Kitty Hawk flight was the starting point of a race for faster, larger, and more powerful vehicles that still continues today. Low Reynolds number fluid mechanics research was a secondary problem that did not have a motivation. Only until the early 1990s, technology was mature enough in fields as diverse as electronics, energy storage, and energy conversion to seriously consider practical uses for small flying machines. Technology made a full circle; scientists were once again revisiting the results and contributions of the aeronautic pioneers. This time, however, with the idea of developing smaller and slower vehicles.

1.2 Motivation and Problem Statement

The concept of Micro Air Vehicles (MAVs) was first introduced in 1992 in a DARPA workshop titled “Future Technology - Driven Revolutions in Military Operations”. The idea gained popularity, and a series of feasibility studies were performed in the following years by the Lincoln Laboratories, and the U.S Naval Research Laboratory. The positive outcome of the preliminary studies, led to a DARPA sponsored 35 million dollars program.

The program goal was to develop inexpensive flying robots with no dimension exceeding 6 inches (15.24 cm), an endurance of at least an hour, and a weight of no more than 100 grams. This is an order of magnitude smaller than any previously developed system. The final product was intended to be used in a series of military and civilian mission, such as over-the-hill reconnaissance, indoor/outdoor covert imaging, biological or chemical agent detection, traffic monitoring, and urban intelligence gathering. This meant that practical MAVs had to be capable of real-time imagery and/or sensing with a high degree of autonomy. By the end of phase II of the program a series of prototypes with different configurations were developed by the participants. These included the fixed-wing Lockheed-Sanders “Microstar”, the CalTech-Aerovironment-UCLA ornithopter “Microbat”, the Lutronix Corporation micro helicopter “Kolibri”, MicroCraft’s Small Lift Augmented Ducted Fan “ISTAR” and Aerovironment’s “Black Widow” flying wing.

Figure 1.1 shows the 2003 performance in terms of weight and endurance of a series of small-scale vehicles including the DARPA sponsored designs. The figure clearly shows that the objective set is far from being reached. Fixed wing vehicles meet size and weight constraints, but are lacking in endurance. For rotary and flapping wing vehicles, even with larger and heavier designs, endurance times are shorter than for the fixed wing configurations. After the termination of the program, development continued for the Black Widow and the ISTAR, mainly in the areas of autonomous navigation and control. Since then, only marginal improvements in flight performance have been achieved.

Fixed wing vehicles are well suited for outdoor reconnaissance missions that do not require maneuvering in tightly constrained spaces. However, for missions around or within buildings hovering vehicles have a clear advantage over fixed wings configurations. A stealthy hovering MAV can fly indoors without being detected and can potentially have the ability to “perch and stare”, providing tactical reconnaissance and surveillance for extended periods of time with low risk of being detected. Two different MAV configuration are capable of hovering: flapping and rotary wing vehicles. Up to date, the only hovering flapping wing vehicle built is the MENTOR from SRI International, shown in Figure 1.1. It can achieve stable hover and forward flight but its complex kinematics and loud operating conditions - due to the wing flapping - hindered any further development. On the other hand, rotary wing vehicles can adapt some of the technology used in full-scale vehicles and require simpler mechanics. Aerodynamic noise is not an issue, and if electric power is used, overall noise levels can be kept at a minimum. These characteristics make the rotary wing configurations specially attractive for MAV applications.

The main difficulty in achieving a better performance with rotary wing vehicle comes from the large hover power requirements. Hover is an intrinsically high-power flight state with considerably larger energy requirements than cruise for fixed wing vehicles; this fact is independent of scale. If hover extends for a significant fraction of the mission duration, hover efficiency becomes a key vehicle characteristic that must be carefully addressed.

The size constraints of MAVs, forces wings and rotors to work at Reynolds numbers much closer to the ones faced by small birds and insects than to previously developed man-made systems. Figure 1.2 shows Reynolds number vs. Mass for a wide range of animals and aircraft. MAVs lie within the shaded region at the lower left corner of the graph, bounded by Re between 2,000 and 100,000. At these Reynolds numbers, viscous effects in the flow are dominant over the inertial ones, boundary layers are thick and undergo several complex phenomena. Separation, transition, and reattachment can all occur within a short chordwise distance, forming laminar separation bubbles that have a strong adverse effect on the lifting surface characteristics.

Considering that hover efficiency depends largely on airfoil characteristics, sub-scale rotors are expected to have a lower hovering efficiency than full-scale ones. Before the current investigation was performed, hover efficiency of small-scale rotors below Reynolds numbers of 100,000 was uncharted territory. The only available experimental data could be obtained from model testing intended for full-scale design at Re of one million and above.

In the current investigation, initial hover rotor testing showed that small-scale rotors with airfoils and blade geometries similar to those found in full-scale vehicles had maximum Figures of Merit (FM), of the order of 0.35. This is a very low value considering that full-scale helicopters can reach maximum FMs in the vicinity of 0.8. In order to improve these numbers it is necessary not only to consider two dimensional airfoil characteristics but the overall rotor design. Blade parameters such as taper twist and collective have to be adapted to the radically different flow conditions. Some aspects of these fundamental problems are addressed in the following chapters of the dissertation.

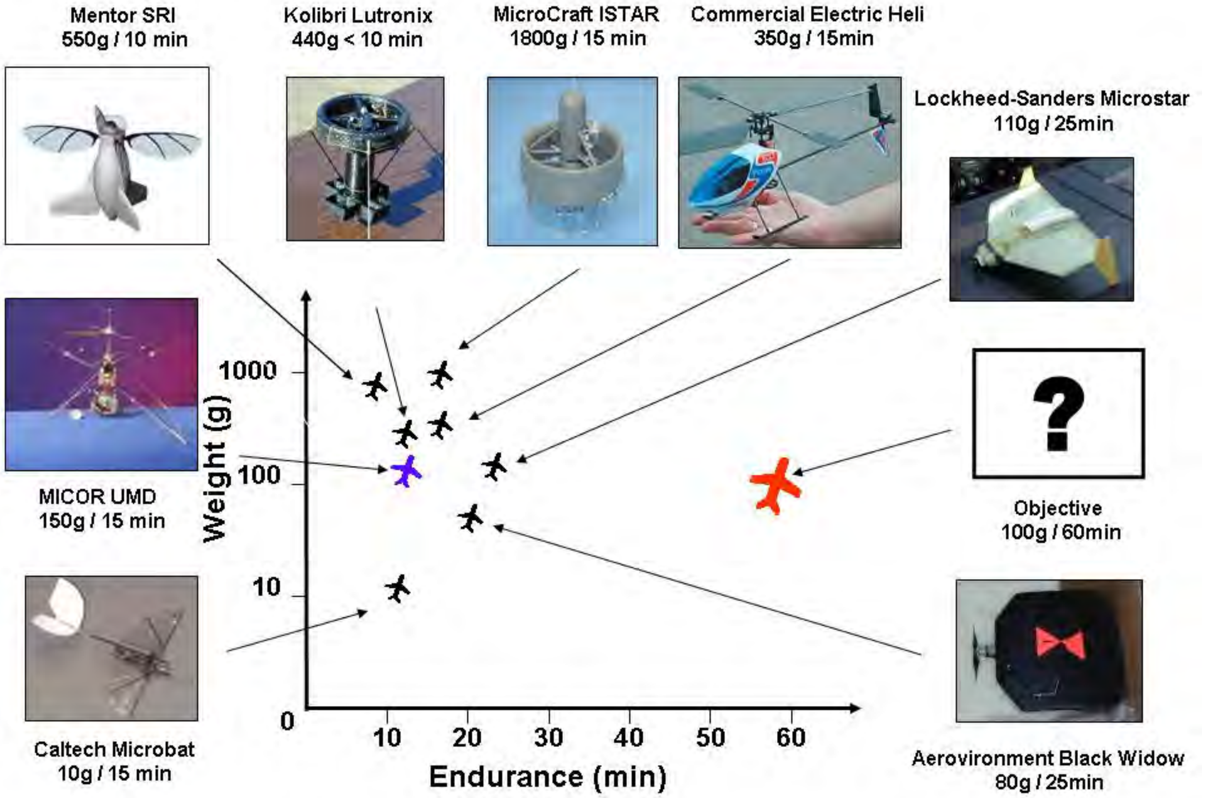

Figure 1.1: Relative performance of various micro air vehicles.

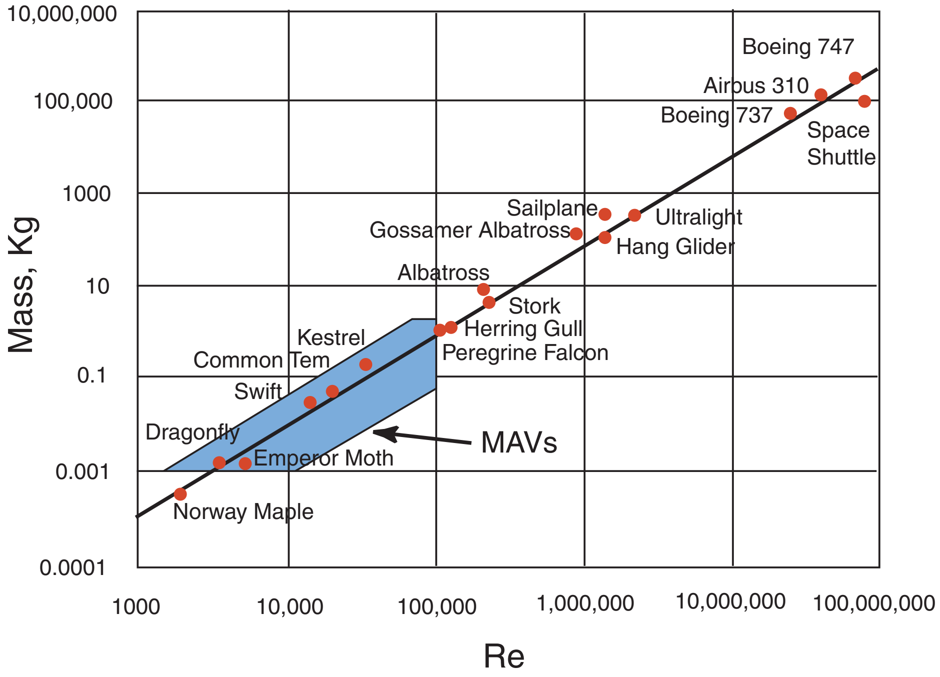

Figure 1.2: Re vs. Mass for animal and Man-made vehicles from data in Ref [19].

1.3 Literature Review

Two main areas of research are relevant for the present investigation, low Reynolds number airfoil aerodynamics, and small-scale single and coaxial hover rotor modeling and optimization. Airfoil aerodynamics have been studied experimentally on wind tunnels since the dawn of the 20th Century, and computationally for no more than 20 years. However, only during the last decade computational models have approached the problem of low Reynolds number flows. The following literature review presents the main contributions on the different areas of interests.

1.3.1 Experimental Low Re Airfoil Studies

One of the most influential publications in the field was published by Schmitz Ref. [1] in 1941. The report "Aerodynamics of the Model Airplane", was awarded the Ludwing Prandtl prize and has a foreword praising the interesting results by Prandtl himself. Schmitz performed his research in a wind tunnel with turbulence levels similar to those found in free flight (0.1%). Under those flow conditions, he was able to observe for the first time the hysteresis loops in the lift and drag of airfoils at Reynolds numbers between 40,000 and 160,000. He also identified the reduction in the critical Reynolds number due to the added turbulence produced by placing a wire upstream of the leading edge.

Bruining published in 1979 lift and drag wind tunnel measurements on two-dimensional circular arc steel plates Ref. [3]. The research studied the effects of a turbulence-inducing spar mounted at different positions along the blade chord. He tested at Reynolds numbers of 60,000, 100,000 and 200,000. This relatively unknown work is relevant to the current research because of the similarities in the airfoils investigated.

In 1980 a comprehensive airfoil catalog was published by Althaus Ref. [4], the measurements were made in a low turbulence wind tunnel at the University of Stuttgart in West Germany. Moment coefficients were not measured, but lift and drag coefficients of 30 airfoils at Reynolds numbers between 40,000 and 250,000 are presented.

Carmichael published in 1981 his "Low Reynold number airfoil survey" (Ref. [5]). This document compiles the state of the art in low Reynolds number flow physics at the time, while giving a historical perspective of the evolution of the field. A detailed bibliography of airfoil, wind tunnel, and free flight testing is presented, as well as a discussion and additional references about the use of boundary layer trips.

Miley Ref. [2] published in 1982 a well known airfoil catalog intended to be used in the design of small wind turbines. Problems associated with presenting airfoil data at large angles of attack were addressed as well as airfoil behavior and the effects of Reynolds number, surface roughness, and turbulence.

Mueller from the University of Notre Dame has been working with low Reynolds number flows since the early eighties; he has performed a wide range of wind tunnels tests, measuring aerodynamic coefficients and documenting flow characteristics. Mueller performed fundamental research at low Reynolds number on flow visualization (Ref. [6]), boundary layers and laminar separation bubbles (Ref. [7, 8, 9]) and two and three dimensional aerodynamic characteristics of wings (Ref. [10, 11]).

Mueller's research is specially relevant since in some of his papers he tested circular arc airfoils, similar to those used in the current work.

Selig, from UIUC, has been working over the last 20 years on systematic wind tunnel testing of more than 200 airfoils at Reynolds numbers between 40,000 and 500,000. This set of data is especially valuable since all tests were performed at the same facilities with the same methodology, making quantitative comparison within the set very accurate. Results have been compiled in a series of 3 volumes (Refs. [12, 13]). Selig has also worked on inverse design methodologies and optimization of airfoils at low Reynolds numbers (Ref. [14, 15]).

Laitone from Berkeley, tried to explain why at Reynolds numbers below 70,000 thin curved plates with sharp leading edges are aerodynamically superior to all other known round-nosed airfoils (Refs. [16, 17, 18]). His research can be considered a continuation of the seminal work of Schmitz. Laitone performed wind tunnel measurements of forces and moment, as well as pressure distribution tests and some flow visualization. His main contribution was showing that for certain airfoils aerodynamic lift is not determined by the Kutta-Joukowsky trailing edge condition.

An excellent review paper that covers the main issues associated with the aerodynamics of small-scale flight was written by Lowson (Ref. [19]). He discusses the flow characteristics that make low Reynolds number testing very sensitive to experimental conditions, leading to a large variation in the results at different experimental facilities.

A few researchers have done experimental work in the ultra-low Reynolds number range of 10,000 and below. This range is so distant from regimes faced by traditional man-made machines, that experimental biologists, and not engineers, have been the ones producing a significant share of the results. Most of their work has been on insect flapping flight; however, some steady-state studies relevant for this dissertation have been performed.

Sunada for example (Refs. [20, 21, 22]), studied the hydrodynamic characteristics of wings at Reynolds number of 4,000. His parametric studies gave results consistent with trends observed at higher Re in air. Okamoto (Ref. [23]) performed a similar study in a wind tunnel. He used steady state measurement as a baseline for unsteady wing characterization.

One of the most recognized scientist that has contributed to the understanding of unsteady low Reynolds number flows is Ellington, a professor of Animal Mechanics at the Department of Zoology in Cambridge University. He identified the existence of leading edge vortices on insect wings, and showed in Ref. [24] how they work as an aerodynamic unsteady mechanism that enhances lift production. A fraction of his results correspond to wind tunnel and rotor tests used as steady data baseline Ref. [25].

Dickinson from Caltech has also contributed to the understanding of insect flight. His research covers several areas including aerodynamics, flight energetics, control of flight maneuvers, and visual flight control. Using a Dynamically scaled model of a flapping insect known as the "Robofly" he identified in Refs. [26, 27] the three main unsteady aerodynamic mechanisms for enhanced lift production: delayed stall, wake capture and rotational circulation. Even though his results are more relevant to flapping flight researchers, they are important for the understanding of the limitations of conventional fixed and rotary wing vehicles.

1.3.2 Vehicle Design and Development

Design and system integration of vehicles is also an aspect of MAVs that has been explored by the scientific community. In this section the most representative study cases that have been published are presented.

In early 2000, Samuel and Sirohi, at the time graduate students of the Alfred Gessow Rotorcraft Center at the University of Maryland, presented in Ref. [28] a preliminary design study of a micro coaxial rotorcraft later known as "MICOR". This study was the starting point for the research presented in this dissertation. The main design issues and challenges faced when implementing a rotary wing MAV were identified in that paper.

Another design report on hovering MAVs comes from Allied Aerospace Ref. [29]. The paper covers the basic configuration, control system, ground and flight-test results of the ducted-fan iSTAR, one of the DARPA funded vehicles shown in Figure 1.1. Aerodynamic performance or rotor design is not addressed, however valuable information about power requirements and control strategies is provided.

The Mesicopter is a multi-rotor rotary-wing vehicle, considerably smaller than an MAV, having a target weight between 3 and 15 grams. Its aerodynamic design and subsystem configuration are presented in Ref. [31]. Several prototypes have been built and evaluated, however successful flight testing has not been reported.

Lockheed Martin and Aerovironment also produced design reports on the "MicroSTAR" and "Black Widow" fixed wing MAVs (Refs. [32, 30]). An explanation of the design methodology and a detailed description of each subsystem are presented is the papers. Aerovironment's custom electronics, shown in its infancy, would evolve over the years to make the Black Widow the most successful autonomous fixed wing MAV.

Flapping wing vehicles are considerably more complex mechanically and aerodynamically than rotary and fixed wing designs. Over the last few years fundamental aerodynamic research has increased the understanding of flapping flight, however few technical publications address the actual design of such vehicles. Wing design, manufacturing processes and wing performance for the Caltech "Microbat" are presented in Ref. [33]. The only successful hovering flapping vehicle up to the publication date of this document is the MENTOR, developed by SRI. The technology used was proprietary and only fragments of design information are available from Ref. [34].

One of the most interesting publications that explores a variety of hovering MAV configurations is Ref. [35]. The paper provides pictures, characteristics and some aerodynamic performance measurements of a quad-rotor, a tandem twin fuselage tilt-rotor, a coaxial helicopter and a morphing fixed/rotary-wing vehicle called the "mini-morpher". All configurations were built and flight tested, making this a particularly useful reference.

A vehicle known as the "GIANT" was developed at the University of Maryland over the course of the research presented in this dissertation. Dr. Sirohi and Dr.

Tishchenko, designed and implemented a ducted fan, single rotor vehicle that uses a set of vanes in the downwash to counter act the motor torque. The vehicle was designed to have high hover endurance and passive stability. The paper in Ref. [36] describes the vehicle configuration and provides experimental data of ducted and isolated rotor performance, as well as the effect of the anti-torque vanes on power consumption.

A paper that makes use of published data to compare flapping, rotating and fixed wing vehicle's performance was published by Woods et al. Ref. [37]. Energy and Power requirements for the three configurations were calculated, and an optimization procedure was used to evaluate the best choice of vehicle for a series of missions. The paper provides first order equations and airfoil coefficients, useful to make comparisons and rough power estimates for a variety of missions. A similar paper by Baxter (Ref. [38]), uses classical flight mechanics equations with simple corrections to introduce Reynolds number effects to calculate power requirements of fixed and flapping wing vehicles.

1.3.3 Coaxial Helicopter Aerodynamics

When designing a helicopter, counter-acting the rotor torque is a key issue. The concept of a coaxial helicopter, with two rotors spinning in opposite directions instead of a tail rotor, has been present since the early stages of vertical flight Ref. [39]. Considering that one of the outcomes of the current research was the development of a coaxial MAV, the most relevant publications that treat the subject are presented.

A NASA report that gives a broad perspective of the aerodynamic issues and state of the art of coaxial helicopters technology was published by Coleman in Ref. [40]. His survey summarizes the main publications on the topic from American, Russian, Japanese, British and German sources. Experimental data and analysis that address rotor separation distance, load sharing between the rotors, wake structure, solidity effects and the unique characteristics of the coaxial configuration are presented.

Few experimental measurements of coaxial rotor performance are available in the literature, these include the full-scale tests performed by Harrington (Ref. [41]) and Dingledein (Ref. [42]) in the Langley full-scale wind tunnel, and the data presented by Nagashima in Ref. [43]. Reference [44] is a recent publication that experimentally explores the maximization of the thrust-torque ratio on a small-scale coaxial rotor. The results presented are not specific for low Reynolds numbers and suggest an interesting result that is discussed in chapter 6.

Modeling of coaxial rotors has been undertaken by various authors such as Saito and Azuma (Ref. [45], Andrew (Ref. [46]) and Zimmer (Ref. [47]). Various approaches that generally combine momentum theory, blade element theory, vortex, and lifting line models have been implemented in an attempt to calculate the power requirements of coaxial rotors. Generally a good predictive capability has been achieved. However, most of the algorithms require empirical models of the wake geometry. Bagai in Ref. [48] uses the Free Vortex Method (FVM) to study the tandem, tilt-rotor and coaxial configurations. The FVM approach makes use of considerable more computational resources, but has the advantage of not requiring a prescribe wake geometry.

1.3.4 Computational Studies

Wind tunnel low Reynolds number experimentation requires expensive infrastructure and a careful and thorough methodology that guarantees the quality of the results. These difficulties and the limited experimental data available, make numerical tools for aerodynamic design extremely useful. Airfoil synthesis and selection, as well as vehicle development can be accelerated through the use of Computational Fluid Dynamics (CFD) as long as proper validation of the numerical results is done. The following are some relevant publications that cover the development and use of CFD tools in the low Reynolds number regime.

The two-dimensional incompressible Navier-Stokes solver INS2d developed by Rogers (Refs. [50, 51]) was used by Kunz in Refs. [52, 53] to analyze and optimize the performance of airfoils at Reynolds numbers below 10,000. In Kunz's work INS2d was used mostly for single grid steady calculations assuming fully laminar flow. Limited experimental validation of the computed airfoil properties was made. Rotor performance calculations were done using two dimensional airfoil characteristics and a blade element model. Rotor experimental results largely disagree with the predictions. Lack of blade structural stiffness and airfoil manufacturing imperfections were blamed for the discrepancies.

At Reynolds numbers above 10,000 the flow is not necessarily fully laminar, and turbulence models should be used. The occurrence of laminar separation bubbles in the range of interest adds another level of complexity to the problem.

Singh and Kellogg (Ref. [55, 56]) used XFOIL, a two dimensional panel method code (Ref. [57]), to perform parametric studies on thin cambered airfoils in the Reynolds number range of 60,000 to 150,000. The quality of the predictions is acceptable, showing how this computationally inexpensive approach can give first order estimates of airfoil coefficients, useful for preliminary design considerations.

Ramamurti implemented a finite element flow solver based on unstructured grids to study the characteristics of MAVs. In Ref. [58], inviscid and viscous flow simulations of two fixed wing MAVS are presented. The simulations use the Baldwin-Lomax turbulence model for the viscous cases. Aerodynamic characteristics of vehicle's finite wings are studied and the effects of the fuselage and propellers on wing performance were investigated.

Shum in Ref. [59] developed a computational model to investigate laminar separation bubbles. His model predicts separation, transition, and reattachment location on two-dimensional airfoils. Drag and bubble size predictions on an Eppler 387 airfoil were compared with experiments showing a good correlation in the Reynolds number range of 200,000 to 1,000,000.

Bohorquez et al. in Ref. [60] investigated experimentally and computationally the rotors of the first generation MICOR MAV, shown in Ref. [62]. The computational aspect of the research was performed using OVERFLOW-D (Ref. [63]), a Reynolds Averaged Compressible Navier-Stokes solver developed by the Army/NASA Rotorcraft Division. Overflow-D was used in Ref. [61] for the computational analysis of a martian prototype experiment. The martian vehicle prototype was designed to work at unique flow characteristics, combining low Reynolds numbers and high Mach numbers of the order of Re=60,000 and M=0.65 at the tip. In Bohorquez work, for cases in which turbulence is considered, the one-equation Baldwin-Barth turbulence model was used for closure. Results showed that rotor drag is well predicted; however, lift was largely over predicted leading to rotor performance values higher than the ones measured experimentally. Surface flow visualization performed on the rotor blades showed that the CFD results differ qualitatively from the experiments which show large areas of separated flow on the upper surface of the blades. This work was one of of the first attempts that compared experiments with CFD three dimensional predictions of MAV rotors.

The CFD group at the Rotorcraft Center of the University of Maryland has been working for more than a decade in the Transonic Unsteady Rotor Navier-Stokes solver - TURNS - . This compressible code was originally developed to solve flows at high Reynold and Mach numbers typical of full-scale helicopters. Part of the doctoral research of Gupta (Ref. [64, 65]) consisted in implementing a low Mach number pre-conditioner that allows now the use of TURNS at much lower Reynolds and Mach numbers. Schroeder (Ref. [66, 67]) validated the use of TURNS with the pre-conditioner for airfoil and rotor predictions at Reynolds numbers typical of MAVs. In his research, Schroeder performed two dimensional calculations for a variety of airfoils, he also did a three-dimensional case study of an MAV rotor. All cases were compared with experimental results from Refs. [10, 13, 69]. The work of Gupta and Schroeder played an important role in the computational aspects of this dissertation, considering that TURNS was used to obtain some of the results presented in chapter 4.

Lakshminarayan et al. also from the University of Maryland's Alfred Gessow Rotorcraft Center continued the work of Schroeder and published in Ref. [68] a computational study of an MAV rotor using an updated version of TURNS. Inviscid phenomena such as thrust, wake structure and tip vortex evolution were accurately predicted; however, drag and power were largely under-predicted when compared to the experimental data of Ref. [69].

1.4 Current Research

1.4.1 Objectives

The research presented in this dissertation has a total of five objectives.

As reported in the literature experimentation at low Reynolds numbers requires not only the appropriate facilities but also the correct methodology. This is true for wind tunnel testing and for hover rotor testing. the first objective of the current research is to develop and implement a test stand and experimental procedure that can be used to characterize small-scale single and coaxial rotors in hover.

The second objective is the experimental identification and characterization of an airfoil or family of airfoils suited for the implementation of efficient MAV rotors. Structural and manufacturing constraints need to be considered in order to apply the findings on a working prototype. Rotor design, and the effect of blade and airfoil parameters on hover performance are also explored in order to determine basic small-scale rotor design guidelines.

A third objective involves the development of a test stand and methodology to study coaxial rotors. Basic coaxial rotor parameters such as rotor spacing and collective settings as well as the effect of lower rotor design on hover performance are explored at a zero torque condition. This part of the investigation is aimed at finding the rotor parameters that guarantee the highest efficiency of a given coaxial rotor system.

The fourth objective is to implement and validate analytical and numerical models that can be efficiently used for the design and eventual optimization of MAV rotor systems. Tools widely used in the analysis of full-scale rotors such as Blade Element Momentum Theory (BEMT) and two-dimensional CFD airfoil calculations, are combined and validated with the rotor experiments used to accomplish the previous two research objectives.

A fifth and final objective of this dissertation is the implementation of a fully functional coaxial rotary-wing MAV that can be used as platform for the evaluation of sensors and the development of control systems. In order to accomplish this, not only rotor design and aerodynamic issues are considered. Powertrain design, vehicle configuration, stability and control strategies, energy storage and overall system integration issues have to be addressed.

1.4.2 Contributions

The key contributions of this research include:

1. Developed a hover stand for the testing of small-scale single and coaxial rotors. Hardware and software were customized to achieve excellent levels of accuracy, minimizing testing time and assuring repeatability of the results.
2. Performed systematic single rotor testing varying airfoil and blade parameters over a range of rotational speeds and collective pitch settings. Rotors with circular arc airfoils were evaluated on rectangular and tapered blades.
3. Circular arc airfoils were validated as a good choice for the implementation of rotary wing MAVs.
4. Identified key rotor parameters that affect hover performance of single small-scale rotors.
5. Performed a CFD parametric study of circular arc airfoils at Reynolds number ranging from 15,000 to 60,000.
6. Implemented and validated a hybrid Blade Element Momentum Theory / 2D-CFD algorithm to calculate hover rotor performance at low Reynolds numbers.
7. Developed a blade parameterization that facilitates blade geometry optimization within a well defined space.
8. Experimentally studied aerodynamic performance of MAV coaxial rotors at zero torque condition exploring the effects of main operating parameters.
9. Extended BEMT/CFD algorithm to use in the coaxial rotor configuration.

10. Designed and manufactured a swashplate ideal for small-scale single and coaxial rotary-wing vehicles.

11. Designed and manufactured working MAV coaxial prototypes stable enough to be easily flown without a control system. Vehicles are capable of perch and stare, indoor and limited outdoor flying. Motor characterization and subsystem integration were issues addressed.

1.4.3 Organization of Dissertation

This dissertation consists of seven chapters that show the logical progression followed through the course of the project. Chapter 1 introduces the topic giving a historical overview and showing the state of the art. A detailed literature review of the relevant topics is given. Chapter 2 describes the rotor test stand and methodology used in this investigation. The chapter presents the results of single rotor tests, where the effect of airfoil and rotor parameters in hover performance are investigated. The geometrical couplings between blade planform and airfoil shape used in this investigation are introduced illustrating with experimental results the performance benefits that can be obtained. Chapter 3 explains the modeling tools and analysis techniques used to model the rotors and to gain insight into the issues affecting their hover performance. Blade element momentum theory (BEMT) numerical implementation is presented, and a methodology to obtain airfoil characteristic from rotor tests is explained. Chapter 4 presents the methodology and results of CFD calculations of two dimensional airfoil characteristics at low Reynolds numbers. Results of a parametric study of aerodynamic characteristics of circular arc airfoils are presented. These are used to generate a database that covers a variety of Reynolds numbers, cambers, thickness ratios and angles of attack. In Chapter 5 the implementation of a hybrid method that uses BEMT and the database generated in Chapter 4 to calculate the performance of single rotors over a wide range of operating conditions. Blade parameterization is explained and the approach to perform a blade geometry optimization is presented. Chapter 6 describes the coaxial rotor testing methodology, and explores the effect on hover performance of key coaxial rotor parameters. BEMT is extended to the coaxial case and predictions are validated with experimental results. The last part of the chapter deals with the development of a practical coaxial MAV prototype. Motor characterization and general system integration is discussed. Special attention is placed on the conceptual design of a simple swashplate ideal for rotary-wing MAVs. Finally, Chapter 7 concludes and gives recommendation for the continuation of this research.

Chapter 2

Single Rotor Tests

2.1 Introduction

This chapter explains and describes the methodology and experimental setup used for evaluating and characterizing small-scale rotors in hover. Experimental results for single rotors are presented, exploring the effect of operational and geometric parameters on hover rotor performance.

2.2 Experimental Setup

In order to experimentally measure the performance of small-scale rotors, a hover tests stand was developed. Based on the performance metrics and the definitions of the coefficients presented in sections A.7.2 and A.7.3, it was clear that thrust and power are needed to establish rotor performance. Hence, three physical quantities need to be simultaneously measured by the test stand: thrust, torque and rotational speed. Through the course of the investigation two generations of test stands were developed. The first generation, shown in Figure 2.1 measured thrust and torque using two axial load cells. Single or coaxial rotor systems could be mounted on a transmission supported by a stem. The whole system could rotate freely, and moment was transmitted to a load cell by a 1 inch arm. Thrust was measured by the second load cell placed directly under the platforms shaft. The rotor system was mounted inverted such that the airflow traveled from bottom to top, avoiding any possible influence of in-ground effect on the measurements. The rotational speed of each rotor was determined using a Hall-effect sensor that was excited by an array of magnets attached to the rotating frame of the setup. Additionally, the voltage and current supplied to the motors were also measured to obtain the electrical power consumption. This first generation test stand was very sensitive to vibrations and imbalances of the rotor system. Hinge alignment and moment arm/load cell contact were a source of experimental error. Similarly the axial bearings supporting the main thrust shaft, introduced small amounts of friction, resulting in hysteresis loops in the thrust measurements when thrust changed direction.

The second generation test stand, shown in Figure 2.2, was designed to correct the flaws of the first setup. In this design, no hinges or bearings were used. Instead, torque was directly measured by a Transducer Techniques RTS-5 reaction torque sensor with a maximum capacity of 5 in-oz, and thrust was measured by a model 31 Sensotec load cell with 1000 g maximum capacity. Both sensors are rated at $1.5\,mV/V$ output.

The thrust cell is mounted directly on top of the torque sensor inside an aluminum housing. Thrust and torque are decoupled by using two horizontally mounted steel membranes that cannot transfer axial loads. Measurement do not present a hysteretical behavior regardless of the changes in thrust and torque, allowing for both positive and negative measurements. Sensitivity to vibrations produced by the rotor system was also greatly improved.

2.2.1 Data Acquisition System

The data from the test stand was collected using an electronic data acquisition system. A National Instruments DAQcard-6062E and a SC-2345 carrier box with NI-SCC modules were used for signal conditioning and data collection. A custom code specially tailored for the tests performed was developed in MATLAB and run on a laptop PC. The user friendly GUI interface is shown in Figure 2.4. The code was designed to simultaneously acquire up to eight channels while sending up to two analog control signals. Sampling rate in all tests was 1000 samples per second for each channel. For single rotor tests, five input channels and one output channel were used. For the coaxial tests, explained in detail in the Chapter 6, two additional input channel and a second output channel were required. Figure 2.3 shows a sketch

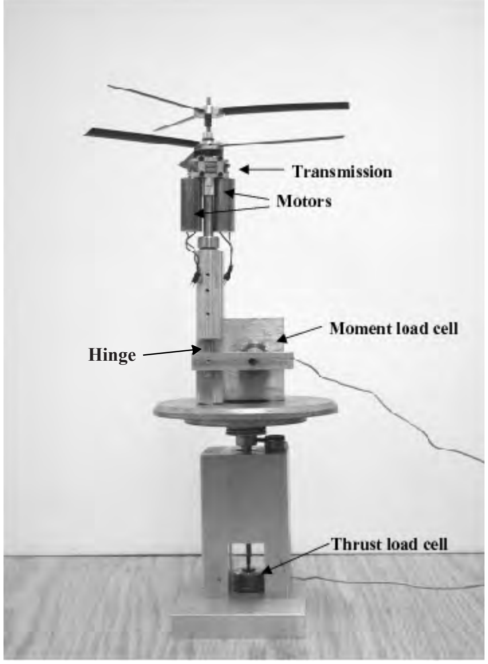

Figure 2.1: First generation hover test stand

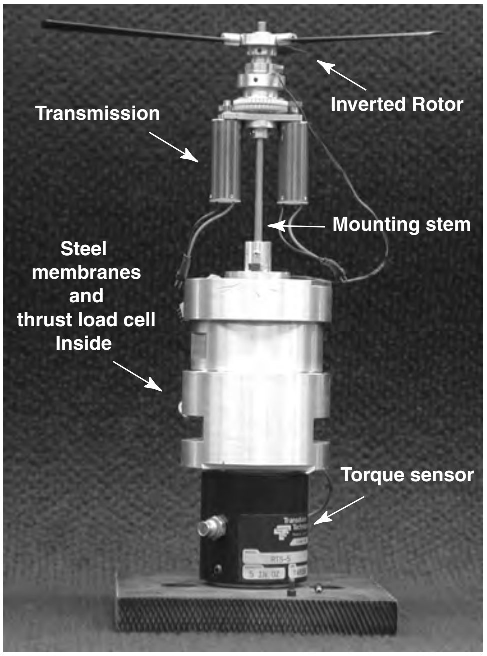

Figure 2.2: Second generation hover test stand

of the experimental setup.

A PI (Proportional - Integral) controller was programmed and embedded in the code, allowing to control the rotors' rotational speed with a feedback signal from any channel. The system was setup such that the desired rotational speed specified by the user was attained using the output from the Hall effect sensors as feedback. The PI controller output signals can be send to a power booster circuit or to a custom programmed micro-controller board, depending on the type of motors used. For conventional dc motors the current of the output control signal just needs to be amplified. However, for brushless motors, a low power pulse-width modulated signal fed to a speed controller varied the power and rotational speed of the motors. The micro-controller changes the duty cycle of the pulse-width modulated signals proportionally with the dc control voltages sent from the DAQ system. DC motors can also be used with speed controllers, so if required this setup is capable of interfacing with any motor or device compatible with standard RC pulse width modulated protocols.

2.2.2 System Calibration

The thrust and torque sensors were calibrated while mounted on the tests stand to avoid any changes in the calibration factors produced by pre-loading of the structure. An excitation voltage of 10V was provided, and maximum thrust and torque calibration values were 200 g and 0.125 N.m (1.37 in.oz) respectively. As observed in the calibration plots of Figure 2.5, over the range of interest the behavior of both sensors is very linear, having each an R^2 of practically one.

The limits of the torque and thrust values that can be measured by the balance are determined by the maximum rating of the sensors. However, it must be taken into account that the thrust cell is preloaded with the stem/transmission structure and by unavoidable compression forces present after the balance assembly. This reduces the thrust range to a maximum of $\approx$ 500 g when using a 1kg load cell. The torque sensor is not preloaded in any way; however, care must be taken not to damage the sensor by introducing large dynamic forces in the measurements.

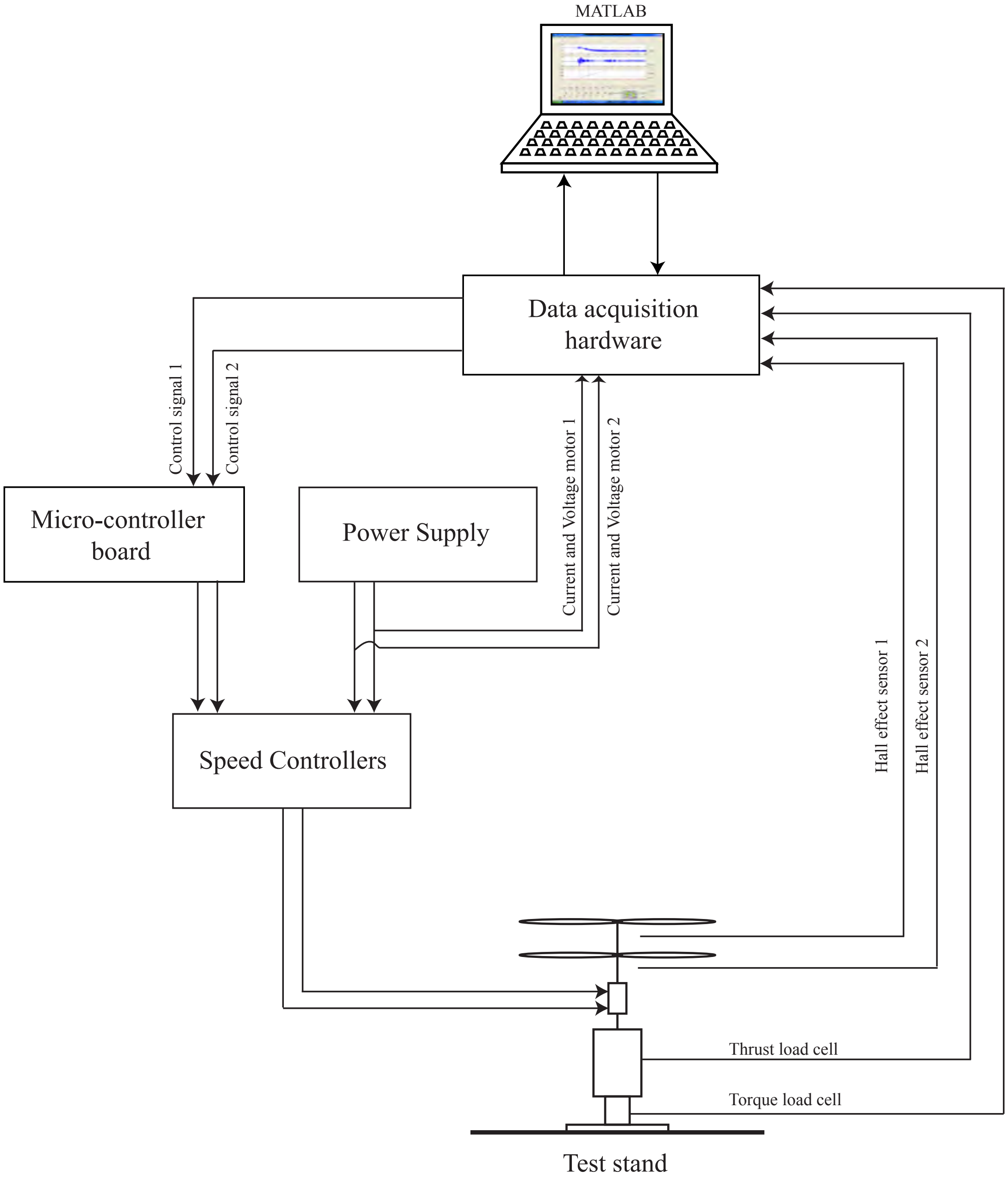

Figure 2.3: Hover stand experimental setup sketch.

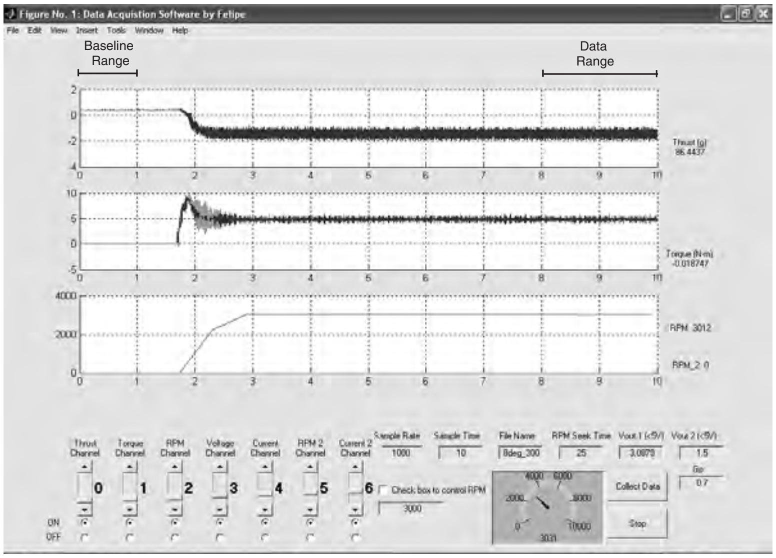

Thrust Channel 0
Torque Channel 1
RPM Channel 2
Voltage Channel 3
Current Channel 4
RPM 2 Channel 5
Current 2 Channel 6
☐ Check box to control RPM 3000
Sample Rate 1000
Sample Time 10
File Name 8deg_300
RPM Seek Time 25
Vout 1 (<5V) 3.0870
Vout 2 (<5V) 1.5
Gp 0.7

Figure 2.4: Sample screen of data acquisition software developed after a single rotor test

Rotational acceleration of the blades need to be kept at reasonable values based on their mass. When testing large rotors with heavy blades or assemblies with large inertias, shrouded rotors for example, the rotational speed needs to be ramped to the desired value to avoid damage to the stand.

2.2.3 Procedure for Data Acquisition

Before starting a new set of experiments, the test stand should always be recalibrated. Torque calibration is not sensitive to balance assembly procedure or external factors such as ambient temperature; however, it is recommended to check thrust calibration if transmission weight changes and when ambient temperature has considerably varied. The test transmission is designed such that the rotor hub can easily be removed by simply loosening a set-screw. Collective pitch of the blades is manually set on the unmounted rotors using a custom made protractor that provides a ±1/4 of degree precision. When performing test that sweep over a range of collectives, it is recommended to start from the angles that will produce the lowest levels of thrust, and gradually increase the collective. This eliminates the danger of accidentally overloading the stand. Every time the collective pitch is changed

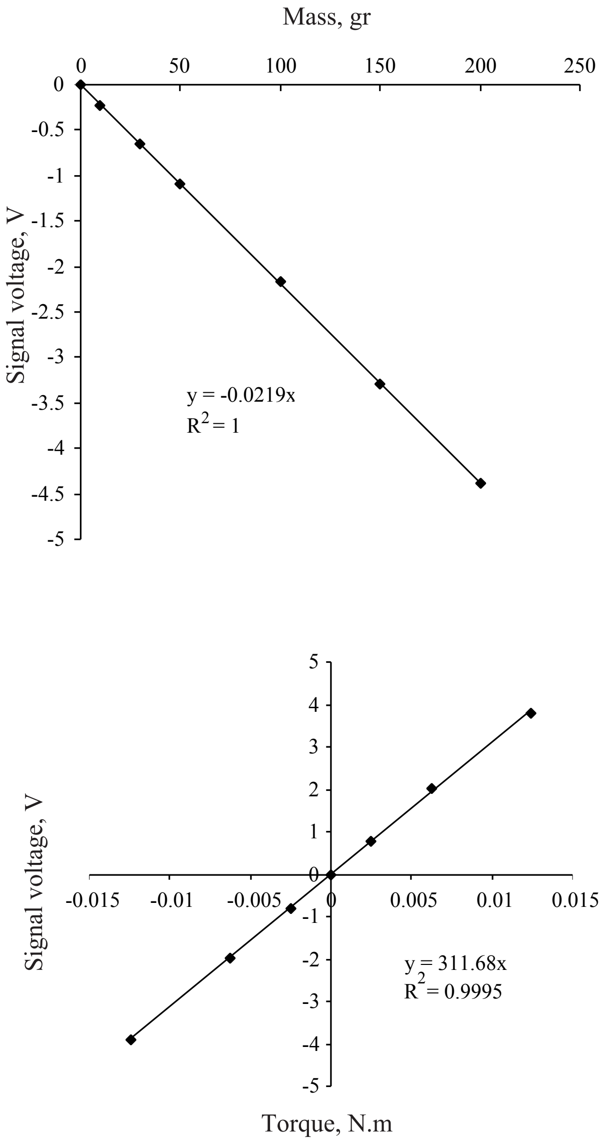

Figure 2.5: Thrust and torque calibration curves

the rotor balance and blade tracking needs to be checked, a standard RC propeller balancer was used for this purpose. After a collective pitch has been set, tests at all rotational speeds should be done sequentially. This minimizes the error in blade pitch setting between tests.

The data acquisition code performs each test in two steps. The first step, where no data is acquired, consists in finding the control signal that produces the desired rotational speed. This process takes between ten to fifteen seconds depending on the controller's constants and rotor settings. The control voltage found in step one is stored in memory and the rotor is stopped. In step two, for the single rotor tests, 10 seconds of data are captured. After the first 1.5 seconds, the control signal is ramped up to its desired value and kept unchanged for the rests of the data acquisition process. Since there is always a small drift in the voltage output of the sensors, an absolute voltage reference for a set of test should not be used. The small drifting values that accumulate over time can introduce significant errors over just a few minutes. This is why, the first second of data is used as baseline for the thrust and torque measurements. The output voltages are found by subtracting the average value of the first second from the average value of the two last seconds of acquired data. The buffer time between baseline and data sample is necessary to avoid any transient effects that might affect the measurements

2.2.4 Experimental Error Analysis

The main sources of error in the experiments are the standard deviations of the rotational speed and the mean voltages from the thrust and torque sensors. Typical values of the standard deviations of torque and thrust are about 1% of the mean values. Rotational speed error is related to the finite number of magnets that excite the Hall effect sensor. In the current tests four magnets were used, this means that for any rotational speed measured there is an uncertainty of a quarter revolution per sample. By counting the number of times a magnet passes over the Hall effect sensor in one second, there is an error of $0.25 \times 60 = 15$ RPM. If a sample of four seconds is considered, the uncertainty in the rotational speed is cut in half, being

3.75 RPM or 0.0131 $rad.s^{-1}$.

In order to calculate the uncertainty of the measurements, the Kline-McClintock (Ref. [74]) method for error propagation was used. For a given quantity R that depends on a series of independent variables x_1, x_2, x_3 the uncertainty of R (ω_R) as function of the uncertainties of the independent variables ($\omega_1, \omega_2, \omega_n$) is given by:

$$\omega_R = \left[\left(\frac{\partial R}{\partial x_1} \omega_1 \right)^2 + \left(\frac{\partial R}{\partial x_2} \omega_2 \right)^2 + \left(\frac{\partial R}{\partial x_n} \omega_n \right)^2 \right] \tag{2.1}$$

The uncertainty in thrust and power coefficients, figure of merit and power loading was calculated considering the errors in the measurements of thrust torque and rotational speed. Starting from the previously defined thrust and power coefficients

$$C_T = \frac{T}{\rho A \Omega^2 R^2} \tag{2.2}$$

First the partial derivatives of the above equation are found

$$\begin{aligned} \frac{\partial C_T}{\partial T} &= \frac{C_T}{T} \cdot 1 \\ \frac{\partial C_T}{\partial \Omega} &= (C_T \cdot \Omega)^2 \cdot \frac{-2}{\Omega^3} = \frac{-2\, C_T}{\Omega} \end{aligned}$$

Applying Kline-McClintock equation (cf. 2.1)

$$\Delta C_T = \sqrt{\left(\frac{C_T}{T} \cdot \Delta T \right)^2 + \left(\frac{-2\, C_T}{\Omega} \cdot \Delta \Omega \right)^2}$$

Finally

$$\frac{\Delta C_T}{C_T} = \sqrt{\left(\frac{\Delta T}{T} \right)^2 + 4 \left(\frac{\Delta \Omega}{\Omega} \right)^2} \tag{2.3}$$

Similarly for the power coefficient

$$C_P = \frac{P}{\rho A \Omega^3 R^3} = \frac{Q\, \Omega}{\rho A \Omega^3 R^3} = \frac{Q}{\rho A \Omega^2 R^3} \tag{2.4}$$

First the partial derivatives of the above equation are found

$$\begin{aligned}\frac{\partial C_P}{\partial Q} &= \frac{C_P}{Q}\,\cdot\,1\\ \frac{\partial C_P}{\partial \Omega} &= (C_P\,\cdot\,\Omega)^2\,\cdot\,\frac{-2}{\Omega^3} \;=\; \frac{-2\,C_P}{\Omega}\end{aligned}$$

Applying Kline-McClintock equation (cf. 2.1)

$$\frac{\Delta C_P}{C_P} \;=\; \sqrt{\left(\frac{\Delta Q}{Q}\right)^2 \,+\, 4\left(\frac{\Delta\Omega}{\Omega}\right)^2} \tag{2.5}$$

The figure of merit equation in terms of the measured quantities is:

$$FM = \frac{C_T^{\frac{3}{2}}}{\sqrt{2}\,C_P} \;=\; \frac{T^{\frac{3}{2}}}{Q\,\Omega\,\sqrt{2\rho A}} \tag{2.6}$$

Now partial derivatives are calculated

$$\begin{aligned}\frac{\partial FM}{\partial T} &= \frac{FM}{T^{\frac{3}{2}}}\cdot\frac{3}{2}T^{\frac{1}{2}} \;=\; \frac{3}{2}\cdot\frac{FM}{T}\\ \frac{\partial FM}{\partial Q} &= (FM\cdot Q)\cdot\frac{-1}{Q^2} \;=\; \frac{-FM}{Q}\\ \frac{\partial FM}{\partial \Omega} &= \frac{-FM}{\Omega}\end{aligned}$$

Applying Kline-McClintock equation (2.1)

$$\frac{\Delta FM}{FM} \;=\; \sqrt{\frac{9}{4}\left(\frac{\Delta T}{T}\right)^2 \,+\, \left(\frac{\Delta Q}{Q}\right)^2 \,+\, \left(\frac{\Delta\Omega}{\Omega}\right)^2} \tag{2.7}$$

Finally for the power loading:

$$PL = \frac{C_T}{\Omega R\,C_P} \;=\; \frac{T}{Q\Omega} \tag{2.8}$$

The partial derivatives are:

$$\begin{aligned}\frac{\partial PL}{\partial T} &= \frac{PL}{T}\\ \frac{\partial PL}{\partial Q} &= \frac{-PL}{Q}\\ \frac{\partial PL}{\partial \Omega} &= \frac{-PL}{\Omega}\end{aligned}$$

Applying Kline-McClintock equation (cf. 2.1)

$$\frac{\Delta PL}{PL} = \sqrt{\left(\frac{\Delta T}{T}\right)^2 + \left(\frac{\Delta Q}{Q}\right)^2 + \left(\frac{\Delta \Omega}{\Omega}\right)^2} \tag{2.9}$$

The error analysis showed that the average uncertainties for thrust and power coefficients at collectives between 8 and 18 deg are 1%. For the figure of merit and power loading the error propagates and the uncertainties are higher being 2% and 1.5% respectively. The previous results do not consider the error that can be introduced through the collective pitch settings. As mentioned before the instrument used to set the blade pitch has an accuracy of a quarter of a degree; however, the pitch angle difference between each blade is very small and can be considered negligible. This is why when comparing tests it is advised to look at the curves defined by the measurements, since the error in collective pitch will move the measured values along the curves without affecting its shape.

2.3 First Generation Rotors - Hover Performance

As explained in the Introduction this research was largely motivated by the development of a coaxial MAV. An initial proof of concept design, show in Figure 2.6 was conceived and implemented by Samuel and Sirohi (cf. Ref [75]). The performance of this first generation design was experimentally studied. This section presents the experimental results obtained.

2.3.1 First Generation Rotor Configuration

When the first generation rotors were conceived back in 1999 there was no existing vehicle or experimental data that could give hints on how to design an efficient small-scale rotor. Experience with full-scale vehicles was used in the choice of airfoil, solidity and number of blades. Each blade had a chord of 1 cm and a length of 7 cm. Three blades were attached to an aluminum hub trough pins designed to facilitate the setting of the collective pitch. No lead-lag or flapping hinges were used and the coning angle was set at zero degrees. The rotor diameter with blades, hub and pins

Figure 2.6: Proof of concept design from Ref. [75]

was 17.2 cm, resulting in a solidity of 0.111. Table 2.1 summarizes the geometric characteristics of this first generation rotor.

The airfoil chosen as baseline was an 8% camber circular arc with rounded leading and trailing edges as shown in Figure 2.8. The blades consisted of three layers of graphite/epoxy weave prepreg with a layup of (+45,0,+45). The symmetric composite layup gave the blades excellent bending and torsional stiffness while keeping weight at a minimum, each blade mass being just ≈ 0.2 g. To manufacture

Radius	86 (mm)
Root cut-out	15% Radius
N_o of blades	3
Blade planform	Rectangular
Blade chord	1o (mm)
solidity	0.111

Table 2.1: First generation rotor geometric characteristics

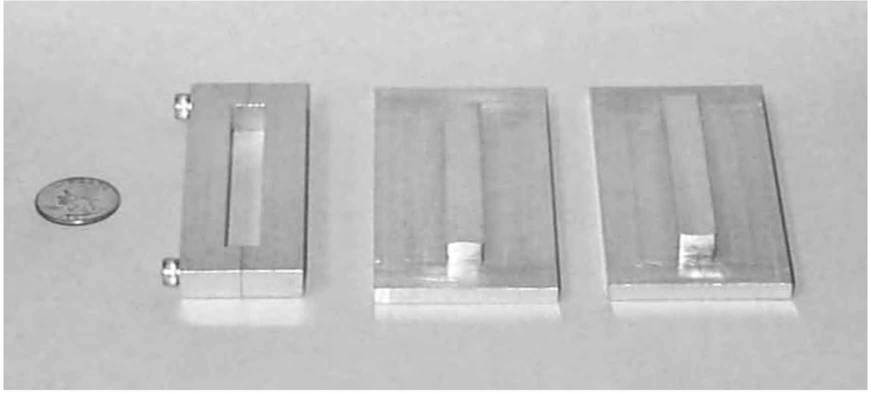

Figure 2.7: Mold used for first generation baseline blades.

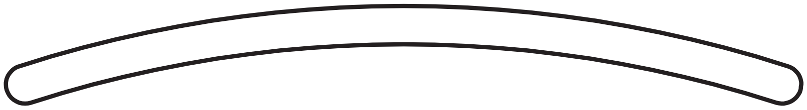

Figure 2.8: First generation 8% camber 5% TR airfoil.

the blades, a mold shown in Figure 2.7 composed of a top concave surface, a bottom convex surface, and an edge dam was machined from aluminum. The total thickness of the composite material was 0.5 mm resulting in blades with a thickness ratio of 5%.

Four different rotors with the same diameter, solidity and number of blades were tested. The baseline 8% camber blades were compared with untwisted NACA 0012 and flat plates with blunt edges having a thickness ratio of 3.7%. The effect of twist was explored by testing 8% camber blades having a linear twist of -10 degrees. The rotor, blades and transmission used in these tests are shown in Figure 2.9. Each rotor was tested at collectives ranging from 0 deg up to 18 deg in steps of 3 deg. Rotational speeds for each rotor were set from 2500 RPM up to 5000 RPM in steps of 500 RPM. Having a uniform chord of 1 cm, the tip Reynolds number varied from 15,000 up to 30,000 for the different rotational speeds.

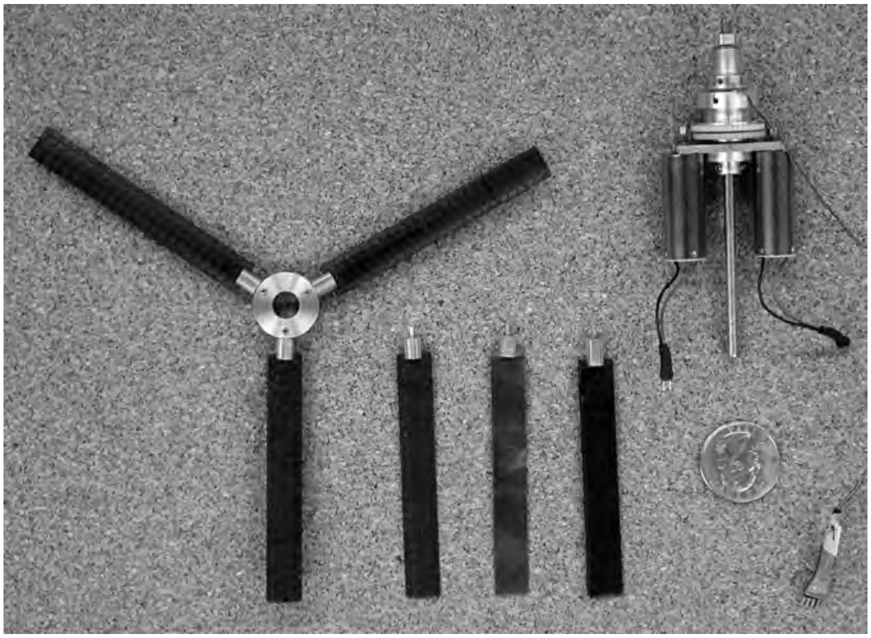

Figure 2.9: Rotor, blades and transmission used in the testing of the first generation rotor.

2.3.2 Experimental Results - First Generation Rotors.

Usually for full-scale helicopters, a specific rotational speed is used to study the performance of a given rotor. However, this is not the case in the current investigation. As opposed to traditional full-scale analysis, a range of rotational speeds is always considered for each rotor configuration. This makes difficult to grasp the relative thrust and power magnitudes when coefficients are used. Collective pitch vs. thrust and torque measurement for the 8% camber untwisted blades are presented in Figures 2.10 and 2.11. This is not a common way of showing the results since the quantities plotted have units; however, the figures are useful to have an idea of the magnitude of thrust and torque levels covered through the tests. It can be observed how the measurements define smooth curves for each rotational speed, and how the thrust and torque levels achieved span over two orders of magnitude. When this same information is plotted using thrust and power coefficients the resultant curves are now very close to each other. These relatively small variations in coefficients translate into clear differences in the figure of merit plots shown in Figure 2.14.

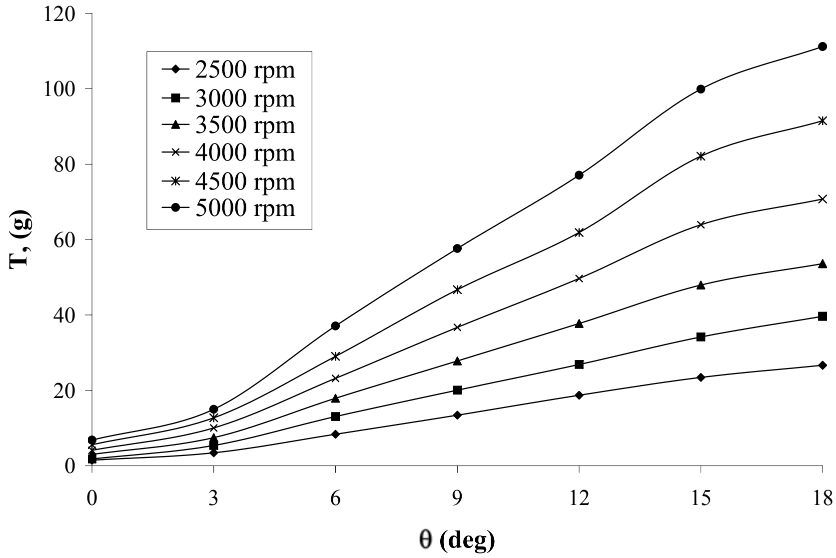

Figure 2.10: Collective vs. thrust first generation rotor with 8% camber circular arcsat various rotational speeds.

The shape of the figure of merit curves is similar to the ones observed in full-scale helicopters, varying from practically zero at low collectives up to a maximum value before reducing in magnitude.

Gessow in his classic book (Ref. [76]) explains the shape of the C_T vs. FM curve as follows. Recalling equation A.23, where the total power required by a hovering rotor is composed of a thrust dependent induced component and a constant profile component, it is expected to have a large denominator at low thrust levels, which results in low FM values. As C_T increases the relative importance of the constant profile term is reduced resulting in a higher figure of merit. The FM curve gradually reduces its slope as the magnitude of the profile power becomes a smaller part of the total power. Eventually the FM drops as a consequence of blade stall, where lift is lost and drag is increased.

The maximum FM reached by the 8% camber blades is achieved for all rotational speeds at a collective between 15 and 18 deg, a smaller collective pitch step was required to determine this angle more accurately. Maximum FM values vary from 0.5 up to 0.54 as tip speed increases, and are relatively low considering that modern full-scale helicopters can have maximum FM of the order of 0.8.

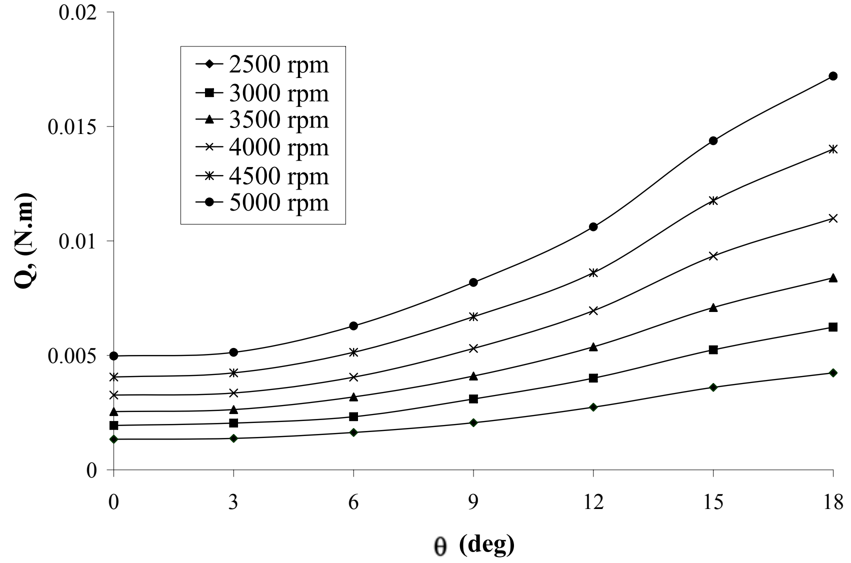

Figure 2.11: Collective vs. torque first generation rotor with 8% camber circular arcs at various rotational speeds.

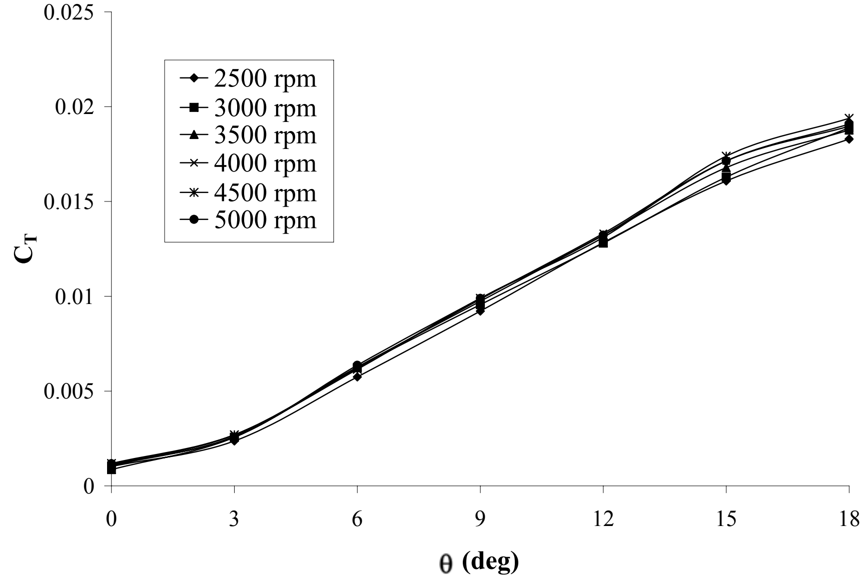

Figure 2.12: Collective vs. C_T first generation rotor with 8% camber circular arcs at various rotational speeds.

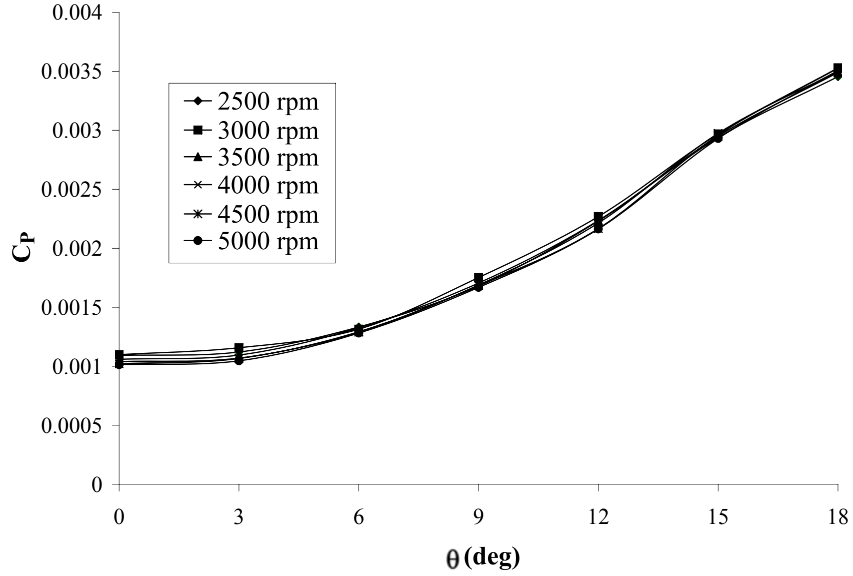

Figure 2.13: Collective vs. C_P first generation rotor with 8% camber circular arcs at various rotational speeds.

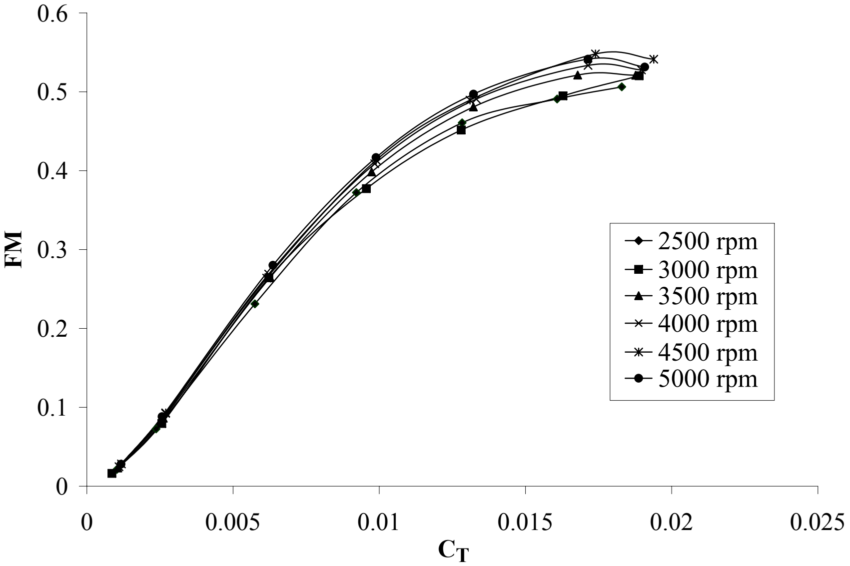

Figure 2.14: C_T vs. FM first generation rotor with 8% camber circular arcs at various rotational speeds.

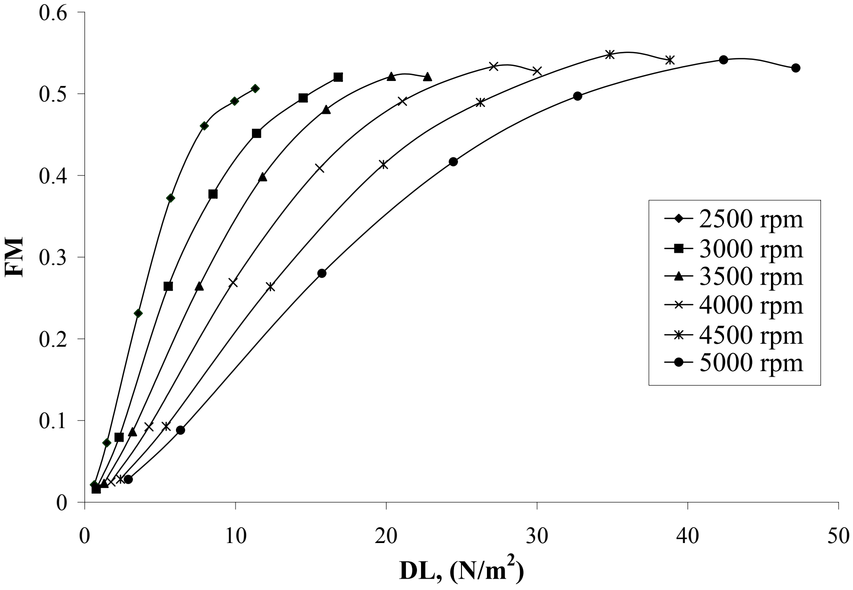

Figure 2.15: DL vs. FM first generation rotor with 8% camber circular arcs at various rotational speeds.

It is very important to clarify that since the C_T vs. FM curves of Figure 2.14 are obtained at different rotational speeds, a given C_T corresponds to different disk loadings (DL). As mentioned in section A.7.4, this results in an invalid comparison since at higher DL the contribution of induced power to the total power is larger, changing the ideal power required for each rotor. To further clarify this, FM is plotted vs. DL for the 8% camber blades in Figure 2.15.

Effect of airfoil shape

Now that some basic characteristics and performance of a baseline rotor have been established the effect of some airfoil and blade parameters can be explored. Two additional sets of rectangular untwisted blades were tested, NACA 0012 and flat plates. Airfoil shape had a dramatic effect on rotor performance in terms of thrust capabilities and hover efficiency. Thrust and torque experimental results for the NACA 0012 and flat plate blades as a function of the collective pitch are show in Figures 2.16, 2.17, 2.18 and 2.19. This same information is shown in coefficient form in Figures 2.20, 2.21, 2.22 and 2.23.

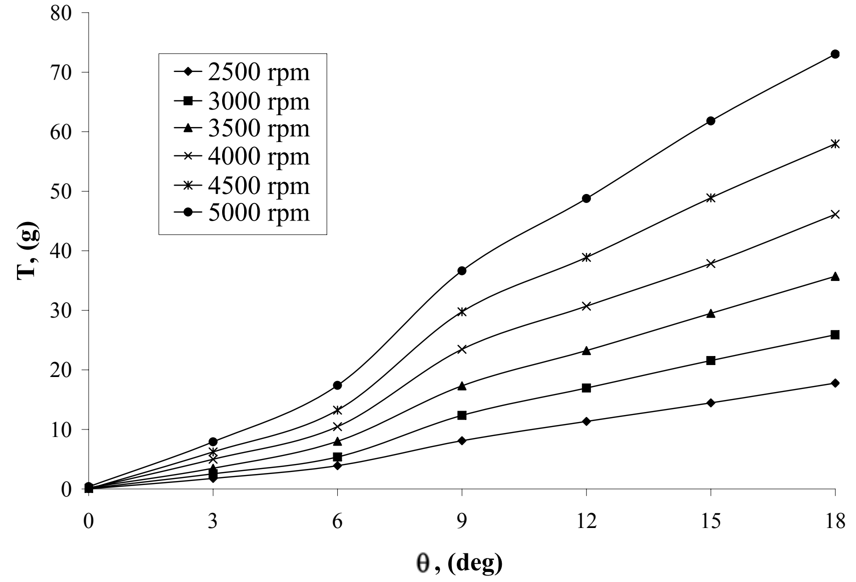

Figure 2.16: Collective vs. thrust of first generation rotor with NACA 0012 airfoil at various rotational speeds.

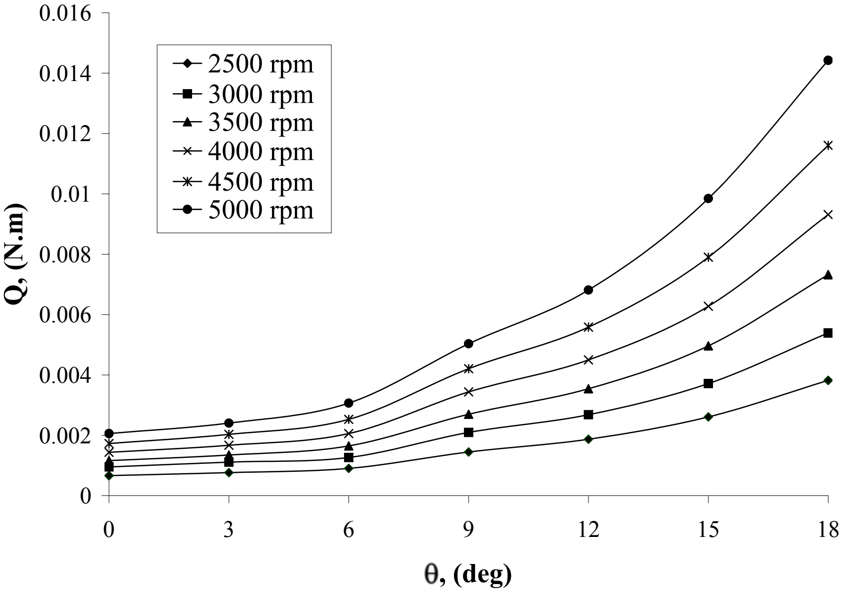

Figure 2.17: Collective vs. torque for first generation rotor with NACA 0012 airfoil at various rotational speeds.

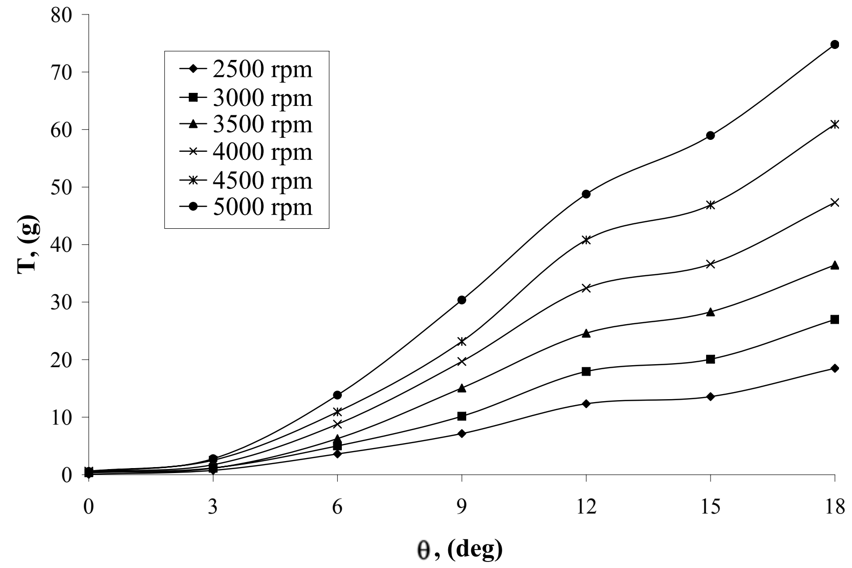

Figure 2.18: Collective vs. thrust of first generation rotor with flat plate airfoil at various rotational speeds.

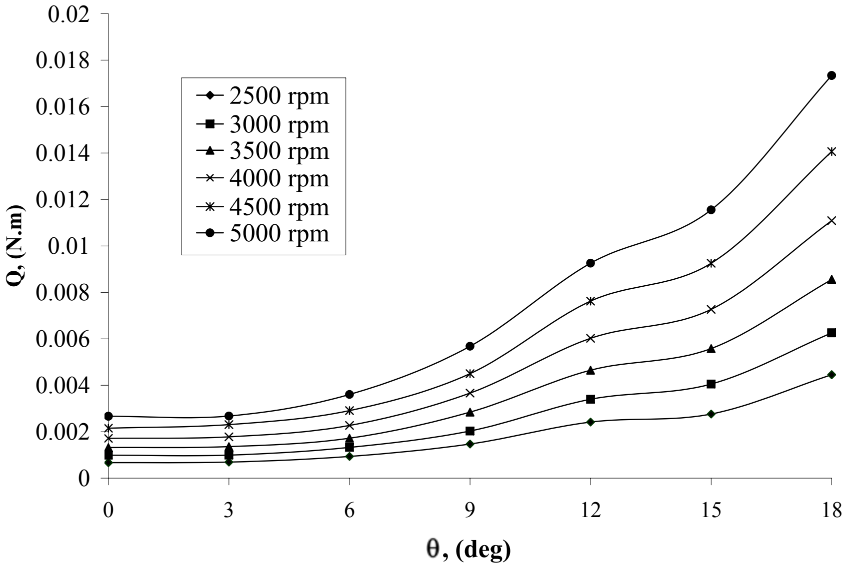

Figure 2.19: Collective vs. torque for first generation rotor with flat plate airfoil at various rotational speeds.

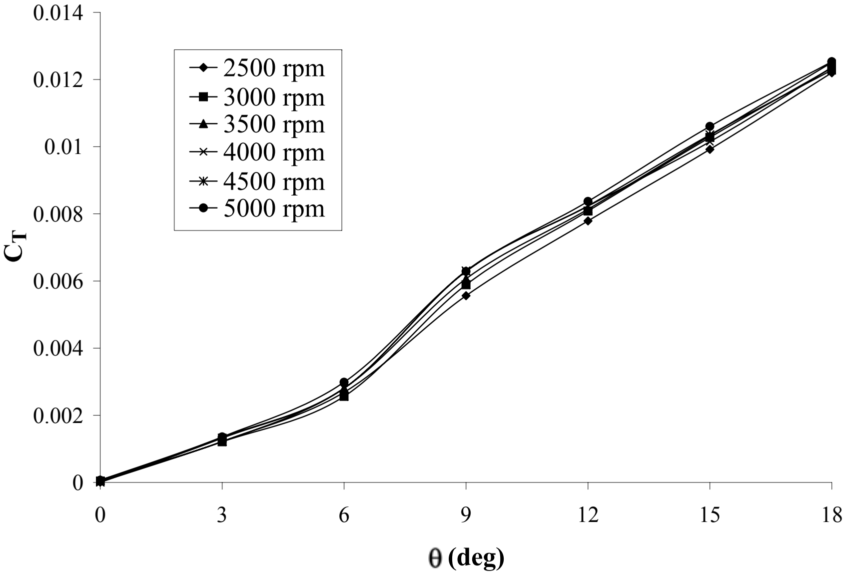

Figure 2.20: Collective vs. C_T of first generation rotor with NACA 0012 airfoil at various rotational speeds.

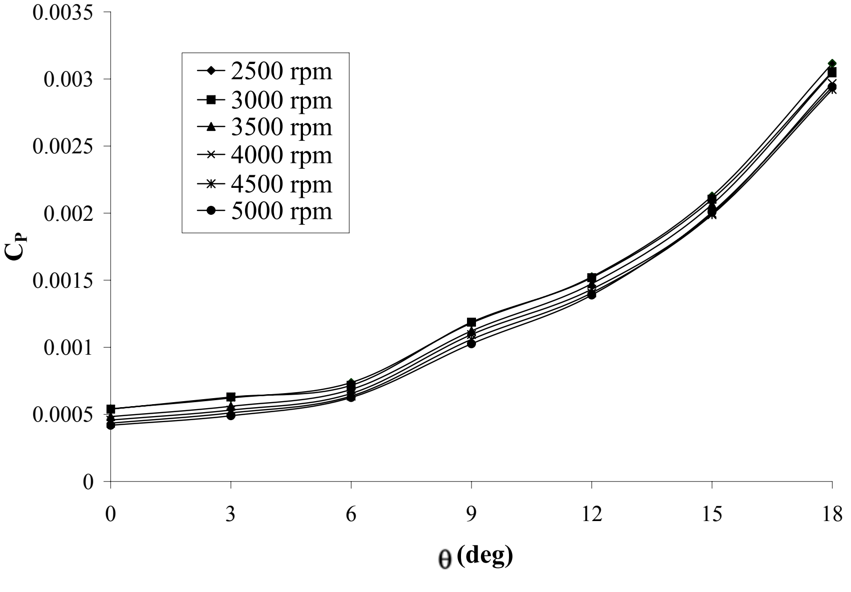

Figure 2.21: Collective vs. C_P for first generation rotor with NACA 0012 airfoil at various rotational speeds.

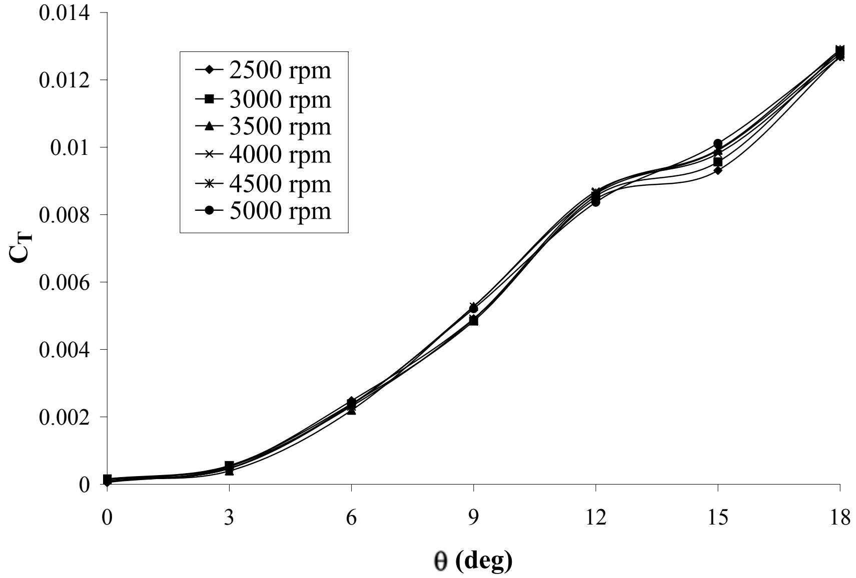

Figure 2.22: Collective vs. C_T of first generation rotor with flat plate airfoil at various rotational speeds.

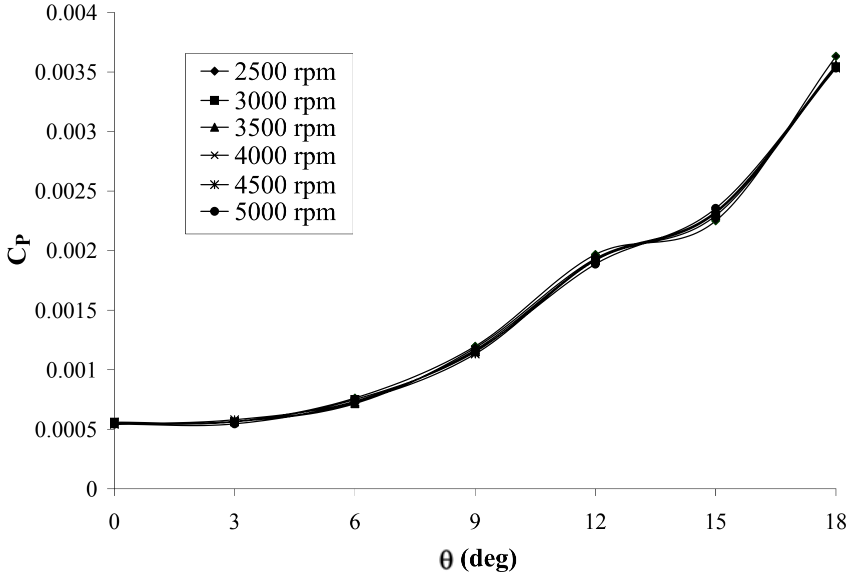

Figure 2.23: Collective vs. C_P for first generation rotor with flat plate airfoil at various rotational speeds.

In order to compare the performance of the various rotors, a rotational speed of 4500 RPM was chosen. This corresponds to a tip Reynolds number of ≈ 27,000. Thrust vs. power coefficients are plotted in Figure 2.24. It can be observed how flat plates and NACA blades have very similar thrust levels while the 8% cambered plates achieve the largest thrust coefficients at every collective pitch. In fact, the maximum C_T of the 8% camber blades at 18 deg collective is about 50% larger than the ones achieved by the other two rotors. In terms of power, the flat plates require higher C_P than the NACA blades for the whole C_T range, and at collectives below 9 deg, the cambered plate blades require more power than the other two rotors. Considering now figure of merit, Figure 2.25 shows that above thrust coefficients of 0.01, the cambered blades provide the highest hover efficiency, reaching a maximum FM of 0.54. The NACA 0012 rotor follows with a maximum FM of 0.37 being substantially higher than the rotor with flat plates which has a maximum FM of only 0.3. When using power loading as a performance metric results have to be interpreted in a different way. Figure 2.26 shows that an overall maximum PL of 0.147 N/W is achieved with the NACA 0012 rotor, being just a few percent higher than the maximum PL achieved with the 8% camber blades. However, this maximum occurs at the low disk loading of 12.6 N/m^2 which corresponds to a thrust of 29.7 grams. Even though the 8% camber rotor has a lower maximum PL, it can sustain acceptable PL levels for a wide range of disk loadings. The NACA rotor would be a better choice for the specific case of a vehicle that has to operates at very low thrust levels with a fixed solidity and at that particular tip speed. In section 2.6.4 it is explained how if blade geometry and tip speed are considered as design parameters, the rotor's operational and geometric characteristics can be matched with the thrust requirements allowing to use the configuration that achieves the highest hover rotor performance.

Effect of blade twist

A second rotor having 8% camber blades and a linear negative twist of -10 deg was tested. As explained in section A.7.4 the induced power component of a hovering

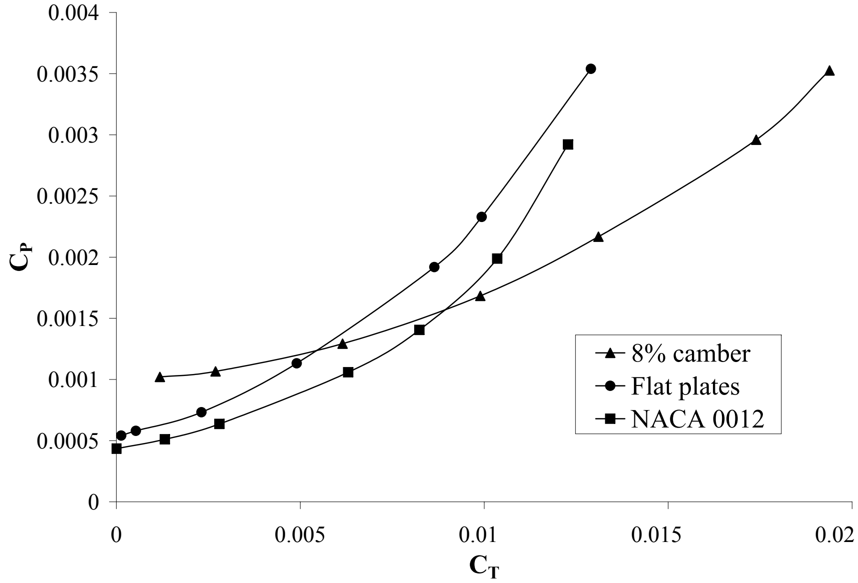

Figure 2.24: Comparison of C_T vs. C_P for 8% camber plates, flat plates and NACA 0012 airfoils at 4500 RPM i.e Re=27,000 using the first generation rotors.

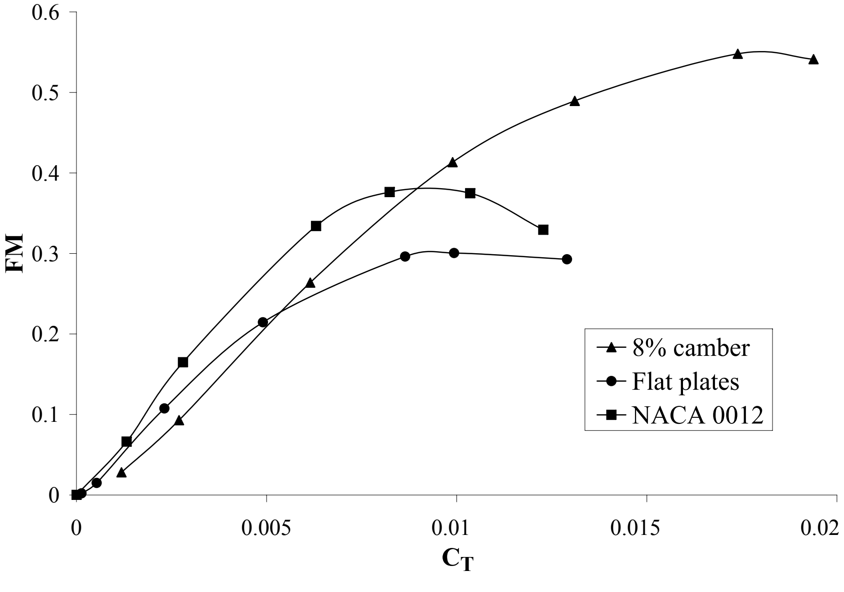

Figure 2.25: Comparison of C_T vs. FM for 8% camber plates, flat plates and NACA 0012 airfoils at 4500 RPM i.e Re=27,000 using the first generation rotors.

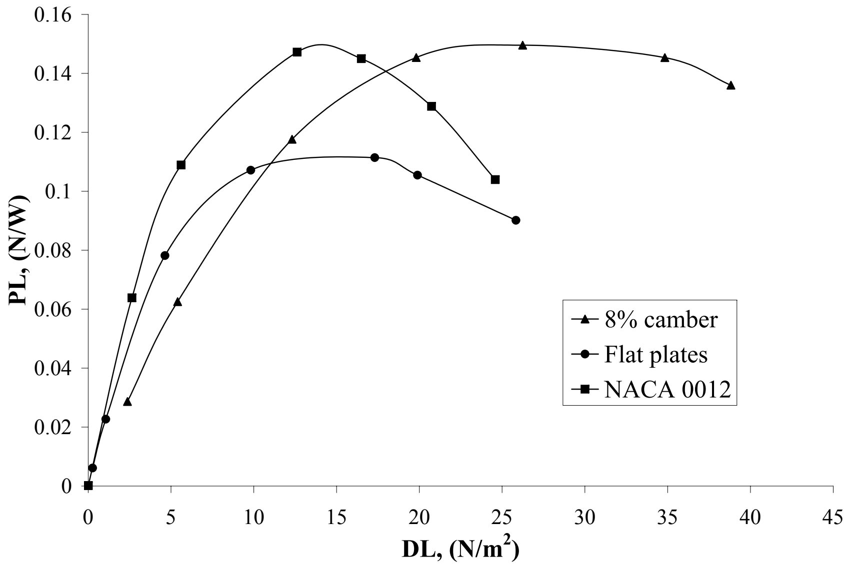

Figure 2.26: Comparison of DL vs. PL of rotors with 8% camber plates, flat plates and NACA 0012 airfoils at 4500 RPM i.e Re=27,000 using the first generation rotors.

rotor is at a minimum when having uniform inflow. By introducing negative twist in the blades the inflow at the root is increased while reducing it at the tips. This produces a more uniform inflow distribution, thus reducing the induced losses of the rotor. There is always a tradeoff between hover and forward flight performance. Full-scale helicopters use linear twists that range from -10 deg down to -20 deg depending on the mission they are designed for. In general forward flight design requirements are the ones that limit the use of twist in the rotor blades. For the twisted blades the local blade pitch at 75% of the span is used as reference. The experimental results that compare the twisted and untwisted rotor blade performance are presented in Figures 2.27, 2.28 and 2.29.

The results were surprising considering that practically no change in the performance was discernible. Thrust and power measurements for most collectives were very close to each other, except at the higher values were the stalling characteristics of the rotor were enhanced, allowing for higher thrust values. The maximum figure of merit measured for the rotor with twisted blades is slightly lower than for the untwisted rotor; however, it seems that because of the large discretization of collective

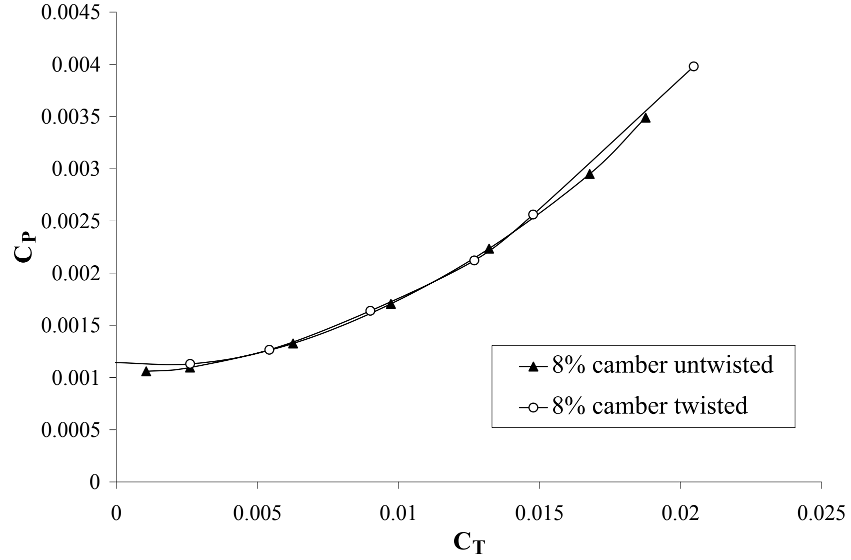

Figure 2.27: Comparison of C_T vs. C_P of rotors with twisted and untwisted 8% camber plates, at 4500 RPM i.e tip Re=27,000 using the first generation rotors.

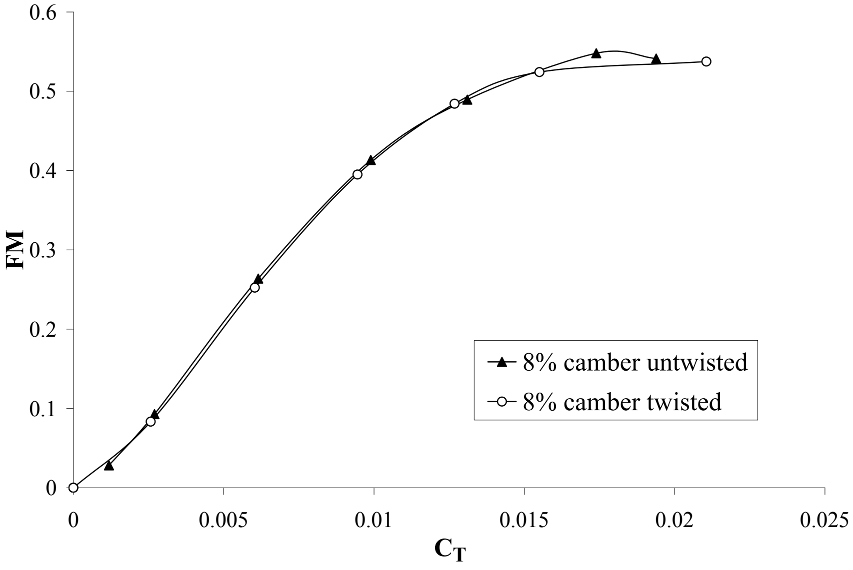

Figure 2.28: Comparison of C_T vs. FM of rotors with twisted and untwisted 8% camber plates, at 4500 RPM i.e tip Re=27,000 using the first generation rotors.

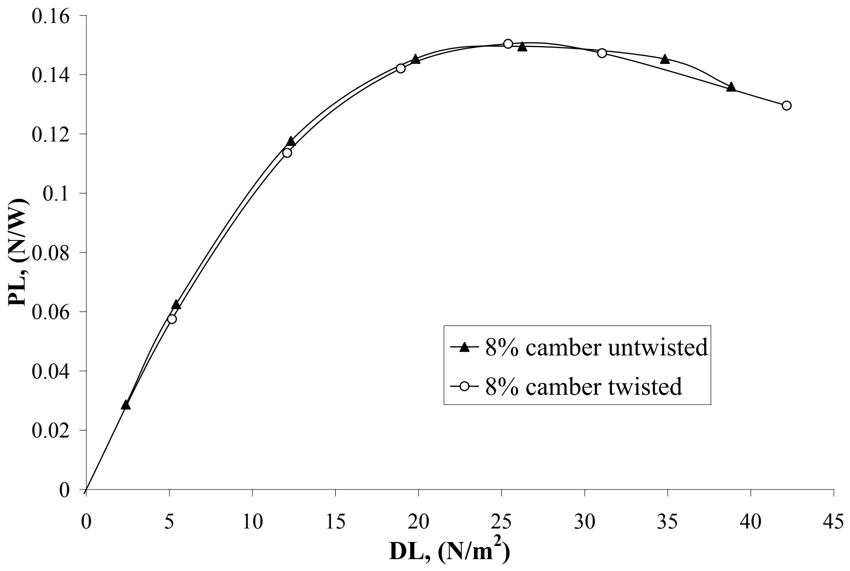

Figure 2.29: Comparison of DL vs. PL of rotors with twisted and untwisted 8% camber plates at 4500 RPM i.e Re=27,000 using the first generation rotors.

settings (steps of 3 deg), the maximum value was missed. Nevertheless considering the observed trends, it is not expected to achieve a substantial increase in maximum FM.

2.3.3 Effect of Number of Blades on Rotor Performance

Tip losses have a large impact on hover rotor performance, experience with full-scale helicopters has shown that by increasing the number of blades tip losses are reduced. This is why three-bladed rotors were used in the first generation prototype. At MAV scale, blade weight considerations are not important since each blade accounts only for $\approx 0.2\%$ of the total vehicle mass. A more important design driver is the mechanical complexity of the hub and vehicle's subsystems. A larger number of blades adds complexity to the rotor assembly and increases trimming and balancing times, but more importantly the implementation of a swashplate can be substantially simplified if only two blades are used. Before these tests were performed, it was not clear if the aerodynamic benefits of a larger number of blades outweighed the mechanical disadvantages. This is why it was essential to measure experimentally

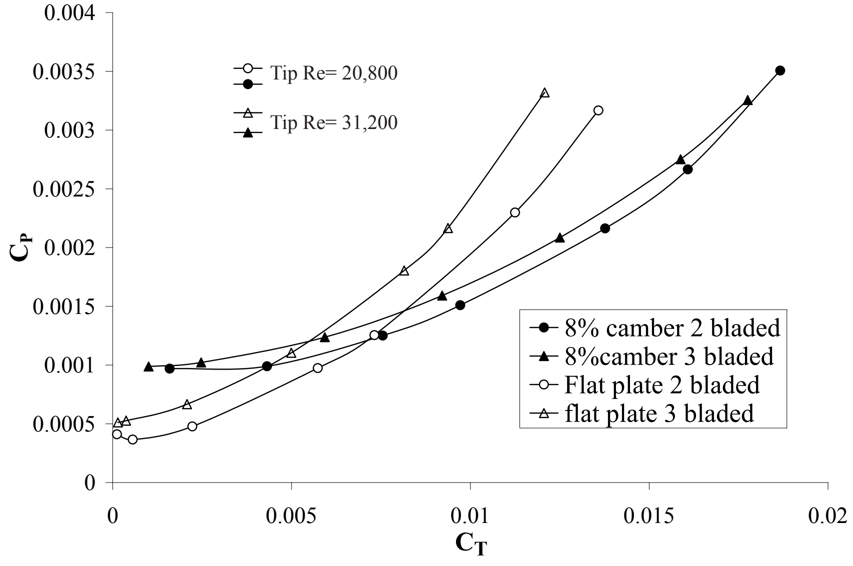

Figure 2.30: Comparison of CT vs. CP of two and three-bladed rotors with 8% camber and flat plates at 3500 RPM, σ=0.111

the aerodynamic effects of the number of blades on hover efficiency at MAV scale.

Two-bladed rotors with rectangular planform and a solidity equal to that of the rotors of the first generation were assembled. Two different airfoils were tested, flat plates and 8% camber plates. The chord of the two-bladed rotors was set as 1.5 cm and the root cut-out was left unchanged being 15% of the rotor radius. The comparison tests covered the same collectives and rotational speeds than the first generation tests. Experimental results showed that for a given rotational speed and collective, the 8% camber two bladed rotor was able to produce higher thrust than the three bladed rotor. In other words power requirements for the two-bladed rotor were reduced, improving the aerodynamic efficiency of the system. These results are presented in Figures 2.30, 2.31 and 2.32 for a rotational speed of 3500 RPM.

Established helicopter theory predicts a reduction in the tip losses when increasing the number of blades assuming all other parameters constant. However, at MAV scale keeping some of these parameters unchanged is a difficult task due to manufacturing and scaling issues. This is the case for airfoil shape and tip Reynolds number. When the wider blades were manufactured, even though the

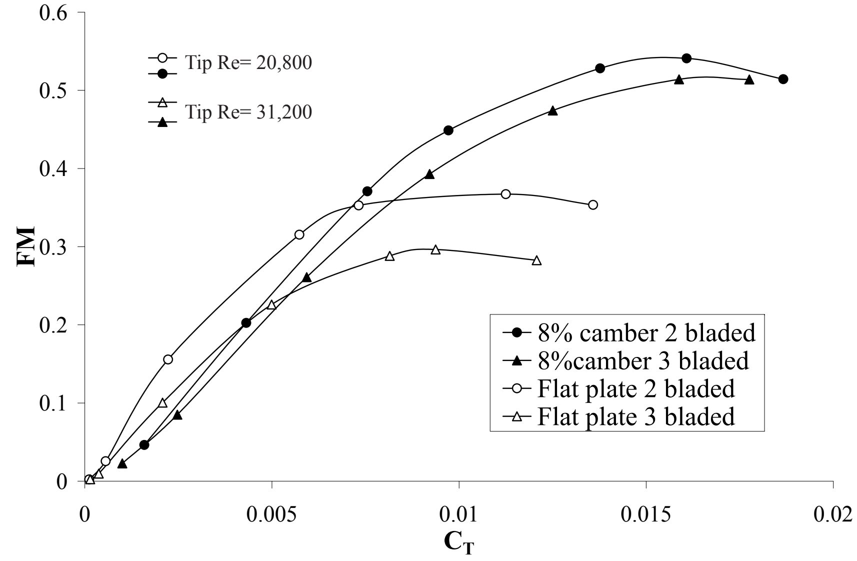

Figure 2.31: Comparison of CT vs. FM of two and three-bladed rotors with 8% camber and flat plates at 3500 RPM, σ=0.111

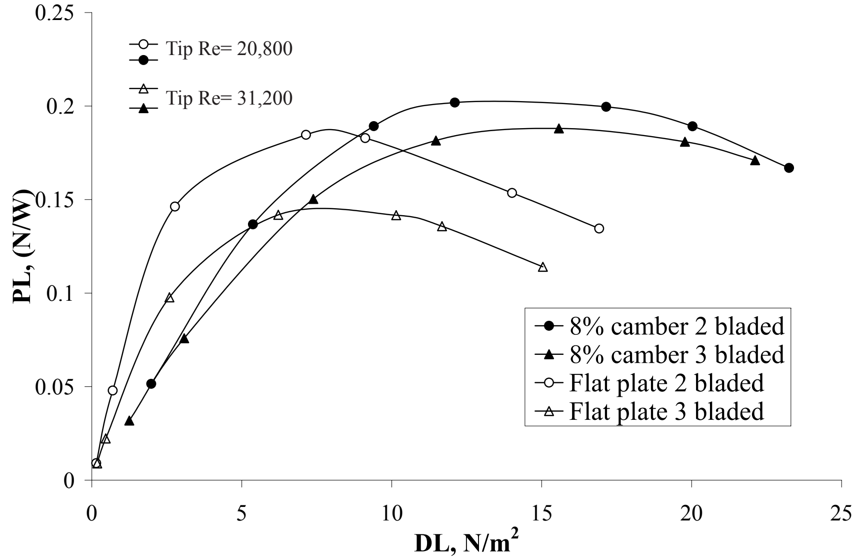

Figure 2.32: Comparison of DL vs. PL of two and three-bladed rotors with 8% camber and flat plates at 3500 RPM, σ=0.111

Radius	86 (mm)
Root cut-out	15% Radius
N_o of blades	2
Blade planform	Rectangular
Blade chord	15 (mm)
solidity	0.111

Table 2.2: Second generation rotor geometric characteristics

camber matched exactly the one of the first generation blades, thickness could not be changed proportionally to the increase in chord. This produced a difference in the airfoil thickness ratio. The first generation blades had an airfoil with 5% thickness ratio. By increasing the chord 50%, from 1 cm to 1.5 cm, the thickness ratio was reduced to 3.33%. Tip speed in the two sets of tests was kept constant, this produced an increase of 50% in the chord-based Reynolds number of the two-bladed rotors. Thinner airfoils and higher Reynolds numbers may be factors that benefit the airfoil's aerodynamic performance at the MAV scale. These two factors may explain the better performance of the two-bladed rotors. Reynolds number and thickness ratio effects on thin-plate airfoils are studied experimentally in section 2.4 and computationally in Chapter 4.

Since substantial performance gains were achieved with the two bladed rotor, it can be considered as a second generation design, Table 2.2 summarizes its geometric characteristics. In fact, this two bladed rotor was used in the implementation of a second generation coaxial vehicle that used a swashplate for lateral control.

2.4 Third Generation Rotors - Flat Plate Research

Based on the performance requirements of the MAV prototypes that were developed in parallel to this research, it was decided to increase the rotor diameter by 30% from 17.2 cm (6.77 in) to 22.4 cm (8.81 in). Rotors with this new diameter were used in the rest of the experimental results of this dissertation. This configuration

Radius	112 (mm)
Root cut-out	13.5% Radius
N_o of blades	2
Blade planform	various
Blade chord	various
solidity	various

Table 2.3: Third generation rotor geometric characteristics

LE shape	chord=1.5cm thickness=0,05cm TR=3.3	chord=2.25cm % thickness=0,08cm TR=3.3	chord=2.25cm thickness=0,05cm TR=2.2
1)	$\surd$	$\surd$	$\surd$
2)	$\surd$	$\surd$	$\surd$
3)	$\surd$	$\surd$	$\surd$
4)	$\surd$	$\surd$	$\surd$

Table 2.4: Test Matrix for rectangular blades with flat plates, four LE shapes and three chord-thickness configurations

is considered the third generation, and its main characteristics are summarized in Table 2.3

The performance improvements observed in the second generation rotor presented in Section 2.3.3 can be attributed to the higher Reynolds numbers and the smaller blade thickness ratios product of a larger blade chord. In order to quantify the aerodynamic effects of various geometric and operating parameters on thin plates, a set of experiments using flat plates were performed.

Two different chords and plate thickness were combined to obtain three different sets of blades. Two of those had an equal thickness ratio of 3.3%, and a third one had a smaller thickness ratio of 2.2%. Additionally the three sets of blades were tested with four different leading edge shapes shown in Figure 2.33. Table 2.4 summarizes the blade configurations tested.

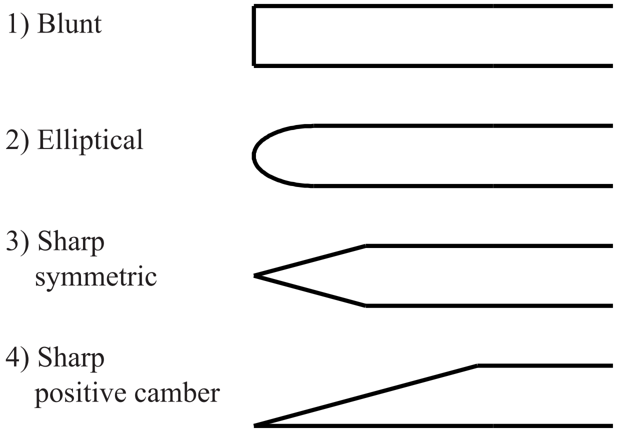

Figure 2.33: Leading edge shapes tested with flat plate airfoils

2.4.1 Zero Lift Drag Measurements

All the blade configurations of Table 2.4 were tested over a range of rotational speeds such that the tip Reynolds numbers of the rotors varied from 21,000 up to 71,000. The zero-lift torque was measured and used to calculate the equivalent zero-lift drag coefficient of the airfoil shapes. Transmission losses and hub drag were measured without blades, and were two orders of magnitude smaller than the torque produced by aerodynamic drag, ruling out any significant contribution to the measurements. In order to relate power coefficient and profile drag coefficient, a simple blade element analysis was carried out. The profile drag coefficient is a function of Reynolds number and Mach number, which vary along the blade span. Profile power is obtained by integrating the sectional drag force along the blade span as follows.

$$P_0 = \Omega N_b \int_{R_c}^{R} Dy\, dy. \tag{2.10}$$

Where Ω is the rotational speed, N_b is the number of blades, R_c is the root cutout and D is the drag force per unit span at a distance y from the rotational axis. The drag force is given by

$$D = \frac{1}{2}\rho(\Omega y)^2 c\, C_d. \tag{2.11}$$

Where c is the blade chord. Assuming an average drag coefficient Cd_0 it can be shown that

$$C_{P0} = \frac{1}{8}\sigma C_{d0} \quad hence \quad C_{d0} = \frac{8C_{P0}}{\sigma}. \tag{2.12}$$

For full-scale helicopters, the zero lift drag coefficient C_{d0} is generally used as an average drag coefficient over the operational range of angles of attack of the rotor. This approach is used to calculate the profile drag contributions in the FM calculation (cf. Eq.A.23). As it is shown in Chapter 3, this is not a good methodology at MAV scale. However, at zero lift, an average value of C_{d0} can be used to calculate profile power. Using equations 2.10 and 2.12 with the Blasius expression for laminar drag coefficient (cf. Eq. A.7), it was found that the blade section at 75% of the rotor span has the average drag coefficient of a rectangular blade.

At each rotational speed the zero-lift profile drag coefficient for the different blades was calculated using Equation 2.12. Results were compared with the laminar and turbulent theoretical predictions for a flat plate using the Reynolds number that corresponds to the blade section at 75% span. Since the C_{d0} values obtained experimentally correspond to flat plate with two surfaces, theoretical predictions from equations A.7 and A.9 were multiplied by two in the figures that show the experimental results.

The effect of thickness ratio on blunt, elliptical, and symmetrically sharp leading edges is shown on Figures 2.34, 2.35 and 2.36. For the blunt leading edge plates (Figure 2.34), it can be observed how Reynolds number has a minimal effect on the drag coefficients. The three curves exhibit a slight negative slope as Re increased, much smaller than for the other two leading edge shapes. As expected an increases in TR produces a large increase in C_{D0} of the order of 40%. These results suggest that the boundary layer is separating in extensive regions of the blades. Since C_{d0}

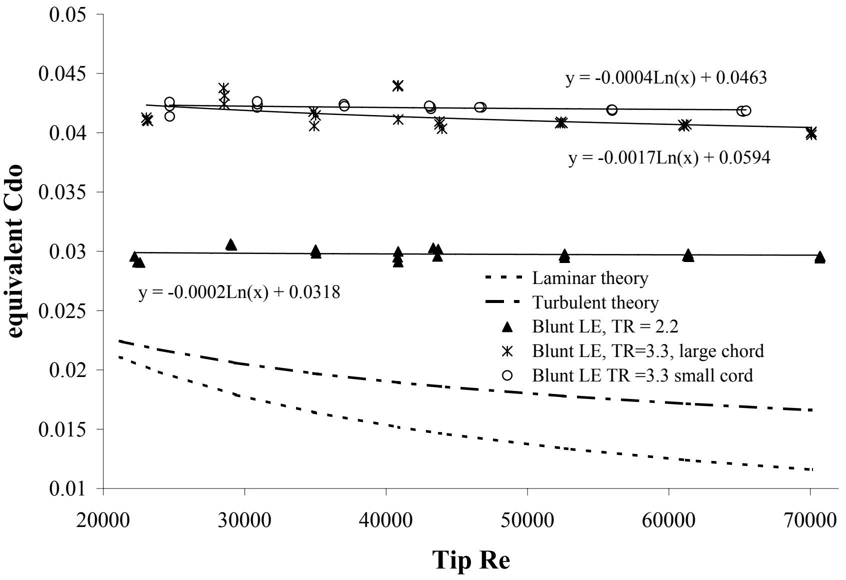

Figure 2.34: Re vs. equivalent zero lift drag coefficient C_{d0} for rotor blades with blunt leading edges and various TR and chords

values barely change with Re, the extent of those regions is not being affected by the increased tip speed.

For the plates with elliptical leading edges (Fig. 2.35),Reynold number has a substantial effect on drag coefficient. C_{d0} values are largely reduced as tip speed increases. For the lowest TR, which as in the previous case has the lowest C_{d0}, a change of the order of 30% was observed. The larger thickness ratios not only increased C_{d0} values, favorable Reynolds number effects were also reduced. This is quantified by the coefficient of the logarithmic curve fits. The curve that corresponds to the lower thickness ratio has a coefficient with larger absolute value multiplying the logarithm. The strong dependency of C_{d0} with Re suggest that the extent of the regions of laminar, turbulent and separated flow is being modified by the changing flow conditions. Since separated flow regions produce the largest drag forces, these seem to be reducing in size as tip Re increases.

For the symmetrically sharp leading edge case, the blades with lower TR have drag coefficients comparable to the theoretical fully turbulent prediction, having a large dependency with Re. As observed for the other leading edge geometries, an

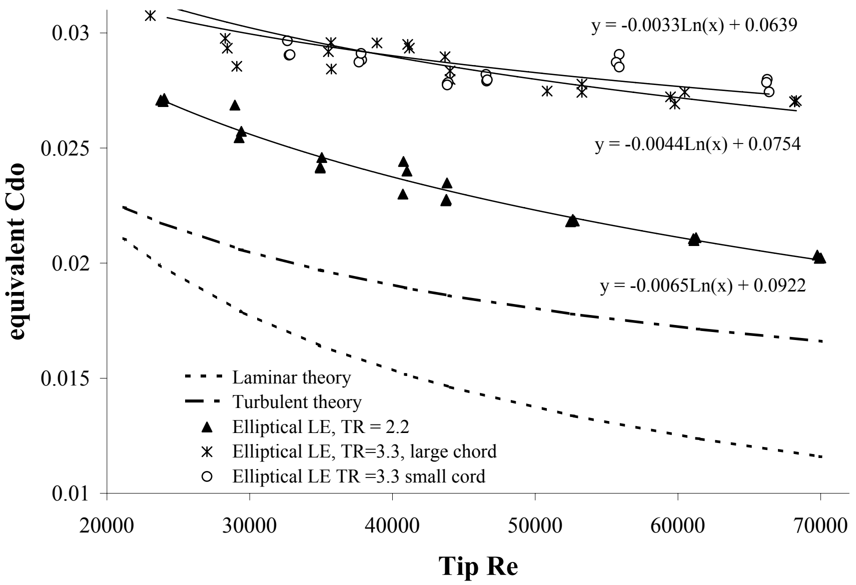

Figure 2.35: Re vs. equivalent zero lift drag coefficient C_{D0} for rotor blades with elliptical leading edges and various TR and chords

increase in TR increases the drag coefficient values. In fact, C_{d0} measurements of the 3.3% TR blades are very similar for the elliptical and symmetrically sharp leading edge geometries. The sharp symmetric leading edge shape is minimizing the drag generation, which can be linked to the behavior of the boundary layer. Lower drag levels suggest larger laminar flow regions and/or smaller separated flow zones.

The idea behind having two blade geometries with different chords but equal thickness ratios is to verify that the non-dimensionalization with TR and Reynolds number is not being affected by unaccounted parameters. Surface finishing, geometric manufacturing accuracy, blade bending stiffness, all can introduce higher order effects that can make the two geometries non-identical. The results obtained are satisfactory in that respect, even though some differences in the measurements were observed.

By comparing the experimental results of blades having the same TR and chord, the leading edge shape effects can be isolated. In Figures 2.37, 2.38 and 2.39, all the leading edge geometries of Figure 2.33 are compared. For the three TR and chord combinations the highest drag coefficients correspond to the blunt

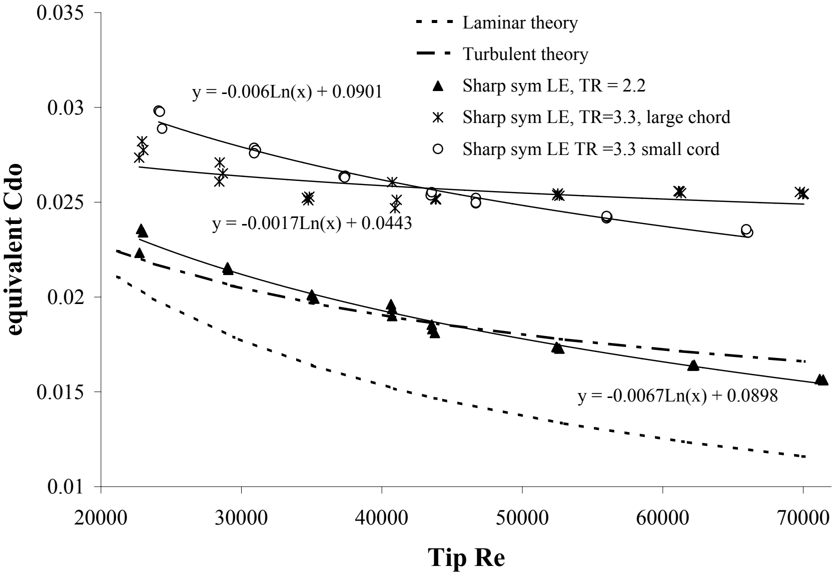

Figure 2.36: Re vs. equivalent zero lift drag coefficient C_{D0} for rotor blades with symmetric sharp leading edges and various TR and chords

leading edge airfoils. Similarly the lowest drag values were always achieved with symmetrically sharp leading edges. Asymmetrically sharp leading edges produced lower drag than the elliptical ones in two of the TR-chord combinations. Only for the blades with the shorter 1.5 cm chord and a TR of 3.3% elliptical blades had slightly lower C_{d0} values.

In ideal conditions an infinitely thin and smooth plate parallel to the flow develops a laminar boundary layer on both surfaces. Transition of the boundary layer occurs after a given length at a critical local Reynolds number (Re_c). The critical Re value may vary depending on surface roughness and free flow turbulence levels. Experiments have shown (cf. Ref. [1]) that critical Reynolds numbers for flat plates are usually between 500,000 and 1 million. Since the Reynolds numbers covered in the current tests are much lower than Re_c for flat plates, flow transition and/or separation are being produced by factors other than surface friction. Previous wind tunnel investigations on flat plates (Ref. [1]) have shown that when rounded leading edges were used, only turbulent drag measurements were obtained. Since the test plates have a finite thickness, the flow undergoes a local acceleration from the stag-

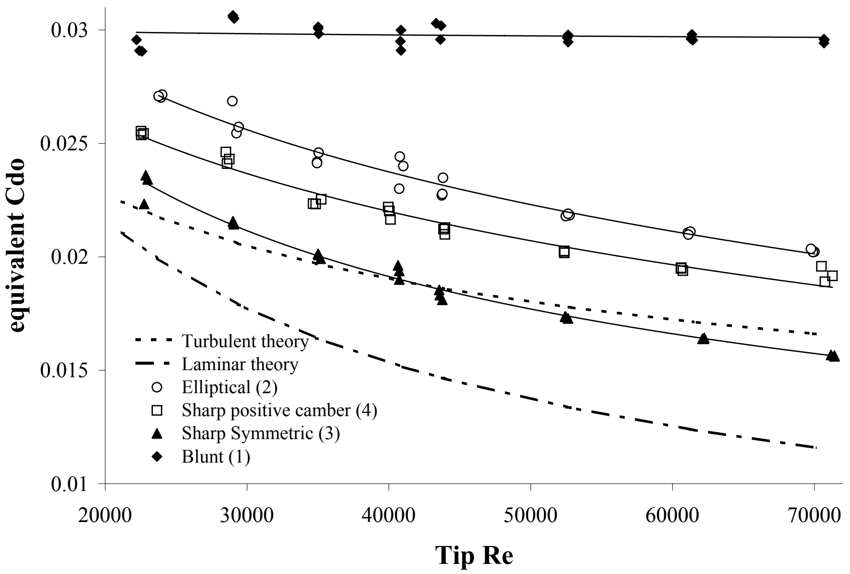

Figure 2.37: Re vs. equivalent zero lift drag coefficient C_{d0} for blades with various LE shapes with TR=2.2% and chord=2.25 cm

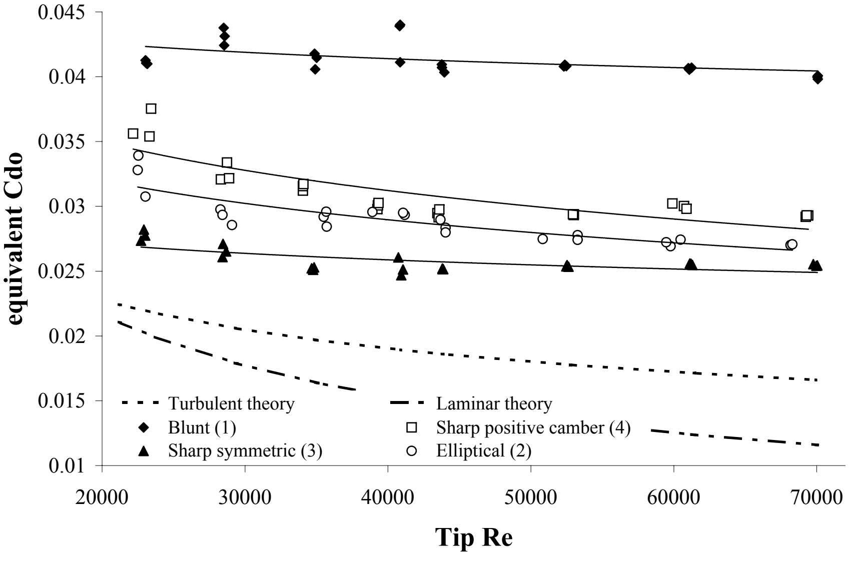

Figure 2.38: Re vs. equivalent zero lift drag coefficient C_{d0} for blades with various LE shapes with TR=3.3% and chord=2.25 cm

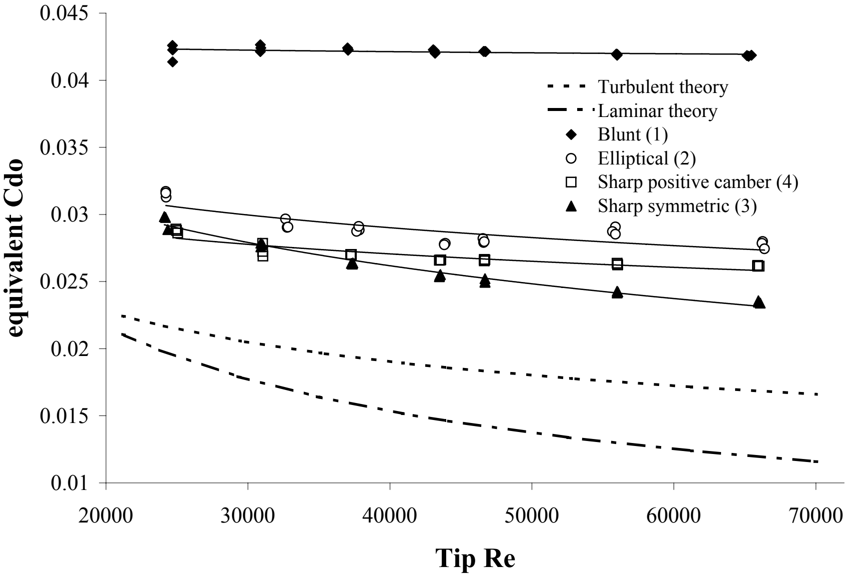

Figure 2.39: Re vs. equivalent zero lift drag coefficient C_{d0} for blades with various LE shapes with TR=3.3% and chord=1.5 cm

nation point to the upper and lower surfaces along the leading edge curvature as shown in Figure 2.40. The adverse pressure gradients faced by the boundary layer can induce early transition, and if large enough, they can lead to separation as it seems to be the case for the blades with blunt leading edges. The pressure gradients generated are reduced by tapering the leading edge, gradually increasing the plate's thickness forming a sharp wedge similar to shape 3) of Figure 2.33. This delays transition and avoids massive separation at the leading edge.

The previous discussion supports the experimental results obtained with the different leading edge shapes and thickness ratios. The higher drag coefficients were measured with the configurations that are expected to produce the largest adverse pressure gradients. However, there is another factor that helps explain the large drag coefficients measured. So far it was assumed that the free flow and the plate were perfectly aligned. However, in practice a perfect alignment is hard to achieve, specially in a rotor environment. Even a small deviation in angle of attack may have an effect on the location of the stagnation point, possibly resulting in strong pressure gradients. This makes difficult to achieve laminar or fully attached flow in

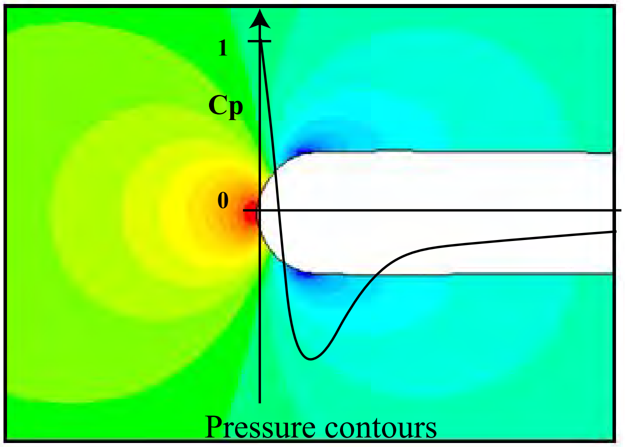

Figure 2.40: Pressure distribution at the round LE of a flat plate at zero angle of attack

the experiments performed.

The experimental results presented show that thickness ratio and leading edge shape play an important role in the drag characteristic of flat plate blades. As thickness ratio is increased, drag coefficients are adversely affected independently of leading edge geometry. Nevertheless, leading edge shape has a large influence in the drag characteristics. The minimum values measured correspond to a symmetrically sharp leading edge with a TR of 2.2%, and are very close to the fully turbulent theoretical prediction (cf. Fig. 2.36). It is important to keep in mind that the turbulent skin friction models are not exact analytical solutions, but just approximations that are valid for a specific Reynolds number range. The model used in the plots is the one from Eq. A.9, and it is generally used down to a Re of about 100,000. Below that value, laminar flow is usually assumed. Since the theoretical turbulent predictions are not reliable, based on the experimental result presented in this section it can be concluded that the flow in the rotor blades cannot be assumed laminar in spite of the low Reynolds numbers faced by the rotor blades. Most likely the flow is transitional, and is separating at different regions of the blades surface. These experiments do not provide the information necessary to identify regions of laminar, turbulent or separated flow, but clearly show that even when no lift is produced and

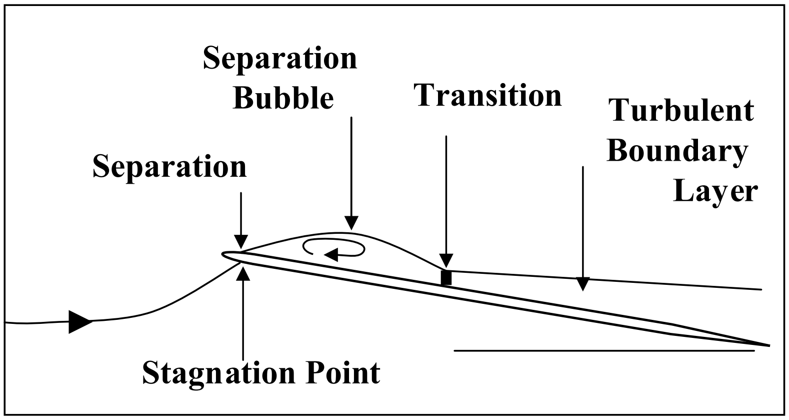

Figure 2.41: Flow around the LE of a flat plate at low angles of attack

when the adverse pressure gradients along the chord are kept at a minimum, the flow is separating producing large amounts of drag. It is possible that root and tip effects or an axial flow produced by centrifugal forces are influencing the boundary layer, increasing the values of the equivalent drag coefficients calculated.

2.4.2 Hover Performance of Rotors with Rectangular Flat Plate Blades

The rotor configuration that consistently had the lowest zero lift drag coefficients (chord = 2.25 cm , TR=2.2%) was tested for a range of collective pitch angles and rotational speeds with each of the leading edge blade shapes of Figure 2.33. The objective of the experiments is to experimentally determine if the reductions in drag measured at the zero lift condition translates into hover performance gains when thrust is produced by the rotor. Collective pitch was varied from 8 deg to 18 deg in steps of two degrees, and rotational speeds ranged from 1500 to 2500 RPM in steps of 500 RPM. Figures 2.42, 2.43 and 2.44 show a representative set of results at 2500 RPM, this corresponds to a tip Reynolds number of 33,400.

From the previous plots it can be observed that leading edge shape has a strong influence in hover performance. Maximum FM values were increased from 0.35 for the blades with blunt leading edges up to 0.42 with the sharp positive camber leading edges, this is a 20% improvement. The rotors with sharp symmetric

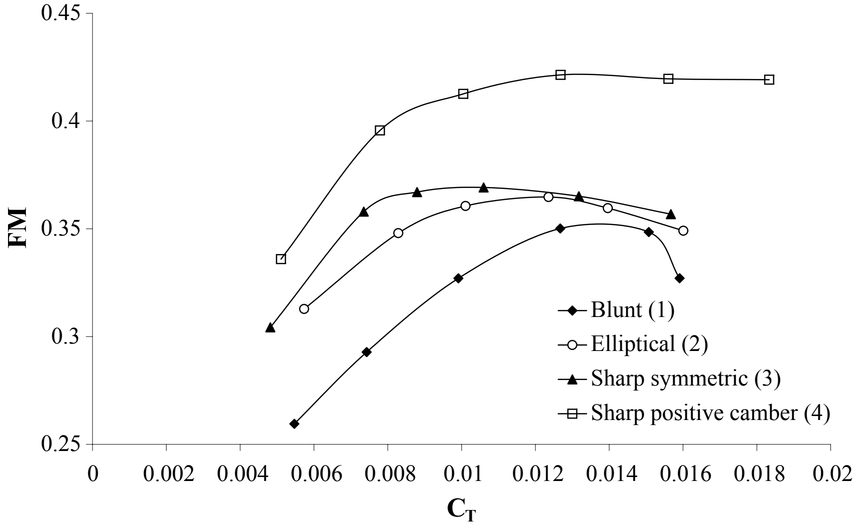

Figure 2.42: C_T vs. FM at 2500 RPM for rotors with flat plate blades and various LE shapes, chord=2.25cm, TR=2.2%, tip Re = 43,700

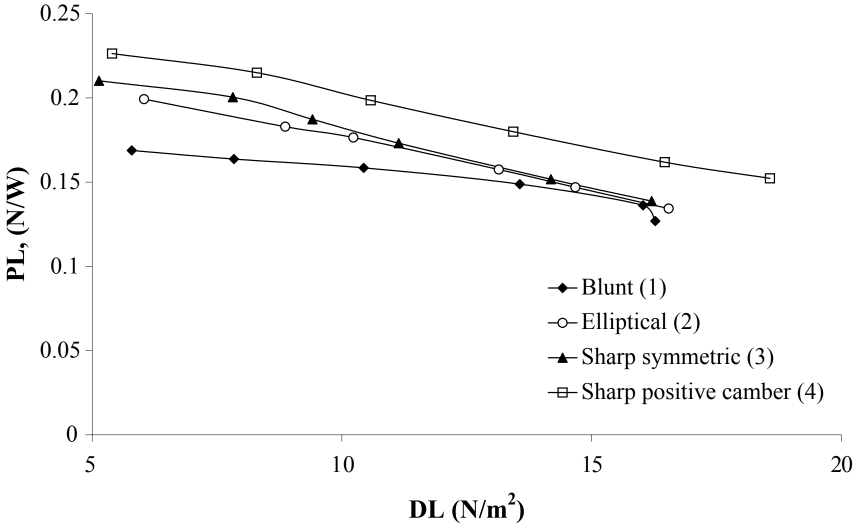

Figure 2.43: DL vs. PL at 2500 RPM for rotors with flat plate blades, and various LE shapes, chord=2.25cm, TR=2.2%, tip Re = 43,700

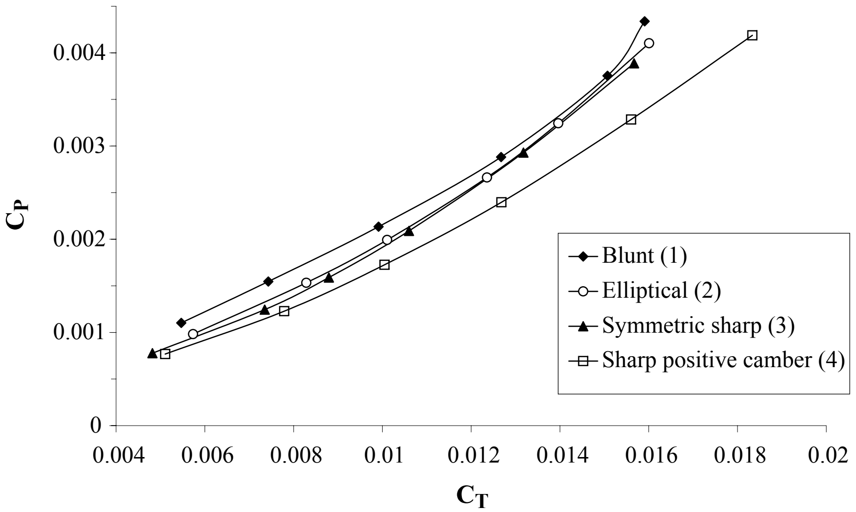

Figure 2.44: C_T vs. C_P at 2500 RPM for rotors with flat plate blades, and various LE shapes, chord=2.25cm, TR=2.2%, tip Re = 43,700

and elliptical leading edge blades had a similar performance, with a maximum FM of about 0.36, being slightly superior for the sharp symmetric geometry. The blades with the sharp asymmetric leading edge (LE geometry (4)) not only achieved the highest FM values but had improved stall characteristics. As opposed to the other configurations that stalled at collectives below 16 deg, the rotor with asymmetric sharp leading edges reached a FM plateau at 12 deg collective that continued until 18 deg collective.

There is a link between the zero-lift drag values measured and the hover performance of the rotors. Blunt leading edges which tend to produce flow separation, achieved the lowest FMs, while the rotors with sharp symmetrical leading edges, that had the lowest zero-lift drag values, only achieved intermediate FM levels. Figure 2.44 can be used to discern were the hover performance gains originate. The best performing rotor not only is requiring less power for a given thrust, but is able to produce more thrust at any given collective than the other configurations. This result can be linked to a good behavior of the boundary layer, separation regions seem to be smaller int this case due to the leading edge effects on the boundary layer. These experiments cannot provide insight of the boundary layer behavior;

however, they have been useful to recognize the importance of leading edge shape in flat plate airfoils and served to identify a specific leading edge geometry that maximized rotor performance.

2.5 Third Generation Rotors - Cambered Rectangular Blades

As was observed in the experimental results of the first generation rotors (cf. 2.3.2) camber has a strong effect on the hover performance of rotors that use thin plate airfoils. In the previous sections only results for flat plates and 8% circular arc camber blades were presented. Here the effect of camber magnitude and maximum camber location are explored.

2.5.1 Hover Performance - Effect of Maximum Camber

Based on the geometric characteristics of the third generation rotors (two-bladed, 22.4 cm in diameter), three additional maximum camber magnitudes on circular arc airfoils were experimentally studied. Two different blade chords were used such that Reynolds number and thickness ratio effects were considered. Table 2.5 presents the test matrix used in this section.

Max camber	c=1.5cm TR=3.3% $\sigma = 0.0909$	c=2.25cm TR=2,2% $\sigma = 0.1279$
0%	$\surd$	$\surd$
3%		$\surd$
6%	$\surd$	$\surd$
9%	$\surd$	$\surd$

Table 2.5: Test matrix for rectangular blades with circular arc airfoils with various cambers and solidities

For the rotor configurations of Table 2.5, collective pitch angles were varied from 0 deg to 18 deg in steps of 2 deg, and rotational speeds were varied from 2000 RPM to 3000 RPM in steps of 500 RPM. Figures 2.45, 2.47 and 2.46 show the

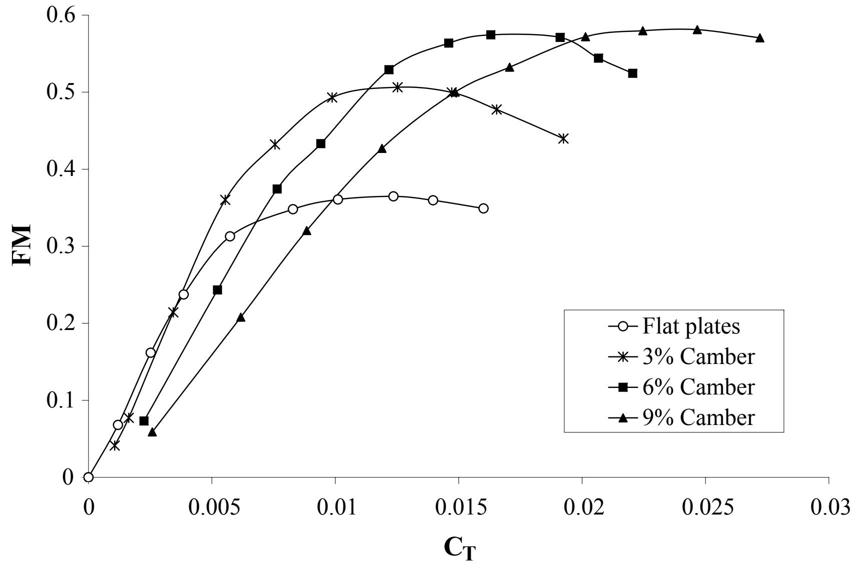

Figure 2.45: C_T vs. FM at 2500 RPM for rotors with circular arc airfoils of various cambers and elliptical LE, chord=2.25cm, TR=2.2%, tip Re = 43,700

results for the rotors with a chord of 2.25 cm ($\sigma = 0.1279$) at a rotational speed of 2500 RPM (tip Re $\approx$ 43,700)

From Figure 2.45 it can be observed that as camber increases, the maximum FM that the rotors achieve also increases. As expected the poorest performance in terms of FM was obtained with the flat plates, that had a maximum FM of 0.36. With the 3% camber blades maximum FM jumped to 0.51, achieving a 41% increase with respect to the rotor with flat plate blades. A more moderate but still significant improvement was achieved with the 6% camber blades that reached a maximum FM of 0.57 being just 1 percentage point below the maximum of 0.58 measured with the 9% camber blades. Maximum FM occurred at different C_T and collective pitch for all rotors. With increasing camber, maximum FM moved to gradually higher collectives and C_T values. Figure 2.46 shows the C_T vs. C_P plots for the set of rotors considered. As in the C_T vs. FM plot (cf. 2.45), it can be observed that the rotor's maximum thrust increases at the expense of additional power. The envelope for minimum power for any given thrust is delimited by the dotted line in Figure 2.46. Each rotor configuration defines a section of the boundary. If a infinite number

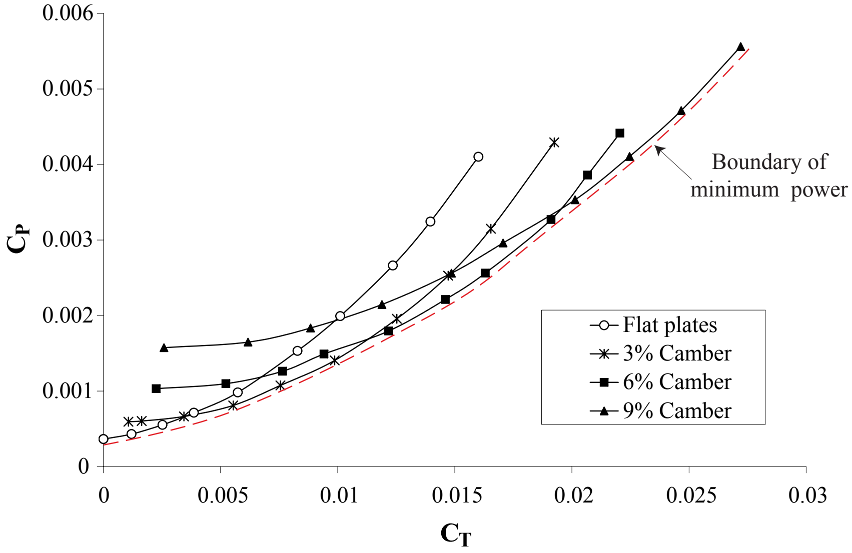

Figure 2.46: C_T vs. C_P at 2500 RPM for rotors with circular arc airfoils of various cambers and elliptical LE, chord=2.25cm and TR=2.2%, tip Re = 43,700

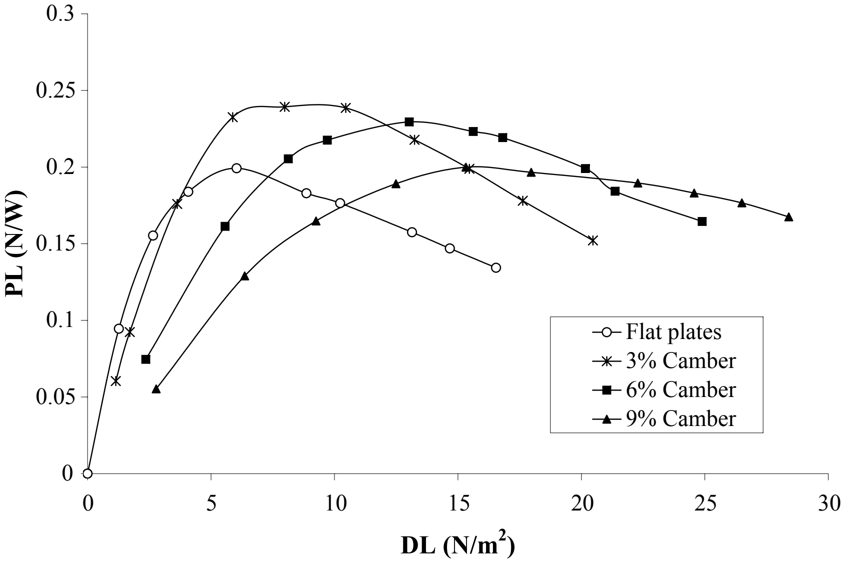

Figure 2.47: C_T vs. C_P at 2500 RPM for rotors with circular arc airfoils of various cambers and elliptical LE, chord=2.25cm and TR=2.2%, tip Re = 33,400

of cambers were used, each point of the dotted line would correspond to a single camber magnitude.

Experimental results are presented in terms of power loading in Figure 2.47. This figures shows that even though maximum figure of merit is higher with the 9% camber blades, depending on the disk loading at which the rotor is operating, 0% 3%, 6% and 9% camber airfoils can be an optimum choice. This is essentially the same observation that was performed in the C_T vs. C_P plot when a line for minimum power for a given thrust was defined.

However, since the tests were performed with rotors having similar geometric characteristics and the comparisons are performed at a fixed rotational speed of 2500 RPM, care must be taken not to draw an erroneous conclusion. Figure 2.48 has an additional curve that corresponds to the PL for the rotor with 9% camber blades at a lower rotational speed of 1666 RPM. It can be observed that in the lower disk loading range (3 to 13 N/m^2) the rotor with 9% camber blades easily outperforms the other configurations. What these results are saying is that for a given disk loading or thrust coefficient, rotational speed and rotor solidity should be adjusted such that the required thrust is produced with the airfoil that can achieve the highest FM.

The performance of the rotor with 9% camber blades over a range of rotational speeds is shown in Figure 2.49. It is important to note that for all rotational speeds maximum FM occurs at the same collective, in this particular case somewhere in the vicinity of 16 deg (cf. Figure 2.49(a)). On the other hand, maximum PL for each rotational speed corresponds to a collective of about of 9 deg (cf. Figure 2.49(b)). The envelope for maximum PL, shown as a dotted line, corresponds to a curve defined by the power loading at maximum FM for the range of rotational speeds considered. This means that in order to minimize the power requirements of a rotor for a given thrust, collective pitch should be set such that the rotor is working at its maximum FM. Thrust is then controlled by varying the rotational speed. This is a radical difference with respect to full-scale helicopters where rotational speed is fixed and collective is used to control thrust. Having a fixed collective not only

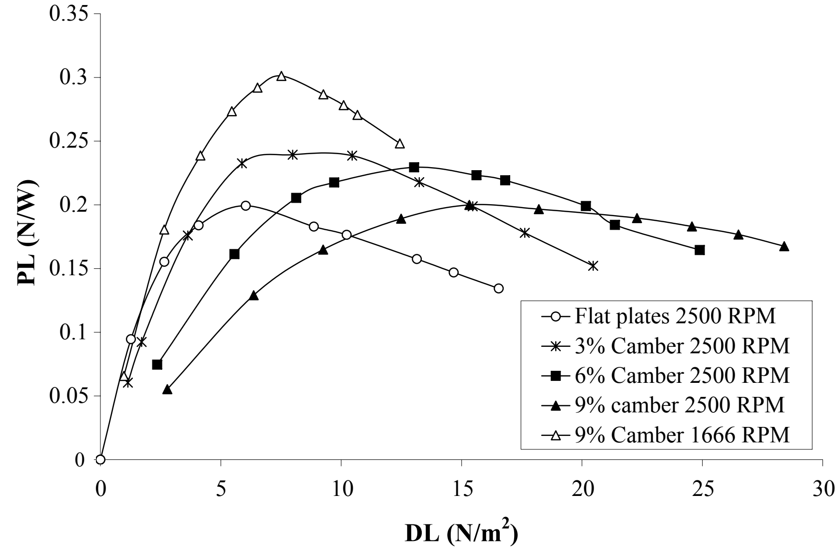

Figure 2.48: C_T vs. C_P for rotors with circular arc airfoils of various cambers and elliptical LE, chord=2.25cm and TR=2.2%, various tip speeds

gives performance benefits, but also simplifies the design and implementation of a working prototype as discussed in Chapter 6.

2.5.2 Hover Performance - Effect of Maximum Camber Chordwise Location

The effect of maximum camber location was investigated by manufacturing and testing blades very similar to the Go 417a thin cambered airfoil, which was studied by Schmitz in his wind tunnel experiments (Ref. [1]). The Go 417a, shown in figure A.7, is a thin cambered airfoil with 5.8% maximum camber at 40% of the chord and 2.9% TR. The airfoil manufactured for the rotor tests has a nominal maximum camber of 6% at 0.4c with a chord of 1.5cm and a TR of 3.33%. Both leading and trailing edges were rounded. By inverting the airfoil, a camber location at 60% of the chord was achieved. Table 2.6 shows the test matrix for this set of experiments. Collective pitch was varied form 0 deg to 18 deg in steps of 2 deg, except for the rotor with aft camber that reached only 16 deg. The measurements presented correspond to a rotational speed of 3000 RPM (tip Re $\approx$ 35,000).

Figure 2.50 shows that maximum camber chordwise location has a marked

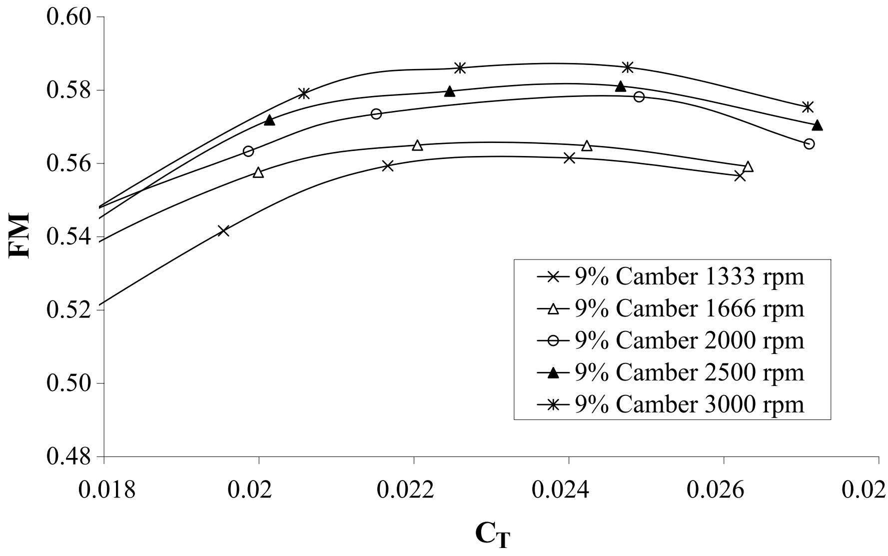

(a) C_T vs. FM for various RPM, 12deg to 18deg collective

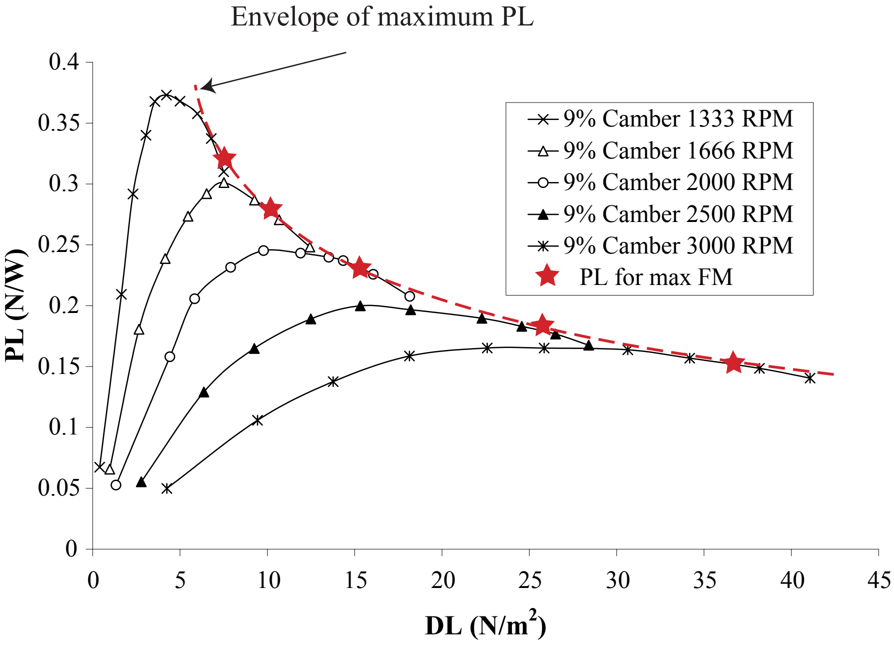

(b) DL vs. PL various RPM - envelope for max DL

Figure 2.49: Hover performance of rotor with 9% camber rectangular blades at various RPM.

Max camber	Max camber @ 0.4c	Max camber @ 0.5c	Max camber @ 0.6c
6%	√	√	√

Table 2.6: Test matrix for rectangular blades with various max camber locations, chord = 1.5 cm, σ=0.0909

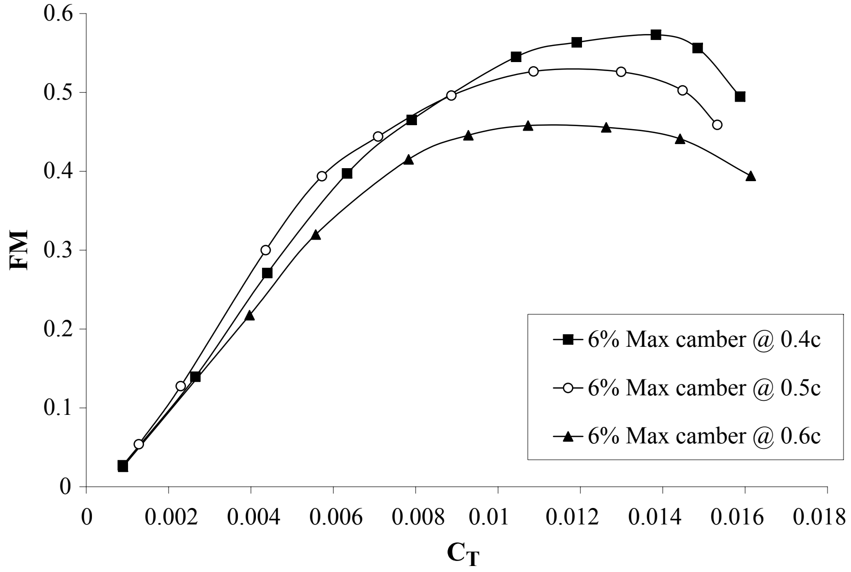

Figure 2.50: C_T vs. FM for rotors with 6 % camber airfoils, max camber at different chordwise locations, chord=1.5cm, TR=3.3%, tip Re= 35,000

effect on hover rotor performance. The blades with the maximum camber at 40% chord achieved a maximum FM of 0.57, almost 10% higher than the rotors with circular arc airfoils. On the other hand, performance was degraded down to a maximum FM of 0.45 when the camber was shifted aft of the midchord. Based on the results of Figure 2.51 it seems that the forward camber enhanced the lift to drag ratio mostly by increasing lift. For each collective, similar power levels were achieved with the circular arc and forward camber airfoil; however, thrust levels with the circular arc were lower. The rotor with the aft camber airfoil required for each collective considerably more power than the other two cases and reached the highest thrust levels.

The results presented only consider the maximum camber location disregard-

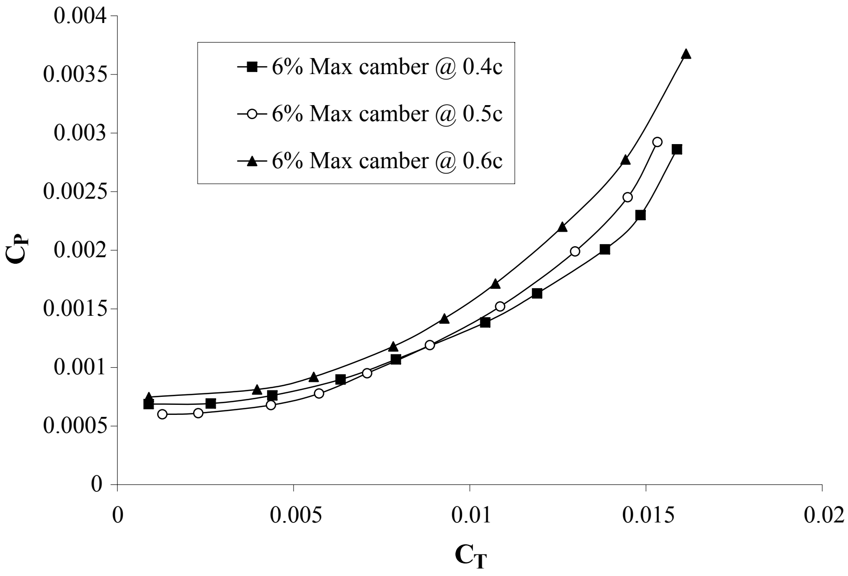

Figure 2.51: C_T vs. C_P for rotors with 6 % camber airfoils, max camber at different chordwise locations. chord=1.5cm, TR=3.3%, tip Re= 35,000

ing the camber distribution. Different camber lines will affect the velocities along the surface and the adverse pressure gradients faced by the boundary layer, altering the sectional aerodynamic characteristics. Maximum camber magnitude and location are not enough to determine the sectional characteristics of a uniform thickness curved plate airfoil; however, the experimental results show that there is plenty of room to improve on the performance of circular arc airfoils by optimizing this geometric parameter.

2.5.3 Hover Performance - Effect of Rotor Solidity

Rotor solidity is one of the most important parameters chosen in the rotor design process. In this section, the effect of rotor solidity using circular arc airfoils is explored by comparing the performance of the two pairs of rotors with 6% and 9% camber airfoils of Table 2.5. For each airfoil, rotors having solidities of $\sigma_1 = 0.0909$ and $\sigma_2 = 0.1279$ were tested. The differences in solidity corresponds to an increase in chord of 50%, from 1.5 cm to 2.25 cm. Collective pitch angles ranged from 0 deg to 18 deg in steps of 2 deg, rotational speeds ranged from 2000 RPM up to 3500

RPM in steps of 500 RPM.

When there is a difference in solidity between rotors, the blade loading coefficient defined C_T/σ is generally used as abscissa when comparing figures of merit. By doing this, the effects of operating conditions are minimized and the rotors can be judged on their design alone. The blade loading coefficient is defined as

$$\frac{C_T}{\sigma} = \frac{T}{\rho A(\Omega R^2)} \left(\frac{A}{A_b}\right) = \frac{T}{\rho A_b(\Omega R)^2}. \tag{2.13}$$

Where A_b is total blade area. Fixing the rotational speed at 2500 RPM, the hover performance of rotors with similar airfoils but different solidities were compared. The results plotted on Figures 2.52 and 2.53 show that for the 6% and 9% camber blades, the maximum figures of merit and range of C_Ts achieved are considerably higher for the rotors with larger solidities.

For a fixed rotational speed, as it is usually the case in full-scale helicopters, the rotor operating at the highest C_T/σ for a fixed DL or C_T generally has a higher FM, assuming that airfoil characteristics and induced losses are not affected by the chord change and that the rotors are operating at collectives well below stall. The better hovering efficiency of lower solidity rotors is a result of the reduced wetted blade area that minimizes viscous losses. This case is illustrated in Figure 2.52 by points A and B. On the C_T vs FM plot, A and B are vertically aligned; however, when plotted vs. C_T/σ, point A is at a higher blade loading coefficient.

At MAV scale there are a series of factors that question the use of that design rule. Figure 2.52 shows that the rotor with higher solidity is the best choice at C_Ts above 0.01 since FM values for this rotor are higher in that range. As shown by points C and D, blade loading coefficients are lower for the more efficient rotor. The difference in maximum FM values between the two rotors can be explained by the degraded airfoil performance of the lower solidity rotor that is operating at a lower tip Re. Additionally, manufacturing constraints become relevant. Blades with larger chords can be manufactured with airfoils having smaller thickness ratios, improving sectional aerodynamic characteristics and simultaneously maximizing the chord-based Reynolds number. It seems that the reduction in net blade area of the rotor does not compensate for the increased viscous loses resulting from the lower Reynolds numbers and the increase in airfoil thickness ratio. This is a similar explanation as the one given in Section 2.3.3 where the effects of number of blades were explored.

Rotational speed

There is another difference with respect to full-scale rotors that affects the design consideration and the choice of solidity for an MAV rotor. As previously mentioned rotational speed is usually fixed for full-scale vehicles, and thrust differences produced by different solidities are usually compensated with a collective pitch adjustment. At MAV scale, rotational speed can be varied over a wide range, adding another dimension to the problem. For example, an MAV rotor designer may have to determine what is the best choice between a rotor with low solidity and higher rotational speed or a rotor with high solidity and low rotational speed. Experimental results of Figure 2.54 show that for both the 6% and 9% camber blades, rotors with wider chords achieved higher performance levels at a lower rotational speed than the lower solidity rotors over a given range of disk loadings. The rotors with wider blades, in spite of the lower rotational speeds, have a higher tip Reynolds number than the lower solidity ones. Since the thickness ratio of the airfoils could not be kept constant, it is not possible to know in what measure the better performance was a result of the higher Reynolds numbers or the lower airfoil thickness ratios. Anyhow, by having blades with larger chord, two of the parameters that affect rotor performance were improved.

It is important to understand that the results obtained define some trends that apply to the test space explored, for radically different configurations, airfoil shapes or operating conditions, the effect of the factors considered needs to be reevaluated.

Leading edge shape effects on cambered blades

As discussed in sections 2.4.1 and 2.4.2, leading edge shapes had a strong effect on the zero-lift drag and hover performance of rotors with flat plate blades. The next

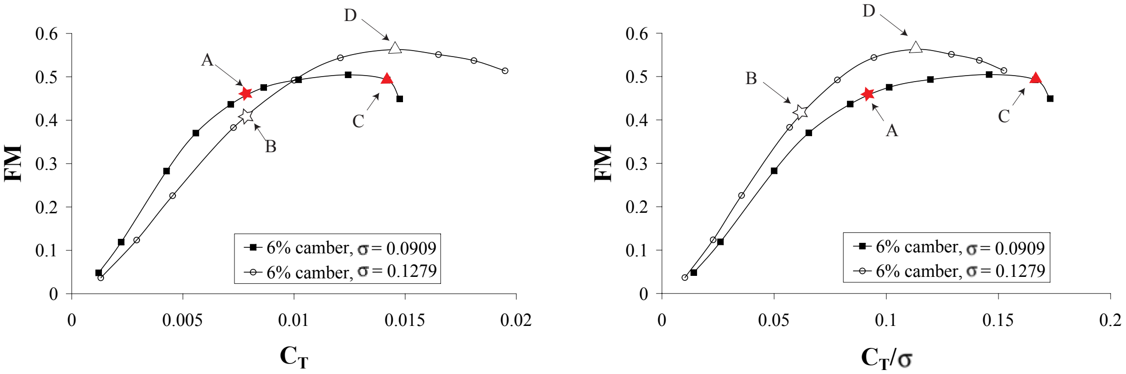

(a) C_T vs. FM (b) C_T/σ vs. FM

Figure 2.52: FM of two rotor with 6% camber blades and different solidities at 2500 RPM as function of C_T and C_T/σ.

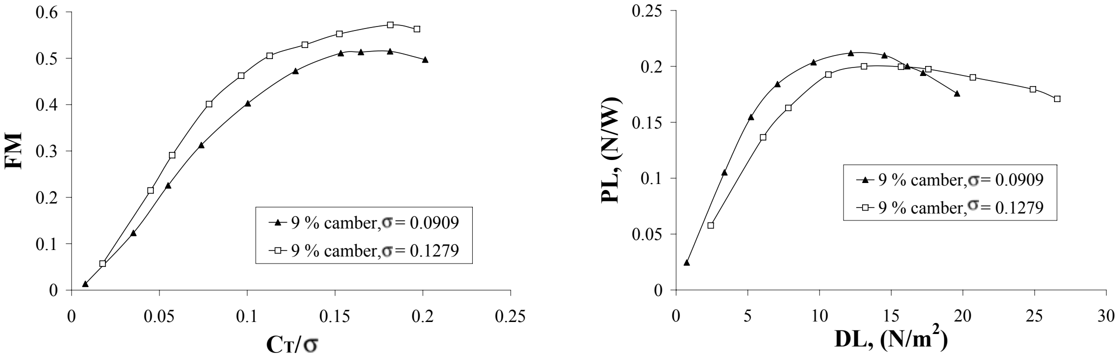

(a) C_T/σ vs. FM (b) DL vs. PL

Figure 2.53: Hover performance of rotors with 9% camber blades at 2500 RPM.

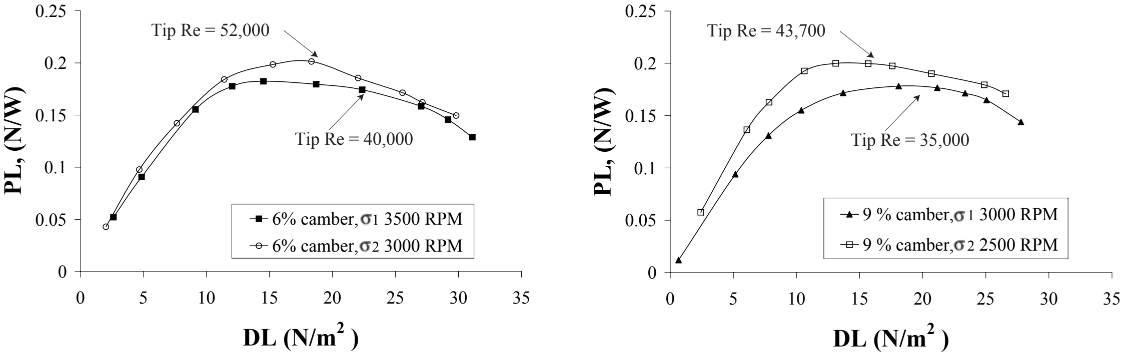

(a) DL vs. PL for 6% camber rotors

(b) DL vs. PL for 9% camber rotors

Figure 2.54: DL vs. PL for rotors with 6% and 9% camber blades at different rotational speeds.

logical step is to investigate if the performance of rotors having cambered blades can be further improved by the choice of leading edge. In order to do this, the rotors that achieved the highest FM with elliptical leading edges were also tested with leading edge (4) of Figure 2.33. That particular leading edge, called "sharp positive camber", had the best results on flat plate blades (cf. Fig 2.42), producing the highest figures of merit.

Figure 2.55 compares the performance of the 6% and 9% camber rotor with elliptical and sharp positive camber leading edges at a rotational speed of 2500 RPM. For the 6% camber blades, maximum FM was increased from 0.57 to 0.6, while simultaneously reaching higher thrust coefficients. For the 9% camber blades leading edge had a more subtle effect, maximum figure of merit did not have a substantial change; however, stalling characteristics were clearly enhanced. As with the flat plates, 6% and 9% camber rotors showed improved stalling characteristics when using sharp leading edge shapes. At the higher collectives, the rotors reached a plateau were FM suffered only minor chages. For the 6% camber blades the plateau extended from 12 deg to 18 deg and for the 9% camber blades from 14 deg to 18 deg.

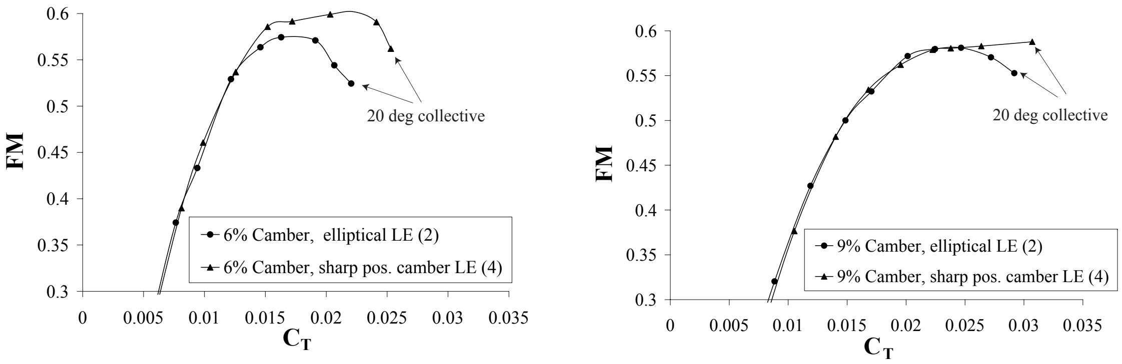

(a) C_T vs. FM for 6% camber rotors

(b) C_T vs. FM for 9% camber rotors

Figure 2.55: C_T vs. FM for rotors with rectangular 6% and 9% camber blades with elliptical and positive sharp leading edges at 2500 RPM, chord =2.25 cm

2.6 Third Generation Rotors - Non-Rectangular Blades

Up to this point, rotor hover performance has been studied using rectangular blades. In this section the effect of blade planform shape on flat and cambered blades is presented.

2.6.1 Blade Tip Shapes - Full-scale vs. MAV-Scale

In full-scale helicopters blade tips play an important role in the aerodynamic performance of the rotor since they face the highest dynamic pressures and highest Mach numbers. Advanced full-scale helicopter blade tips make use of sweep, taper or a combination of two. The positive effects in performance originate from the reduction of the Mach number normal to the leading edge and the change of tip vortex characteristics. Blade tip shape effects in full-scale helicopters are not completely understood and are a topic of ongoing research. MAV rotor operating conditions differ considerably from larger size vehicles (cf. Fig. A.1): while for full-scale helicopters a typical hover tip Mach number is about 0.6, for the third generation MAV rotors at 3000 RPM Mach number is only M=0.102. The lower tip speeds and smaller pressure gradients between upper and lower surfaces of the blades radically change the design drivers of the blade tips. Since compressibility effects are negligible and rotary-wing MAV vehicles are designed to spend a large fraction of their mission duration in hover, blade tips main design driver is to reduce the power requirement by promoting a more uniform inflow while keeping profile loses at a minimum.

In general, when blades are tapered the only geometric rotor parameter that changes is the solidity. The blade area is reduced along the span without changes in the airfoil or twist distribution. For the tests performed in this investigation, rectangular blades with a uniform airfoil shape along the span were modified by simply removing some material from the tips. By doing this, four rotor and airfoil parameters can be simultaneously affected:

- Solidity
- Twist distribution
- Airfoil camber
- Airfoil thickness ratio

If the baseline rectangular blade has a flat plate airfoil, only solidity and airfoil thickness ratio will be modified. However, if the airfoil is cambered all the four geometric parameters listed above are modified as function of the resultant blade shape. The use of this methodology with baselines blades having circular arcs is specially convenient considering that when cutting a circular arc in two, the resultant segments are circular arcs too. This fact, as will be shown Chapter 5, facilitates the parameterization of the airfoil geometry and implementation of a table lookup algorithm.

Figure 2.56 illustrates how the use of linear taper at the tip of a blade with baseline 9% camber circular arc changes the parameters previously mentioned. The use of asymmetric taper with respect to the midchord along the blade span with the offset toward the leading edge introduces negative twist (cf. Fig. 2.56(b)). If the taper is symmetric, no twist is introduced (cf. Fig. 2.56(a)). Obviously, if positive twist is required, the taper would be offset towards the trailing edge.

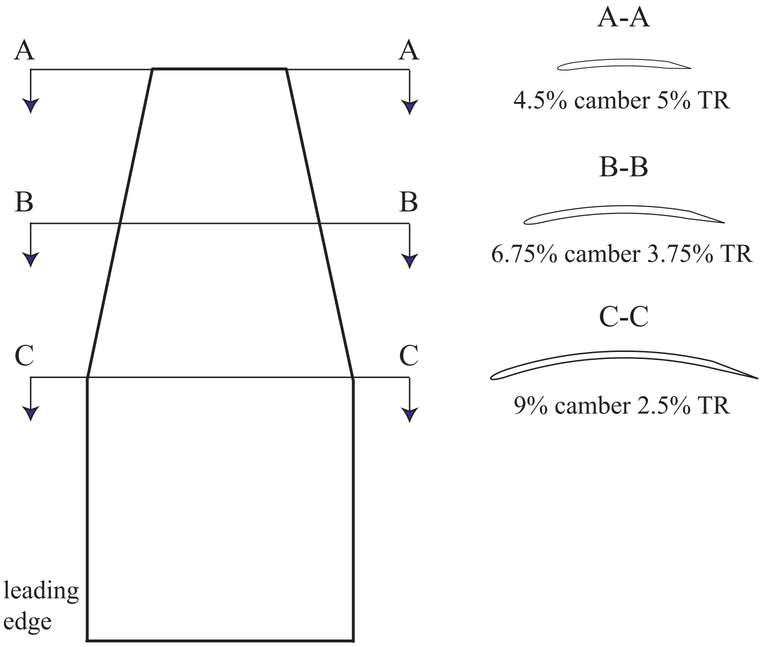

(a) 2:1 taper ratio symmetric

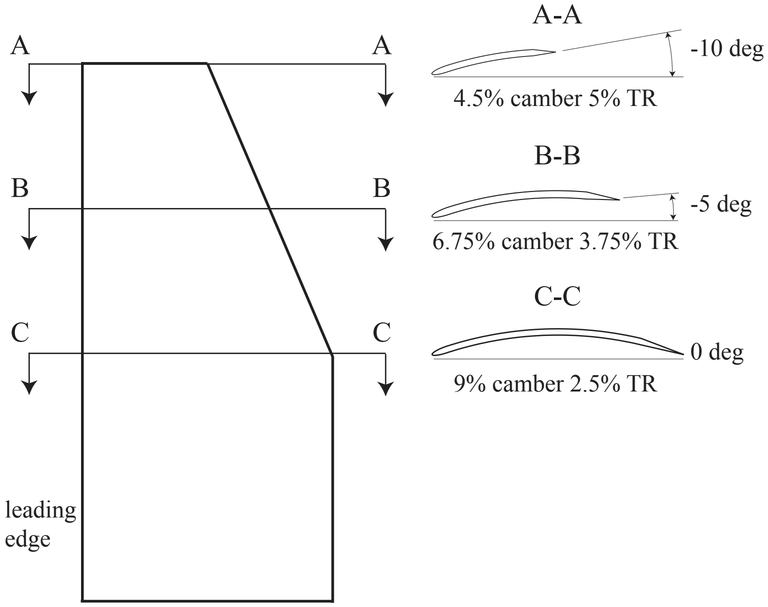

(b) 2:1 taper ratio asymmetric

Figure 2.56: Geometric effects of symmetric and asymmetric 2:1 linear taper on blade with baseline 9% circular arc airfoil.

As explained in Section A.7.4, blade and airfoil parameters determine in large part the power required by a hovering rotor. Taper and twist are generally used to optimize the rotor performance by reducing the induced and profile power requirements. Taper reduces the local solidity of the blades and consequently the inflow. With the right combination of twist and taper, a more uniform inflow and higher lift to drag ratios can be achieved along the blade span. In the following sections, the experimental results for rotors having various representative tip shapes on blades with flat and cambered airfoils are presented.

2.6.2 Blade Planform Effects on Hover Performance of Rotors with Flat Plate Blades

The effect of different planform shapes on rotors with flat plate blades with elliptical leading edges is studied in this section. In order to isolate the effects of taper alone, the airfoil shape needs to be kept unchanged over the blade span. In larger scale vehicles this can be easily achieved by proportionally reducing the airfoil thickness as the chord is reduced. However, because of manufacturing constraints, the thickness of the blades used in this investigation is fixed to a single value along the blade length. This leads to an increase in thickness ratio proportional to the taper, even though airfoil camber is unmodified and equal to zero.

Three different blade geometries were tested and compared with the results for rectangular blades; these are shown in Figure 2.57. Blade planform was modified by simply cutting material from tips and carefully reshaping the leading edge. Ideally, these tests should have been performed using a single baseline rotor with rectangular blades. However, two baseline rotors with different chord were used to compare the effect of the linear and nonlinear tapers. Nevertheless, this should not affect the conclusions drawn. Table 2.7 shows the test matrix used.

Figure 2.58 shows the effect on performance of the elliptical tip shapes. As expected there is no significant difference between the symmetric and asymmetric shapes. This is not surprising considering that both geometries have the exact same solidity and thickness ratio distribution. However, with respect to the rectangular

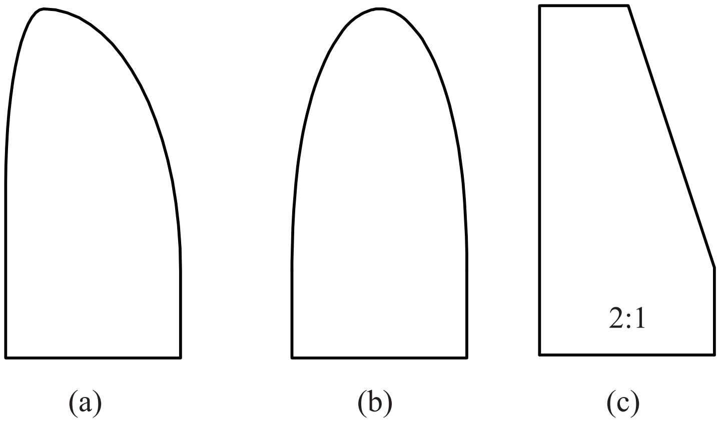

Figure 2.57: Blade tip shapes used with flat plate blades, (a) elliptical asymmetric, (b) elliptical, (c) 2:1 asymmetric linear. For geometries taper starts at 0.8R.

Planform	Baseline chord=1.5cm	Baseline chord=2.25cm
Rectangular	$\surd$ ($\sigma = 0.0909$)	$\surd$ ($\sigma = 0.1279$)
Elliptical sym	$\surd$ ($\sigma = 0.0722$)	
Elliptical non-sym	$\surd$ ($\sigma = 0.0722$)	
2:1 lin taper @ 0.8R		$\surd$ ($\sigma = 0.1222$)

Table 2.7: Flat plate tests matrix for three different tip shapes, and elliptical leading edge

blades, a clear reduction in rotor efficiency was observed. This drop in FM is mostly a result of loss of thrust at the blade tips due to the reduced blade area.

Comparing the performance of the rotors with rectangular and linearly tapered tips leads to the opposite result. Figure 2.59 shows an increase in maximum FM from 0.35 to 0.37 as a result of the linear taper. The difference between the two tip geometries, other than the solidity, are the solidity and thickness ratio distributions. The linearly tapered blades have a larger blade area closer to the tip, which results in a higher thrust weighted solidity than the elliptical blades. These issues are explored in more detail in the following section using cambered blades.

From the results presented in this section, it can be concluded that when using flat plate airfoils, blade planform only matters in the extent it affects solidity distribution. As long as the thrust weighted solidity is kept constant, the effects on rotor performance will be minimal. Nevertheless, blade planform can be modified to reduce rotor power consumption as was observed with the linearly tapered blades.

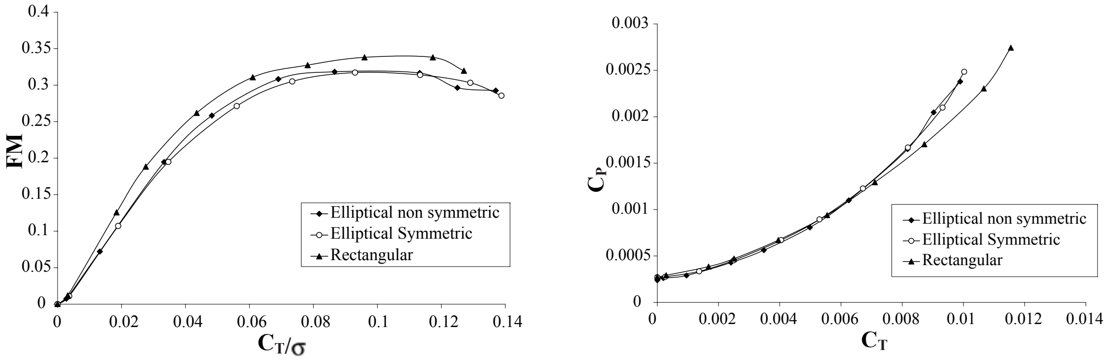

(a) C_T/σ vs. FM base chord=1.5 cm (b) C_T vs. CP base chord=1.5 cm

Figure 2.58: Effect of symmetric and asymmetric elliptical taper starting @ 0.8R on flat plate blades with elliptical leading edges.

2.6.3 Blade Planform Effects on Hover Performance of Rotors with cambered blades

This section explores the combined effects of different blade tip shapes on three different baseline rotors. The first set used a rotors with a 9% camber airfoil and

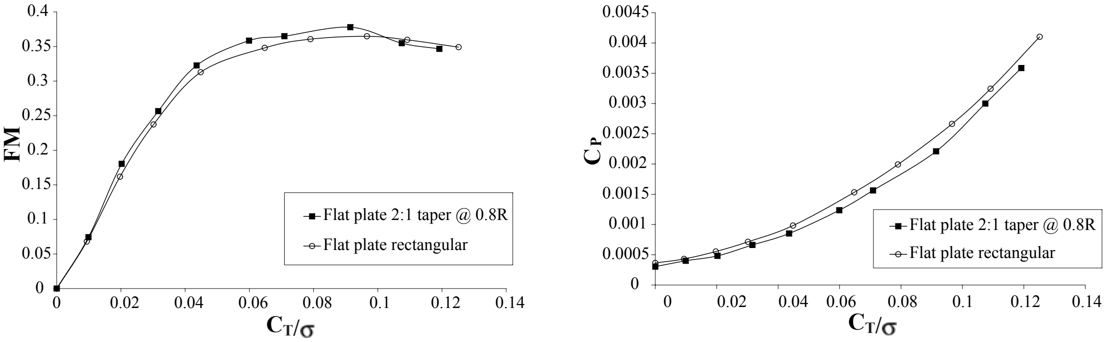

(a) C_T/σ vs. FM base chord=2.25 cm

(b) CT vs. CP base chord=2.25 cm

Figure 2.59: Effect of 2:1 taper ratio starting @ 0.8R on flat plate blades with elliptical leading edges.

Tip shape	9% camber	Solidity
Rect. baseline	√	$\sigma = 0.0.0909$
Elliptical sym	√	$\sigma = 0.0882$
Elliptical non-sym	√	$\sigma = 0.0882$
lin taper 1.66:1, sym	√	$\sigma = 0.0882$
lin taper 1.66:1, non-sym	√	$\sigma = 0.0882$

Table 2.8: Tests matrix for five different tip shapes with elliptical leading edges and equal solidity. Linear taper starts at 0.85R

a chord of 1.6 cm ($\sigma = 0.909$), and was used to evaluate five different tip shapes. The other two sets focused on the study of 6% and 9% circular arc airfoils using as baseline the higher solidity rotor ($\sigma = 0.1279$). Tables 2.8 and 2.9 summarize the tests performed.

Effect of solidity distribution

The blade shapes of Figure 2.60 have a equal solidity of 0.0882 but different solidity distributions. Tips a) and b) are nonlinear and shapes c) and d) are linear tapers. In terms of thrust weighted solidity (σ_e), geometries a) and b) have a σ_e of 0.0832, and geometries c and d have a σ_e of 0.0836. The thrust weighted solidity is a concept similar to the mean chord used for fixed wing analysis. It is used in helicopter

Taper start	Tip shape	6% camber	9% camber	Solidity
Taper @ 0.8R	Rect. baseline	$\surd$	$\surd$	$\sigma = 0.1279$
	Lin taper 1.33:1 asym	$\surd$	$\surd$	$\sigma = 0.1247$
	Lin taper 1.66:1 asym	$\surd$	$\surd$	$\sigma = 0.1228$
	Lin taper 2:1 asym	$\surd$	$\surd$	$\sigma = 0.1215$
	Lin taper 2:1 sym	$\surd$	$\surd$	$\sigma = 0.1215$
Taper @ 0.6R	Lin taper 2:1 asym		$\surd$	$\sigma = 0.1151$
	Lin taper 2:1 asym		$\surd$	$\sigma = 0.1151$

Table 2.9: Tests matrix for 6% and 9% camber blades with various linear taper ratios starting at various chordwise locations

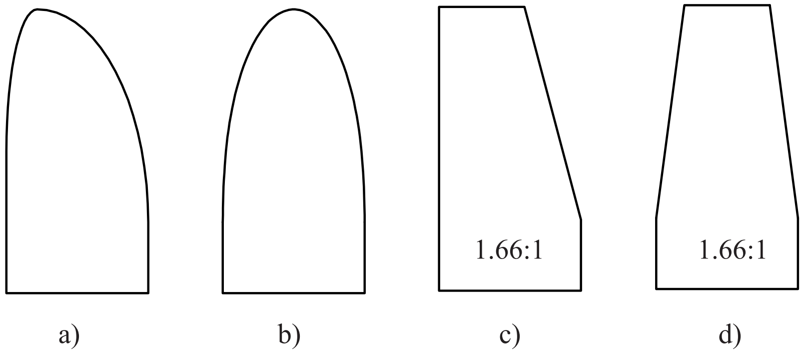

Figure 2.60: Blade tip shapes used with 9%, (a) elliptical asymmetric, (b) elliptical, (c) 1.66:1 asymmetric linear, (d) 1.66:1 symmetric linear. For geometries taper starts at 0.85R.

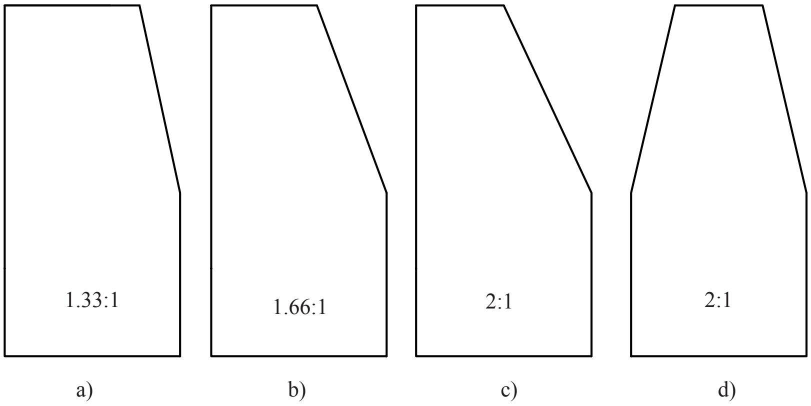

(a) Linear taper with various ratios starting at 0.8R

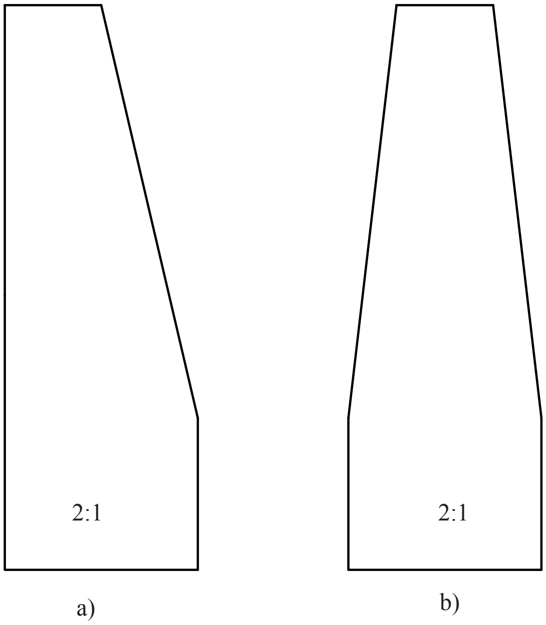

(b) Linear 2:1 taper starting at 0.6R

Figure 2.61: Tip shapes tested with 6% and 9% camber airfoils with 2.25 cm chord

rotors to account for the effect of the planform, weighting the influence of the tips more heavily than the inner rotor regions. The equivalent thrust weighted solidity is defined as

$$\sigma_e = 3 \int_0^1 \sigma(r) r^2 \, dr. \tag{2.14}$$

Where σ is the local solidity and r is the radial station. The difference in thrust weighted solidities between the linear and nonlinear taper distributions is small; however, its effects were clearly measured. Figure 2.62 shows the C_T vs. FM and C_T vs. C_P plots for the symmetric linear and elliptical tapers of Figure 2.60(b and d). In both cases maximum FM increased with respect to the rotor with the baseline rectangular blades, being higher for the symmetric elliptical tip shape. The performance gains are a product of the lower power requirements of the rotor over the thrust range covered. However, maximum thrust coefficients were reduced, as it occurred with the flat plate blades, because of the smaller blade area.

The thrust weighted solidity definition makes use of an important assumption. As for the mean-wing concept in fixed wings, lift coefficient is assumed constant along the span and equal for all the rotors compared. This means that the definition breaks down if rotors with radically different planforms or airfoils are compared. This is what is happening in this case. For the rotors considered there are airfoil differences produced by the various planform shapes. This is why thrust weighted solidities are not used in this dissertation to compare the various rotor configurations.

Figure 2.63 shows the results for the asymmetric tip configurations. In this case the performance gains are higher than with the symmetric blade geometries. The maximum figure of merit achieved with the asymmetric linear taper is 0.585, being 11.5% higher than with the rectangular baseline blades. The use of the asymmetric elliptical tip also improved FM. Maximum FM reached a value of 0.570 at a slightly lower C_T. In both cases, the asymmetric geometries were superior to the symmetric ones, trading off higher efficiency for lower thrust levels.

The effects of blade tip geometry on twist distribution, airfoil camber, thick-

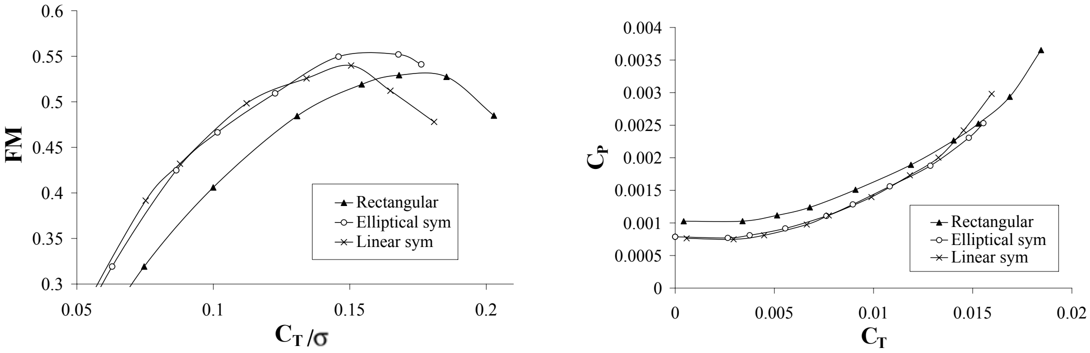

(a) C_T/σ vs. FM base chord=1.6 cm (b) CT vs. CP base chord=1.6 cm

Figure 2.62: Effect of symmetric taper distribution on blades with baseline 9% camber airfoils and elliptical leading edges at 3000 RPM.

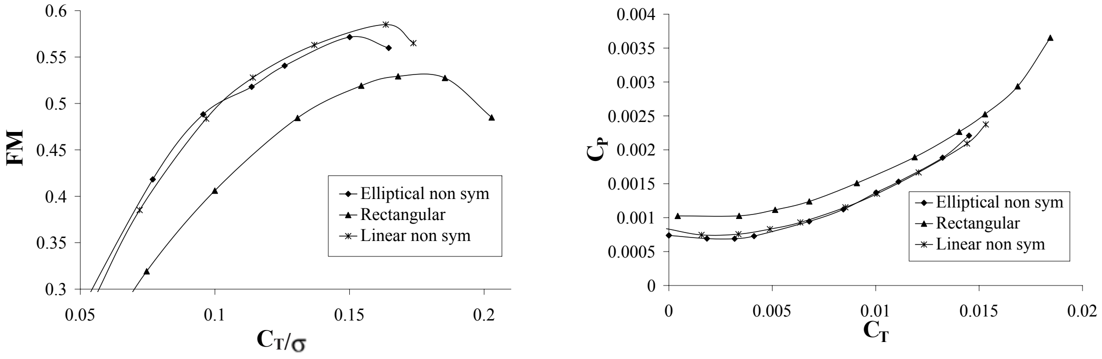

(a) C_T/σ vs. FM base chord=1.6 cm (b) C_T/σ vs. CP base chord=1.6 cm

Figure 2.63: Effect of asymmetric taper distribution on blades with baseline 9% camber airfoils and elliptical leading edges at 3000 RPM.

ness ratio and Reynold number, are plotted in Figure 2.64. The elliptical tip shape gradually reduces the blade chord to the point where it becomes zero at the tip of the blade. This has negative consequences on the airfoil parameters that determine the aerodynamic sectional characteristics. As can be observed in Figure 2.64, thickness ratio becomes very large over the outer 5% of the rotor, while the airfoil camber rapidly approaches zero. Similarly, the chord Reynolds number is reduced to extremely low values. The linear tapered blades undergo similar airfoil geometric changes. However, because of the finite chord length, thickness ratio, Reynolds number and camber are kept at reasonable values even at the blade tip.

Now that the airfoil differences between the elliptical and linearly tapered tips have been identified, the results of Figure 2.62 can be better understood. Both symmetric elliptical and linearly tapered blades outperform the rectangular baseline. However, the linearly tapered blades suddenly stalled at collectives above 14 deg, while the elliptical ones had a more gradual stall that allowed the rotor to reach higher efficiency levels. It seems that the outer portions of the blades that have the smaller cambers and face relatively low Reynold numbers are stalling at the higher collectives producing large amounts of drag. Since these regions of separated flow are smaller in the elliptical blades, less drag is produced.

On the other hand, when asymmetric taper is used, negative twist angles are introduced. Figure 2.64(b) shows how the tip negative twist delays the stall of the outer blade regions. The final result is that the asymmetric linearly tapered blades with a finite blade tip chord and negative twist outperformed the elliptical blades (cf. Fig. 2.63). The performance gains are not only a result of improved airfoil characteristics and operating conditions. The negative twist and reduced blade tip area have also a strong influence in the rotor inflow, helping in the reduction of induced power. In order to have a quantitative interpretation of the experimental results a model that considers the varying airfoil characteristics and the inflow changes needs to be used. Chapter 5 addresses that issue in detail. For now, the experimental results are presented and used to identify the trends and relevant parameters that affect rotor performance.

Now that the elliptical and linear taper blade tips have been compared, the effects of geometric variation of linear tapers on rotor performance are explored.

Effect of taper ratio, baseline camber and taper start location

In this segment of the chapter, the experimental results of the test matrix of Table 2.9 are presented. For the tip geometries with camber starting at 0.8R the taper ratio is gradually increased using two rectangular baselines blades with 6% and 9% camber. Figure 2.65 shows the camber and twist distributions along the tapered

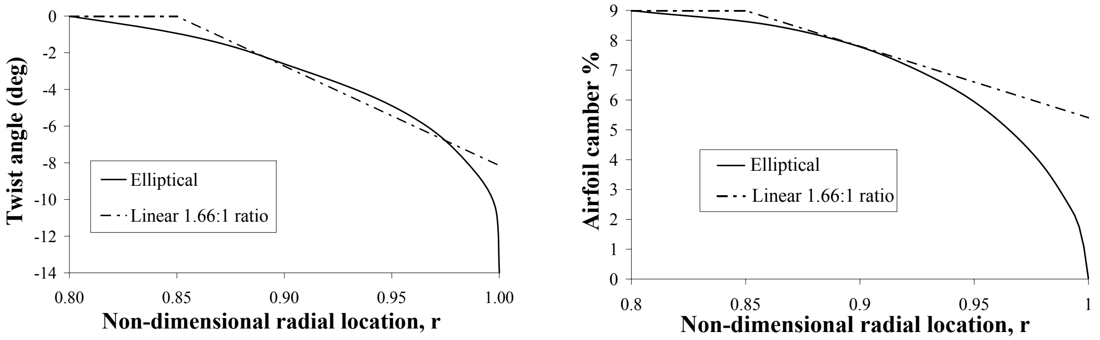

(a) Twist along asymmetric tapered tips (b) Airfoil camber along tapered tips

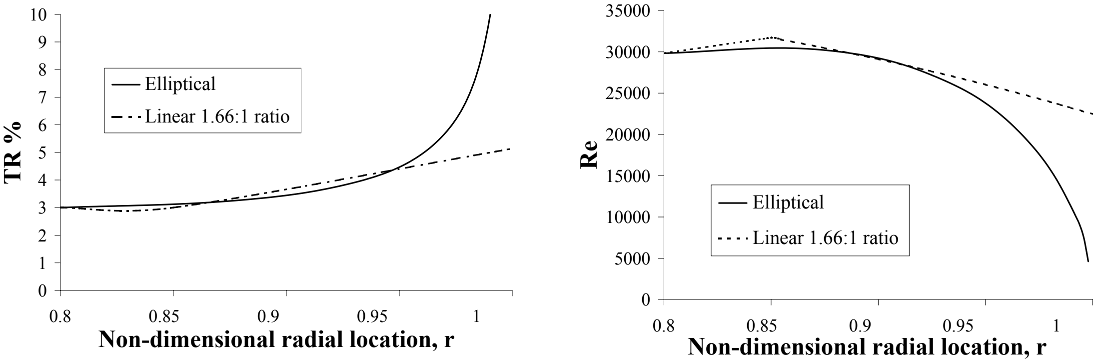

(c) Thickness ratio along tapered tips (d) Re along tapered tips at 3000 RPM

Figure 2.64: Tip shape geometry effects on twist distribution, airfoil camber, thickness ratio and Reynolds number for elliptical and linear tapers on rotors with equal solidity

portion of the blade for the the various taper ratios. The Figure shows the very large negative twist angles that are achieved over such a short radial distance. For the 6% camber blades with a taper ratio of 2:1 a negative twist of ≈ -6 deg is obtained, while with the baseline 9% camber, the 2:1 taper ratio produces a negative twist of -10 deg. The effect in hover performance of the different tip configurations was studied in experiments where collective pitch angles were varied from 0 deg to 18 deg in steps of 2 deg, and rotational speeds were varied from 2000 RPM up to 3000 RPM in steps of 500 RPM. Some representative results at 2500 and 3000 RPM are presented in Figures 2.66 and 2.67 where FM is plotted vs. blade loading coefficient for the different tip geometries and the two baseline cambers.

Results show that the blade tip geometric modification had a strong and clear beneficial effect on rotor performance at all rotational speeds. For all cases, the asymmetric taper increased the maximum FM with respect to the baseline case. For the blades with 6% baseline airfoil, the 2:1 and 1.66:1 taper ratios had similar performance levels reaching maximum FM of ≈ 0.62 at 3000 RPM and ≈ 0.60 at 2000 RPM. This is an improvement over the baseline of ≈ 7% at 3000 RPM and ≈ 5% at 2500 RPM. The 2:1 taper ratio provided slightly higher FM values of about 1% over the entire blade loading coefficient range. The use of the 1.33:1 taper ratio produced a substantial reduction in thrust, however, maximum FM increased only by 2.5% with respect to the baseline.

The blade tip modifications on the blades with a baseline 9% camber are shown on Figure 2.67. Large performance improvements were also observed in these set of tests. At 3000 RPM maximum figures of merit of ≈ 0.64 were achieved with the 1.66:1 taper ratio. The rotor with 2:1 taper performed almost as well, reaching a maximum FM of 0.63. These improvements correspond to a increase of approximately 8.5% and 7% in maximum FM. As tip speed is reduced, the gap in performance between the rotors with rectangular and tapered blades tends to be reduced. However, it still is significant even at the lower rotational speeds. As opposed to the tests with the 6% camber baseline airfoil, which showed sign of stall at collectives between 14 deg and 16 deg, the tapered blades with 9% baseline

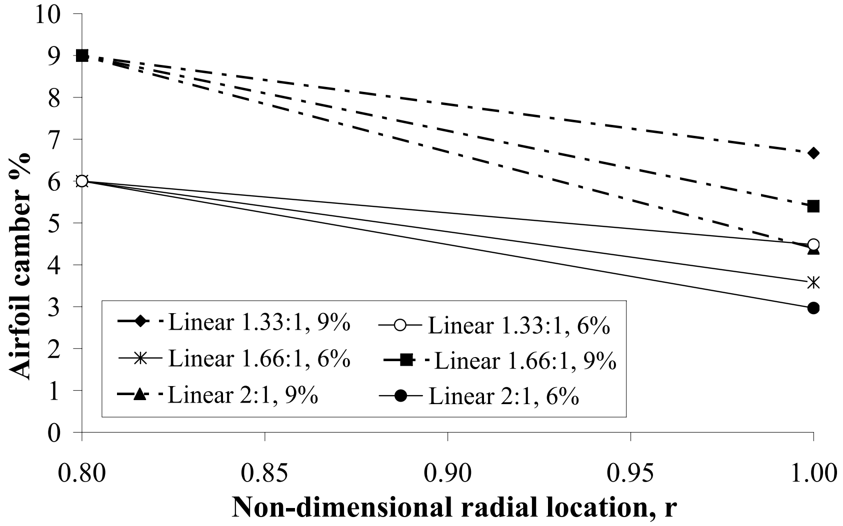

(a) Camber along asymmetric tapered tips

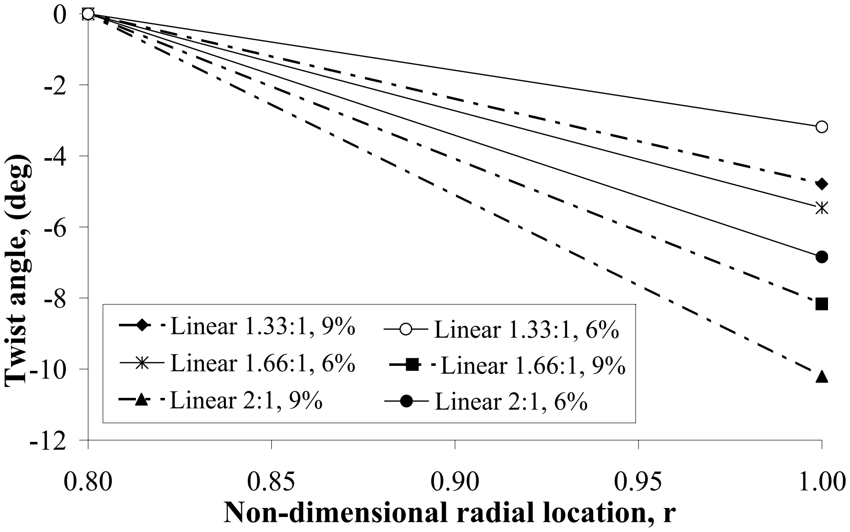

(b) Twist along asymmetric tapered tips

Figure 2.65: Tip shape geometry effects on twist distribution and airfoil camber on blades with baseline 6% and 9% camber airfoils and various linear asymmetric taper ratios.

camber stalled at higher collectives closer to 18 deg.

In the rotors with different taper ratios, the changes in camber and twist along the span have been coupled. In order to isolate the effect of twist, rotors with blades having symmetric taper are now compared to blades with asymmetric taper. A representative result for the 2:1 taper ratio blades with 6% baseline camber is shown in Figure 2.68. The results show that the lack of negative twist in the tapered blades practically eliminates any advantages of the planform modification. With the symmetric tips, the maximum FM dropped $\approx$ 5.5% from 0.62 to 0.585 with respect to the asymmetric taper. This illustrates how the right combination of both airfoil and rotor parameters are required to obtain a gain in performance.

Taper start location was the final parameter studied in this set of tests. The taper radial starting point was moved from 0.8R to 0.6R, and a 2:1 taper ratio was used on the baseline 9% camber blades. By doing this, the rotor solidity was reduced to $\sigma = 0.1151$. The initial and final values of the camber and twist distributions of Figure 2.65 do not change, but the starting taper radial location is now 0.6R. The experimental result are presented in Figure 2.69. In terms of maximum FM, practically no change was obtained by moving the taper start inwards. However, since the solidities are different, and the maximum FM occurred at the same C_T/σ, lower thrust levels were achieved. Higher collectives could be reached (20 deg) before rotor stall occurred. But, even at the highest collectives, the maximum blade loading coefficient reached were below the ones achieved by the higher solidity rotor. The result obtained with the symmetric taper starting at 0.6R are consistent with the previous results, where the advantages from the planform modifications are minimized when no negative twist is introduced.

Effect of leading edge shape on tapered blades

The effect of leading edge shape has been explored in the zero-lift drag generation of flat plates and in the hover performance of flat and cambered rectangular blades. It was found that the zero-lift drag coefficients and the maximum figure of merit improved with respect to a baseline elliptical leading edge. In this section, the best

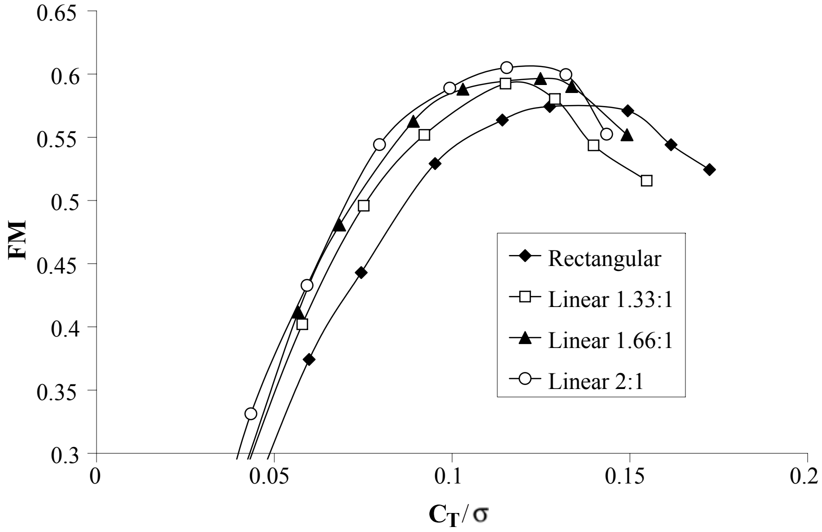

(a) C_T/σ vs. FM at 2500 RPM

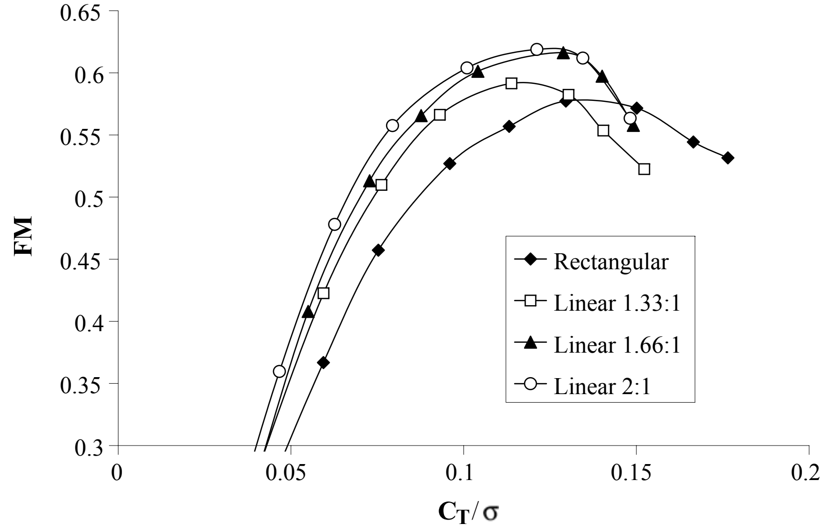

(b) C_T/σ vs. FM at 3000 RPM

Figure 2.66: C_T/σ vs. FM for rotors with baseline 6% camber airfoils with elliptical leading edges and various tip taper ratios at two rotational speeds.

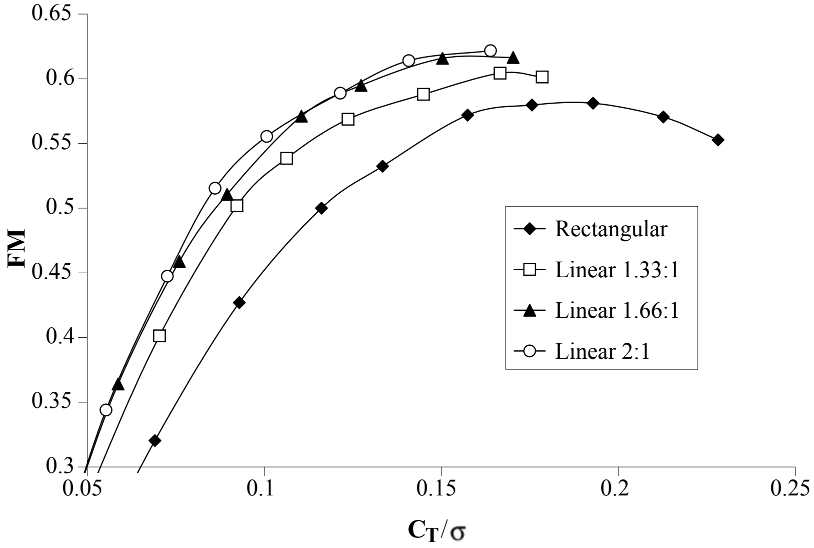

(a) C_T/σ vs. FM at 2500 RPM

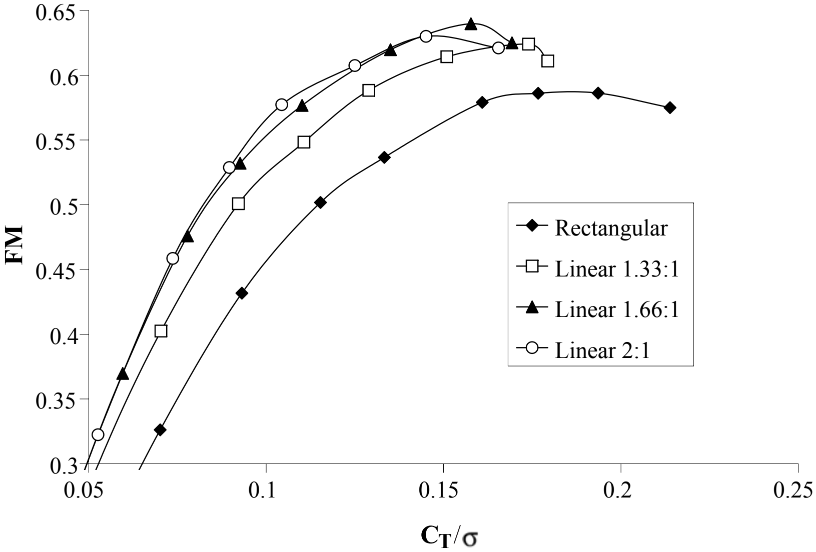

(b) C_T/σ vs. FM at 3000 RPM

Figure 2.67: C_T/σ vs. FM for rotors with baseline 9% camber airfoils with elliptical leading edges and various tip taper ratios at two rotational speeds.

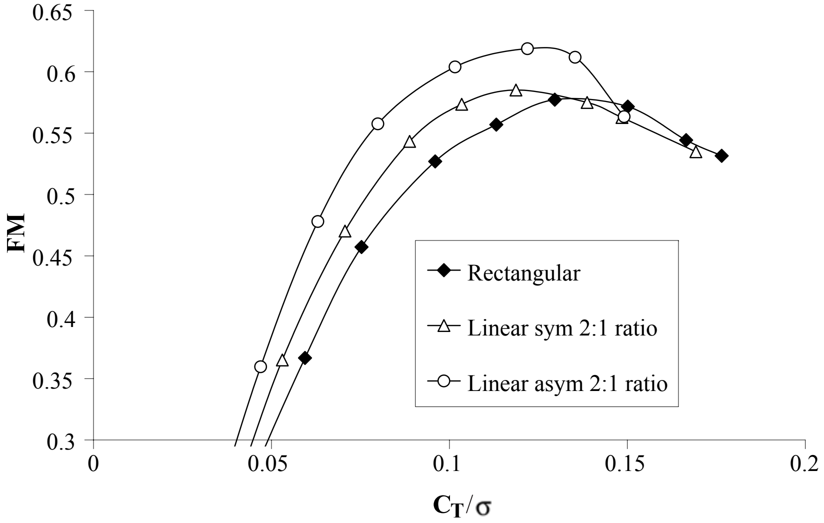

Figure 2.68: C_T/σ vs. FM for rotors with rectangular, symmetric and asymmetric 2:1 taper ratio blades with elliptical leading edges at 3000 RPM.

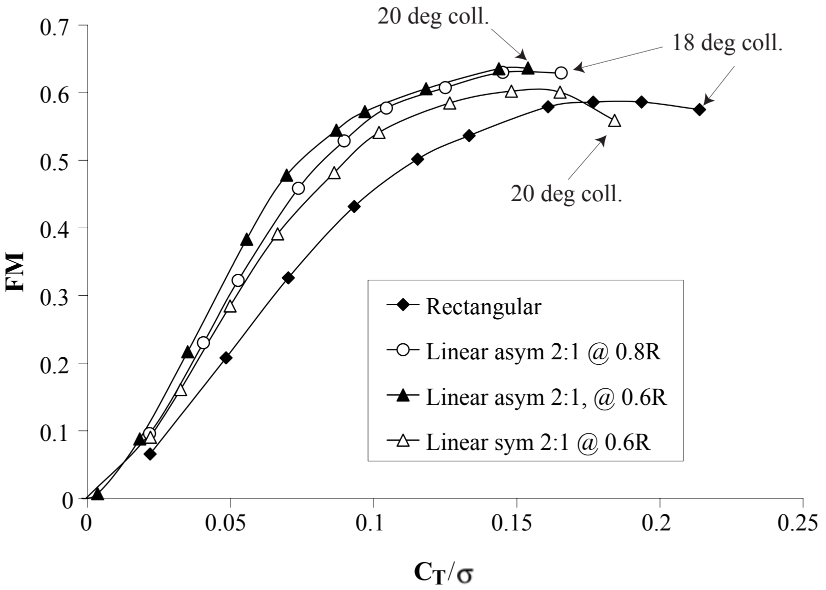

Figure 2.69: C_T/σ vs. FM for rotors with asymmetric 2:1 taper ratio starting at 0.8R and 0.6R and symmetric 2:1 taper ratio starting at 0.6R. Baseline 9% camber blades with elliptical leading edges at 3000 RPM.

performing linear tapered blades with elliptical leading edges were modified in order to evaluate their performance with sharp leading edges (geometry (4) of Figure 2.33). The experimental results for blades with the 2:1 and 1.66:1 taper ratio and the 6% and 9% baseline camber airfoil are shown in Figure 2.70. Representative results at 3000 RPM are compared with rotors having blades with the same planform but elliptical leading edges and with rectangular baseline blades. On the 6% baseline camber (cf. Fig. 2.70(a)), the sharpening of the leading edge improved even further the hover rotor performance of the rotor, reaching a maximum FM of 0.65. This is a ≈ 5% increase with respect to the tapered blades with elliptical leading edges and a ≈ 13% increase with respect to the rectangular baseline. A more moderate effect was observed in the blades with 9% baseline camber (cf. Fig. 2.70(a)), where maximum FM moved from 0.64 to 0.65 with the leading edge modification. However, with respect to the baseline rotor with rectangular blades an overall maximum FM increase of about 10% was achieved with the combined effects of planform and leading edge modifications.

Another important aerodynamic characteristic affected by the leading edge modifications is the rotor stall behavior. As observed before with the rectangular blades, the sharp leading edges produced a high efficiency plateau where FM had minor changes keeping a value close to its maximum for a range of thrust coefficients and collectives. While the tapered blades with elliptical leading edges showed signs of stall at 14 deg and 16 deg collective for the 6% and 9% baseline camber respectively, when sharp leading edges were used collectives up to 18 deg and 22 deg were achieved without observing a substantial drop in FM.

2.6.4 Maximum FM and Maximum PL Envelope

Hover rotor performance has been studied and quantified in terms of FM and in some cases power loading. Maximum FM has been used as the metric to compare the efficiency of different rotor and blade configurations. However, the large number of cases considered forced the experiments to be performed at fixed operational conditions of tip speed and collective settings. This resulted in measurements that

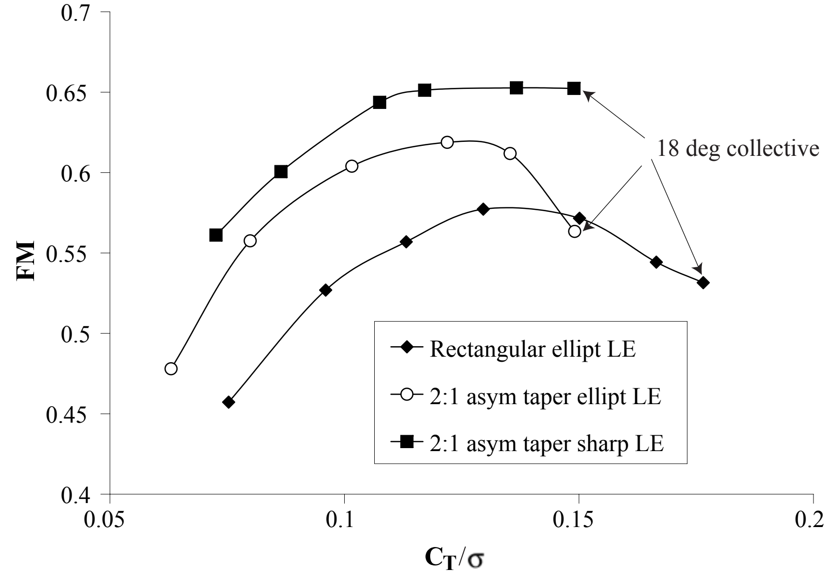

(a) C_T/σ vs. FM 6% camber base airfoil at 3000 RPM

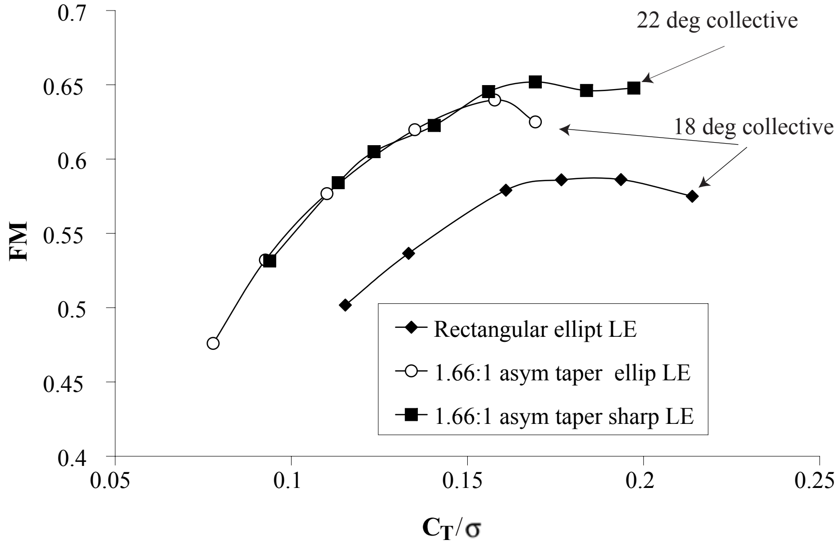

(b) C_T/σ vs. FM 9% camber base airfoil at 3000 RPM

Figure 2.70: C_T/σ vs. FM for rotors with baseline 6% and 9% camber airfoils, effect of leading edge on tapered blades.

covered a wide range of disk loadings. As explained in Section A.7.4, figure of merit comparisons should be performed at the same disk loading in order to be valid, and only for a few cases where solidity or baseline blade camber did not change this condition was met. In order to determine the best rotor configuration for a given DL, which is the situation faced by a designer that has a fixed vehicle weight and rotor diameter, the envelope for maximum power loading has to be considered. In Section 2.5.1 it was shown how for a given rotor configuration, maximum FM occurred at the same collective pitch at all rotational speeds. In order to match thrust requirements, the best power consumption is achieved by varying rotational speed while keeping the collective pitch for maximum FM fixed. In this way, the envelope for maximum PL is defined for a given rotor over a range of rotational speeds. Figure 2.71(a)) shows the various thrust vs. PL curves at several rotational speed, and the maximum PL envelope for a rotor with 2:1 taper ratio starting at 0.8R and with 9% baseline camber and elliptical leading edges.

A good approach to choose the best rotor for a given application within a pool of candidates is to compare the envelopes of maximum PL at the DL of interest. For the MAV design space a reasonable thrust range to consider is between 50g to 100g. Figure 2.71(b) shows the maximum PL envelopes for some rotors with rectangular and tapered blades having 6% and 9% baseline camber airfoils. It is important to clarify that for each rotor configuration, a given thrust is produced at different rotational speeds. From the figure it can be observed that in general the rotors with the highest maximum FM at a given rotational speed also achieve the highest PL values over the entire DL or thrust range. Configurations having similar maximum FM values at a given tip speed will have comparable power loadings over a wide range of disk loadings.

The highest power loading of all the configurations tested was achieved by the tapered blades at 0.8R. Small differences exist between the rotors with baseline 6% and 9% camber airfoils, however the exact performance values are hard to estimate accurately considering the reduced number of data points used to obtain every PL curve.

An important conclusion that can be drawn from this plot is that various blade configurations can produce very similar hover performance levels at the same disk loading while having different rotational speeds. This is an important point when designing the transmission of an MAV. As it is shown in Chapter 6, matching the motor with the transmission can be as important as the aerodynamic hover efficiency of the rotor, a good transmission choice is a key factor in the overall efficiency of a vehicle. Being able to operate a rotor at very different rotational speeds without sacrificing aerodynamic efficiency gives the designer flexibility in the development of a practical system.

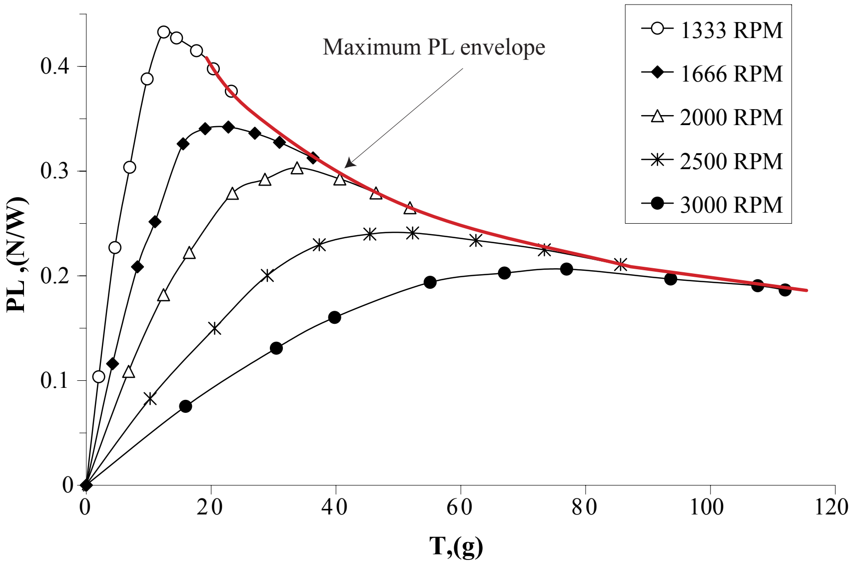

(a) Envelope of max PL from T vs. PL plots at various rotational speeds for rotor with 2:1 tapered blades @ 0.8R, 9% baseline camber and elliptical LE

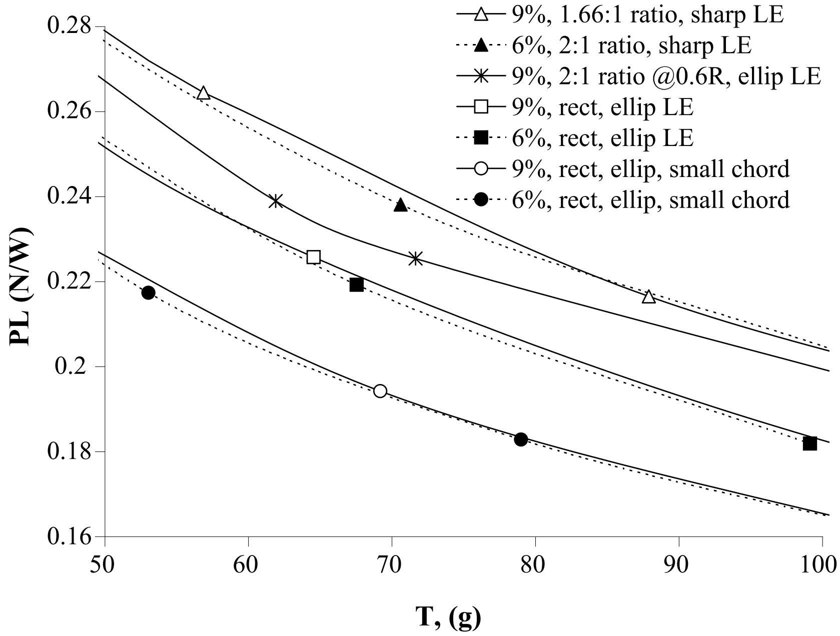

(b) Comparison of maximum PL envelopes over a thrust range of 50g to 100g.

Figure 2.71: Maximum PL envelopes for rotors with various blades configurations

2.7 Summary

The first part of this Chapter presented the hardware, methods an approaches used to experimentally study the hover performance of single small-scale rotors. The hover stand used for data acquisition was described in detail, explaining its capabilities, calibration and accuracy limitations. The second part presented the results of tests designed to explore a series of geometric airfoil, blade and rotor parameters as well as operational conditions that determine the rotor's hover performance. Using rectangular blades, the effect of the following geometric parameters was studied:

- Number of blades
- Solidity
- Twist
- Airfoil shape (streamlined vs thin plate)
- Airfoil camber
- Airfoil maximum camber location
- Airfoil thickness ratio
- Leading edge shape
- Zero lift drag (using flat plates)

The investigation used mostly circular arc airfoils since they offer a unique series of advantages in terms of manufacturing ease and parameterization. The fact that a section of a circular arc is also a circular arc was used to study the coupled effects of camber reduction, taper and twist along tapered sections of the blade span. Blade material was removed from the blade tips in order to obtain the coupling between the previously mentioned parameters. Several taper geometries were studied on flat plates, and blades with 6% and 9% baseline camber. The effects on hover performance of taper distribution (linear vs. non linear), taper ratio, taper offset (symmetric vs asymmetric), and taper radial starting location were also measured.

The systematic investigation of geometric rotor, blade and airfoil parameters helped identify rotor configurations that achieved large improvements over the rotors used in the first generation coaxial MAV prototype, which had limited thrust capabilities and poor hover efficiency. Maximum figures of merit of up to 0.65 were measured on two-bladed rotors with 1.66:1 asymmetrically tapered blades and sharp leading edges. Experimental results were used to determine that the collective for maximum FM is practically independent of rotational speed. This has important implications in vehicles implementation which should control rotational speed rather than collective pitch for varying thrust levels.

Even though FM is a good performance metric, its use is limited by the fact that valid FM comparison can only be performed at equal disk loadings. The large variations in solidity, twist and blade camber of the different configurations tested produced large differences in the DL at which maximum FM occurred. In order to have a clear method of comparison that can be used over a range a DL, the boundary of maximum power loading can be obtained for each rotor considered. The resultant PL vs. DL curves can be compared to unequivocally determine the most efficient rotor over a range of DL.

Chapter 3

Blade Element Momentum Theory and Average sectional Airfoil Characteristics

3.1 Introduction

On Chapter 2, systematic experimentation was used to explore the effects on hover performance of a series of parameters. Results served to identify the combinations of airfoil and blade geometries within a well defined test space that had a beneficial effect on hover efficiency. Qualitative knowledge of the airfoil and rotor physics was used to converge to configurations with improved performance. However, a purely experimental approach is not sufficient to have a deeper understanding of the problem. It is important to implement a model that can capture the relevant aerodynamic phenomena and the effect of the parameters identified in the experiments.

The first part of the chapter explains the implementation of a mathematical model using Blade Element Momentum Theory (BEMT). A methodology to obtain from rotor tests an estimate of the average sectional aerodynamic characteristics of the airfoils is explained. Other results of the analysis such as the induced and profile power contributions, the inflow and induced angles of attack distributions are discussed and used to have a better understanding of the experimental results of Chapter 2.

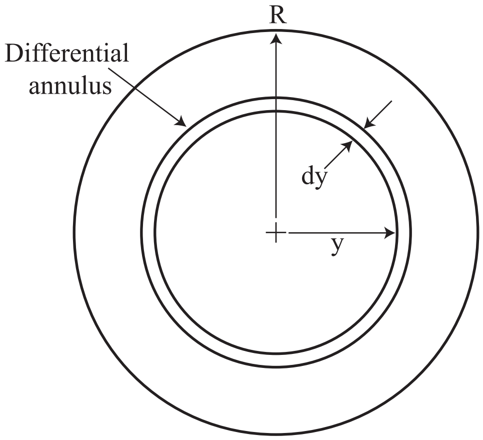

Figure 3.1: Discretization of rotor disk used for BEMT analysis.

3.2 Blade Element Momentum Theory

While simple momentum theory can be used as a first approximation to estimate the efficiency of rotors, a more accurate aerodynamic theory is needed to incorporate blade geometry, sectional orientation, twist distribution, and airfoil characteristics. The blade element momentum theory (BEMT) is a method that combines the momentum and blade element theories and allows one to estimate the inflow distribution along the blade.

3.2.1 Derivation of Equations

The rotor disk area can be discretized into concentric annuli of a area $dA = 2\pi\, y\, dy$, as show in Figure 3.1. Applying simple one dimensional momentum theory, to a rotor in axial vertical flight, the thrust produced by each annulus is:

$$dT = 2\rho\,(V_c + v_i)v_i\, dA \;=\; 4\pi\,\rho\,(V_c + v_i\, y\, dy. \tag{3.1}$$

Where v_i is the induced velocity and V_c is the climb speed. Normalizing the previous equation, the differential thrust coefficient is

$$dC_T = \frac{2\rho\,(V_c + v_i)v_i\, dA}{\rho\pi\, R^2\,(\Omega\, R)^2} \;=\; 4\frac{V_c + v_i}{\Omega R}\left(\frac{v_i}{\Omega\, R}\right)\left(\frac{y}{R}\right) d\left(\frac{y}{R}\right). \tag{3.2}$$

In terms of the total inflow ratio λ and the induced inflow ratio λ_i the equation becomes simply:

$$dC_T = 4\lambda\lambda_i\, dr \;=\; 4\lambda(\lambda - \lambda_c)\, r\, dr. \tag{3.3}$$

Where λ_c in the component of the total inflow ratio product of the climb speed of the rotor. Using blade element theory (BET) the incremental thrust coefficient of the annulus is:

$$dC_T = \frac{1}{2}\,\sigma\, C_l\, r^2\, dr \;=\; \frac{\sigma\, C_{l_\alpha}}{2}(\theta\, r^2 - \lambda r)\, dr. \tag{3.4}$$

Now the key step is taken, the differential thrust coefficient expressions from momentum (Eq. 3.3) and blade element theories (Eq. 3.4)are combined to obtain a quadratic equation in λ:

$$\frac{\sigma\, C_{l_\alpha}}{2}(\theta\, r^2 - \lambda r)\, dr \;=\; 4\lambda(\lambda - \lambda_c)\, r\, dr. \tag{3.5}$$

Factoring λ the canonic form is obtained:

$$\lambda^2 + \left(\frac{\sigma C_{l_\alpha}}{8} - \lambda_c,\right)\lambda - \frac{\sigma C_{l_\alpha}}{8}\theta r \;=\; 0. \tag{3.6}$$

The solution to this equation is:

$$\lambda(r,\, \lambda_c) \;=\; \sqrt{\left(\frac{\sigma C_{l_\alpha}}{16} - \frac{\lambda_c}{2}\right) + \frac{\sigma C_{l_\alpha}}{8}\theta r} - \left(\frac{\sigma C_{l_\alpha}}{16} - \frac{\lambda_c}{2}\right). \tag{3.7}$$

In this chapter only a hovering condition is considered, such that $\lambda_c = 0$. This simplifies Equation 3.7 to :

$$\lambda(r) \;=\; \frac{\sigma C_{l_\alpha}}{16}\left[\sqrt{1 + \frac{32}{\sigma C_{l_\alpha}}\theta r} - 1\right]. \tag{3.8}$$

It is a common practice to solve the BEMT equations numerically by discretizing the blades into a series of small elements. The rotor inflow ratio at each n element, $\lambda(r_n)$, is given in the numerical implementation of the BEMT in hovering conditions by:

$$\lambda(r_n) = \frac{\sigma C_{l\alpha}}{16}\left[\sqrt{1 + \frac{32}{\sigma C_{l\alpha}}\theta(r_n) r_n} - 1\right] \tag{3.9}$$

where r_n and $\theta(r_n)$ are the radius and the pitch angle at the midspan of each of the n elements, respectively. Equation (3.9) allows one to solve for the inflow as a function of the radius for any given airfoil section and blade geometry. After the inflow is determined, the incremental thrust of each blade element is obtained using

$$\Delta C_T = \frac{\sigma C_{l\alpha}}{2}(\theta(r_n) r_n^2 - \lambda(r_n) r_n)\Delta r \tag{3.10}$$

The total thrust is calculated by numerically integrating over the blade. The induced power coefficient, C_{Pi}, and profile power coefficients, C_{P0}, are also calculated numerically using the following equations:

$$C_{Pi} = \int_{r=0}^{r=1} \lambda \, dC_T \tag{3.11}$$

$$C_{Po} = \frac{\sigma}{2}\int_{r=0}^{r=1} C_d(r) \, r^3 \, dr \tag{3.12}$$

The induced power factor is found using Eq. (3.13) after solving Eq. (3.11) to find the induced power coefficient and numerically integrating Eq. (3.10) along the blade span to calculate the rotor thrust coefficient C_T.

$$\kappa = \frac{C_{Pi}}{C_T^{\frac{3}{2}}/\sqrt{2}} \tag{3.13}$$

The preceding equations are modeling the viscous losses through the airfoil's drag coefficient, and part of the induced losses by calculating a non-uniform inflow distribution. However, the induced effects of the finite number of blades have not been considered. The tip and root losses are a product of the pressure differences between the upper and lower surfaces of the blade. This results in an increased inflow at the root and tip, reducing the induced angles of attack in these regions. The inflow distribution with tip losses is such that the lift produced at the inner and outer-most sections of each blade have to be zero. Tip loses were included in the present model using Prandtl's tip-loss function. Prandtl derived a factor to adjust the inflow as function of the number of blades N_b, and radial position r. The correction factor F is given by:

$$F = \left(\frac{2}{\pi}\right) \cos^{-1} e^{f}. \tag{3.14}$$

And f is:

$$f = \frac{N_b}{2} \left(\frac{1 - r}{r\phi}\right). \tag{3.15}$$

Where the induced inflow angle ϕ is a function of the inflow and the radial position:

$$\phi = \frac{\lambda(r)}{r}. \tag{3.16}$$

Prandtl's tip loss factor is included in the model by modifying the momentum equation of the differential thrust coefficient. Equation 3.3 for a hovering rotor case ($\lambda_c = 0$) becomes:

$$dC_T = 4\, F\, \lambda^2\, r. \tag{3.17}$$

Equating the differential thrust coefficient from BET with Eq. 3.17, a quadratic equation in λ is obtained again. Following the same procedure as in equations 3.5 to 3.8, an expression for the inflow as function of the radial position is derived:

$$\lambda(r) = \frac{\sigma C_{l_\alpha}}{16F} \left[\sqrt{1 + \frac{32F}{\sigma C_{l_\alpha}}\theta r} - 1\right]. \tag{3.18}$$

However, since F is a function of λ, equation 3.18 needs to be solved iteratively. An initial values of F equal to 1 is assumed, and the resultant λ is used in Eq. 3.14 to recalculate F. Only a few iteration are necessary to achieve convergence. Figure of merit and power loading can be calculated by applying their definitions using the thrust and power obtained from BEMT. Details of the previous derivations can be found in Refs. [76], [77], and [78].

3.2.2 BEMT and Sectional Airfoil Characteristics

In the BEMT equations presented in the previous section, the airfoil characteristics were included through the use of the lift coefficient slope (C_{l_α}) and the local drag coefficient C_d. For full-scale helicopters excellent results can be achieved assuming an average drag coefficient equal to the zero-lift drag (C_{d_0}) and a constant C_{l_α}. However, at low Reynolds numbers that approach may not yield good result. As shown in Figures A.8 and A.11, lift coefficient curves can be highly non-linear, while drag coefficients usually have a rapid growth with angle of attack. BEMT calculations at low Re using an ideal C_{l_α} of 2π, and a C_d equal to C_{d_0} will produce very inaccurate thrust and power predictions. One way to overcome this problem is to implement a table look-up scheme. Lift and drag coefficients for a given airfoil can be tabulated as function of the angle of attack, and used by a BEMT code that uses that interpolates the coefficient tables to calculate the induced angles of attack along the elements of the blade.

The BEMT equations derived use C_{l_α} to calculate C_l and obtain the differential thrust at each blade station. Since the airfoil tables give a lift coefficient, a C_{l_α} can be defined for each point of the lift coefficient curve such that $C_{l_\alpha}(\alpha) = C_l/\alpha$. This approach works well in most cases, however for cambered airfoil at very low angles of attack, $C_{l_\alpha}(\alpha)$ becomes very large resulting in numerical problems. To implement a robust algorithm that can use airfoil tables at all angles of attack, the inflow equation(Eq. 3.5) was left as a function of C_l. The resultant equation is not a quadratic equation in λ anymore:

$$\frac{\sigma\, C_l}{2} r^2\, dr \;=\; 4\lambda F(\lambda - \lambda_c)\, r\, dr. \tag{3.19}$$

Since C_l is a function of the induced angle of attack which is dependent on the inflow, a solution for the inflow is found numerically using a table look-up scheme for C_l. After convergence is achieved, the induced angles of attack along the span are used to interpolated the drag coefficients from the tabulated data and calculate the profile power. The use of BEMT at low Reynolds number needs the use sectional airfoil characteristics in order to provide reasonable results. As discussed in the Appendix, the existing airfoil databases are still limited in size and rarely cover the Reynolds number range of interest for MAV development. Sectional aerodynamic characteristics of any airfoil can potentially be obtained from wind tunnel tests. However, wind tunnel experimentation is time consuming, expensive and requires vast amounts of infrastructure, making difficult to perform comprehensive parametric studies. The other possibility is the use of CFD to obtain, for a fraction of the cost and time, the sectional characteristics to feed the BEMT model. Both experimental and computational choices require expertise, and have specific advantages and shortcomings.

3.3 Inverse Method to Obtain 2D-Airfoil Characteristics from Rotor Tests

During the initial stages of the present investigation the computational resources to use CFD were not available, and the use of a wind tunnel was not possible. Nevertheless, the sectional airfoil characteristics of the rotors investigated were required to advance in the understanding of the problem. With this motivation, a methodology to obtain the "average" two dimensional airfoil characteristics solely from rotor tests was developed.

The appendix presents wind tunnel tests that show the strong dependency of airfoil characteristics with Reynolds number. For a rotor, the local chord-based Reynolds number varies along the span. If only one set of C_l and C_d curves are used at all the blade sections, these can be considered "average", or representative airfoil characteristics.

Ideally, the rotor blades should be rectangular with a single airfoil shape along the span. In this way the airfoil characteristic obtained will be "averaged" in terms of Reynolds number only. If the blades have various airfoil shapes, the resultant lift and drag coefficient can be considered as equivalent aerodynamic characteristics. Figure 3.2 shows a block diagram of the algorithm with the inputs and outputs and the iterative processes involved. The following section explain in more detail how the algorithm was implemented.

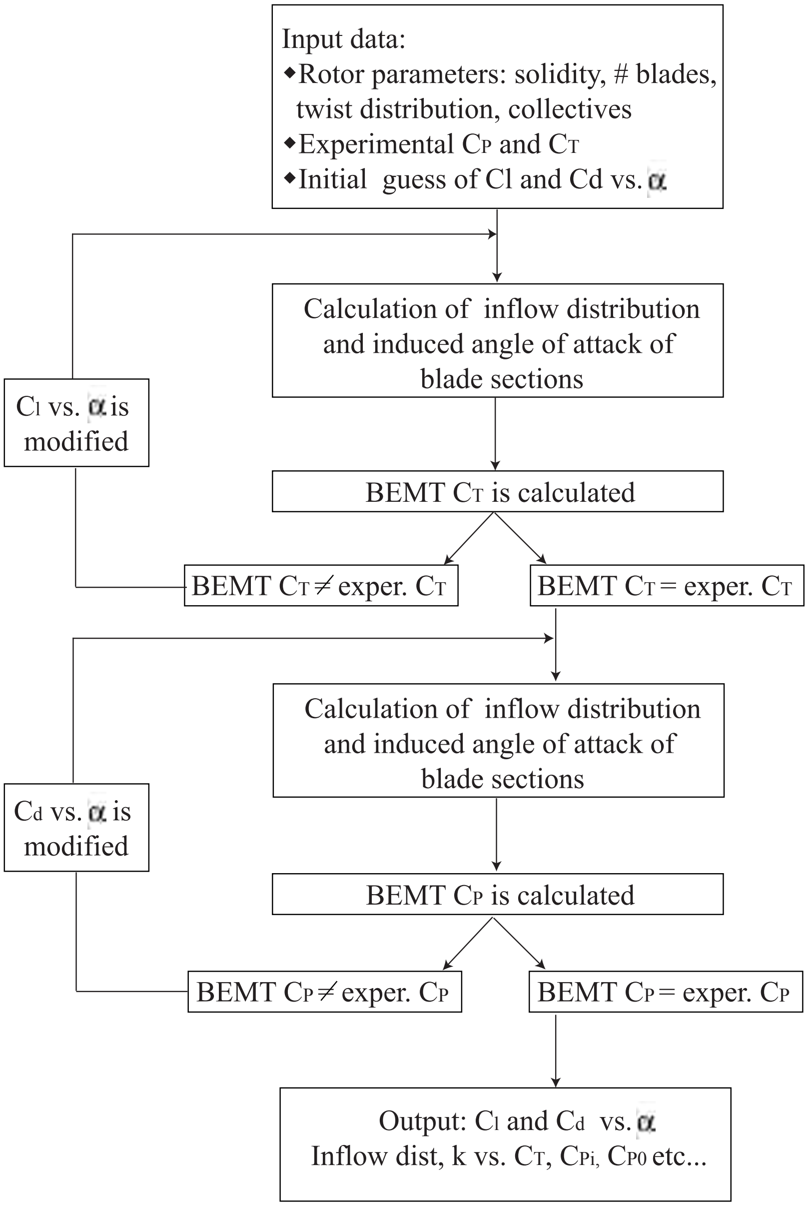

Figure 3.2: Algorithm used to obtain average airfoil characteristics from rotor tests using BEMT.

3.3.1 Iteration algorithm

The algorithm requires as inputs the experimental thrust and power coefficients and the physical parameters of the rotor such as collective pitch, taper and twist distribution, number of blades, solidity etc. An initial guess of the C_l vs. α and C_d vs. α functions is also needed. There are three main iterations in the algorithm. One to find the C_l vs. α curve, another to find the C_d vs. α curve, and a third one for the inflow calculations.

Lift coefficient iteration: Using the initial guess of the airfoil's C_l vs. α function, the rotor thrust coefficient (C_T) is calculated for each collective pitch setting. These values are compared with the experimental ones, and depending on the sign of the error the C_l vs. α curve is modified until there is a good agreement between the calculated and the experimental values.

Drag coefficient iteration: The drag coefficient iteration has to be performed after the C_l vs. α curve has been found. This is required because the power coefficient has an induced component that will directly depend on the lift characteristics of the airfoil. Again, an initial guess of the C_D vs. α curve is given. For each collective, the calculated power coefficients (C_P) are compared with the experimental ones. The C_l vs. α plot is modified until good agreement between the calculated and the experimental values is obtained.

Inflow calculation iteration: Every time the inflow distribution is calculated, an initial guess of the local lift coefficient for each blade element is required. Solving Eq. (3.19) the inflow is calculated and the induced angle of attack is obtained ($\alpha = \theta - \frac{\lambda}{r}$). The induced angle of attack is used as an input in a table look-up subroutine that interpolates the C_l vs. α vector. The local C_l value is updated and the cycle continues until the difference in C_l between two consecutive iterations is negligible. This inflow calculation occurs in each of the lift coefficient iterations.

By implementing this simple algorithm it is possible to calculate the airfoil characteristics by using just the hover rotor tests. A simple numerical error analysis was performed to determine the minimum number of elements to use. The blade span was initially divided into 10 elements and the BEMT power and thrust coefficients were calculated. The number of elements was then increased in steps of 5, until the difference between two consecutive runs was below 0.5%. A minimum of fifty elements was required to meet the error criteria.

3.4 BEMT Analysis Results

In this section some sample results of the inverse BEMT algorithm are presented. Experimental results are used to apply the inverse BEMT algorithm. The calculated airfoil characteristics and the model results are presented and discussed.

3.4.1 Inverse BEMT Results

The experimental data of the first generation rotors at 4500 RPM, (cf. section 2.3.2) was used in the inverse BEMT algorithm. The C_l and C_d curves obtained for the flat plates, NACA 0012, and 8% circular arc airfoils are presented in Figure 3.3. The tip Reynolds number of the rotor tests at 4500 RPM is approximately 27,000 and the BEMT results correspond to a representative blade section at 75% span with a Re of about 20,000.

The experimental results obtained with the third generation rotor using rectangular blades and an airfoil very similar to the Go417a were used to tests the algorithm (cf. 2.5.2). Since the Go417a was tested by Schmitz at a Reynolds number of 42,000, reliable experimental wind tunnel data was available for validation.

Rotor measurements at positive and negative collectives at a rotational speed of 3000 RPM were used in the inverse BEMT algorithm. At the operating condition considered the Re at 75% span was approximately 26,000. Figure 3.4 shows for collectives between 4 deg and 18 deg the induced angles of attack distributions along the span, and the comparison between experimental and BEMT predictions for FM, C_T and C_P. The plots show that the experimental rotor performance parameters over the entire collective range are well matched.

The the C_l and C_d curves calculated and the experimental data of Schmitz

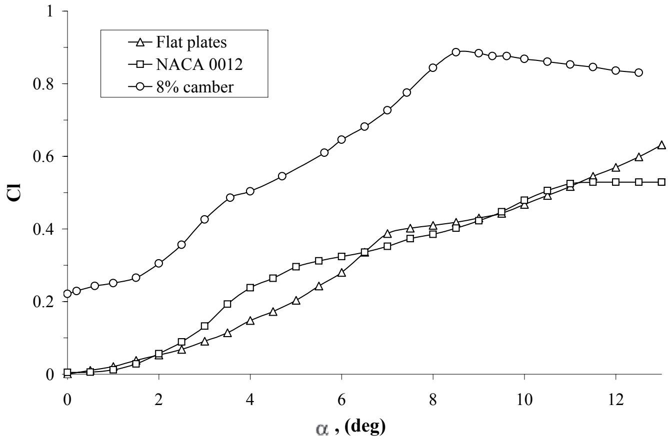

(a) Lift coefficient vs. α

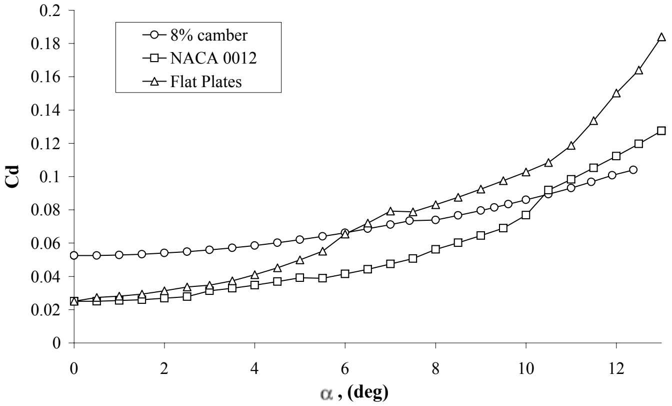

(b) Drag coefficient vs. α

Figure 3.3: Average lift and drag coefficients vs. angle of attack from Inverse BEMT using experimental data of first generation rotors at 4500 RPM for flat plates, 8% camber circular arcs, and NACA 0012 airfoils.

are shown in Figure 3.5. The BEMT predictions for this case are much closer to the wind tunnel measurement. However, the lift coefficient curve slope is shallower than in Schmitz experiments and has a lower C_{lmax}. The drag coefficient predictions showed a good qualitative agreement with the experiments in the range of -5 deg to 8 deg angle of attack, were the shape of the curve was captured. Nevertheless, drag was overpredicted by about 40% over most of that range. At 7 deg the curves intersect resulting in lower drag values for the BEMT C_d.

The result obtained have a good qualitative correlation with the Go417a exper-

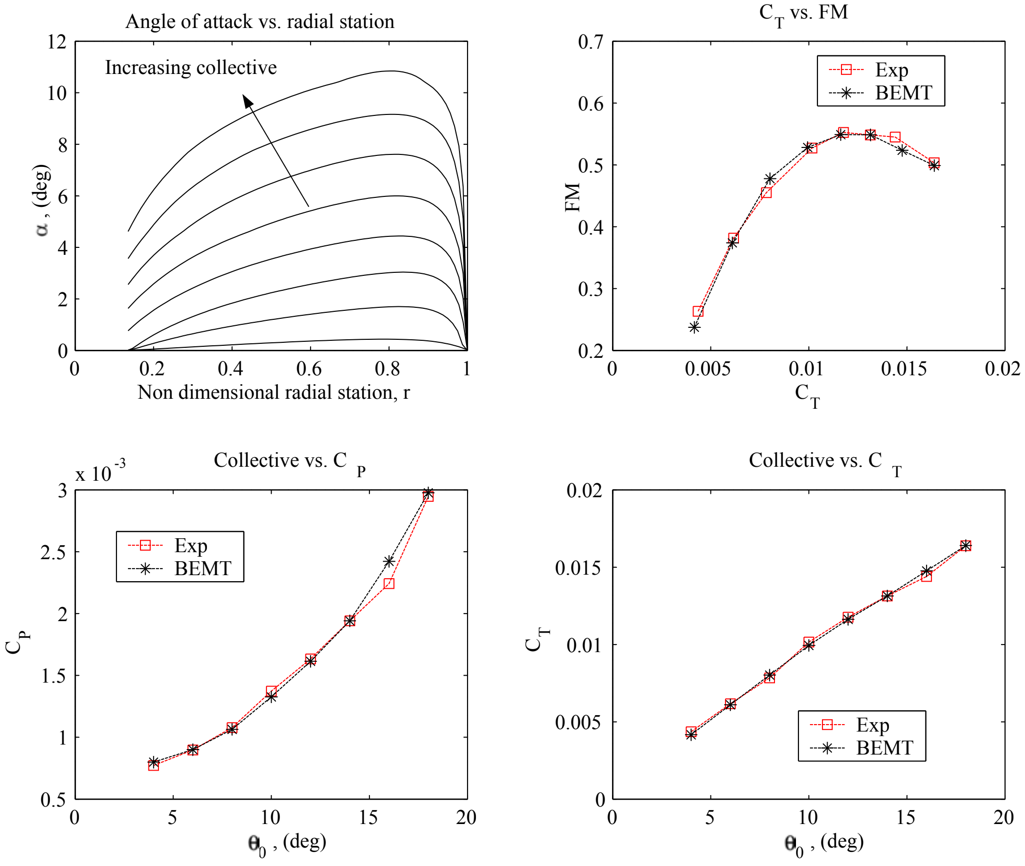

Figure 3.4: BEMT results for the rotor with 417a airfoils: AoA span distribution, C_T vs. FM, collective vs. C_P, and collective vs. C_T.

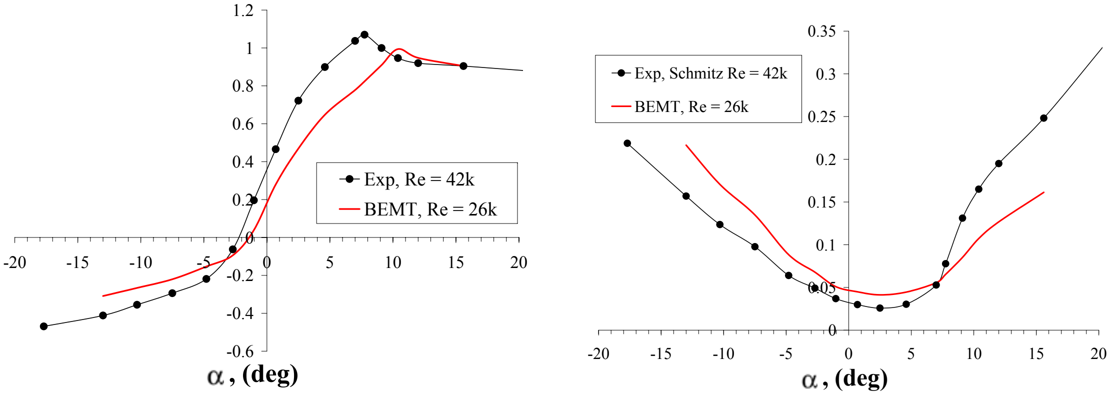

(a) C_l vs. α from BEMT (b) C_d vs. α from BEMT

Figure 3.5: Lift and drag sectional characteristics of curved plate with 6% max camber at 40% chord and 3.33% TR from BEMT compared to wind tunnel tests of Go417a from Ref. [1]

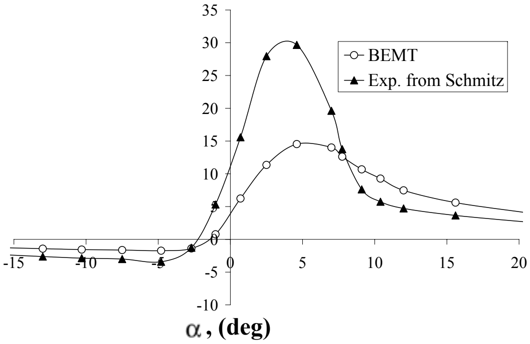

Figure 3.6: Experimental and BEMT calculated lift to drag ratio of Go417a airfoil.

imental data, the general curve shape and magnitudes are capture by the model. The results achieved can be considered satisfactory, specially taking into account the differences in Reynolds number, airfoil shape, turbulence levels, surface finishing, and three-dimensional effects that modify the airfoil aerodynamic characteristics. The wind tunnel data, should only be considered as a rough estimate of the performance expected.

3.4.2 Induced and Profile Power, FM revisited

The BEMT model implemented provides analytical tools that can help in the understanding of the issues influencing the rotor performance. In Chapter 2 the induced and profile contributions to the total rotor power could not be determined experimentally. However, by using the rotor tests to obtain a set of averaged airfoils characteristics, the components of the power requirements can be identified.

As derived in section A.7.4, the profile component in the denominator of the figure of merit equation (cf. Eq A.23) is obtained by assuming a constant drag coefficient equal to the zero-lift drag coefficient of the airfoil. For full-scale helicopters this is an approach that gives good results. For more detailed analysis it is common to approximate the sectional drag coefficients below stall by using a second order polynomial:

$$C_d(\alpha) = C_{d_0} + d_1\alpha + d_2\alpha^2 \tag{3.20}$$

Where d_1 and d_2 are empirically determined coefficients. Typical values for full-scale helicopter airfoils are C_{do}=0.01, d_1=0.025, and d_2=0.65. For the BEMT results the drag coefficient at low angles of attack (< 5 deg) can be also be approximated using Eq. (3.20). For the NACA 0012 blades C_{do} is 0.025 d_1=0 and d_2=1.5, and for the 8% camber flat plate C_{d_0} is 0.0525 d_1=0 and d_2=1.5. This shows that there is not only a large difference in the value of C_{d_0}, but more importantly, the magnitude of the quadratic coefficient d_2 is considerably larger at the Reynolds numbers faced by the small-scale blades. Additionally, the collectives at which the maximum FM occur are much higher than in full-scale rotors. Hence, the induced angle of attacks along the span cover a wide range; this is shown for the rotors with the Go 417a airfoil in Figure 3.4. These two facts explain why, assuming a drag coefficient independent of the angle of attack in Equation A.23 is ill advised at low Re. In order to have a good estimate of the profile losses, the variation of drag coefficient with angle of attack needs to be included in the analysis. Since the average drag coefficient for a given operating condition changes in function of the Reynolds number and airfoil

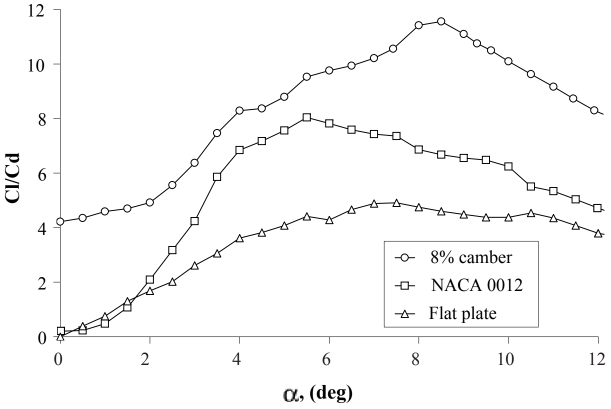

Figure 3.7: Lift to drag ratio for the airfoils of the first generation rotor from inverse BEMT results.

shape it is difficult to define a simplified approach that does not require the airfoil characteristics.

The lift to drag ratio plots of the three airfoils used in the first generation rotor are plotted in Figure 3.7. The highest L/D not surprisingly was achieved by the 8% camber circular arc, reaching a value of about 12, and was followed by the NACA 0012 airfoil, that achieved an L/D of 8. As expected the the lowest lift to drag ratios were obtained with the flat plates, reaching only a maximum of approximately 5. The calculated maximum lift to drag ratios are much lower than the values achieved at higher Re, and the curves are relatively flat and uniform. This means that as long as the airfoils used in MAV rotors have the characteristics discussed, an optimization of the induced angles of attack by tapering and twisting the blades will have a reduced effect on the hover efficiency of the rotor.

Using the airfoil characteristics of the 8% camber circular arcs the BEMT model was used to calculate the profile and induced power contributions to the total power required by the rotor. Additionally, a prediction of the effect of a 10 deg negative linear twist along the blades was performed. Figure 3.8 shows the experimental and the numerical results in terms of C_T vs. FM.

Very small differences were measured between the twisted and untwisted blades at collectives below 15 deg. The rotor with untwisted blades achieved its maximum

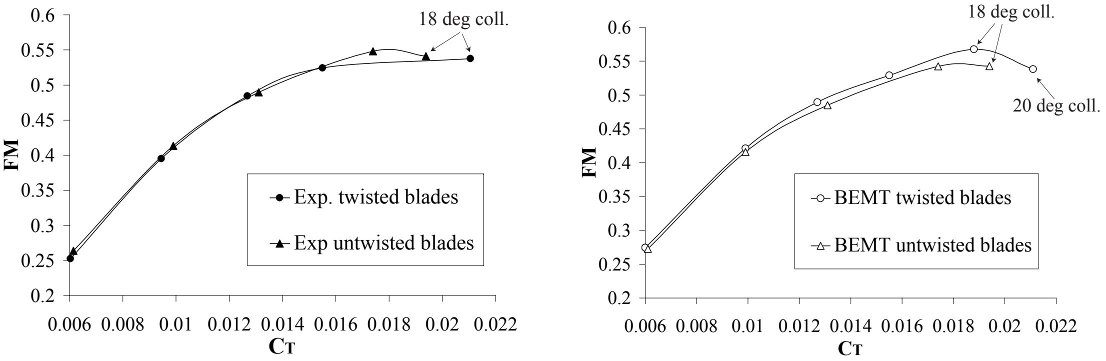

(a) Experimental C_T vs. FM

(b) BEMT prediction C_T vs. FM

Figure 3.8: Experimental and BEMT C_T vs. FM for the first generation rotors with twisted and untwisted 8% camber blades.

FM at 15 deg collective, while the rotor with twisted blades seems to have its maximum FM at a collective between 15 and 18 deg. Because of the coarse discretization in collective it seems that this maximum FM value was missed. The BEMT results of Figure 3.8(b) show that an improvement in maximum FM of approximately 3.5% is predicted by the model at a collective of 18 deg. An additional point was obtained by running the code for a collective of 20 deg. This last point matches the experimental results for 18 deg collective. The difference between the experimental and BEMT results seems to be a result of experimental error, the first generation rotor had a lack of stiffness at the root of the blades, which resulted in a variation of a few degrees in the pitch of the blades at the highest collectives where the bending and pitching moments are larger. The problem was fixed in the second generation rotors by using stiffer blade supporting clips.

Figure 3.9 shows the C_T vs. C_P plots using the model results for the rotors with twisted and untwisted 8% camber blades. For each rotor, the total C_P and its induced and profile components are shown. In a typical full-scale rotor, usually 30% of the power is consumed by the profile losses and 70% by the induced losses. However, from Figure 3.9, it can observed how the profile drag accounts for a larger fraction of the total power. At a C_T of 0.0174, where the maximum FM for the untwisted rotor occurs, the profile losses are 40% of the total power requirement.

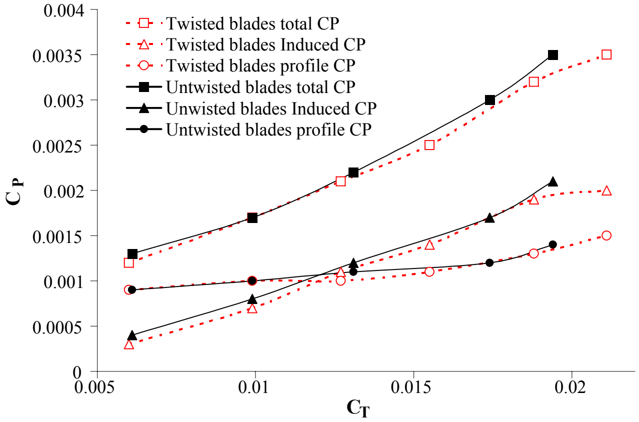

Figure 3.9: C_T vs. C_P from BEMT results for the rotors twisted and untwisted 8% camber blades.

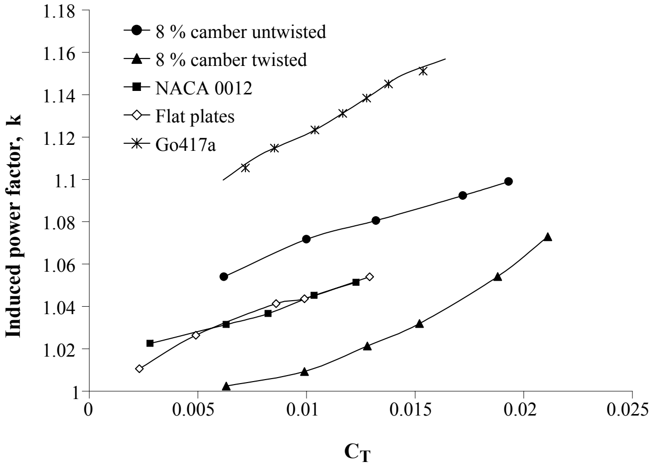

Figure 3.10: BEMT calculated induced power factor κ for the first generation rotors and third gen rotor with Go417a airfoil.

The BEMT calculated induced power factor (κ) for the first generation rotors are shown in Figure 3.10. The values obtained are well below the commonly assumed full-scale value of 1.15. The use of blade twist resulted in a substantial reduction of κ from 1.09 to 1.05 at the C_T for maximum FM for the rotor with 8% camber airfoils.

The BEMT results for the 417a airfoil (Fig. 3.6) show an improved lift to drag ratio with respect to the other airfoils studied, reaching a maximum of 15 at an angle of attack of 4.6 deg. At the C_T for maximum FM, the contribution of the profile power to the total power was reduced to 35%; however, the induced power factor increased with respect to the first generation rotors, being 1.14, resulting in a maximum FM of 0.556.

3.5 Summary

This chapter presented the derivation and numerical implementation of a BEMT single rotor model. An algorithm used to obtain averaged two-dimensional airfoil characteristics from rotor tests was explained, giving some sample results of its use. The results showed that simplifications of the airfoil characteristics by assuming constant lift coefficient slope or a constant drag coefficient, an approach commonly used in full-scale rotor analysis, should not be applied in the modeling of small-scale rotors due to the radical difference in airfoil behavior at the Reynolds numbers considered.

Chapter 4

Sectional Airfoil Characteristics from CFD

4.1 Introduction

In order to accurately predict the performance and to eventually optimize the design of MAV-scale rotors, it is fundamental to have the means to obtain the sectional aerodynamic characteristics of the airfoils used in the implementation of the system. Lift and drag coefficients are key airfoil parameters that need to be provided to the rotor model for performance calculations. For rotary wing vehicles, the Reynolds number varies along the blade span, and depends on the local chord and rotational speed. Thus, for every airfoil considered, lift and drag coefficients for a range of Reynolds numbers and angles of attack are required. The methodology presented in the previous section, where the average airfoil characteristics were calculated using BEMT and experimental hover performance data, is very limited since it can only provide approximate airfoil characteristics at a Reynolds number with a certain degree of uncertainty. This is why other alternatives to obtain the airfoil characteristics had to be considered. The use of CFD for the calculation of two-dimensional airfoil characteristics is an approach that has great advantages over wind-tunnel testing. Even though experimental validation is required, after a successful algorithm and methodology have been developed, CFD can produce results much faster and at a fraction of the cost. This is why CFD was used for the analysis of a family of airfoils that served for the compilation of a database later used in a design code.

	Camber						
TR%	0%	1.5%	3.0%	4.5%	6.0%	7.5%	9%
2.5	√	√	√	√	√	√	√
3.75	√	√	√	√	√	√	√

Table 4.1: Test matrix for CFD calculations, combinations of camber and TR.

4.2 Geometrical Airfoil Parameterization

The experimental aspect of the current research was focused on the study of rotors using thin cambered circular arcs. Rectangular blades had a uniform airfoil shape for the entire rotor span. However, by introducing blade planform modifications, the airfoils' geometrical characteristics were varied in the radial direction. As discussed in section 2.6.1, rectangular blades were tapered by removing material from the leading and/or trailing edges. The resultant airfoil shapes were also circular arcs but with reduced cambers and increased thickness ratios with respect to the original airfoil.

The test matrix of Table 4.1 covers circular arcs with cambers from 0% up to 9% and two thickness ratios of 2.5% and 3.75%. The camber and thickness ratio ranges that were encountered in the different blade geometries tested in Chapter 2 are covered by the test matrix. For each combination of camber and thickness ratio, two airfoil geometries were considered; one with elliptical leading edge and the other with sharp leading edge. In both cases, the trailing edges were tapered into sharp wedges symmetric with respect to the camber line. Figure 4.3 show the entire family of airfoil with elliptical leading edges.

The extent of the leading and trailing edges were defined as function of the thickness and chord respectively, as shown in Figure 4.1. The proportions for the airfoil with elliptical leading edge in Figure 4.1, were used by Mueller in Ref. [10] in the wind tunnel tests of a 4% camber 1.93% TR airfoil. The parameterization produces airfoils with leading edges that extend for larger chordwise distances as thickness ratios are increased. This is consistent with the airfoil proportions used in the rotor experiments of Chapter 2. Nevertheless, due to manufacturing limitations, the shape of the leading and trailing edges of the airfoils used in the rotor tests do not match exactly the idealized shapes used in the CFD calculations. The manufactured blades, instead of having the initially intended elliptical leading edge have a rounded shape that approaches an ellipse and that undergoes small variations along the span. Similarly, for the blades with sharp leading edges, the extent and angle of the leading edge wedge is not uniform, varying by small amounts along the span.

Computational considerations play an important role in the way the airfoil geometries are defined, specially at the leading and trailing edges. Rounded, smooth leading edges are required for a good resolution of the stagnation point. This mean that even if the experimental airfoil geometry has a razor sharp leading edge, better results will be achieved in the CFD calculations by approximating the sharp edge by a small diameter circle or curve. Figure 4.2 shows a detail of the the leading edge geometries studied. Experimentally, it has been observed that trailing edge geometry does not play a determinant role in the lift and drag sectional characteristics at low Reynolds numbers (cf. Ref [10]). However, most of the grid generation algorithms require a sharp trailing edge to close the grid and define the wake cut boundary condition. This is why trailing edge geometries slightly differ from the experimental ones, which are not perfectly sharp. The geometrical approximations used are expected to improve the quality of the CFD calculations, allowing the flow solvers to converge to an accurate solution.

4.3 CFD Methodology

This section explains the grid generation methodology, the flow field assumptions and boundary conditions used for the calculations of two-dimensional airfoil characteristics with TURNS and two other CFD codes: INS2d and Fluent.

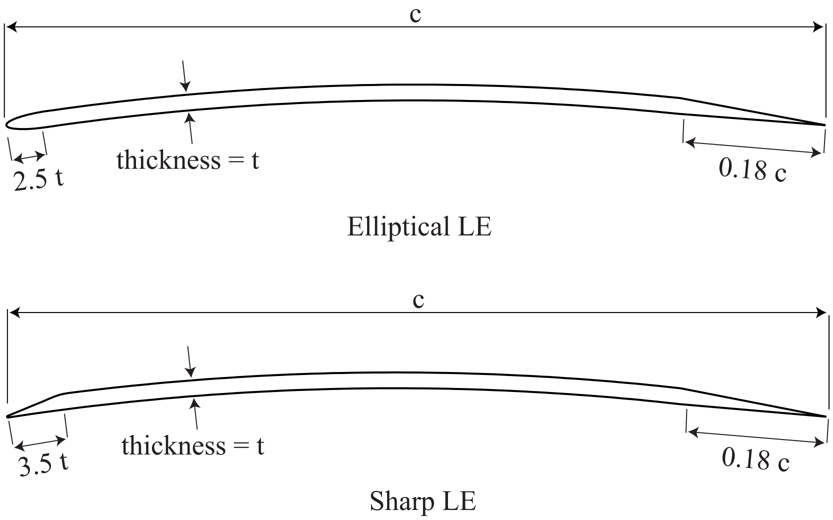

Figure 4.1: Geometrical proportions of circular arc airfoils with elliptical and sharp leading edges. 4% camber, 1.93 TR shown.

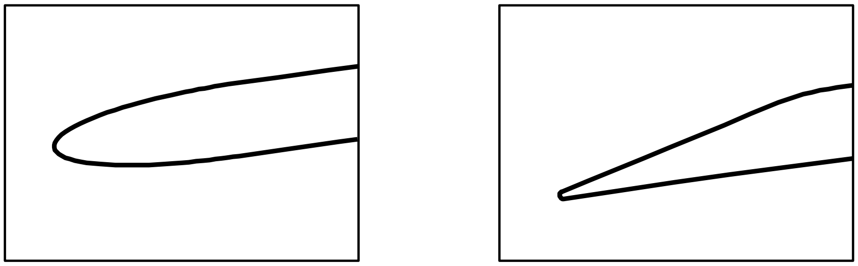

Figure 4.2: Detail of elliptical and sharp leading edges.

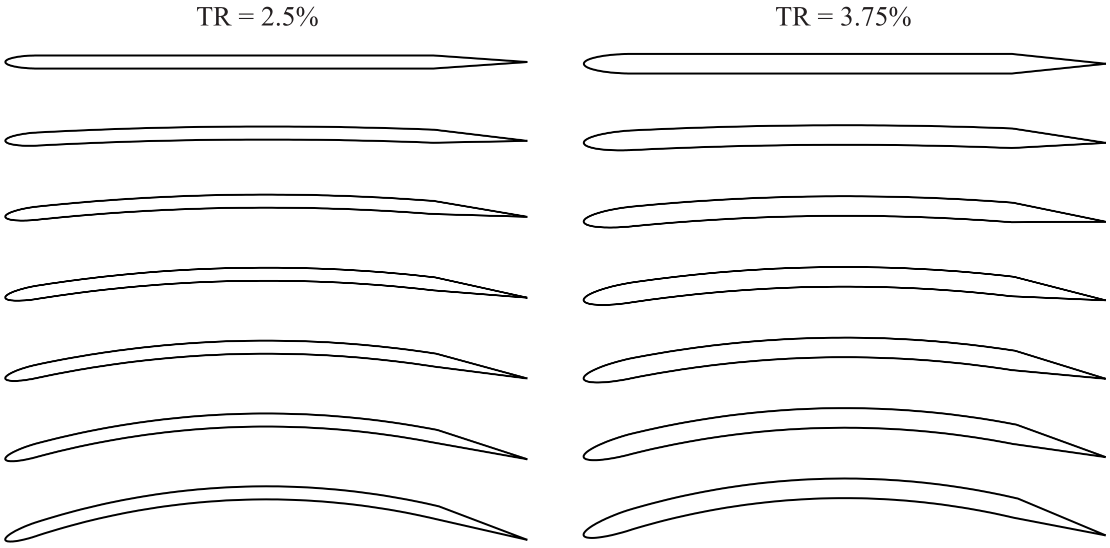

Figure 4.3: Family of circular arcs with elliptical LE, cambers ranging from 0% to 9% and TR of 2.5% and 3.75%.

4.3.1 Flow Solvers

The literature review of this dissertation references the works of Schroeder and Gupta as being the basis for the computational part of the present research. Schroeder as well as Gupta worked with the structured-grid Euler/Navier-Stokes solver TURNS (Ref. [80]). TURNS is a compressible fully implicit solver that includes all the viscous terms in all directions using the Spalart-Allmaras turbulence model. The original code was modified by Gupta (Refs. [64, 65]) to include a low-Mach number preconditioner. Schroeder used the modified code for two-dimensional airfoil and three-dimensional rotor calculations at low Reynolds numbers (Refs. [66, 67]).

The second code evaluated was INS2d, an incompressible Navier-Stokes solver developed by Rogers (Refs. [50, 51]). The code solves the incompressible Navier-Stokes equations in two-dimensions using the method of artificial compressibility. As for TURNS, an implicit line-relaxation scheme is used. Kunz used INS2d to perform an airfoil camberline optimization at ultralow Reynolds numbers assuming fully laminar flow(Ref [53, 52]).

The third code evaluated was Fluent, a commercially available flow solver widely used in the industry. Fluent was configured as a two-dimensional incompressible implicit solver. Fluent, TURNS and INS2d can handle steady and time accurate calculations. Details of the flow field assumptions are presented in section 4.3.4.

4.3.2 Grid Generation

Grid generation is an essential aspect of all numerical methods that use finite differences, finite volumes or finite element to solve partial differential equations. The quality of the grid not only affects the convergence time, but can also have a large influence in the quality of the results. For the current research a hyperbolic grid algorithm that generates structured C-Type grids was used.

Hyperbolic methods are very effective for generation of grids where the wall boundaries are well defined and the far field boundaries are arbitrary, the grids generated with this method are orthogonal to the airfoils surface. Computational cost of two-dimensional grid generation is minimal when compared to the total computational cost of the flow solution. In the algorithm used, the total number of points along the surface can be specified, as well as clustering factors to increase the grid density at the leading and trailing edges. These regions are of interest at low Re since it is where key boundary layer phenomena are expected to occur.

Initial normal spacing was set to obtain approximately 25 cells in the boundary layer. Figures 4.4 and 4.5 show respectively a typical C-type grid and the grid around a curved plate airfoil showing the clustering at the leading and trailing edges. All the grids used in this investigation had a J_{max} of 217 points and a K_{max} of 81 points. The airfoil contour was defined with 160 points leaving 57 points for the definition of the wake-cut boundary. The outer grid radius was placed at 15 chord lengths. A simple grid sizing study was performed by increasing the J and K grid dimensions in three steps: 109 by 41, 217 by 81 and, 435 by 163. The relative errors in lift and drag coefficients were calculated with respect to the results of an 871 by 327 grid using a 4% camber circular arc at 60,000 Re. The 217 by 81 grid had a relative error

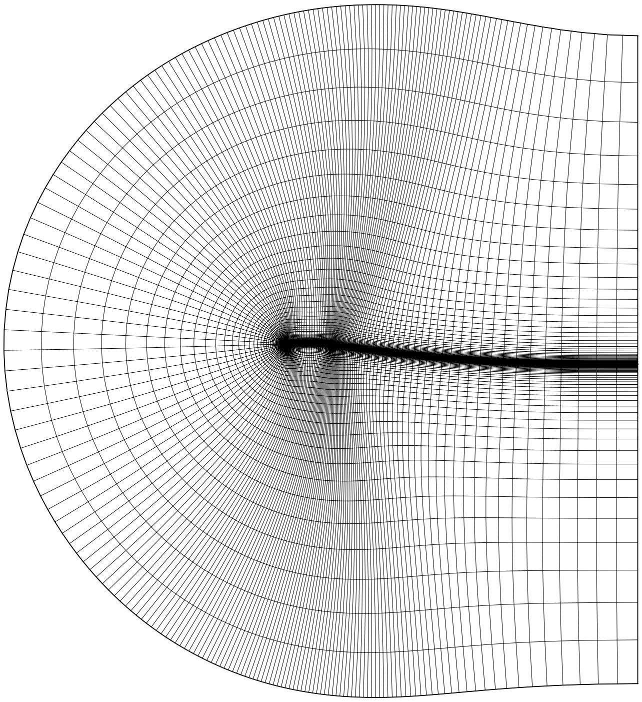

Figure 4.4: Sample C-type grid used in the CFD calculations.

close to 0.5% in lift and drag. Hence, it was chosen since it was a good compromise between error and computational cost.

4.3.3 Boundary Conditions

The grids used in the INS2D, TURNS, and Fluent calculations were identical. The three solvers used at the airfoil surface a viscous no-slip wall, with wall-normal vector pointing in the positive computational direction. At the outer C-grid boundary TURNS uses a free-stream boundary condition; however INS2D and Fluent divide the outer boundary in two: a boundary that imposes a velocity field based on free stream velocity, and an outflow boundary using extrapolated velocity and constant static pressure. Both INS2D and TURNS also require the specification of a wake-cut boundary condition, where the boundary points are updated by averaging the values of its surroundings. The wake cut boundary cannot be specified in Fluent, instead the wake points need to be defined as interior points.

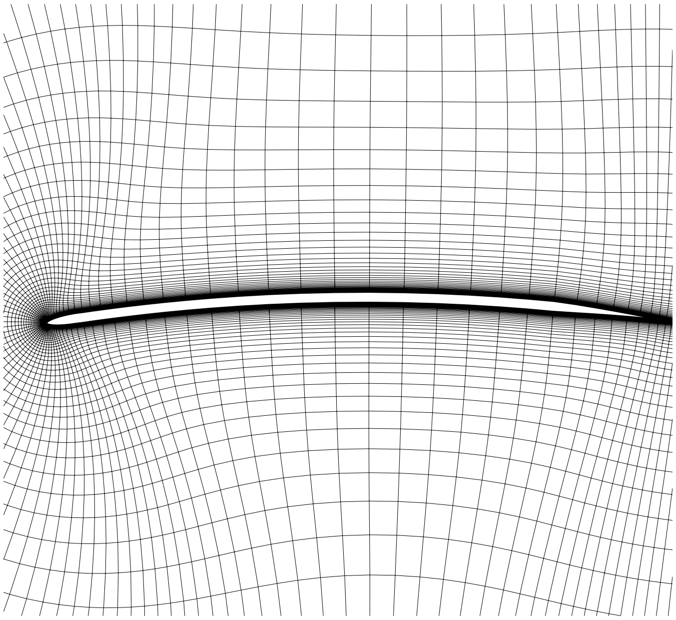

Figure 4.5: Sample grid around curved plate airfoil showing clustering at leading and trailing edges.

4.3.4 Flow Field Assumptions

Two main flow field assumption were used in the computational aspects of the current research. First the flow was assumed fully turbulent, and second the flow was assumed steady.

The experiments performed in Section 2.4.1, showed that zero-lift drag coefficient of flat plates airfoils over the Reynolds number range of interest were consistently above the theoretical laminar prediction. This means that the flow is either laminar and undergoes separation, or that it is transitional. Current CFD state of the art does not appear to be capable to model transition, however three different approaches are possible: The flow can be assumed either fully laminar, fully turbulent, or a transition chordwise location can be can specified. Of these three options, assuming a fully turbulent flow is the more acceptable considering the Reynolds number range of interest (15,000 to 60,000), and the large number of geometries to evaluate. When turbulent flow is assumed,it is necessary to calculate the turbulent viscosity using a turbulence model. Based on previous investigations (Refs.

[66, 67, 68]) it was decided to use the one equation model of Spalart and Allmaras (Ref. [79]). The Spalart-Allmaras model was designed specifically for aerospace applications involving wall-bounded flows and has been shown to give good results for boundary layers subjected to adverse pressure gradients. In its original form, the Spalart-Allmaras model is effectively a low-Reynolds-number model, requiring the viscous-affected region of the boundary layer to be properly resolved. An additional advantage is that its relative simplicity minimizes computational costs, making it specially suited for a large number of calculations when limited computing power is available.

The steady assumption greatly reduces computational cost, however it may be an oversimplification of the problem; specially at the higher angles of attack where separation is occurring, some wind tunnel experimental investigations (cf. [71]) have identified periodic vortex shedding in airfoils under similar conditions. However based on Schroeder's and Lakshminarayan's results, the steady state assumption does not introduce large errors in the calculations.

A third flow characteristics to model is its compressibility. It is reasonable to assume incompressible flow since the highest tip Mach number reached in rotor tests is below 0.3. Hence, Incompressible flow was assumed when using the flow solvers INS2D and Fluent. However, the flow solver TURNS is a compressible code that solves the energy equations. Only for this case the flow was assumed compressible.

4.4 Two-Dimensional Validation

Wind tunnel experiments of a 4% camber 1.93% TR circular arc with elliptical leading edge and the proportions shown in Figure 4.1 were used to validate the CFD calculation at a Reynold number of 60,000. The experiments performed by Mueller (Ref. [10]) at the Hessert Center for Aerospace Research of the University of Notre Dame, are one of the few reliable aerodynamic studies of thin circular plates. The Reynold number of the experiment is an upper bound of the aerodynamic regime faced by MAVs. Nevertheless, due to the limited availability of experimental data, Mueller's results were used for validation.

Figure 4.6 shows the experimental and predicted lift, drag and moment coefficients as well as the lift-to-drag ratio obtained with the three codes evaluated. The lift coefficient curves from TURNS and INS2d have an excellent agreement over most of the angles of attack explored. However, both codes predict an early stall, INS2d 2 deg earlier than TURNS. Fluent's results closely follow TURNS at the higher angles of attack; however, Fluent did not capture the nonlinearities of the C_l curve. This produced a considerable over prediction of the lift coefficient values at angles of attack below 5 deg.

The blades and hubs that used in experimental part of the current investigation have large torsional stiffness and can safely be assumed rigid in the implementation of a model. This makes the accuracy of the moment calculations of low relevance. The computational moment results of TURNS and INS2d are very close to the experiments at angles of attack below stall. However,at angles above stall large differences exist.

Drag calculations were very similar for all three codes, being a few percent higher with Fluent. In all cases, drag was under-predicted at the lower angles of attack. Qualitatively the shape of the C_d vs, α curve was captured by TURNS and INS2d; however, experimental values almost doubled the CFD prediction over the region of -1 to 4 deg. These differences translate into large errors in the predictions of the lift-to-drag ratio of the airfoil. While the experiments obtain a maximum L/D of 23, computational results predict an L/D between 27 and 31. Nevertheless, TURNS and INS2d accurately predict the angle of attack for maximum lift to drag ratio. The objective of this computational study is to identify the relative performance of the airfoils studied and the effects of various geometrical and operational parameters on lift and drag. Hence, results are still useful as long as there is a good qualitative correlation with the experimental results, even when substantial quantitative differences are present.

The large differences in the computational drag predictions, as noted before by Schroeder and Lakshminarayan (Refs. [66, 68], seems to be a consequence of the fully turbulent flow assumption. At low angles of attack the turbulence model is likely to under-predict the length of the separation bubble and possibly the extent of regions of separated flow at the lower surface of the airfoil, where at low angles of attack large adverse pressure gradients exist.

Nevertheless, not only the simulations face challenges. As discussed by Mueller and Barber (Refs. [10, 81]), the lift and drag wind-tunnel measurements can be affected by the presence of endplates; used when two-dimensional flow wants to be achieved. The interaction between the endplate's boundary layer and the flow around the wing creates a corner flow that can largely increase the two dimensional drag measured. At Reynolds numbers between 60,000 and 200,000, Ref. [82] shows an increase in the measured minimum drag coefficient of 18% when endplates were used. These unresolved experimental issues difficult the validation of codes and models, slowing the development of CFD algorithms (cf. Ref. [83]).

The comparisons of the performance of the three CFD solvers led to a choice of a single code to perform the parametric airfoil studies and to generate the airfoil databases. The failure of Fluent to match qualitatively and quantitatively the experimental results reduced the choice to INS2d and TURNS. Lift predictions were more accurate in TURNS at the higher angles of attack, other than that the results were practically identical. However, factors other than accuracy were considered. Computational cost and convergence easy were very different between the two codes. The incompressible nature of INS2D largely reduced the convergence time with respect to TURNS, being typically less than half the time. Additionally at lower Reynolds numbers (45,000 and below) TURNS was harder to converge, being very sensitive to the time step used. This why INS2D was chosen to perform the database calculations presented in this chapter.

4.5 CFD Results

This section presents the effect of various geometrical an operating conditions on the aerodynamic characteristics of the thin plate airfoils studied.

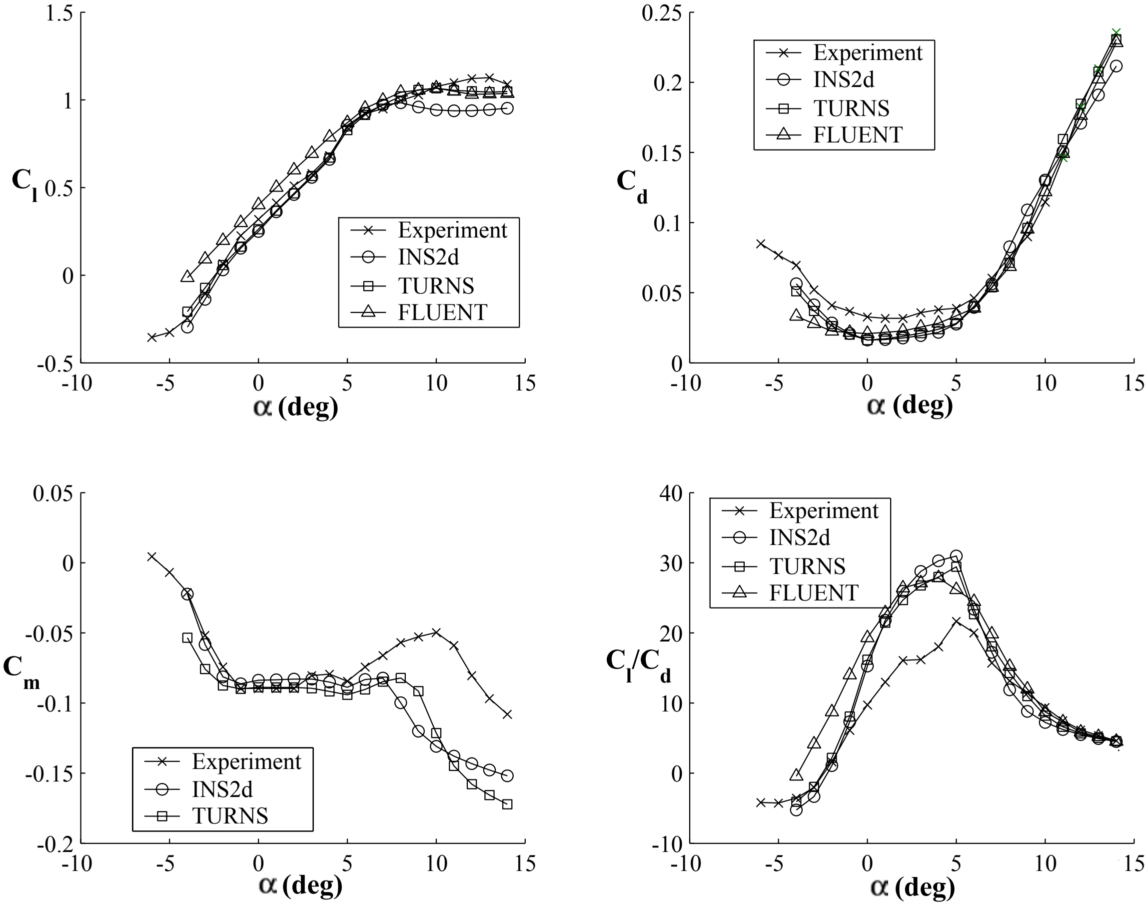

Figure 4.6: Lift, drag, moment, and lift to drag ratio validation of TURNS, INS2d, and Fluent with experimental data at Re=60,000 from Ref. [10].

4.5.1 Parametric Study on 4% Circular Arc

The 4% camber 1.93% TR circular arc airfoil used for the experimental validation is used to show the effects of Reynolds number and thickness ratio on the lift, drag, and moment coefficients.

Reynolds Number Effects using INS2d

Four Reynolds numbers were explored from 15,000, up to 60,000 in steps of 15,000. Figure 4.7 shows the results obtained. As Reynolds number is reduced, the slope of the linear section of the C_l curve undergoes a small but noticeable reduction. However, maximum lift coefficients are practically unchanged, except at a Reynolds number of 15,000, were the lift overshoot that occurred at an angle of attack of 6 deg is not present anymore. Instead, the lift coefficient curve continues to increase without showing signs of stall.

As expected, the reduction in Reynolds numbers results in a drag coefficient increase. However, as opposed to the lift, the drag curves keep the same proportions even at the lowest Reynolds numbers. All the curves show a clear change of slope that consistently occurs between 5 deg and 6 deg. This sudden drag increase identifies the occurrence of the airfoil stall. The changes in lift and drag coefficients with Reynolds number translate into a reduction of the lift-to-drag ratios the airfoil can achieve. Figure 4.8 shows the practically linear evolution of the maximum L/D with changing Reynolds number. One thing to note is that in spite of the radical changes of the C_l curve at 15,000 Re, the angle of attack for maximum L/D does not change, remaining constant at 5 deg.

Thin circular arc airfoils are characterized by relatively large negative pitching moments, CFD results showed that as Reynolds number is reduced there is a tendency for the moment coefficients to approach zero below stall. This is indicative of changes in the pressure distribution of the airfoil.

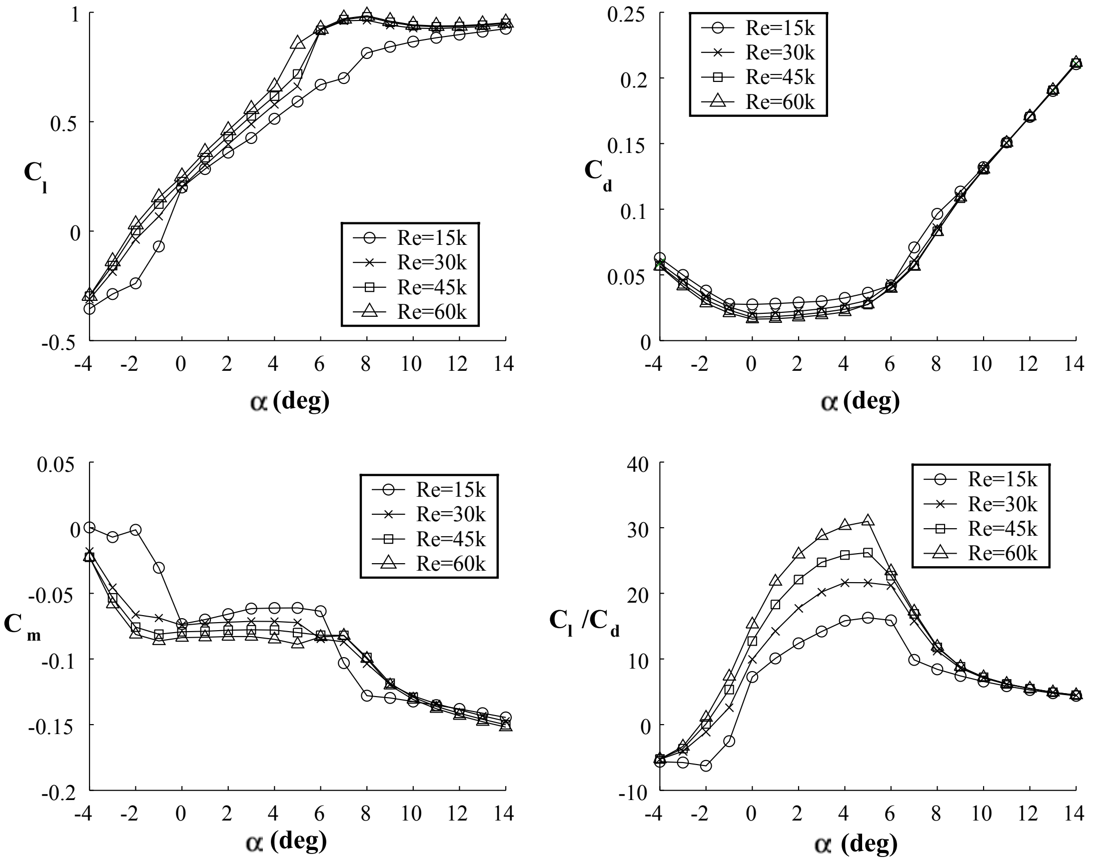

Figure 4.7: Effect of Re in lift, drag, moment coefficients and L/D ratio on a 4% camber 1.93% TR circualr arc.

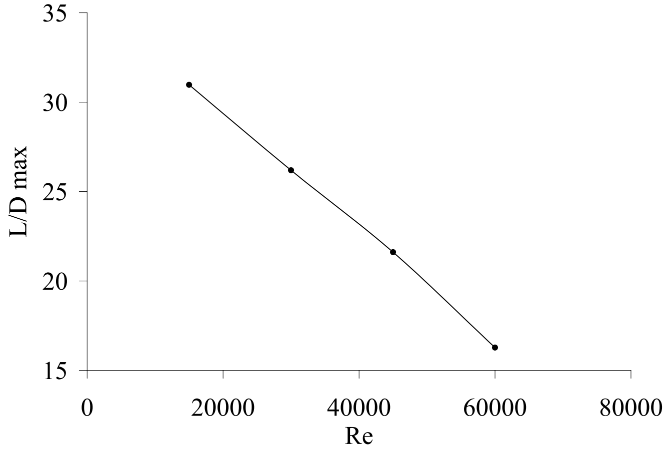

Figure 4.8: Change of maximum lift-to drag ratio with Reynolds number for the 4% camber 1.93%TR circular arc.

Thickness Ratio Effects

Three thickness ratios were evaluated; starting from the baseline 1.93%, the TR was increased to 2.5% and 3.75%. These are the same TR used in the generation of the database. Figure 4.9 shows the results obtained.

As thickness ratio increases, the C_l curves below stall shift slightly to the right without a substantial change in maximum lift coefficient. Drag coefficients increased with TR, showing also a slight shifting to the right at angles above stall. The effects of the curve-shifting and drag increase are clearly observed in the lift-to-drag plot. Maximum L/D reduced in magnitude and occurred at higher angles of attack with increasing thickness ratio. Maximum L/D was $\approx$ 13% smaller for the 3.75% thick airfoil with respect to the baseline.

The only aerodynamic positive effect of the TR increase is observed in the C_m plot. Higher TR reduce significantly the negative pitching moment of the airfoil. A reduction of $\approx$ 13% in the C_m values below stall were obtained with the 3.75% thick airfoils.

4.5.2 Elliptical Leading Edge Database Results

In this section the results obtained in the generation of the database are presented. The combined effects of camber, TR and Reynolds number are shown in graphical format, identifying the trends observed.

Camber Effects

The effects of maximum camber on lift and drag were studied following the test matrix of Table 4.1. Maximum camber was increased in steps of 1.5% from 0% up to 9%. Figure 4.10 shows the lift and drag coefficients at Re=60,000 for the 2.5% and 3.75% thick airfoils.

Results show that as camber increases, the maximum lift coefficients reached before stall also increase. For the lower camber airfoils, lift slope is positive over the entire angle of attack range; for these cases, stall is identified in the C_l curve

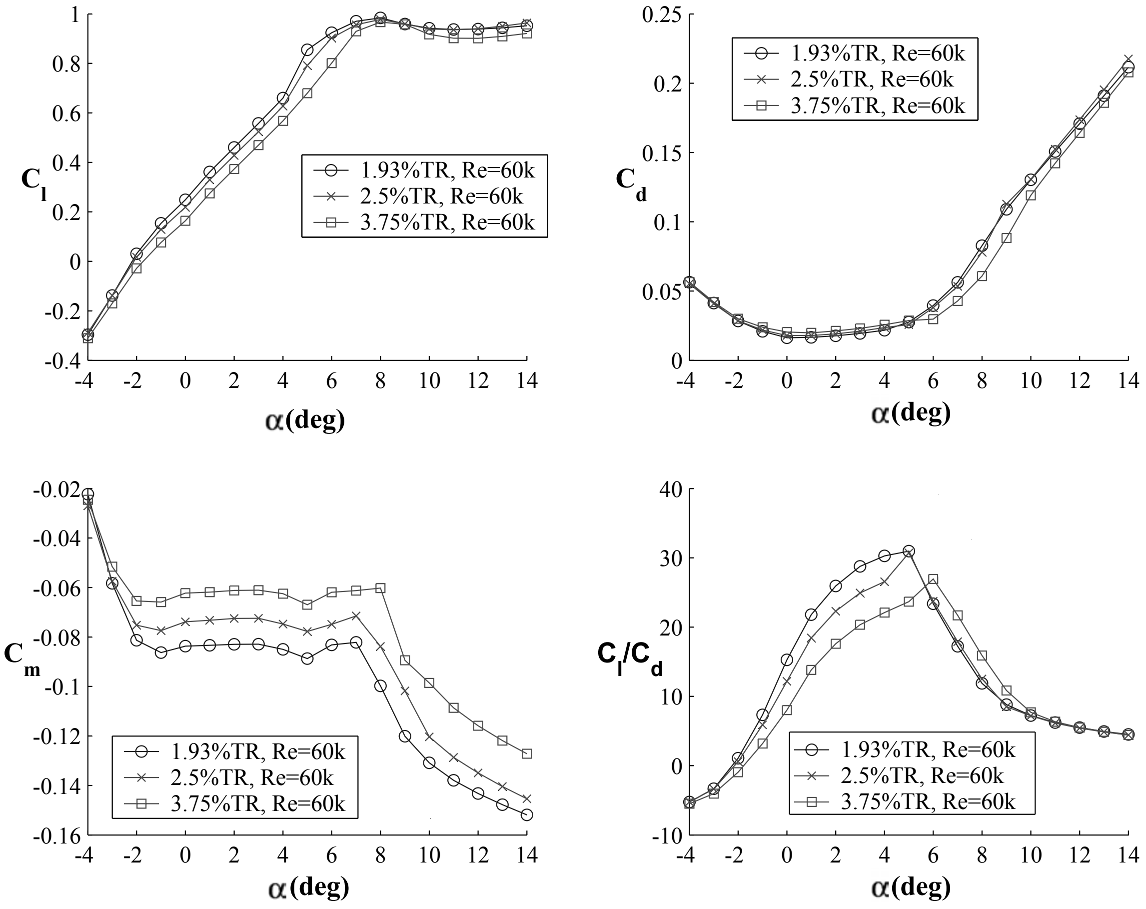

Figure 4.9: Effect of TR in lift, drag, moment coefficients and L/D ratio on a 4%camber circular arc at Re=60,000

by a change in slope. For airfoils having a camber of 3% and higher C_l does not increase monotonically anymore, and stall is identified by a drop in C_l. As for the lift coefficient, overall drag coefficient values increase with camber. In all cases, stall is identified by a clear change in slope, where the drag coefficient start growing at a higher rate.

In terms of lift-to-drag ratio at a Re of 60,000, the highest values were achieved by airfoils with cambers between 4.5% and 6%, reaching maximum L/D in the range of 28 to 31 as observed in Figures 4.11 and 4.13.

Even though similar maximum L/D values can be achieved with a relatively wide range of cambers, there are two important factors to consider: the shape of the L/D curve and the C_l at which the maximum occurs. It is desirable to have a relatively "flat" L/D vs. α curve in order to minimize the performance changes with variations in angle of attack. And it is also desirable to achieve the maximum L/D at a high lift coefficient. Figures 4.11(b) and 4.11(d) show the L/D ratios for the 2.5% TR and 3.75% TR airfoils at Re=60,000. By plotting L/D vs. C_l it is simpler to compare the relative performance of the various airfoils. For example the 3% and 7.5% camber arcs have similar maximum L/D. However, for the 7.5% camber arc, the maximum occurs at more than twice the C_l than for the 3% camber airfoil. When using "high-lift" airfoils lower rotational speed and/or lower solidities can be used. As shown in Chapter 2 these are factors that greatly affect rotor performance.

In the pool of airfoils studied acceptable levels of L/D and C_l are obtained with cambers of 4.5% and above. The 9% camber airfoil is a special case. Even tough its maximum L/D is relatively low (≈ 23) it has a very wide plateau. This allows the airfoil to have an almost constant L/D ratio over a wide range of lift coefficients.

Thickness Ratio Effects

The effect of thickness ratio in the aerodynamic characteristics of a 4% camber circular arc were discussed in section 4.5.1. In this section the effects of increasing the TR over the entire airfoil family are presented. Figures 4.10 and 4.11 show vertically aligned the C_l, C_d, L/D vs. α and L/D vs. C_l for all airfoils with 2.5% and 3.75% TR at a Re of 60,000.

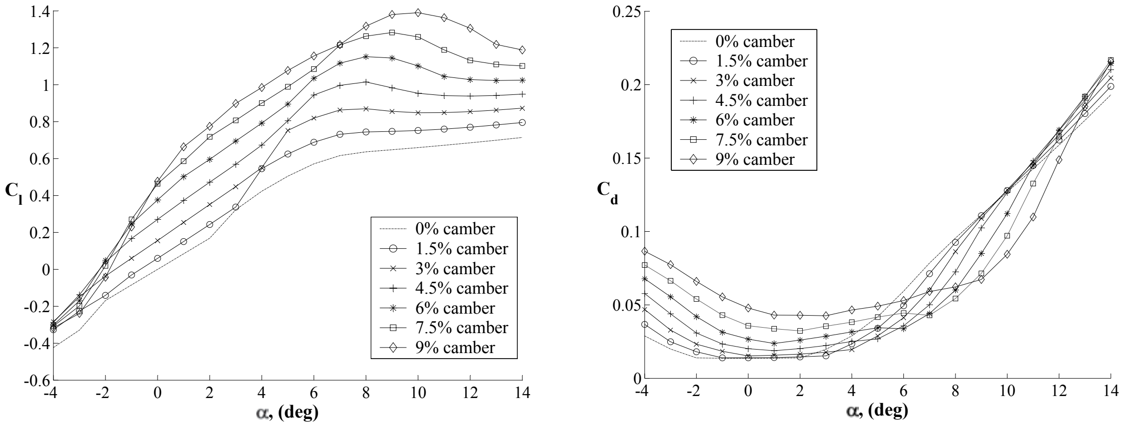

(a) Lift coefficient 2.5% TR (b) Drag coefficient 2.5% TR

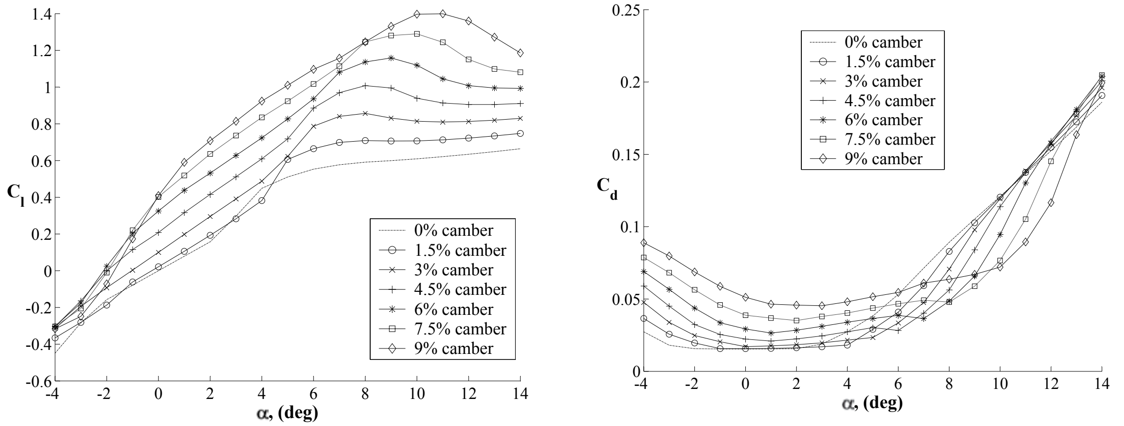

(c) Lift coefficient 3.75% TR (d) Drag coefficient 3.75% TR

Figure 4.10: C_l and C_d vs. α for circular arcs with elliptical LE and two TR at Re=60,000

Most of the trends observed in section 4.5.1 for the 4% camber airfoil are also valid for the entire airfoil family. By increasing the TR both lift and drag curves were shifted to the right; and while maximum lift values were not affected, drag was generally higher, leading to changes in the L/D curves. The relative magnitude of the curves did not change with TR, however the extent of the high L/D plateaus was reduced and overall lower L/D values were achieved. These effects are shown for the 6% camber and 9% camber airfoils in Figure 4.12, these two airfoils are of special importance in this investigation since they were used as baseline in the

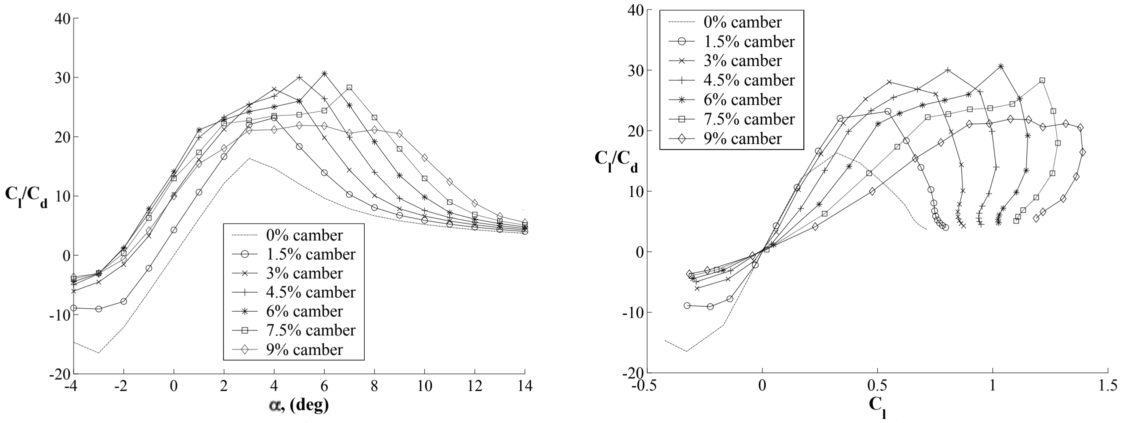

(a) L/D vs. α for 2.5% TR circ arcs.

(b) L/D vs. C_l for 2.5% TR circ arcs.

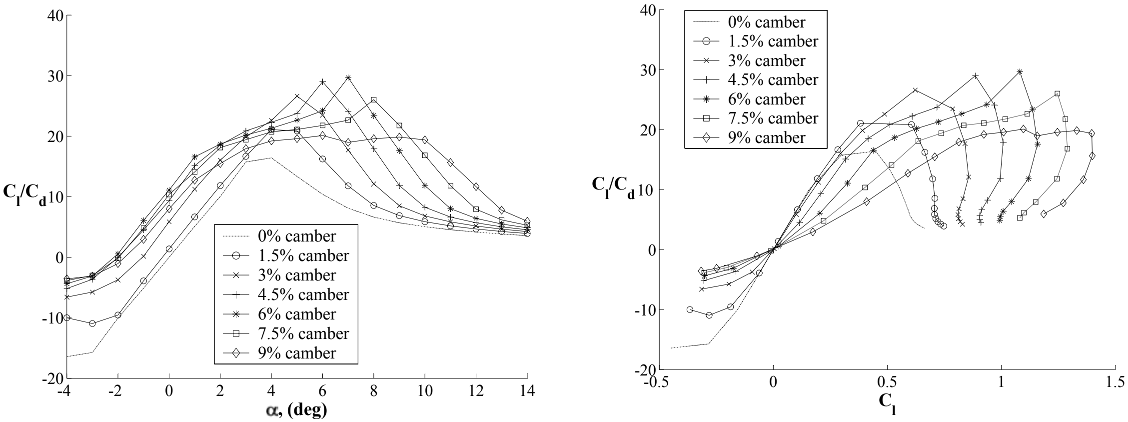

(c) L/D vs. α for 3.75% TR circ arcs.

(d) L/D vs. C_l for 3.75% TR circ arcs.

Figure 4.11: L/D vs. α and L/D vs. C_l for circular arcs with elliptical LE and two TR at Re=60,000.

blades with modified planforms. The results obtained suggest that lower thickness ratios are preferable based on aerodynamic considerations. However, manufacturing constraints may force the use of thicker airfoils at the expense reduced performance.

Reynolds Number Effects

For each airfoil, CFD calculations were performed at four different Reynolds numbers 15000, 30000, 45000, and 60,000. This range covers two of the sub-regimes defined by Carmichael (Ref. [5] and explained in section A.4. The range from 10,000 to 30,000 is practically unexplored and is expected to have mostly laminar flow with a tendency to separate. The range of 30,000 to 70,000 has generally transitional flow.

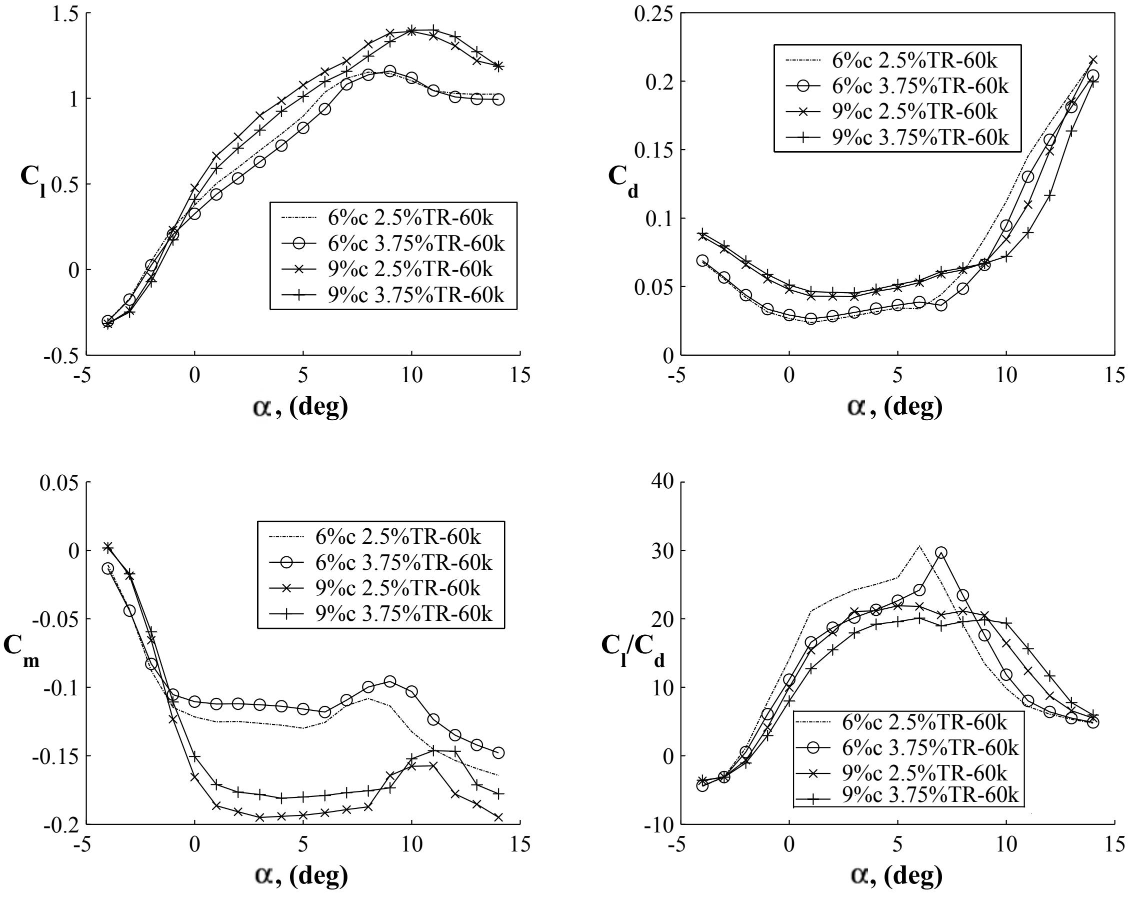

Figure 4.12: Effect of TR in lift, drag, and moment coefficients and L/D ratio on 6% and 9% camber circular arcs with 2.5% TR and 3.75% TR at Re=60,000

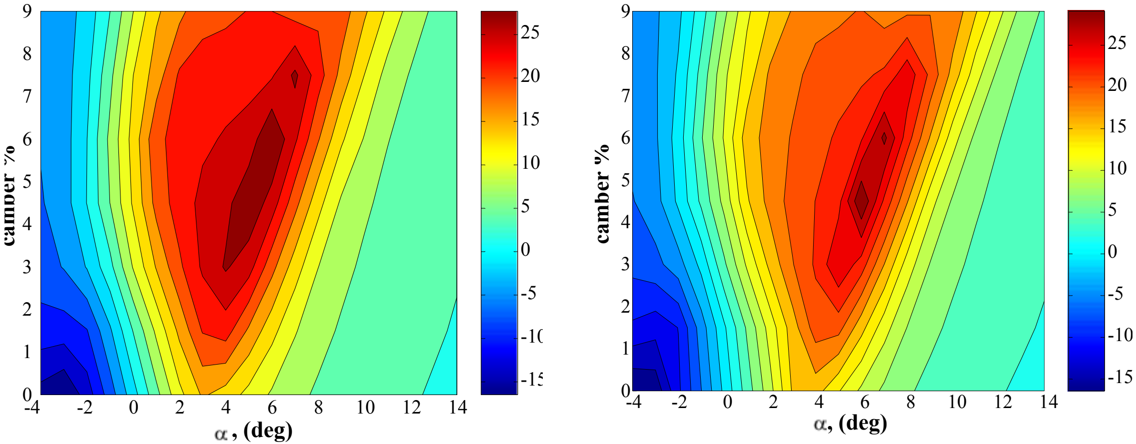

(a) 2.5% TR airfoils at Re=60k (b) 3.75% TR airfoils at Re=60k

Figure 4.13: Contours of L/D vs. α at Re=60,000 for airfoils with elliptical LE and two TR.

This is the regime were laminar separation bubbles and complex boundary layer phenomena usually occur. The assumption of fully turbulent flow approximates the real flow conditions, and hence the Reynolds number effects. Since no reliable experimental data is available for validation at the lower Reynolds numbers, the results should be interpreted as a qualitative guideline of the actual airfoil behavior.

Because of the large number of cases studied, a clear and convenient way of showing the effects of Reynolds number on the airfoils performance is with contour plots. At each Re, the L/D ratio vs. angle of attack values can be compared for the different cambers in a single plot. Figure 4.16 shows the results obtained with the airfoils having 2.5% TR . The color scale used is the same for all four plots such that a given color or contrast value represents the same L/D. As Reynolds numbers are reduced, the maximum L/D ratios that the airfoils achieve reduce gradually from regions of L/D $\approx$ 28 at Re of 60,000, to regions of L/D $\approx$ 13. However not only the overall magnitude of the curves changed, as for the sample case of section 4.5.1 the L/D characteristics curves for all cambers had the tendency to flatten out, reducing the effects of angle of attack in the L/D ratio.

For the family of airfoils studied the maximum L/D is achieved at the higher Re at an angle of attack were a sudden increase in C_l occurs. This nonlinearity was

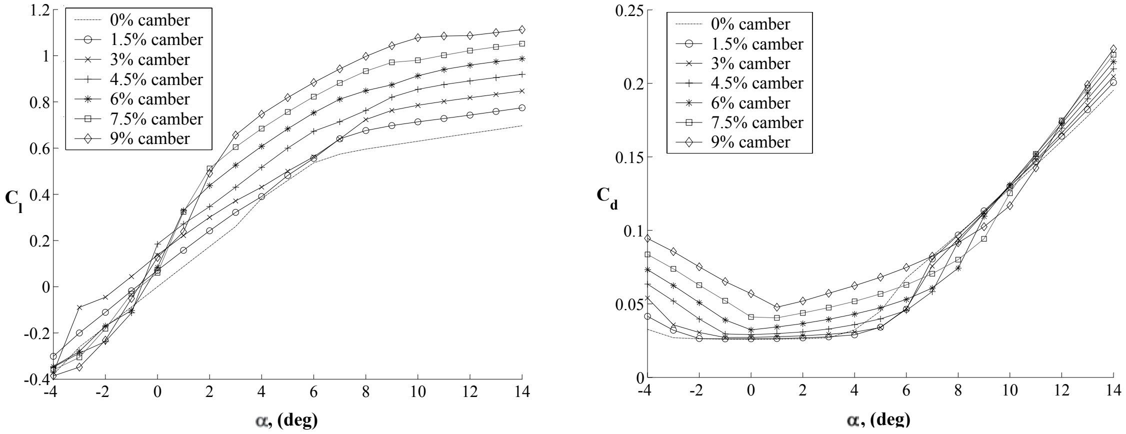

(a) Lift coefficient at Re=15k, TR=2.5%   (b) Drag coefficient at Re=15k, TR=2.5%

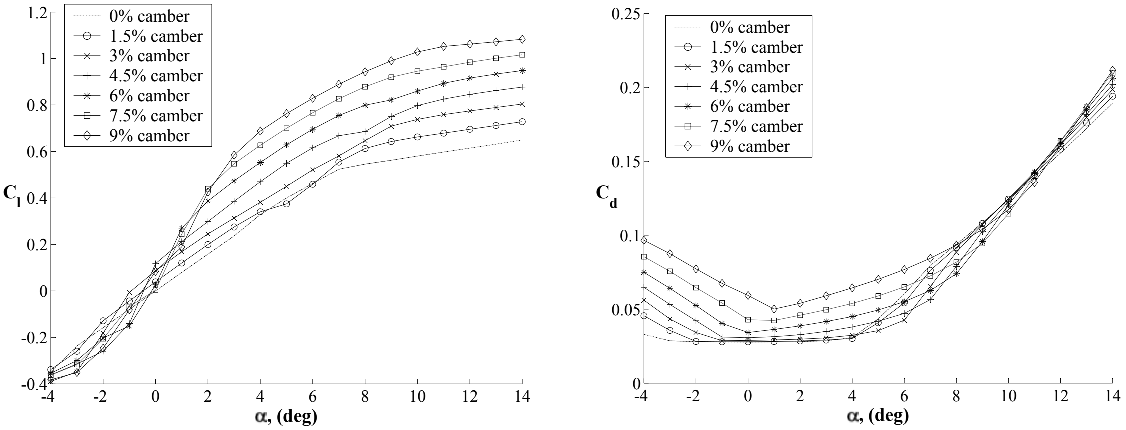

(c) Lift coefficient at Re=15k, TR=3.75%   (d) Drag coefficient at Re=15k, TR=3.75%

Figure 4.14: Lift and Drag coefficients vs. α for airfoils with elliptical LE with 2.5% TR, and 3.75% TR. All cambers at Re=15,000.

present in the experimental validation case and was accurately captured by INS2d and TURNS. The lift "bump" is still present at Reynold numbers as low as 30,000. However at Re of 15,000 for all airfoil geometries the C_l curves become smoother, monotonically growing over the entire angle of attack range. Figure 4.14 shows C_l and C_d vs. α for all the cambers at Re=15,000.

Figure 4.15 shows the lift, drag, and moment coefficients as well as the L/D for a 6% camber airfoil at all Reynolds numbers. This plot is representative of how the Reynolds number affects the lift and drag curves. The behavior illustrated here is useful to have a better understanding of the L/D contour plots of Figures 4.16 and 4.17. As Reynolds number is reduced, the steep lift slope change that took place at α= 5 deg at Re=60,000, moved to α= 6 deg at Re=45,000 and to α= 8 deg at Re=30,000. This shifted the angle of attack for maximum L/D by a degree at Re=45,000. Below Re=45,000 the drag became large enough to negate the effect of the lift increase, shifting the maximum L/D to a lower α. The combined effects of Re on lift and drag gradually moved the angle of attack from 6 deg to 7 deg , then to 4 deg, and finally to 5 deg at Re=15,000. Qualitatively, this behavior was typical of airfoils with cambers of 3% and larger.

A similar behavior was obtained for the airfoils with 3.75% TR that suffered a reduction in the maximum L/D values as Reynolds numbers decreased. The L/D results at the different Re for the 3.75% TR airfoils are shown in Figure 4.17. As for the 2.5% TR airfoils, maximum L/D regions shifted to lower angles of attack at the lower Re as a consequence of the smoother C_l curve shape. The increase in TR had moderate adverse consequences on the performance of airfoils at all Reynolds numbers, lowering by a few percentile points the overall values. However a positive effect was the widening of the high L/D plateaus at all Re.

4.5.3 Sharp Leading Edge Database Results

In the rotor experiments of chapter 2, it was found that the performance of the rotors was improved when using airfoils having a sharp leading edge. In this section the CFD results for the airfoils with sharp leading edges are presented.

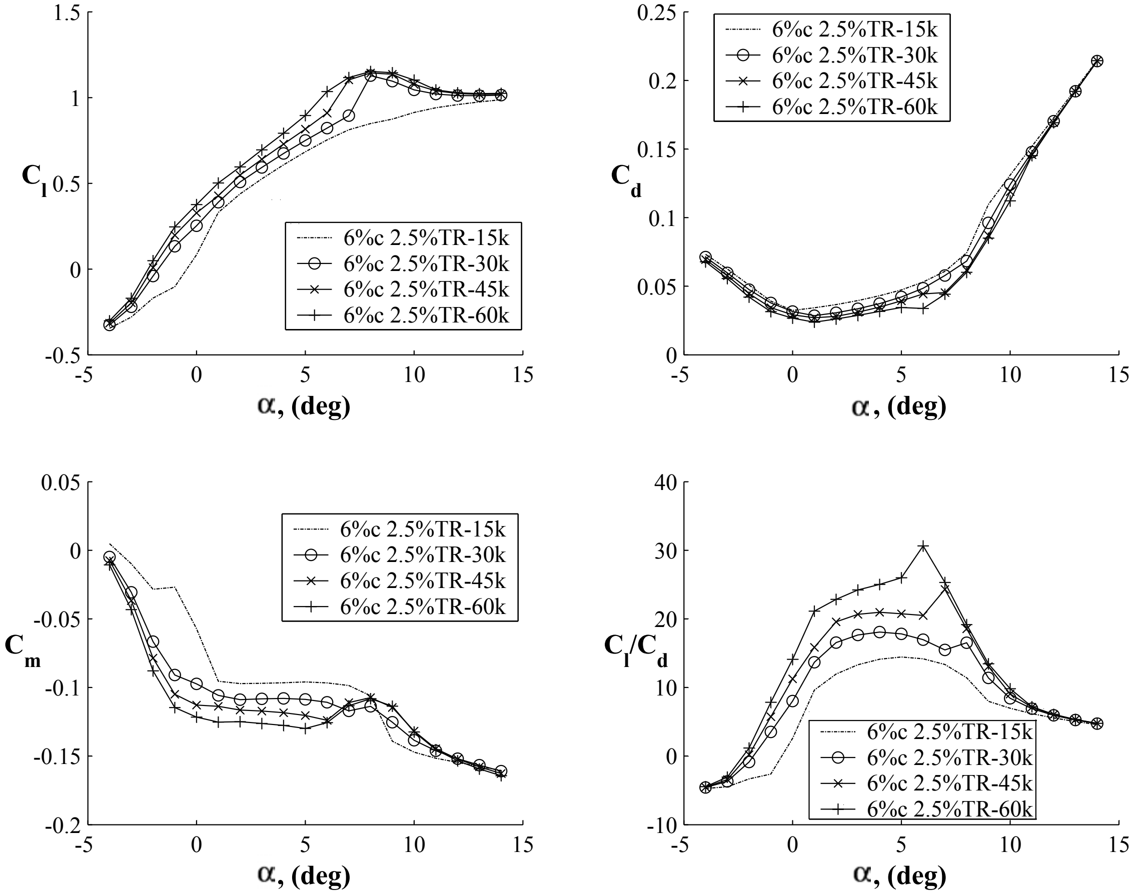

Figure 4.15: Effect of Re in lift, drag, moment coefficient and L/D on a 6% camber 2.5% TR circular arc with elliptical LE.

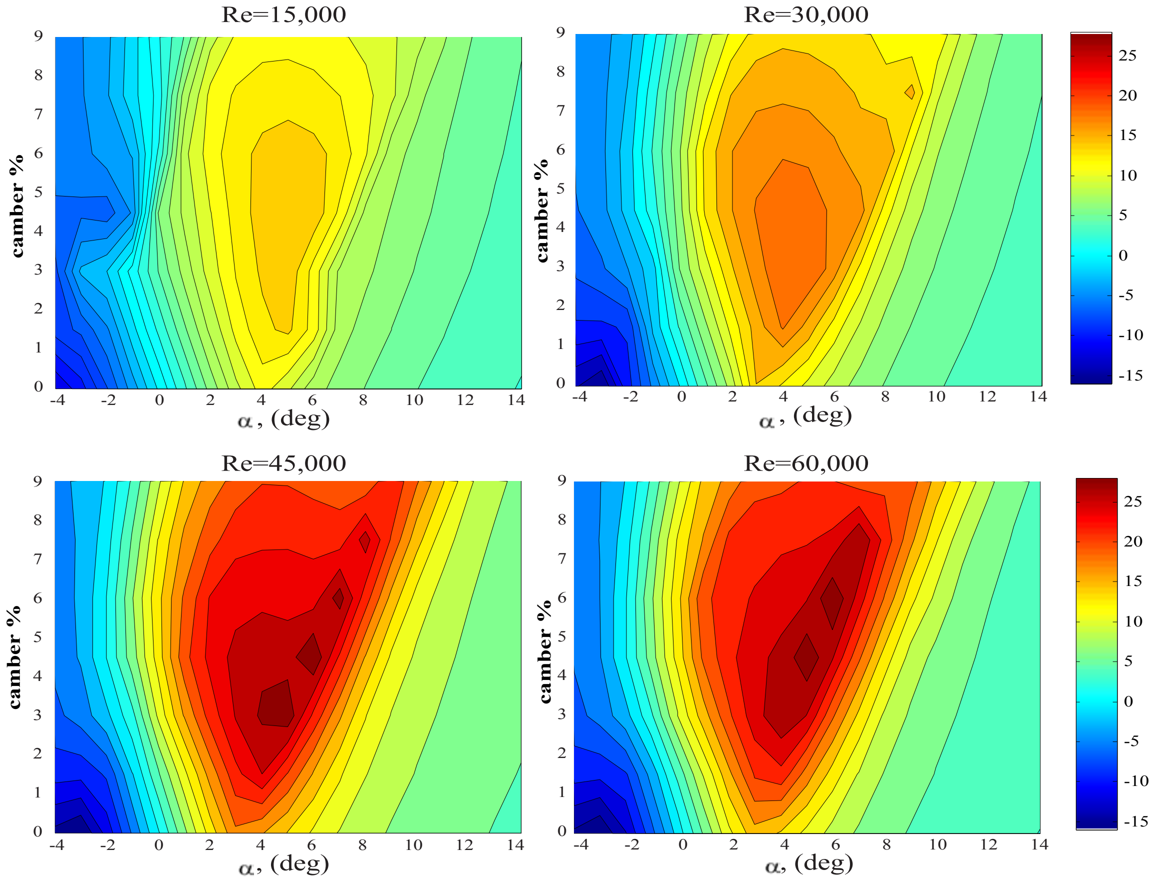

Figure 4.16: Contour plots of L/D as function of airfoil camber and α for airfoils with elliptical LE and 2.5% TR at Re = 15k, 30k, 45k, 60k.

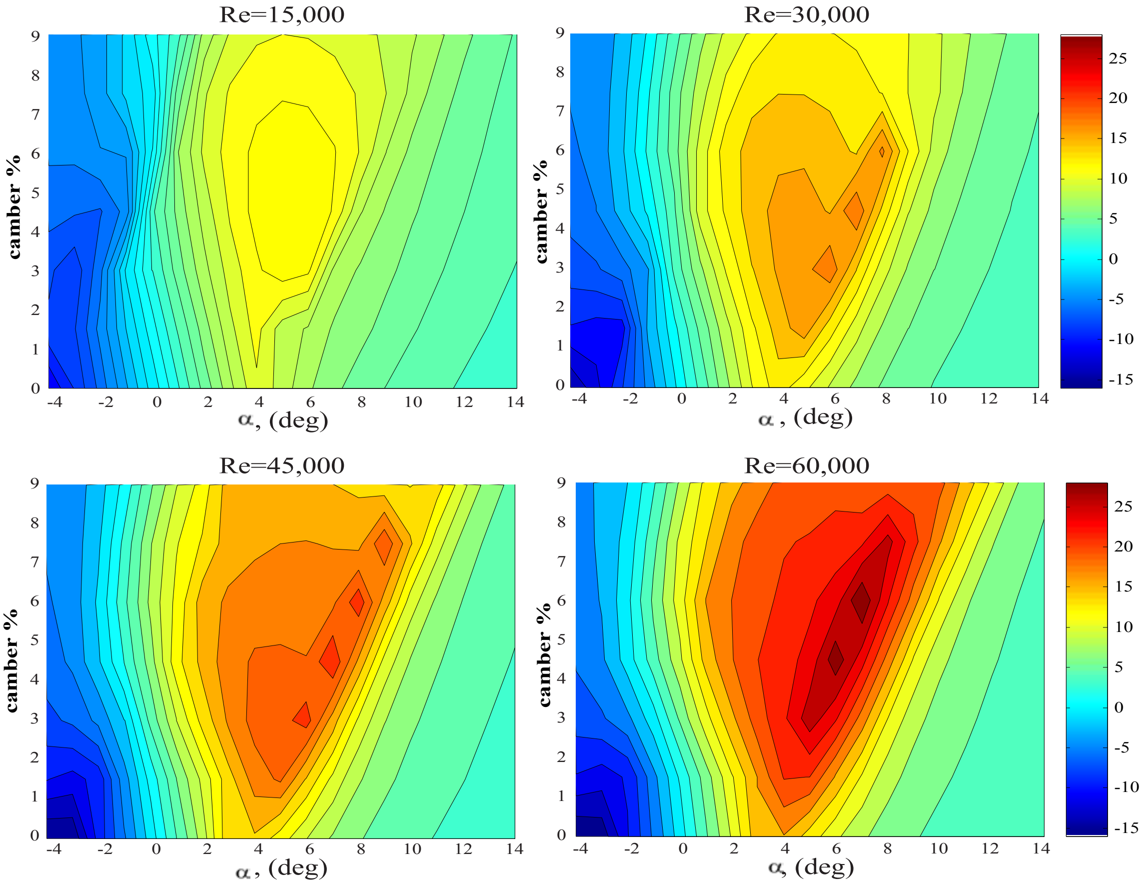

Figure 4.17: Contour plots of L/D as function of airfoil camber and α for airfoils with elliptical LE and 3.75% TR at Re = 15k, 30k, 45k, 60k.

Figure 4.18 shows the lift and drag coefficient curves vs. α for all the database airfoils at Reynolds number of 60,000 and 15,000. The effects of camber did not change with respect to the elliptical leading edge airfoils:

- As camber increases higher lift coefficients are reached below stall.
- As camber increases also does maximum C_l.
- Higher C_l values result also in higher C_d values.
- Airfoil stall occurs at increasingly high angles of attack as camber increases.

A reduction in the Reynolds number did not affect the relative magnitude of the plots. However as for the elliptical leading edge case, at the lowest Re lift coefficient curves did not show signs of stall. Instead C_l curves grew monotonically over the entire angle of attack range. Stall is identified by the drag coefficient behavior, which undergoes a changes in slope as the airfoils stall.

In terms of lift to drag ratio the contour plots as function of airfoil camber and angle of attack are shown in Figure 4.19 for the airfoils with 2.5% TR and in Figure 4.20 for the airfoils with 3.75% TR. Similar qualitative results were observed for the sharp and the elliptical LE in terms of L/D:

- A reduction in Re results in lower L/D.
- A reduction in Re gradually lowers the angle of attack for max L/D.
- A reduction in Re extends the high L/D plateau.

The effect of TR in the aerodynamic performance of the sharp leading edge airfoils was also qualitatively very similar to the results for the elliptical LE airfoils. Figure 4.21 shows the TR effects on the 6% and 9% camber airfoils. These sample results show that:

- An increase in TR increases C_d
- An increase in TR tends to reduces L/D values

- An increase in TR tends shift the lift and drag curves to the right, resulting in an effective reduction in angle of attack.
- An increase in TR resulted in changes in the stall characteristics of the airfoils. Stall was delayed by about 2 degrees for most of the cambers.

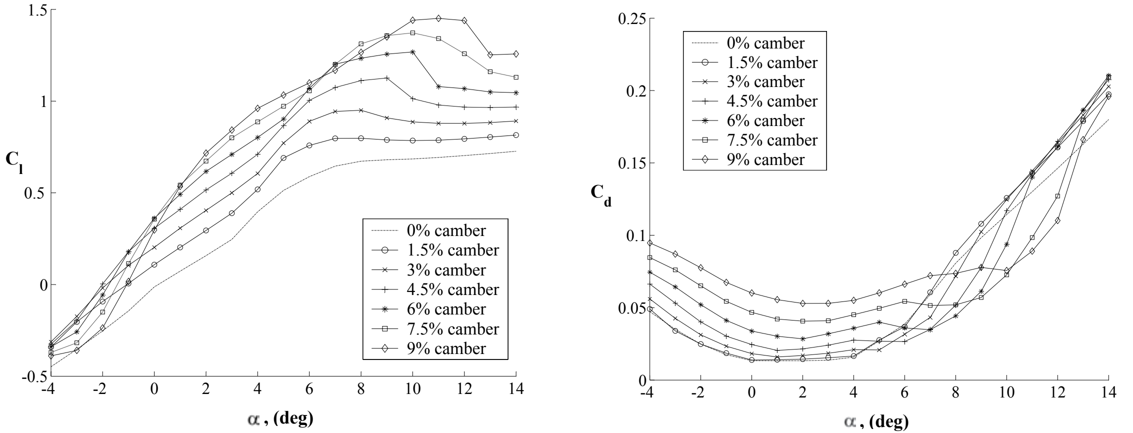

(a) C_l vs. α for 2.5% TR circ arcs sharp LE, Re=60k.

(b) C_d vs. α for 2.5% TR circ arcs, sharp LE, Re=60k.

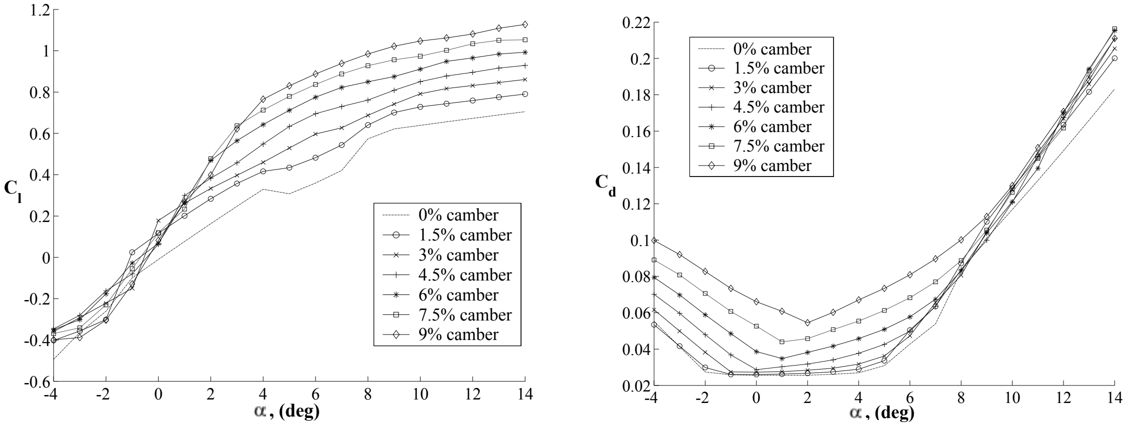

(c) C_l vs. α for 2.5% TR circ arcs, sharp LE, Re=15k.

(d) C_d vs. α for 2.5% TR circ arcs, sharp LE, Re=15k.

Figure 4.18: C_l and C_d vs. α for circular arc airfoils with sharp LE and TR= 2.5% at Re=60,000 and Re=15,000.

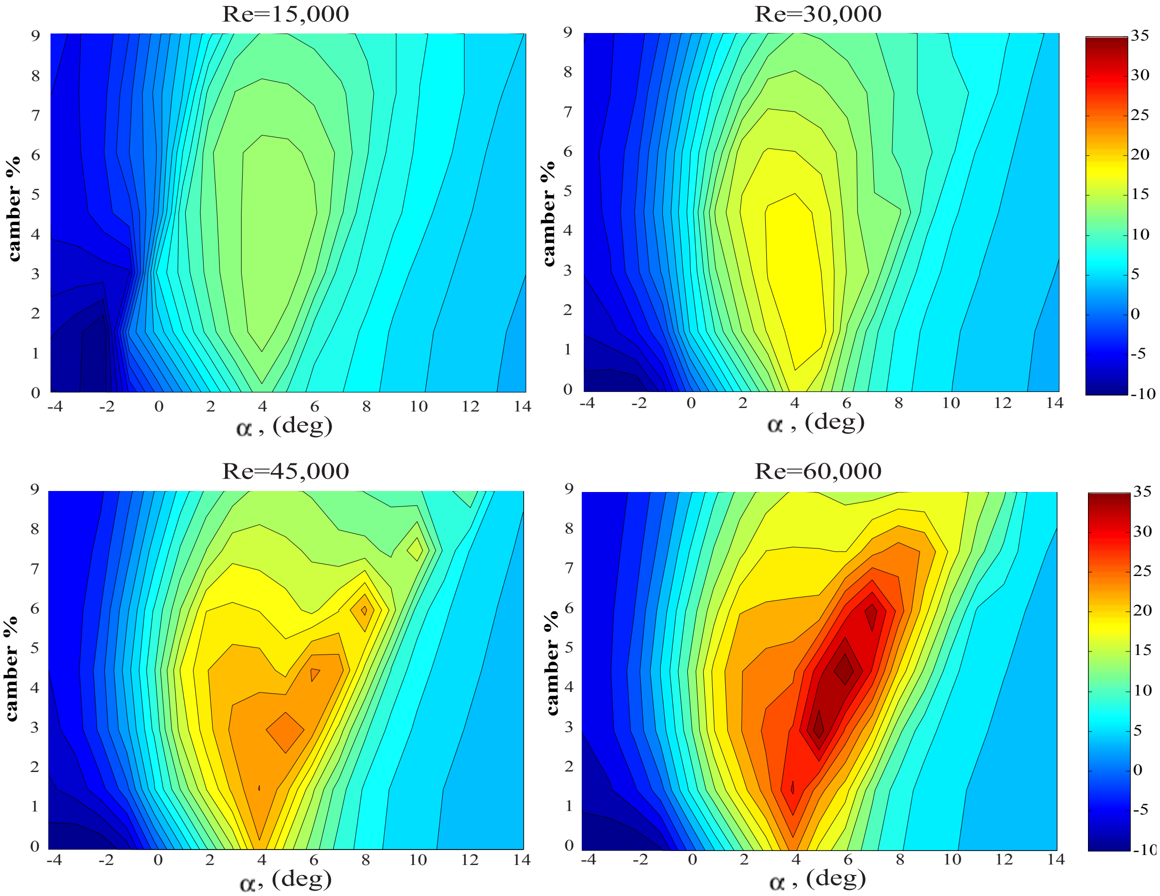

Figure 4.19: Contour plots of L/D as function of airfoil camber and α for airfoils with sharp LE and 2.5% TR at Re = 15k, 30k, 45k, 60k.

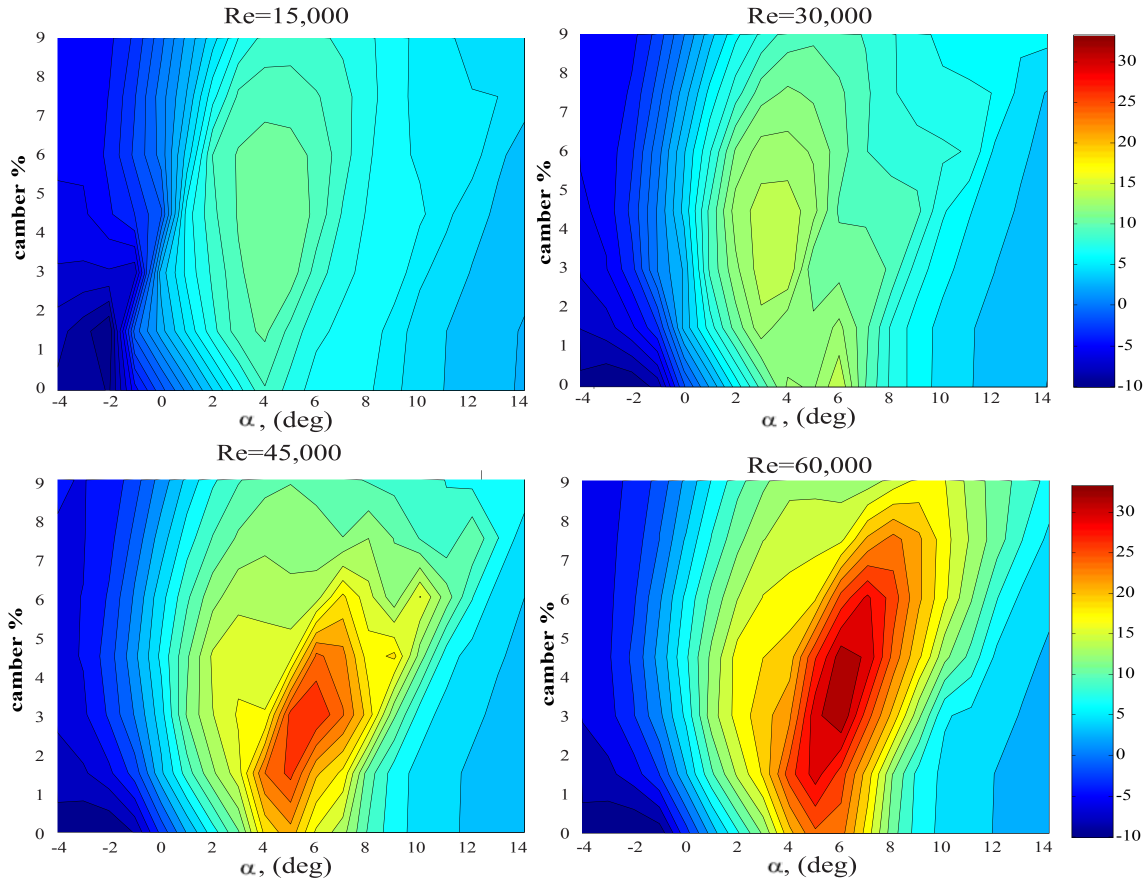

Figure 4.20: Contour plots of L/D as function of airfoil camber and α for airfoils with sharp LE and 3.75% TR at Re = 15k, 30k, 45k, 60k.

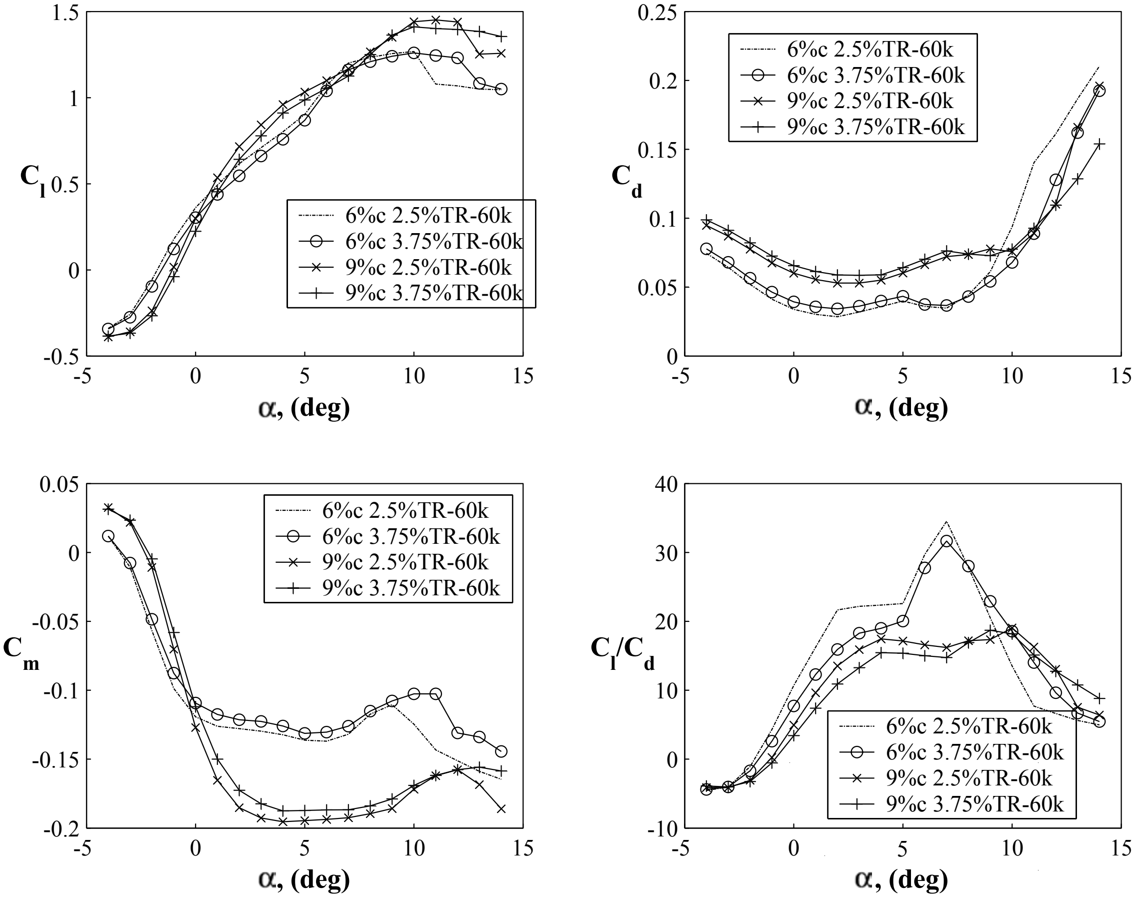

Figure 4.21: Effect of TR in lift, drag, and moment coefficients and L/D ratio on 6% and 9% camber circular arcs with sharp LE having 2.5% and 3.75% TR at Re=60,000.

4.5.4 Sharp vs. Elliptical Leading Edges

In this section some representative CFD results of elliptical and sharp leading edge airfoils are compared. Figure 4.22 shows the lift and drag coefficients for the 6% and 9% camber airfoils at Re=60,000. From the figure it can observed that:

- Sharp leading edges lead to an increase in maximum C_l.
- Sharp leading edges lead to an increase in C_d.
- Sharp leading edges delay stall.
- Leading edge shape had minimum effect on the moment coefficients.
- Sharp leading edges shift the lift, drag, and moment coefficient curves to the right, increasing by about 1 degree the angle of attack with respect to the elliptical LE airfoils.
- Sharp leading edges result in a higher maximum L/D ratio for the 6% camber airfoil. However, for the 9% camber airfoil overall lower L/D were achieved.

By comparing the performance of the 6% and 9% camber airfoils with sharp en elliptical leading edges at Re=15,000 the effects of reducing the Reynolds number can be identified. Figure 4.23 shows that:

- As Reynolds number is reduced the gain in maximum lift coefficient obtained with the sharp leading edges is not present anymore. Both elliptical and sharp LE airfoil geometries produce very similar lift coefficient curves.
- The use sharp leading edges results in higher drag coefficients at all Reynolds numbers. Nevertheless the drag increase is considerably lower at 15,000 than at 60,000 Re.
- As Reynolds number is reduced the difference in lift to drag ratio between elliptical and sharp leading edge airfoils is reduced. However, elliptical leading edges tend to perform better.

From the previous comparisons of the computational results it can be concluded that sharp leading edge airfoils can have beneficial effects in the airfoil performance at specific operational points and with only certain airfoil cambers. For circular arcs with a cambers 6% and below maximum L/D are generally improved thanks to an additional lift production. However for larger cambers the drag increase negates the beneficial lift effects resulting in overall lower L/D values.

The lack of experimental two dimension data makes difficult to validate the trends identified specially the sharp leading edge effects. This is why the observations made have to be carefully interpreted. The flow assumptions used in the simulations can have a strong effect on the final results. Hence, even though full convergence could be consistently achieved, it is possible that the steady flow assumption is overlooking some unsteady phenomena that can accentuate the differences between elliptical and sharp leading edge geometries.

4.6 Summary

This chapter presented the CFD methodology and results used to calculate the two-dimensional airfoil characteristics of a well defined family of circular arc airfoils. The CFD solvers TURNS, Fluent and INS2d were evaluated, validating the results with published wind-tunnel experiments of a circular arc airfoil at a Reynolds number of 60,000. Validation showed that TURNS produced the best lift coefficient predictions, followed by INS2d which under-predicted lift at the higher angles of attack. Fluent was unable to capture the non-linearities of the lift measurements. All three codes under-predicted drag; however, TURNS and INS2d qualitatively captured the trends in L/D ratio.

Because of the compressible nature of TURNS two issues arose:

- Computational cost was considerably higher with TURNS than with INS2d.
- Convergence with TURNS was difficult at the lower Reynolds numbers

This is why INS2d was chosen to calculate a database of airfoil characteristics that explored the effect in aerodynamic performance of the following geometric and op-

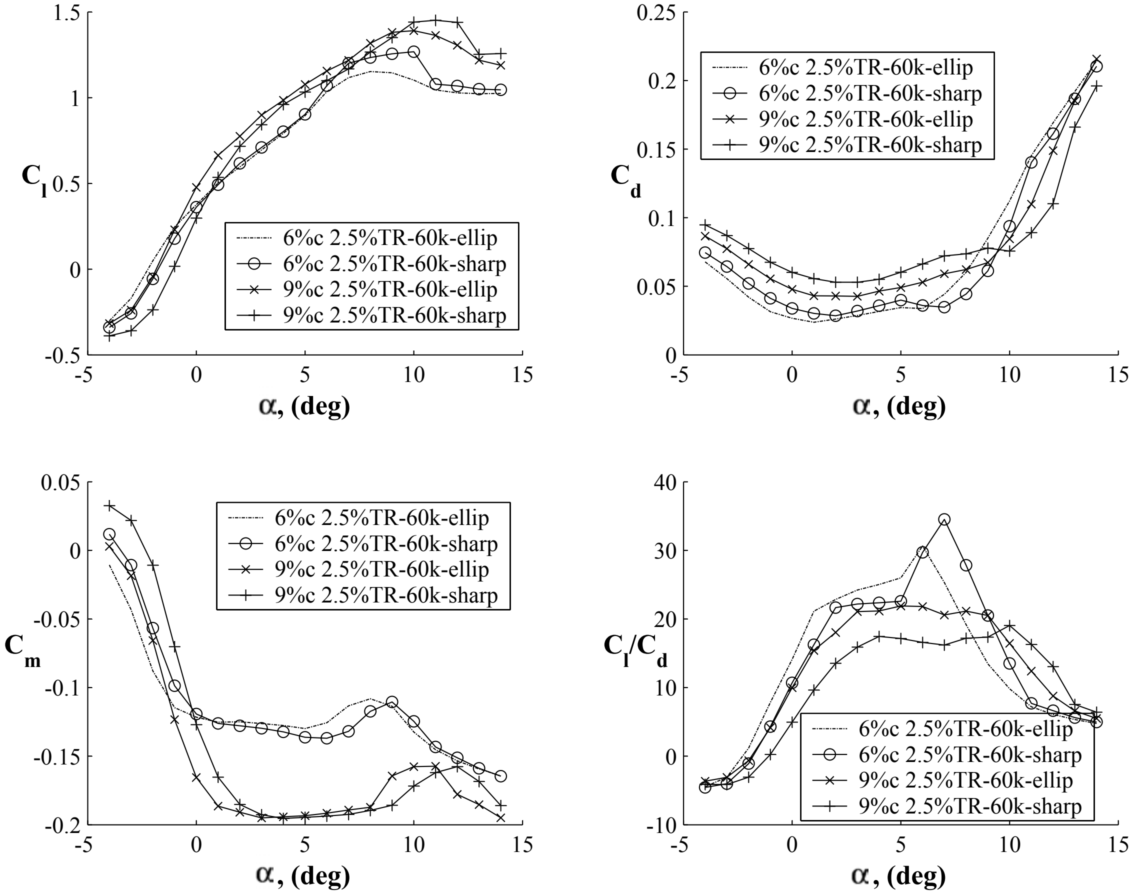

Figure 4.22: Effect of leading edge shape in lift, drag, and moment coefficients and L/D ratio on 6% and 9% circular arc airfoils with 2.5% TR at Re=60,000.

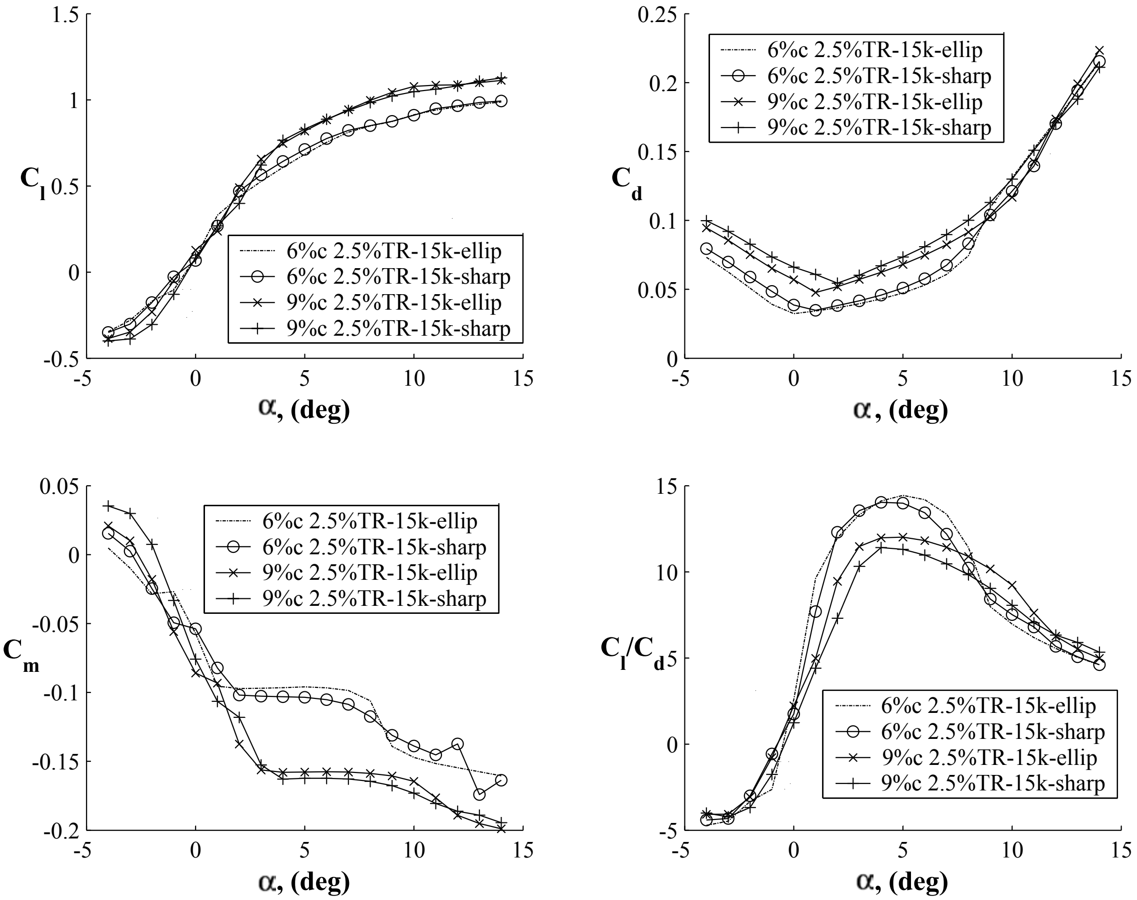

Figure 4.23: Effect of leading edge shape in lift, drag, and moment coefficients and L/D ratio on 6% and 9% circular arc airfoils with 2.5% TR at Re=15,000.

erational parameters:

Operational parameters

- Angle of attack -4 to 14 deg.
- Reynolds number 15,000 to 60,000.

Geometric parameters

- Camber 0% to 9%.
- Thickness ratio 2.5% 3.75%.
- Leading edge shape elliptical and sharp.

The most relevant results of the parametric study are:

- Camber determines maximum C_l achieved by airfoils.
- Camber determines stall angle of the airfoils.
- Increasing TR has adverse effects in drag, lowering L/D values.
- The highest L/D ratios were achieved by airfoils having cambers between 4.5% and 6.0%.
- Sharp leading edges increase maximum C_l values and delay stall; however, only for specific cases improvements in maximum L/D were observed.
- A reduction in the Reynolds number adversely affects L/D ratio as a consequence of a simultaneous reduction in lift slope and an increase in drag.
- Leading edge geometry has a reduced relevance in airfoil performance as Reynolds number decreases.
- A reduction in Re gradually lowers the angle of attack for max L/D.
- A reduction in Re extends the high L/D plateau of airfoils.

The databases generated in this chapter can now be used in rotor design code that can include varying geometric and operational parameters in the predictions of rotor hover performance. Chapter 5 explains the approach used for the implementation of this type of analysis.

Chapter 5

Hybrid BEMT-CFD Method for Rotor Analysis and Design

5.1 Introduction

Blade Element Momentum Theory (BEMT) was introduced in Chapter 3 as a relatively simple and inexpensive but powerful tool for rotor analysis. One of BEMT main features is the capability to incorporate geometric and operational rotor parameters such as: blade planform, twist distribution, number of blades, and collective pitch settings. However, BEMT requires the sectional airfoils characteristics in order to calculate the nonlinear axis-symmetric inflow. At larger scales linear aerodynamics can be used to model the airfoil characteristics. However, at MAV scale Reynolds number effects hinder the use of that approach. This is why obtaining a good estimate of the airfoil characteristics is key to achieve satisfactory results with the model. In this Chapter the coupling of the BEMT algorithm with the CFD databases calculated in Chapter 4 is explained. The use of this approach as a design tool requires the definition of a geometric blade parameterization, the implementation of an interpolation procedure, and a methodology to explore the test space. These are discussed in the following sections.

5.2 Design Algorithm

Figure 5.1 shows the block diagram of the algorithm implemented for the rotor analysis. The inputs to the algorithm can be divided into two categories: the fixed basic rotor configuration and operational parameters, and the parameters that depend on blade geometry. Basic rotor configuration parameters are: diameter, number of blades, rotational speed, and collective pitch. The parameters that depend on the blade planform shape include: solidity, twist distribution, spanwise airfoil geometry and chord-based Re. Based on a blade parameterization that couples the blade and airfoil shapes along the span, the radial distribution of airfoil geometries, twist distribution, and local chord-based Reynolds number are calculated. All the previous geometric and operational parameters are given to the BEMT rotor model. As explained in Chapter 3, an iterative process finds an inflow distribution that is consistent with the airfoil characteristics. For each inflow iteration the lift and drag coefficients need to be obtained at every radial station; this is done by interpolating the CFD database. After inflow convergence is achieved the output parameters are calculated for the rotor studied.

By prescribing changes in the parameterized blade planform the combined effects of airfoil and blade geometries can be explored with a minimum of computational cost. This approach is an alternative to the more sophisticated three-dimensional CFD and vortex models which capture the physics involved with more detail. Nevertheless, not necessarily better results will be obtained with those methods since:

- Similar difficulties and predictive errors faced in the two-dimensional CFD calculations are also found when studying the three-dimensional cases. However, computational cost increases exponentially, greatly limiting the use of this approach as a design tool.

- Vortex methods can be used to model the three dimensional near and far wake effect to calculate the inflow. However, these methods need also the two-dimensional airfoil characteristics, which are obtained from wind tunnel experiments or two-dimensional CFD.

In the next sections the geometric blade-airfoil parameterization and the interpolation implementation is explained in more detail.

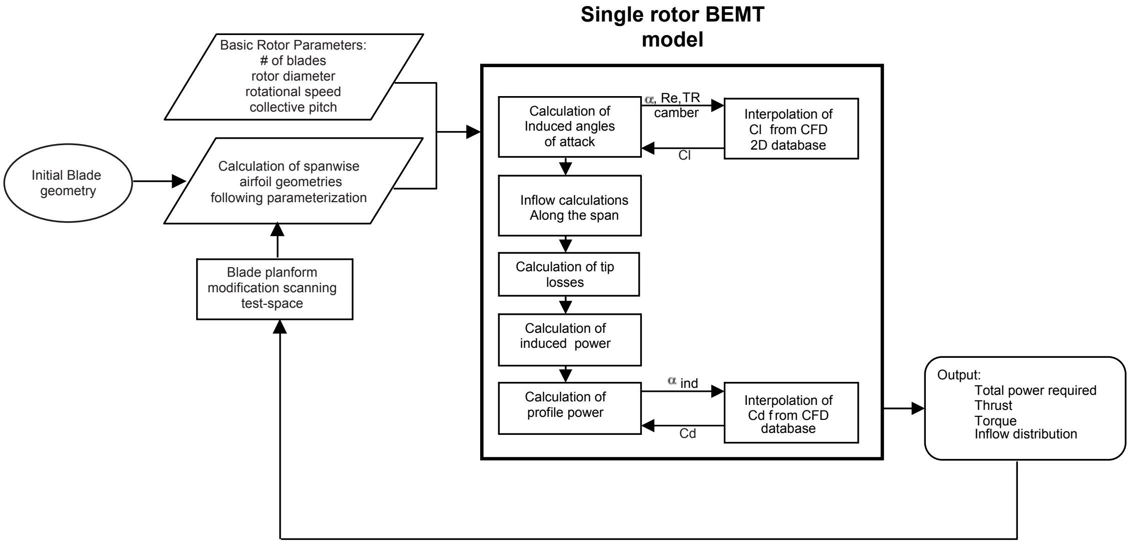

Figure 5.1: Single rotor design algorithm

5.3 Geometric Blade Parameterization

A rotor that has untwisted rectangular blades with a uniform airfoil along the span does not have any varying geometric blade or airfoil parameters. This is the simplest possible case where the only variable along the blade is the chord-based Reynolds number.

On the other hand, if the blades have a non-rectangular planform with more than one airfoil along the span, the analysis becomes more complex due to the larger number airfoil sectional characteristics that the model needs. For a single rotor configuration operating at a specified design point it is reasonable to perform wind tunned tests or a detailed CFD studies to obtain the airfoil characteristics. However, if an open design problem is faced a different approach needs to be taken. This is the case for MAV rotor design. Rotary-wing MAVs can be used for a wide range of mission that will cover a broad range of payloads, rotor diameters and rotational speeds. Hence, it is desired to have a flexible design tool that can adapt to changing requirements. By coupling the BEMT model with the circular arc database through a geometric blade/airfoil parameterization, a large design space can be explored. The following blade planform constraints were used in the implementation of the model and are mainly based on manufacturing limitations:

- Planform is defined by 8 points shown in figure 5.3. Each point location is defined in a cartesian plane by a radial and chordwise coordinate: P(r,c).
- Points that define the root edge (points 1 and 8) must be at the same radial position. The chordwise location of these two points can be at any intermediate position between C_{LE} and C_{TE} as long as $c(1) > 0$ and $c(8) < 0$.
- The points that define the tip edge (points 4 and 5) must be at the same radial position equal to r=1. As for the points that define the root edge, points 4 and 5 can be at any intermediate chordwise position between C_{LE} and C_{TE} as long as $c(4) > 0$ and $c(5) < 0$.
- The pairs of points 2-3 and 7-6 must have the same chordwise coordinate such

that $c(2) = c(3) = C_{LE}$ and $c(7) = c(6) = C_{TE}$. In this way the line segments defined by points 2-3 and 7-6 are always parallel to each other and to the radial axis.

Additionally to the blade planform constraints, the following airfoil constraints were imposed too:

- Airfoils must be circular arcs.
- Cambers must be in the range of 0% to 9% (range covered in database).
- Camber is defined based on a rectangular baseline blade, were points 1,2,3 and 4 are aligned defining the leading edge, and points 5,6,7 and 8 are also aligned defining the trailing edge.
- Camber can be defined as constant or varying linearly between the root and the tip edges - based again on a rectangular blade -. This is equivalent to have a conical section.
- Material thickness can be defined as uniform or linearly varying along the span. Chord and material thickness should be defined to have realistic thickness ratios, in the range of 1.5% to 6%.

These geometrical constraints can results in a quadrilateral or a 5, 6, 7 or 8 side polygon. The previous blade planform parameterization is consistent with the non-rectangular geometries tested experimentally in section 2.6. The points are essentially defining the areas to be removed from a baseline rectangular blade. As explained in section 2.6.1 this results in changes in the solidity, twist, camber, and thickness ratio distributions of the blades. Figure 5.3 shows the geometric blade and airfoil parameters along a sample non-rectangular blade. In this case the airfoil shape of the baseline rectangular blade (dashed lines) was 6% at the root and 9% at the tip.

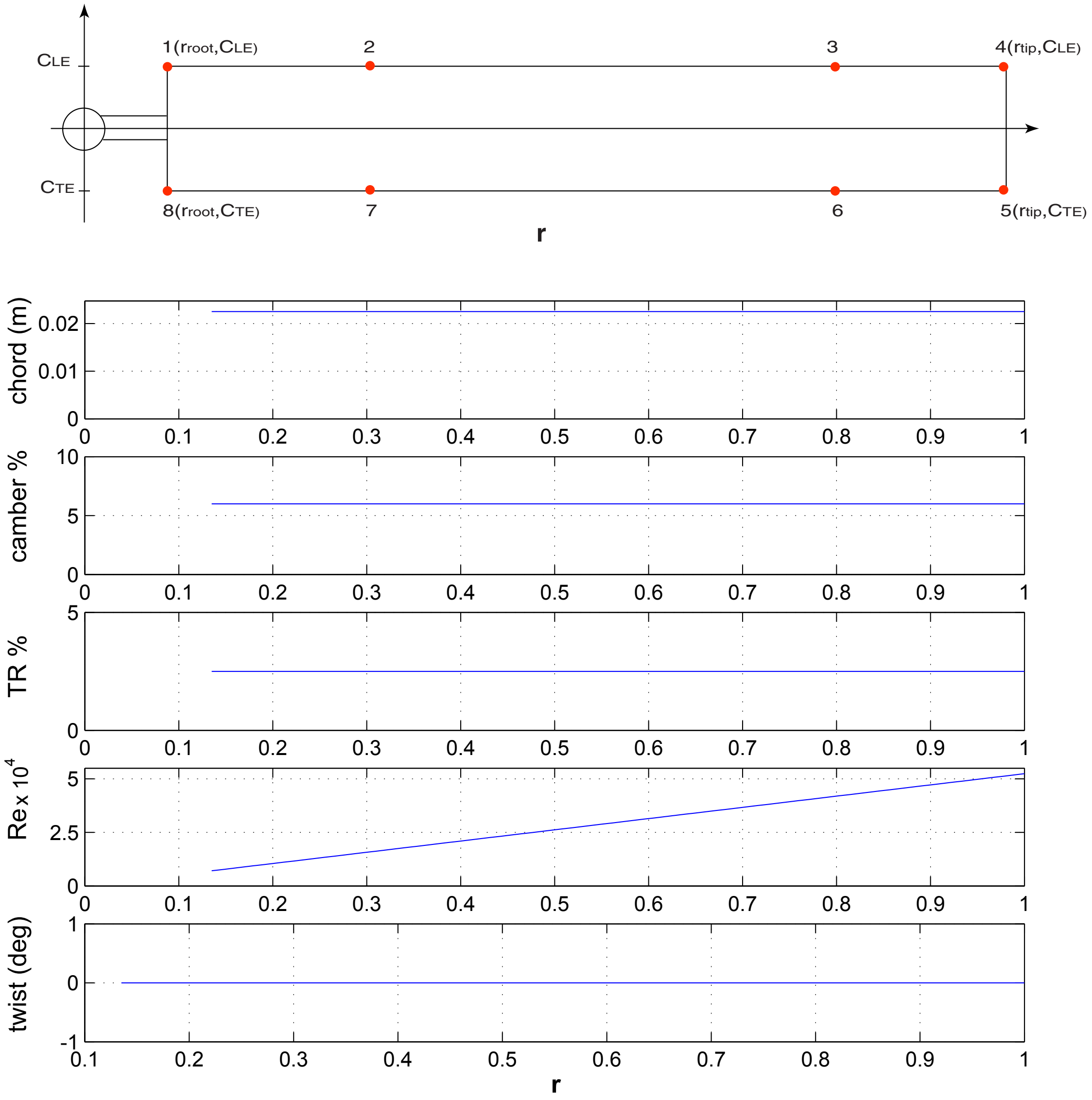

Figure 5.2: Radial parameters for rectangular blade with uniform 6% camber airfoil.

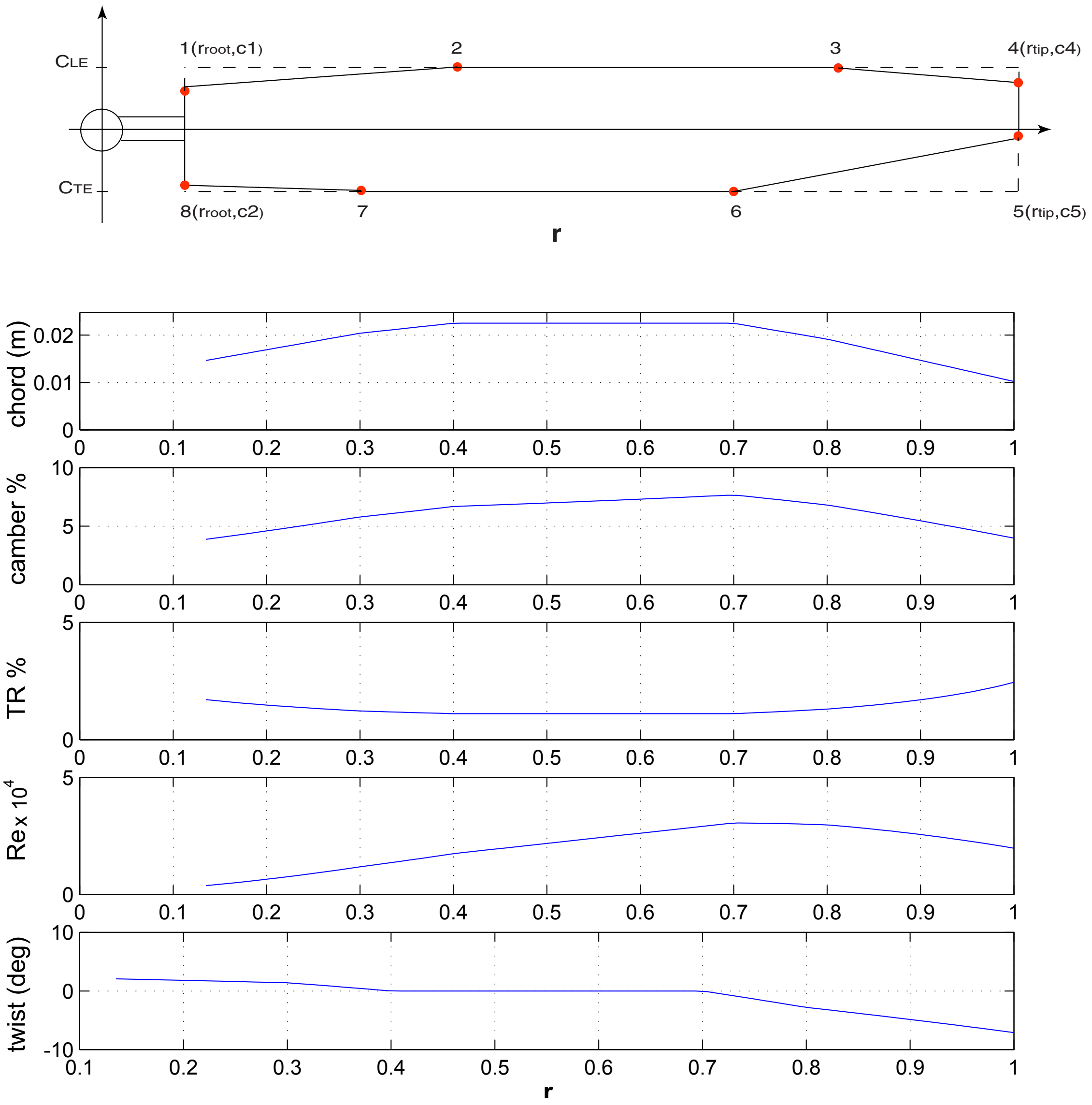

Figure 5.3: Radial parameters for non-rectangular blade with baseline 6% camber airfoil at root and 9% camber airfoil at tip.

5.4 Airfoil Database Interpolation

The airfoil databases calculated in Chapter 4 covered four parameters: Reynolds number, camber, thickness ratio, and angle of attack. Hence, for a each blade section interpolation in these four dimensions has to be performed. In order to minimize the computational cost of the interpolation the parameter that depend on blade geometry are interpolated first, obtaining the C_l and C_d curves vs. α. Finally during the inflow calculations, the local C_l and C_d curves obtained in the previous step are interpolated in angle of attack until convergence is achieved.

The successive database interpolation is performed using simple linear methods that allow for extrapolation in case boundaries are exceeded. Linear interpolation is a good option when very few or many data points are available. In the current investigation only two thickness ratios and four Reynolds numbers were considered. Based on the results presented in Chapter 4 it was decided to implement a simple linear approach in order to avoid overshooting or unwanted oscillations in the predictions. Polynomial and cubic spline methods are likely to face these problems due the proximity of the points. Other interpolation schemes such as the Akima (Ref. [84]) splines minimize the overshooting or over-fitting problems; however, Akima splines need a minimum of 5 points to be used. Akima or cubic spline methods could have been implemented in the angle of attack interpolation; however, since lift and drag data points are uniformly spaced at one degree intervals the gains in accuracy were insignificant.

5.4.1 Interpolation Validation

The interpolation methodology was validated by comparing the lift and drag coefficients obtained from a direct CFD calculation with database interpolated results. A 4% camber, 1.93% TR airfoil with elliptical leading edge was used for this purpose, it is the same airfoil used in the experimental CFD validation of Chapter 4. The results obtained are shown in Figure 5.4 where lift, drag, and L/D at various Re are plotted. For the most part interpolation results show a good agreement with the CFD calculations. At Re = 60,000 maximum percentile differences in L/D ratio are of the order of 3%. At the other Reynolds numbers (45,000,30,000 and 15,000) similar errors are obtained over most of the angle of attack range. However, for negative angles and at an angle of attack of 6 degrees, differences can be as large as 15% (@Re=30k). In general the interpolation errors are a result of an under estimation of the lift coefficient. The highly nonlinear C_l vs. α curves introduce errors in the vicinity of steep changes in the curve's slope. These errors can be minimized by increasing the number of interpolating points. An increase in the number of Reynolds numbers and thickness ratios data points would have a noticeable impact on the predictive capability of the interpolating algorithm.

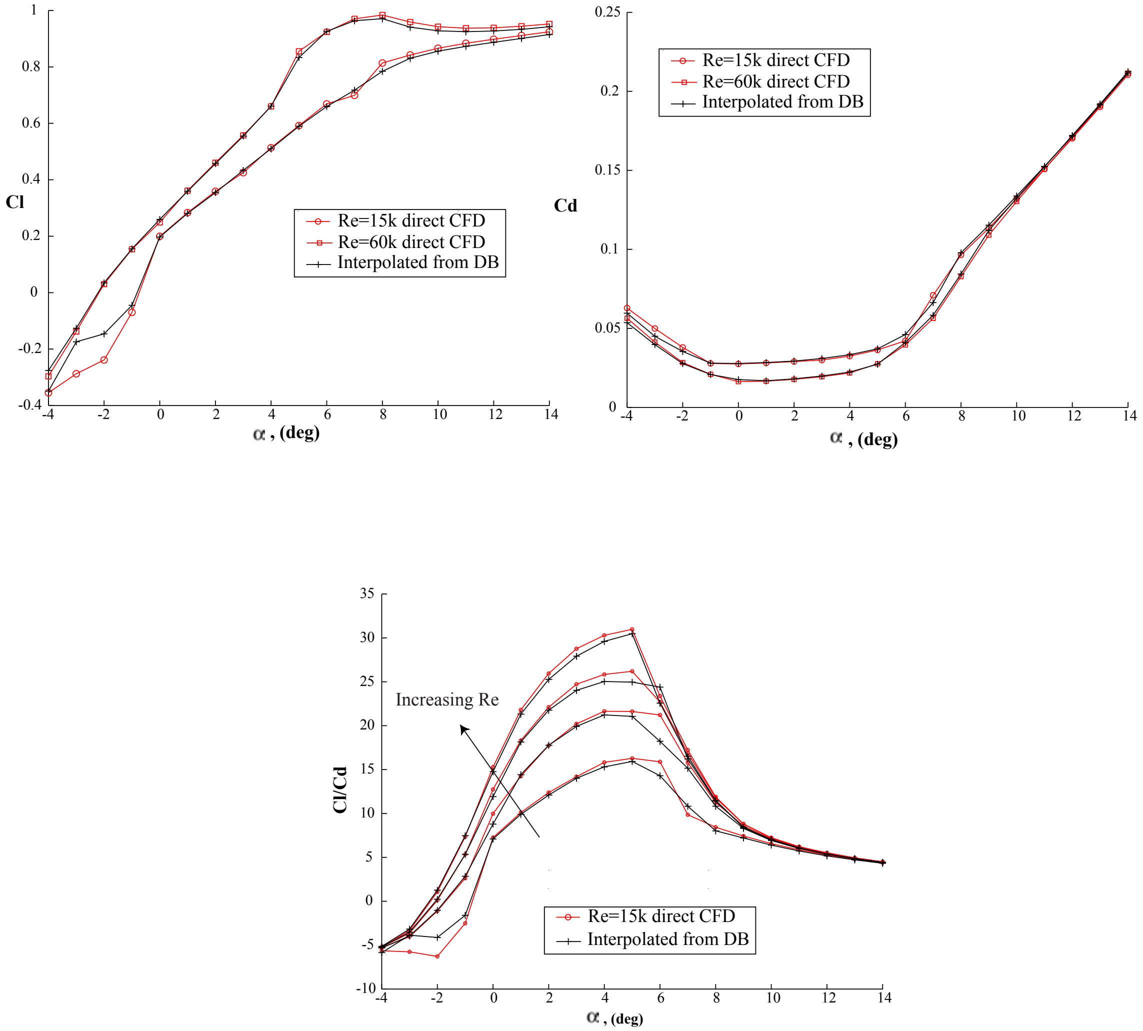

Figure 5.4: Comparison of lift drag and L/D results from direct CFD and interpolated results for a 4% camber, 1.93% TR at various Re.

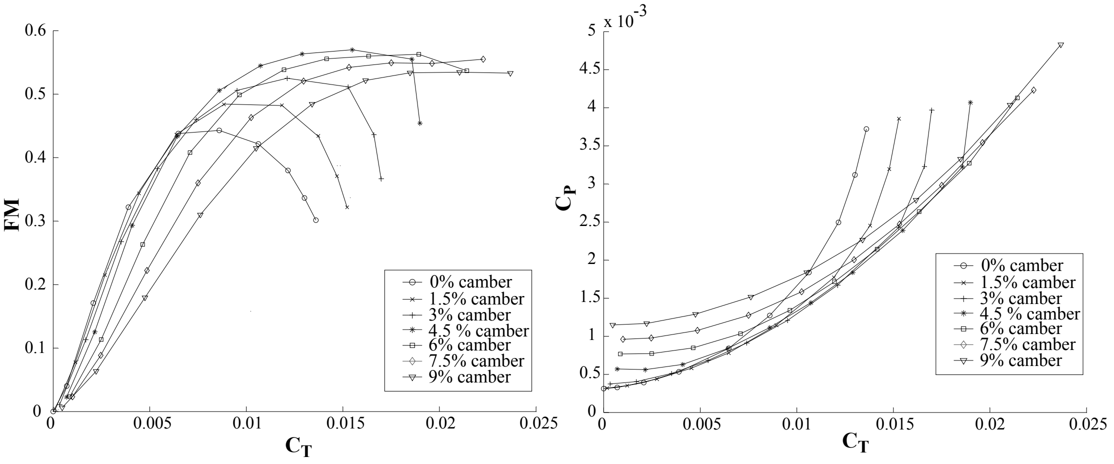

Figure 5.5: Predicted C_T vs. FM and C_T vs C_P for rotor with rectangular blades and various airfoil cambers at 2500 RPM.

5.5 Approach Validation

The accuracy and predictive capabilities of the present approach were validated using some of the experimental results of Chapter 2. First, The effects of basic rotor parameters such as rotational speed, collective pitch, solidity, and airfoil camber are validated using rectangular bladed rotors. Second, calculations using non rectangular planform shapes that include the combined effects of spanwise twist distribution and airfoil geometry are presented.

5.5.1 Rectangular Blades - Camber Effects

The effect of airfoil camber on third generation rotors (i.e. 2 blades, R=112mm, chord=22.5 mm) was explored using the BEMT code coupled with the database of airfoils with elliptical leading edges. The individual results for the different airfoils are explored further into this section; for now the general trends observed in the calculations are identified. Figure 5.5 shows the C_T vs. FM and C_T vs C_P plots for rotors with airfoil having cambers ranging from 0% up to 9% at 2500 RPM.
As it was experimentally confirmed the following trends are present:

- As camber is increased the range of thrust coefficients the rotors can achieve is extended.

- Rotor stall occurs at increasingly higher collectives as airfoil camber is increased.
- Maximum FM occurs at increasingly higher collectives as airfoil camber is increased.
- Airfoil camber has a strong influence on maximum hover efficiency of the rotors.
- However, maximum FM values using cambers between 3% and 9% range between 0.52 and 0.57.
- Maximum FM above 0.5 are achieved with cambers equal or larger than 3%.
- Below stall power coefficient is directly dependent on airfoil camber.

Now that the rotors are modeled as a whole system two main sources of errors are present: errors linked to the inflow calculations resulting from the assumptions of BEMT, and errors from the airfoil sectional characteristics calculated in Chapter 4. Since rotational speed and blade geometry are identical for all the rotors of Figure 5.5, the predicted performance is directly linked to the airfoil characteristics. Hence, any errors in the two-dimensional airfoil characteristics will propagate affecting the thrust and power calculations. Based on the validation results of the CFD calculations (section 4.4) maximum lift coefficients and drag coefficients at the lower angles of attack were under-predicted by the flow solver.

The Analytical and experimental FM vs. C_T plots for flat plates, 3%, 6%, and 9% camber circular arcs are shown in Figure 5.6. There is a clear qualitative agreement between experimental and numerical results, however the following differences consistent with the errors in sectional characteristics are present:

- Experimental maximum FM tends to be larger than predicted.
- Experimental maximum C_T tends to be larger than predicted.

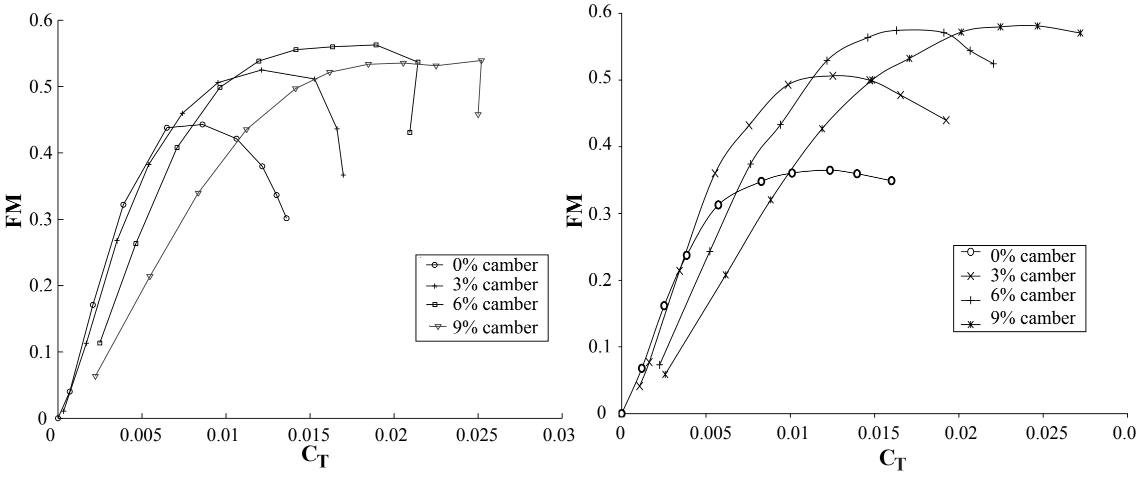

Figure 5.6: Predicted and experimental C_T vs. FM for 0%, 3%, 6% and 9% camber airfoils with elliptical leading edges at 2500 RPM.

- Rotor stall is smoother in the experiments than in the predictions.

The following figures compare in more detail the experimental and predicted performance for the rotors with 3%, 6%, and 9% camber airfoils.

Figure 5.7 compares the experimental and numerical results of the rotor with 3% camber airfoil. There is an excellent agreement in thrust coefficients for collectives of 16 deg and below. The experimental and predicted values differ by about 2% at a collective of 12 deg. These are very small errors considering that experiments are not perfect, and that small deviations in pitch might occur due to centrifugal and aerodynamic forces. In terms of figure of merit, BEMT predicts a maximum FM $\approx$ 5% larger than the experimental one, there is a vertical offset between the experimental and BEMT curves, resulting from an under-prediction of the power required.

For the rotor with 6% camber airfoils Figure 5.8 shows the experimental and predicted results. As for the 3% camber blades there is good agreement in the trust predictions. The average difference between experimental and numerical thrust values at collectives of 14 and below is 2.25 grams which is about 3% of the thrust produced at 14 deg collective. FM is over predicted at the lower collectives, however as collective is increased the errors are reduced, under-predicting the maximum FM

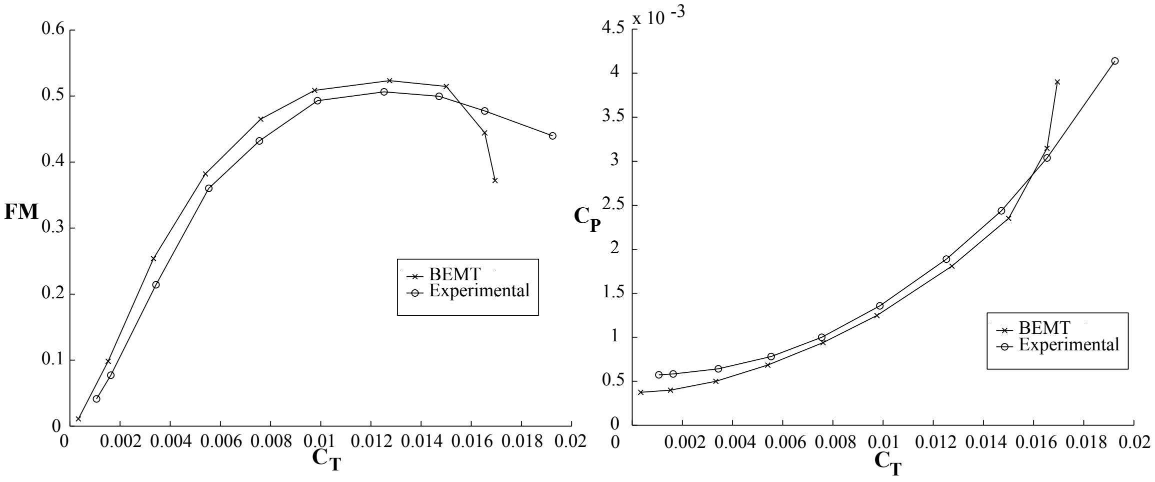

Figure 5.7: Predicted and experimental C_T vs. FM and C_T vs C_P for rotor with 3% camber airfoils, elliptical leading edges at 2500 RPM.

by only 2.5%.

The results for the rotor having the 9% camber airfoils are presented in Figure 5.9. In this case the thrust prediction are not as good as for the other rotors. Above collectives of 8 degrees the BEMT predictions largely under estimate the thrust produced, resulting in a maximum figures of merit $\approx 8\%$ below the experimental values at a thrust coefficient 10% smaller.

In the three cases considered the effects of under-predicting the sectional drag coefficients are clearly observed in the C_T vs C_P plots (Figures 5.7, 5.8, 5.9). Using the 6% camber blades as example, the calculated spanwise induced angles of attack and the induced and profile power components for the different collectives are plotted in Figure 5.10. At the lower collectives (0 deg $\leq \theta_0 \geq$ 4 deg) where profile power is dominant or comparable to induced power, experimental C_P values are greater than predicted, this results in higher FMs over the lower collective range. As collective is increased larger portions of the blades work at angles of attack were sectional characteristics were accurately calculated by the CFD flow solver producing a good agreement between experimental and model results. At the collective for maximum FM, profile power is $\approx 30\%$ of the total power, and induced angles of attack do not exceed 6 deg. At the highest collectives ($\theta_0 \leq 16$) large blade sections work in the

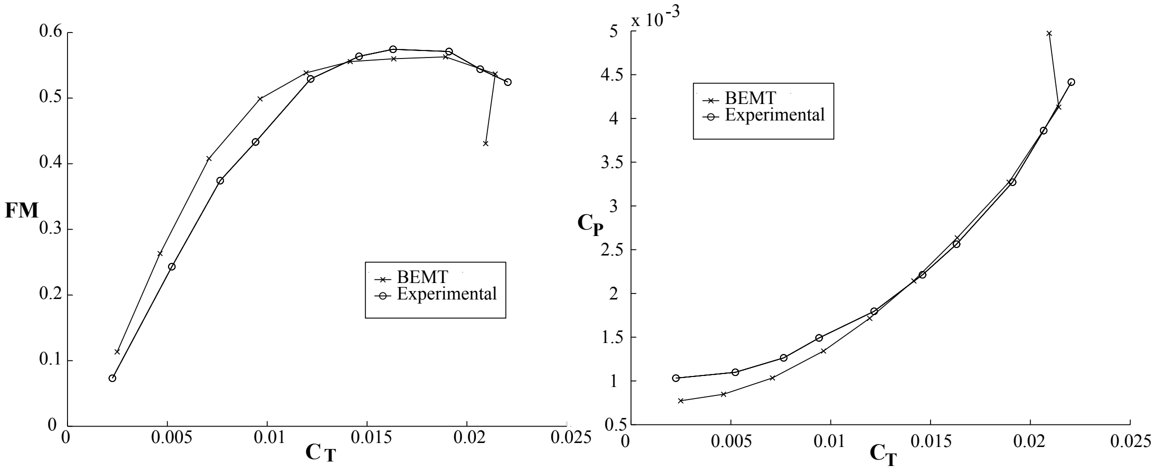

Figure 5.8: Predicted and experimental C_T vs. FM and C_T vs C_P for rotor with 6% camber airfoils, elliptical leading edges at 2500 RPM.

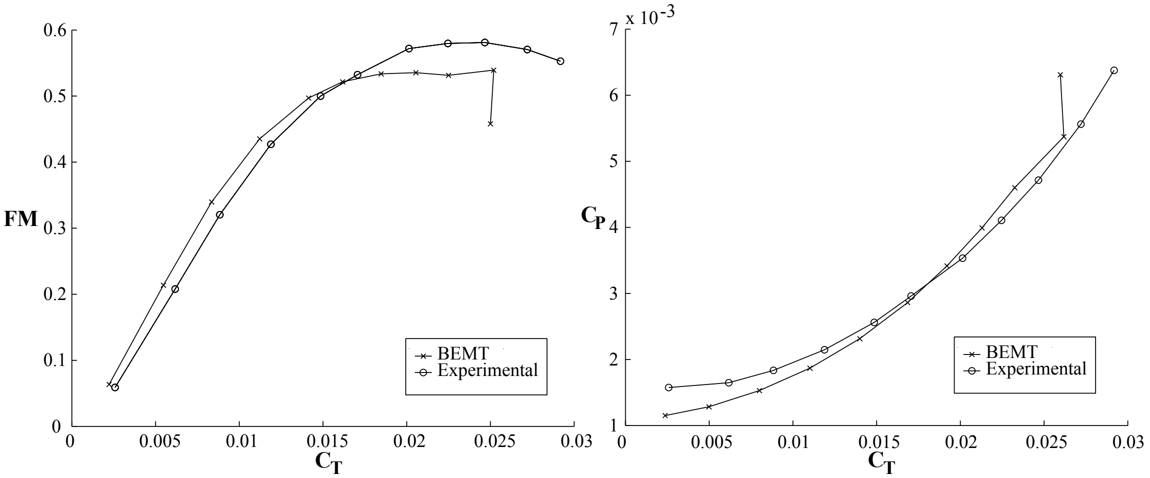

Figure 5.9: Predicted and experimental C_T vs. FM and C_T vs C_P for rotor with 9% camber airfoils, elliptical leading edges at 2500 RPM.

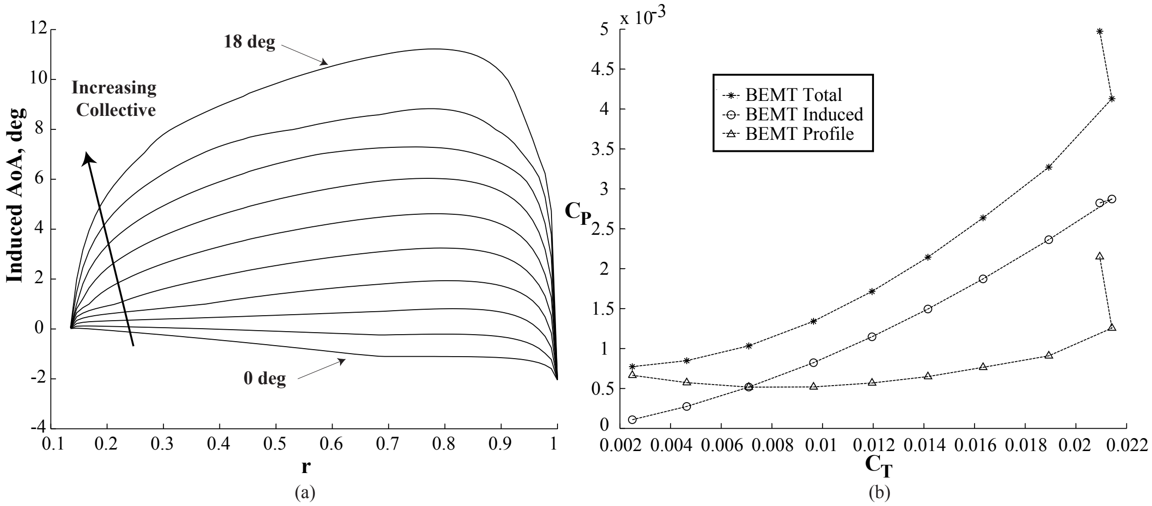

Figure 5.10: Induced angles of attack(a), and Induced and profile power components (b), at various collectives of a 6% camber rectangular blades.

range were airfoil lift coefficients are under-predicted.

From the experimental validation it can be concluded that for rotors having uniform airfoils with cambers of 6% and smaller, the BEMT-CFD model used provides reasonable performance estimates, being able to predict the thrust and power of the rotor within the experimental error at the operating points of interest, i.e in the vicinity of the maximum FM. Since experimental data for airfoils with intermediate camber between 6% and 9% was not obtained, it is not possible to evaluate the quality of the predictions for those airfoils, however results for the 9% camber airfoils show that in that range the predictive capabilities of the model degrade.

5.5.2 Rectangular Blades - Rotational Speed Effects

Using the rotor with 6% camber airfoils the rotational speed effects on the model results are explored. Since BEMT implementation is done using non dimensional coefficients, the effects of rotational speed on FM, which is also non-dimensional, can only be included through changes in the airfoil characteristics which depend on the local chord Reynolds number. Figure 5.11 shows C_T vs. FM , C_T vs. C_P, and the thrust vs. power loading predictions for the rotor with 6% camber at various rotational speeds. The Figures show how as rotational speed increases,hover efficiency in terms of FM increases, this is consistent with the experimental results of Chapter 2. Nevertheless, since rotational speeds are different for the cases considered, rotors are working at very different disk loadings, making FM comparisons meaningless. Power loading is a better performance metric for this case. The bottom plot of Figure 5.11 shows the experimental and calculated thrust vs. power loading curves. For all cases thrust was predicted over most of the collective range within the experimental error, except at the highest collectives ($\theta_0 \geq 16$) where variation is larger. Errors in the power loadings calculations are significant at the lower collectives, but in the range of interest -close to maximum FM condition- power loading predictions have errors in the order of 2%-5%.

A common practice used to simplify the analysis of rotors with rectangular blades is to assume constant sectional airfoil characteristics along the span. If the blades have a uniform airfoil, a representative blade section at 75% span is generally used. Using the BEMT model and the database generated in Chapter 4, the validity of that simplification can be easily asserted. Figure 5.12 compares The C_T vs. C_P plots of a rotor with 6% camber airfoils at 2500 RPM when the Re variation a long the span is modeled and when an equivalent section at 75% span is used. The differences observed are very small over the range of interest. Figures 5.13 (a) and (b) show the percentile differences in thrust and power coefficients at the different collectives. The resultant differences in FM are shown in Figure 5.13 (c). The results show that differences in FM predictions between 1% and 2% are obtained using the representative airfoil section approach. For a quick estimate of rotor performance CFD airfoil characteristics at a single Re could be used to do the calculations without a significant loss in accuracy. Nevertheless, this method can only be used with rotors having rectangular blades and a uniform airfoil along the span.

5.5.3 Rectangular Blades - Leading Edge Effects

Experimentally it was found that sharp leading edges improved the rotor performance by increasing maximum FM and by improving the rotor stall characteristics.

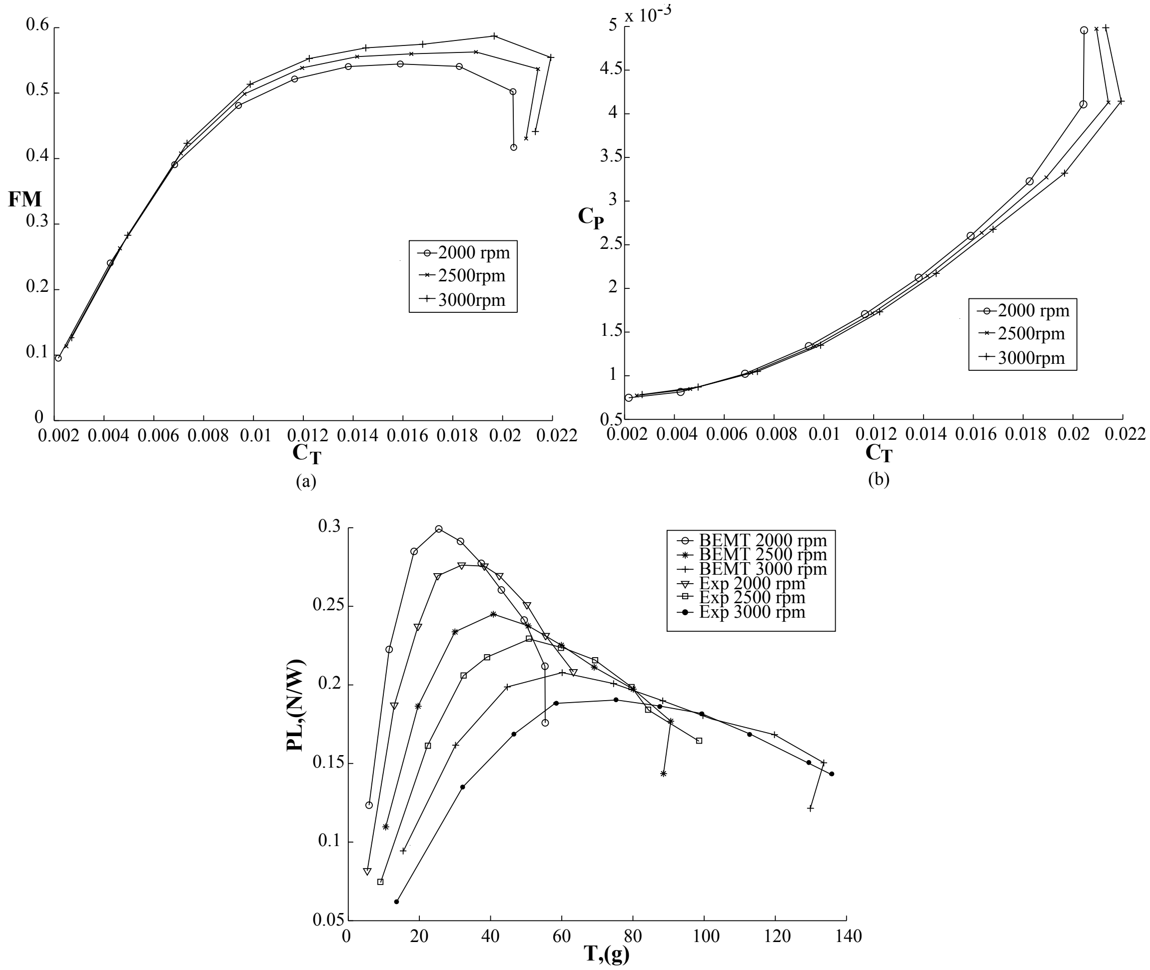

(a) (b)

(c)

Figure 5.11: C_T vs. FM, C_T vs C_P, and PL vs. T for rotor with 6% camber airfoils, elliptical leading edges at three different RPMs.

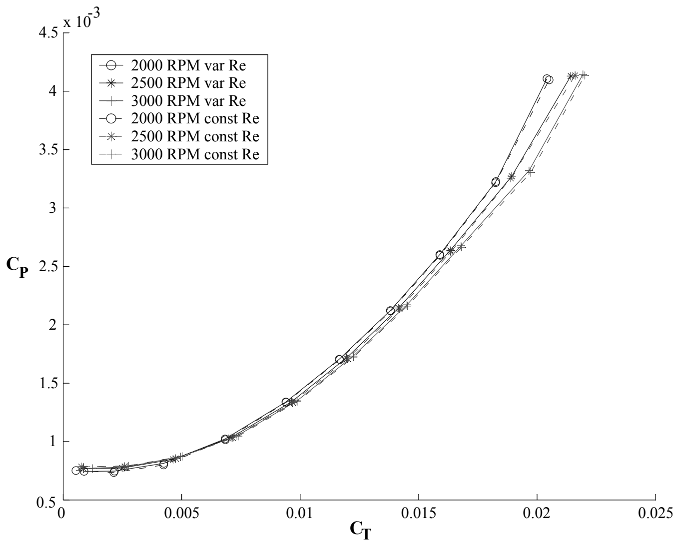

Figure 5.12: C_T vs. C_P considering Re change along span, and assuming constant Re of section at 75% span. Rotors with rectangular blades and 6% camber airfoils.

Up to this point, the BEMT model used only the database of airfoils with elliptical leading edges for the calculations. In this section the sharp leading edge airfoil database is used in a validation case in order to verify if the trends observed experimentally can be captured by the model.

Figure 5.14 shows the C_T vs. FM and the C_T vs. C_P plots of rotors with 6% camber airfoils at 2500 RPM. The figures show a trend that contradicts the experimental results presented in Chapter 2. The model predicts a reduction in maximum FM and an earlier rotor stall. The lower performance of the rotors with sharp leading edges is a result of higher power coefficients at the lower collectives and lower thrust levels at the higher collectives. Since rotor geometry and operating conditions are identical for the rotors compared, the performance differences are directly linked to the airfoil characteristics. In section 4.5.4 the effects of sharpening the leading edges at a Reynolds number of 60,000 were presented. Under those flow conditions, beneficial effects in the thrust coefficients were observed, obtaining in some cases an increase in maximum lift to drag ratio. However, at lower Reynolds numbers those benefits are no longer present, negatively affecting the airfoil performance. Figure 5.15 shows the sectional characteristics at Re=30,000 for a 6%

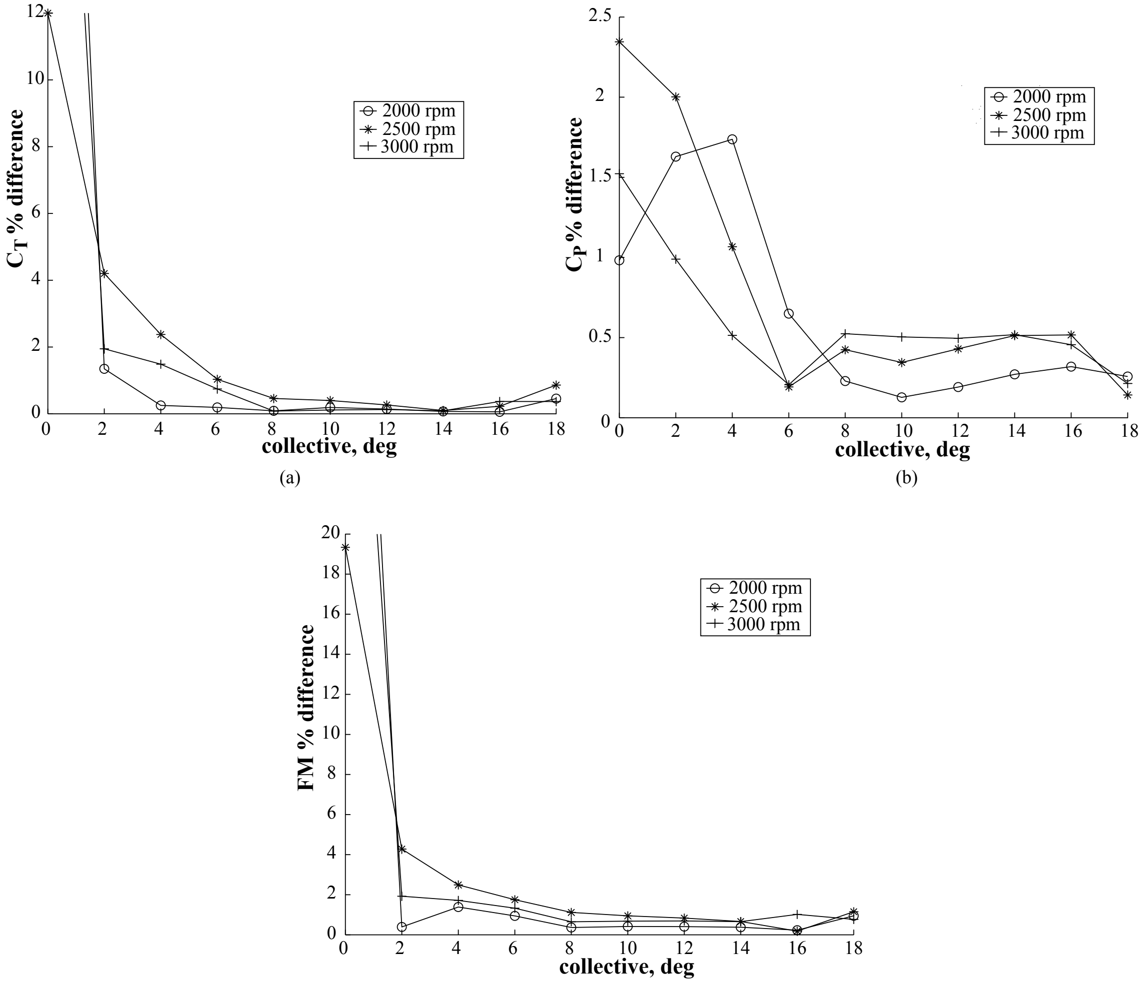

(a)

(b)

(c)

Figure 5.13: Percentile difference in C_T, C_P, and FM, when Re change along span is modeled, and when constant Re of section at 75% span is used. Rotors with rectangular blades and 6% camber airfoils

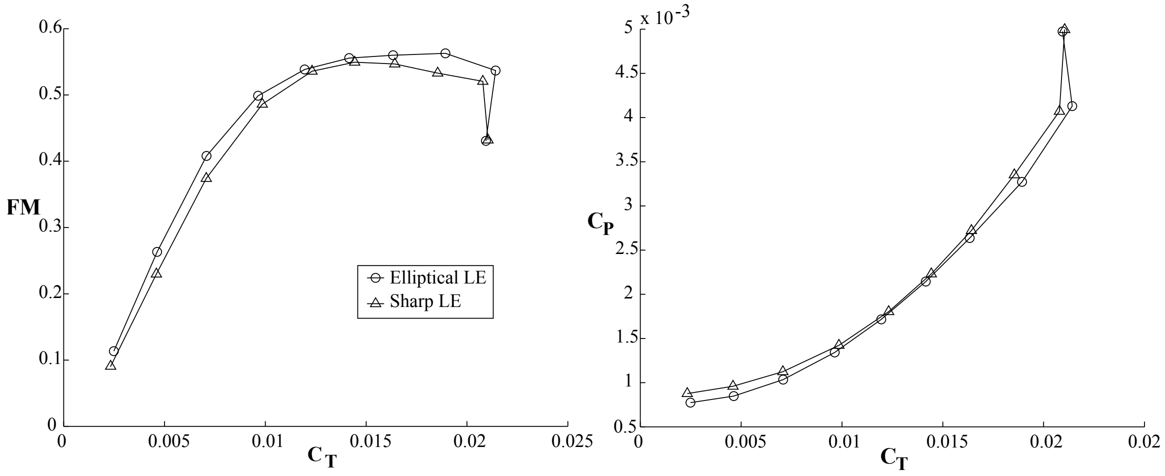

Figure 5.14: C_T vs. FM and C_T vs.C_P for rotors with 6% camber, sharp and elliptical leading edges, 2500 RPM, Tip Re≈43000.

camber airfoils with sharp and elliptical leading edges. These airfoil characteristics are very close to the operating conditions of the representative 75% span section that has a Re of 32700 at 2500 RPM. The figure shows that the overshoot in lift coefficient that occurs at an angle of attack of 8 deg with elliptical leading edges disappears in the sharp leading edge case. Additionally, there is an increase in drag coefficient that results in a reduction in lift to drag ratio over the range of 4 deg to 9 deg angle of attack. From these results it can be concluded that the sharp leading edge database generated in Chapter 4 does not provide reliable airfoil data for the implementation of the BEMT model. Even though general airfoil behavior at a Reynolds number of 60,000 showed the expected trends, the database as a whole seems to have fundamental problems. CFD methodology for that case should be reviewed, it may be possible that a time accurate solution needs to be implemented since it is likely that transient phenomena are responsible for the benefits obtained in the rotor tests. Hence, only the airfoil database with elliptical leading edges is used in the analysis of non rectangular blades.

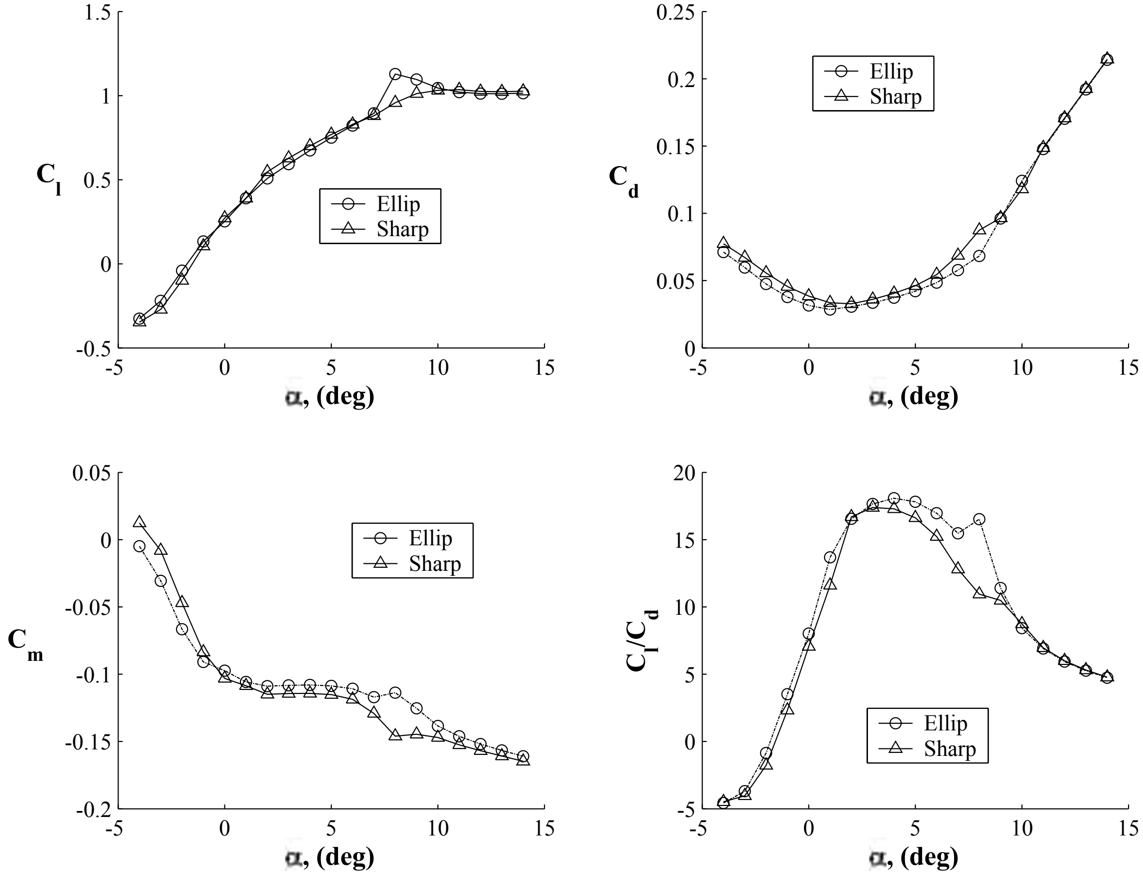

Figure 5.15: Comparison of sectional aerodynamic characteristics of 6% camber circular arcs with elliptical and sharp leading edges at Re=30,000.

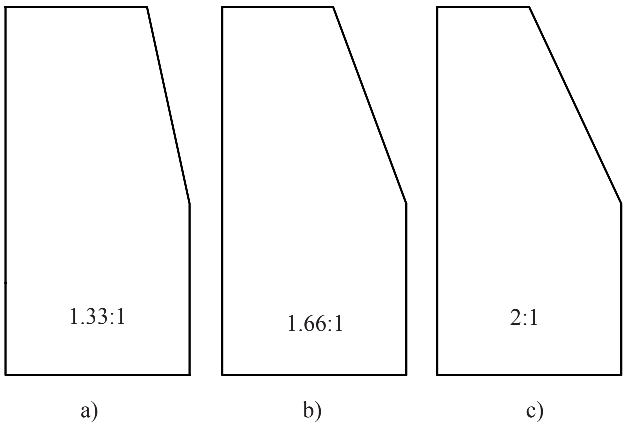

Figure 5.16: Linear taper with various ratios starting at 0.8R

5.5.4 Non-Rectangular Blades

In this section the model capability to predict the performance of rotors having non rectangular blades is evaluated. As explained in section 5.3 blade planform is coupled with spanwise twist and airfoil camber. Hence, for a single blade configuration the database needs be interpolated in four dimensions: Reynolds number, thickness ratio, camber, and angle of attack.

An initial validation with experimental results needs to be performed before exploring new configurations. Blades with a baseline airfoil camber of 6% with elliptical leading edges were tested having three taper ratios: 1.33:1, 1.66:1, and 2:1. The taper radial start location was set at 0.8 R and material was removed only from the trailing edges, producing fully asymmetric tapers as shown in Figure 5.16. Experimental and model results at a rotational speed of 3000 RPM are presented in Figure 5.17(a) and (b). The values plotted correspond to collectives that range from 6deg to 18 deg. Figure 5.18 compares in the same figure experimental and predicted values for a selected case. The model is able to predict the following trends observed experimentally:

- As taper ratio is increased thrust coefficients are reduced. Accuracy of the predictions is similar to the ones obtained with rectangular blades.

- As taper ratio is increased maximum FM improves.
- The highest Figure of merit of the four configurations plotted is achieved with a 2:1 taper ratio.

The following differences between predictions and experiments are present:

- Maximum FM occurs experimentally at lower collectives.
- Experimental maximum FM values are higher than predicted. However, errors are relatively small, on the order of 2%.

The results obtained are encouraging and show that quantitative differences in performance that are present in the experiments are captured by the model. Nevertheless, as previously stated, inaccuracies in the airfoil database and some of BEMT assumptions limit the use of the current approach as a preliminary design tool. Experimental results may even be used to fine tune the model by introducing empirical corrections to the database.

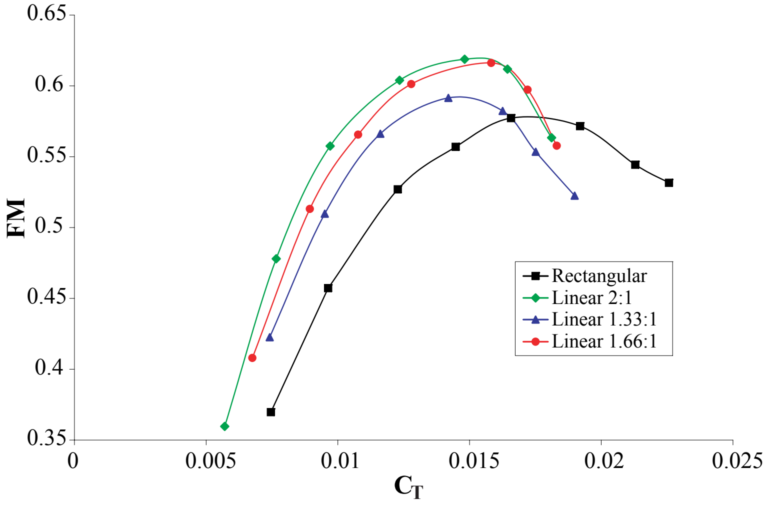

(a) Experimental C_T vs. FM

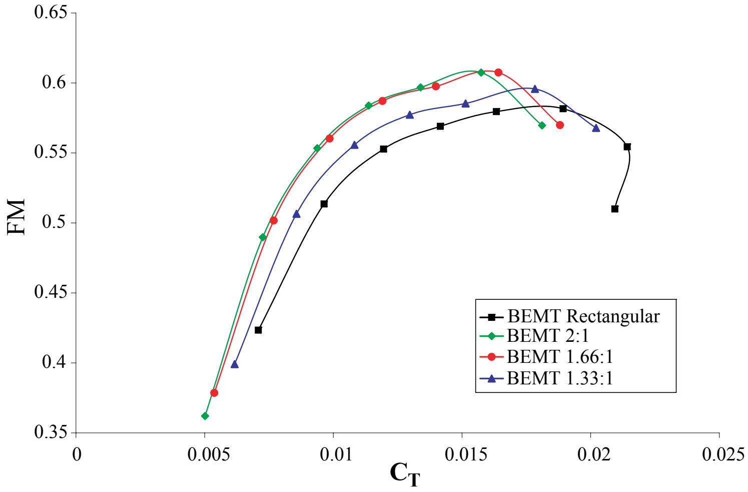

(b) Predicted C_T vs. FM

Figure 5.17: Experimental and predicted C_T vs. FM at 3000 RPM for rotors with various taper ratios on blades with baseline 6% camber airfoils, elliptical leading edges.

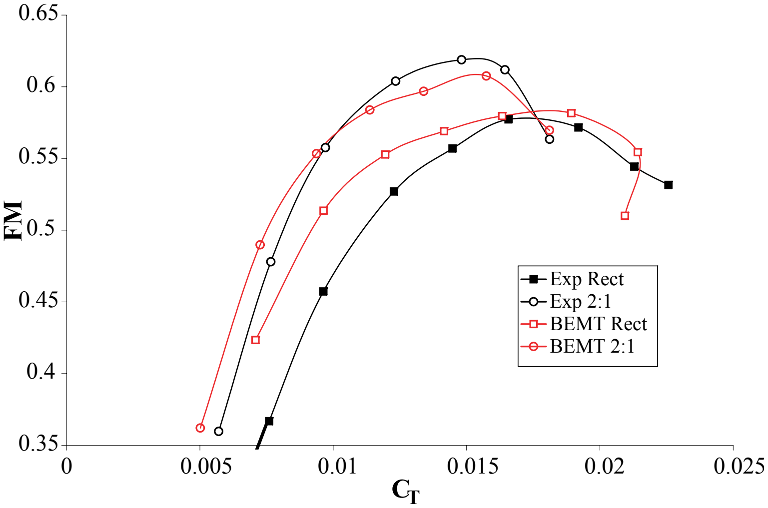

Figure 5.18: Experimental and predicted C_T vs. FM for rotors with rectangular and 2:1 tapered blades, baseline camber 6%

5.6 Blade Planform Optimization - Case Study -

In this section a simple grid search method is used to find the rotor planform with the highest maximum FM at 3000 RPM. Using a baseline rectangular Blade , airfoil camber and tip geometry were the only parameters explored. The design space was bounded by baseline cambers between 0% to 6%, a linear taper ratio that ranged from 1:1 to 2.33:1, and a taper start location from 0.75R to 0.9R. The taper offset, defined with respect to the rectangular blade's radial axis was also varied over its entire range. Figure 5.19 shows the geometric blade variables described.

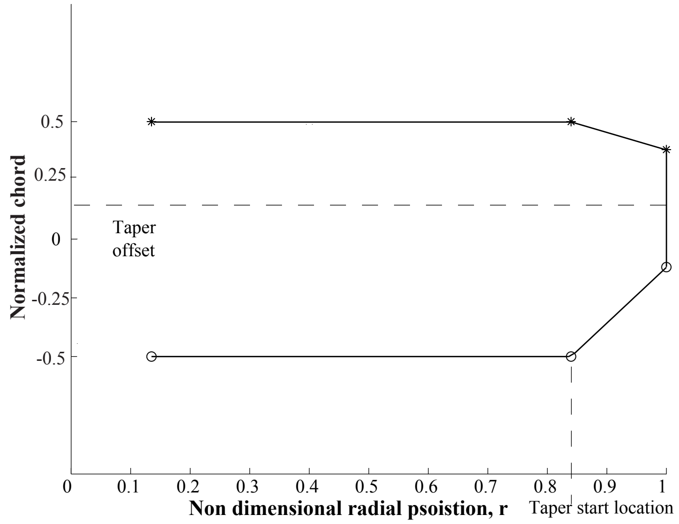

Figure 5.19: Blade planform parameters of sample optimization case.

The grid search was automated to find the collective pitch for maximum FM within 0.25 deg for each blade configuration. Local maximums were then compared to find the global maximum within the defined space. It was found that the highest FM equal to 0.6084 was obtained with a baseline 6% camber airfoils with a fully asymmetric 2:1 taper (only cutting the trailing edge) starting at 84% of the span. Even though differences between the different configurations are small, clear gradients are identified. For example Figures 5.20 (a)and (b) show how maximum FM changes with taper offset and taper radial start location for the optimal configuration found.

Additional trends were identified by plotting the results of the grid search.

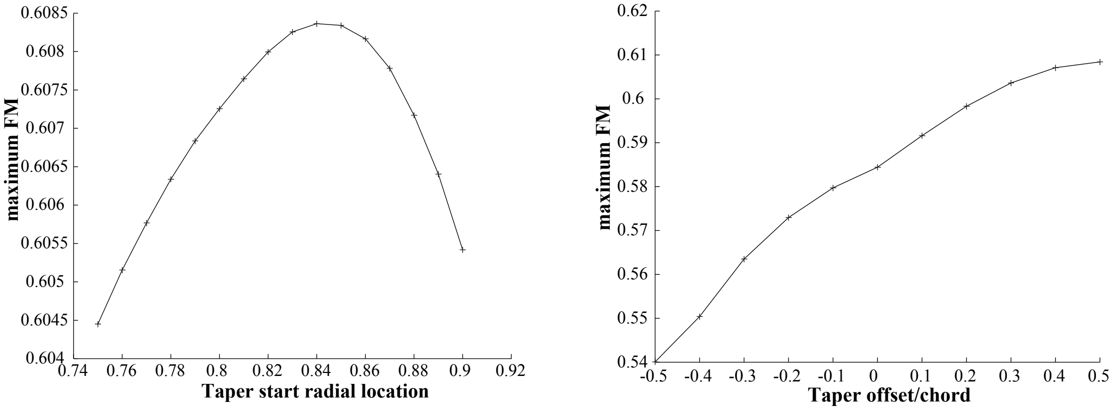

(a) FM vs. taper start radial location

(b) FM vs. taper offset

Figure 5.20: Variation of maximum FM with taper start location and taper offset for a 2:1 taper ratio on blades with 6% baseline camber airfoil.

An interesting observation present in the analytical and experimental results of this research is the dependency of the best taper start location with baseline camber. As airfoil camber is reduced the optimal planform shape converges to an almost rectangular blade when flat plates are used. For the blades with 6% camber airfoils and a 2:1 taper ratio the best performance was achieved with the taper starting at 0.84 R. This point moved gradually to 0.86R, 0.89R, and 0.97R for blades with cambers of 4.5%, 3% and 0% respectively. Figure 5.21 shows these results.

The previous case study explored just a subset of the parameters that define the blade geometry and rotor operating conditions. The design space can be largely expanded by tapering the blade root in order to introduce positive twist, and by using a baseline rectangular conical section that has a camber distribution along the span as explained in section 5.3. Blade parameterization could be taken a step further by increasing the number of points that define the blade planform. Currently, the BEMT model implementation uses 80 radial sections along the span. The points that define the blade's leading and trailing edges could be splined, producing smooth blade planforms. An example of such approach is shown in Figure 5.22 were the chordwise position of 20 control points joined by Akima splines were used to define the blade's edge.

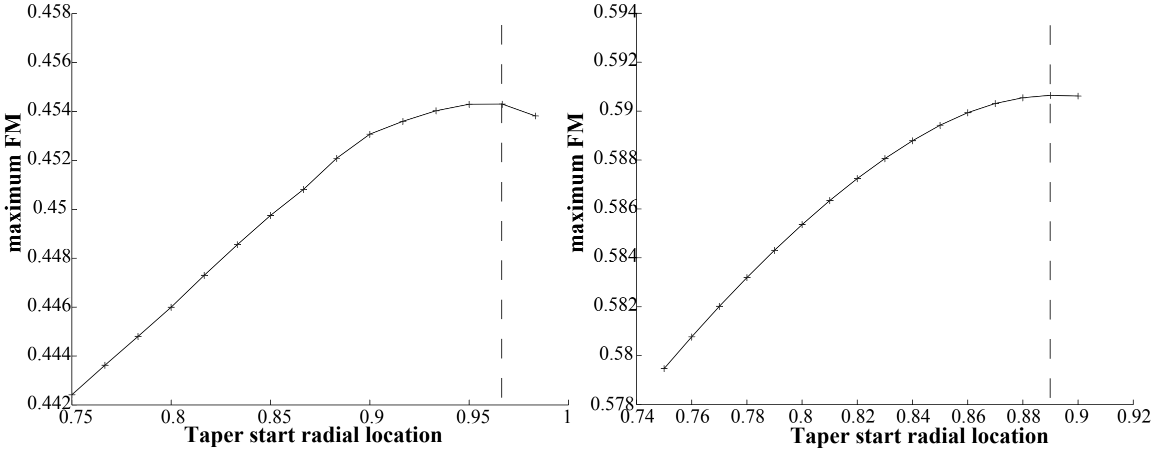

(a) 0 % camber

(a) 3 % camber

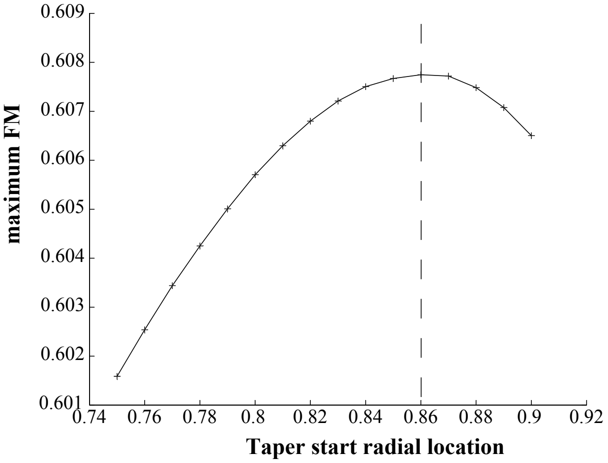

(a) 4.5 % camber

Figure 5.21: Variation of maximum FM with taper start location for a 2:1 taper ratio on blades with 0% 3% and 4.5% baseline camber airfoil.

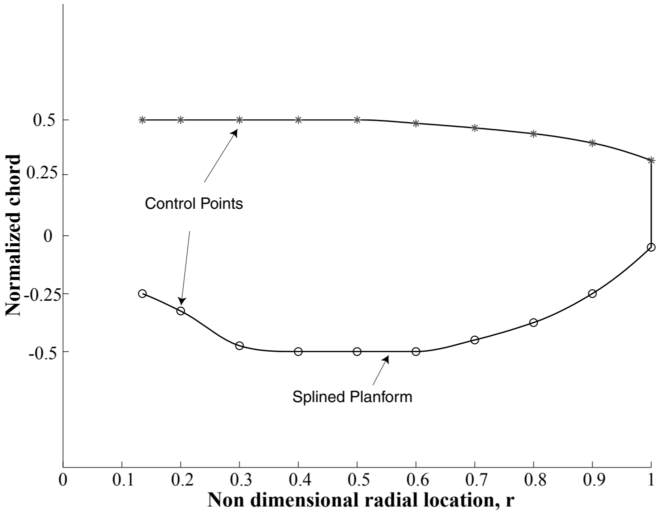

Figure 5.22: Blade planform defined by 20 control points and Akima splines.

However, model limitations and assumptions have to be taken into account. First of all the airfoil database needs to be refined by improving the CFD solution or by empirically correcting the values. Even though for the validation cases good qualitative and quantitative results were obtained, these represent only a fraction of the potential design space. Second, the blade geometries considered never diverged from the traditional shapes used in full-scale helicopters. Radically different geometries may have a strong effect on tip losses, possibly introducing large errors in the calculation of the inflow and producing misleading results. This is why the current research was limited to simple cases.

In spite of its limitations the model implemented is a valuable design tool. Reasonable estimates of power and thrust can be obtained for a wide range of rotor geometries and operating conditions in a fraction of the time it would take to perform an experiment or a 3D CFD simulation. Additionally, The computational cost of calculating the entire database is negligible when compared to fully 3D calculations. This makes the current approach ideal for preliminary vehicle design where basic configuration parameters need to be chosen prior to the fabrication of a prototype.

5.7 Summary

This chapter presented the methodology and validation of a rotor design tool that integrates a BEMT rotor model with a CFD calculated airfoil database. Using a blade parameterization that couples blade planform with spanwise twist and airfoil shape (restricted to circular arcs), the effect of geometric and operational parameters on hover performance were modeled. The approach was validated first on rectangular blades with uniform airfoils along the span having elliptical leading edges. The model was able to predict within the margins of experimental error the thrusts produced by the rotors below stall having cambers of 6% and smaller. However power predictions were not as satisfactory, agreeing with experimental results only over a limited collective range that corresponded to the regions where maximum FMs are achieved.

The effect of the spanwise Reynolds number variation was studied in rectangular blades. It was found that assuming representative airfoil characteristics corresponding to 75% span had a minor effect on the model results. However this method can only be applied in rectangular blades with uniform airfoils.

Errors in the CFD calculations are responsible in large part for the inaccuracies of the model. At lower collectives the underestimation of the drag coefficients by the CFD solver produced FMs that exceed the experimental values, and at higher collectives, when airfoils with cambers larger than 6% were used, early lift stall resulted in lower thrust and FM values.

The beneficial effects of using sharp leading edge airfoils were not captured by the model. Even though the right trends in airfoil sectional characteristics were present at Re = 60,000, at lower Re lift coefficients were underestimated producing inadequate rotor efficiency results. CFD methodology for the sharp edged airfoils needs to be reviewed and may need the use of time accurate solutions replacing the steady state assumption.

The model's predictive capability using non-rectangular blades was satisfactory. Planform changes followed the trends identified experimentally; however, similar difficulties as the ones observed with rectangular blades were faced. A simple case study that used a grid search algorithm to find the optimal blade configuration within a well defined design space was presented.

Chapter 6

Coaxial Rotor Performance and Vehicle Design

6.1 Introduction

The modeling and design of small-scale single isolated rotors has been addressed in the previous chapters of this document. Understanding the operational and geometric parameters that govern single rotor performance was a required step before looking into the issues involved in coaxial rotor design. This chapter shows the methodology and results of experiments designed to measure the hover performance of small-scale coaxial rotors, and extends BEMT to the coaxial rotor case. The last sections of the chapter discuss the implementation of a fully functional coaxial MAV. Subsystems design, integration and overall vehicle configuration are presented.

6.2 Experimental Setup

The hover test stand and data acquisition system used for single rotor tests and described in section 2.2 is a flexible system that can handle up to 16 input channels and 2 output channels. In the coaxial tests performed, the number of inputs channels increased by 3, adding to a total of 8. An additional output control signal was required to control the rotational speed of the second rotor. The input channels acquired the following signals:

- Coaxial thrust
- Coaxial torque
- Rotational speed upper rotor
- Rotational speed lower rotor

- Current upper rotor
- Voltage upper rotor
- Current lower rotor
- Voltage lower rotor

For a coaxial rotor system at zero torque condition measuring the aerodynamic power consumed by the system is not as straight forward as for a single rotor. The ideal approach would be to mount each rotors on independent transmissions each attached to thrust and torque sensors. This would allow to simultaneously measure the aerodynamic power required by each rotor and to determine the thrust distribution between rotors. However, this is difficult to implement and requires additional hardware that was not available at the time the experiments were performed. Another discarded option was to use the electrical power consumed by each rotor -each driven by a different motor- to calculate the torque. However, current consumption is a function of motor temperature, which changes constantly. It was finally decided to perform two sets of tests that would allow to determine the power and thrust of each rotor.

A first set of tests measured the total coaxial thrust, rotational speed, and electrical power consumption of each rotor. The key characteristic of this setup is that measurements are performed at a zero torque condition with a very small margin of error. The setup was designed as follows:

- Rotors were mounted inverted, directing their thrust toward the ground.
- Each rotor was driven by an independent motor.
- Rotors were attached to a single transmission on top of the test stand. The rotor assembly was free to rotate within a certain range due to a bearing at the bottom of the mounting stem.

- A rate gyro controlled the rotational speed of the upper rotor such that a stable zero torque condition is achieved (upper and lower locations are referenced to the flow, upper rotor is the one closer to the stand).

A second set of tests was used to measure the upper rotor thrust and torque, rotational speed and electrical power of both rotors. In this case measurement can be performed at any torque condition. The setup had the following characteristics:

- Rotors were mounted inverted, directing their thrust toward the ground.
- Each rotor was mounted on an independent transmission such that no torque can be transferred form one transmission to the other.
- Upper rotor is attached as a single rotor would be to the test stand.
- rotational speeds for zero torque conditions found in the first set of experiments are used to set the operating conditions in these tests.

The two test configurations are shown in Figure 6.1. In both cases rotor spacing can be changed from a minimum distance of a few mm up to 8 cm in the coaxial transmission. By combining the information provided by each setup the thrust and torque of upper and lower rotors at zero torque condition can be obtained. The details of this procedure are explained in a following sections.

6.3 Coaxial Tests Objectives

The main motivation of the tests performed is to determine the coaxial rotor parameters that affect hover efficiency. This information is crucial for the implementation of an efficient coaxial rotary wing MAV. The main questions to answer were:

- How does rotor spacing affect rotor performance at MAV scale.
- How should the collective pitch of rotors be set to maximize hover performance.
- What is the thrust distribution between rotors.

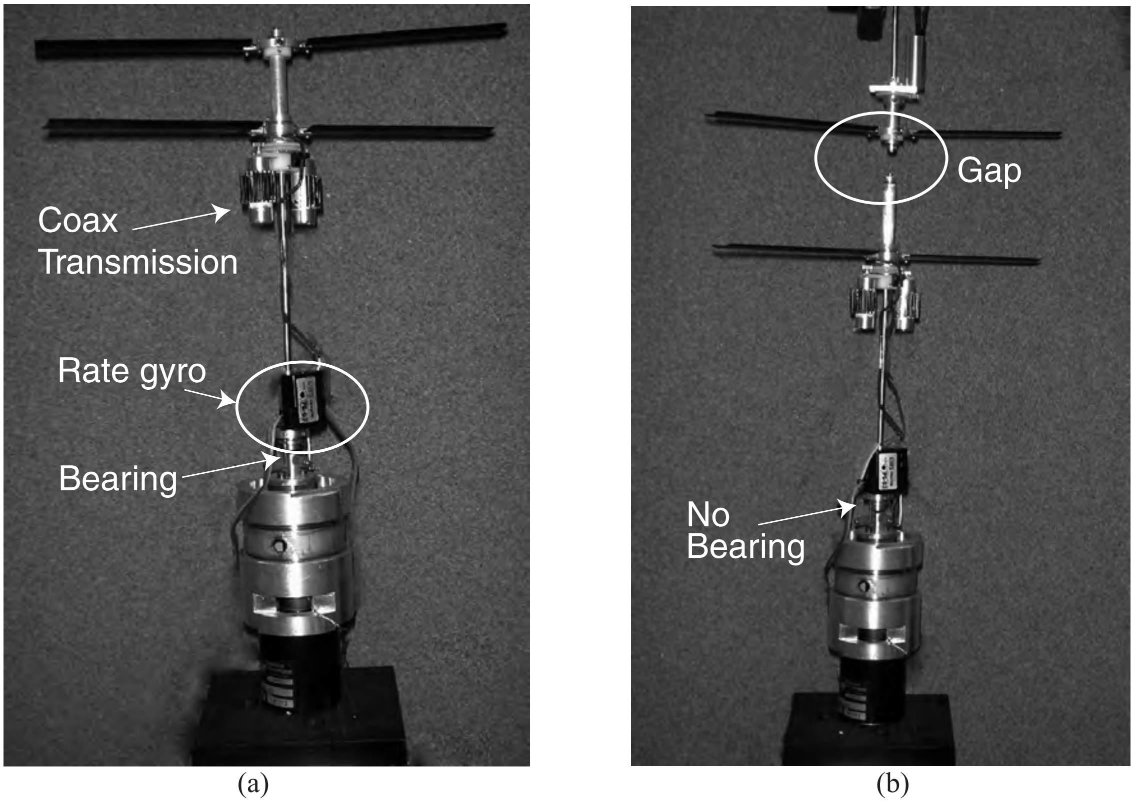

Figure 6.1: Coaxial experimental setups a) single coax transmission b) independent single rotor transmissions.

Upper Rotor Col. (deg)	lower Rotor Col. (deg)
16	14
16	15
16	16
16	17
16	18

Table 6.1: Test matrix for coaxial tests using 6% camber rectangular blades.

Radius	112 (mm)
Root cut-out	13.5% Radius
N_o of blades	2
Blade planform	rectangular
Blade chord	22.5 mm
solidity	0.1279

Table 6.2: Third generation rotor geometric characteristics

To answer these questions the following series of experiments were performed:

- Rotor spacing tests in coaxial transmission
- Rotor spacing tests in independent transmissions
- Hover performance tests on coaxial transmission with different collective pitch combinations over a range of rotational speeds.

6.4 Coaxial Test Results

This section presents the methodology and results of the various tests performed. Third generation rotors as defined in Table 2.3 with baseline blade chord of 22.5 mm were used in all the experiments. The results in this section correspond to the test matrix of Table 6.2, were the various collective pitch combinations for rectangular blades with 6% camber airfoils are specified.

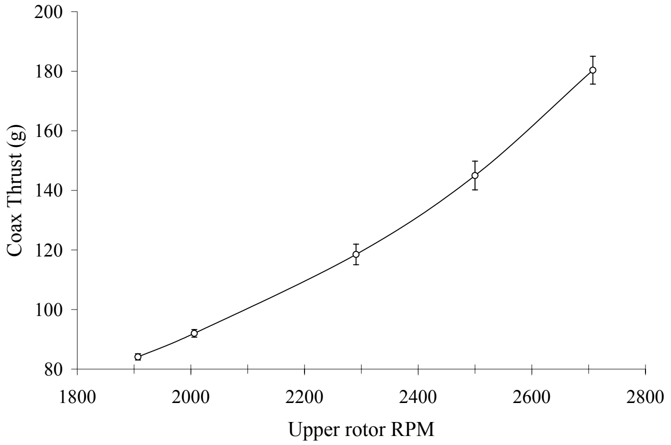

Figure 6.2: Average coaxial thrust at 6 different rotor separations vs. upper rotor rotational speed. Error bars cover 3 standard deviation, calculated using all data points at each spacing.

6.4.1 Rotor Spacing

Using the coaxial transmission (Setup (a) of Figure 6.1) rotor spacing was increased from 20 mm to 70 mm ($0.178 < h/R < 0.625$) keeping the zero torque condition. The upper and lower rotors were identical and had a rectangular blade planform. Results for the configurations of table 6.1 showed similar trends, this is why only a representative case corresponding to blades with upper and lower collectives of 16 deg is presented. Figure 6.2 shows the total coaxial thrust vs. the upper rotor's rotational speed. The plotted values correspond to the average thrust of all the values acquired at the six different rotor spacings, and the error bars cover three standard deviations of all the values at all the rotor spacings tested. Figure 6.3 shows the coaxial rotor thrust as function of the normalized rotor spacing h/R (where h is rotor spacing and R is the rotor radius). In these figures error bars extend for three standard deviations.

In these tests, upper rotor rotational speed was fixed, and the lower rotor speed was set such that the zero torque condition was achieved. Consistently it was observed that there was minimal or no need at all to retrim the system for the different rotor separations. In other words, torque required by each of the two

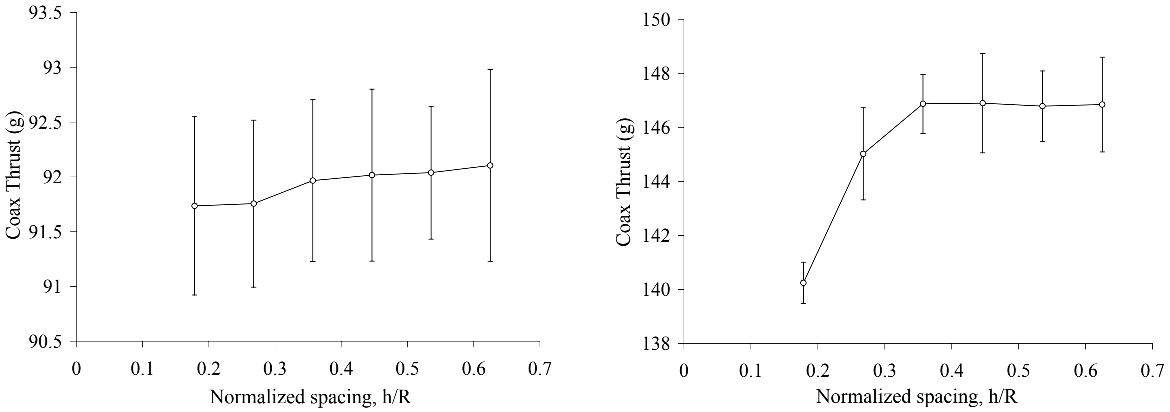

(a) Coax thrust vs. rotor spacing at 2000 RPM (b) Coax thrust vs. rotor spacing at 2500 RPM

Figure 6.3: Variation of coaxial thrust with rotor spacing for rectangular 6% camber blades. upper and lower collectives set at 16deg.

rotors did not change as rotor spacing was modified. However, small but measurable changes on the total rotor thrust occurred. At the lower thrust levels the average values were practically constant as shown in Figure 6.3(a); but at higher rotational speeds and disk loadings coaxial rotor thrust had a tendency to increase with rotor spacing as shown in Figure 6.3(b). The percentile variation of thrust with rotor spacing measured at the highest thrust was of the order of 5%. In general thrust values suffered minor changes beyond a rotor separation of 4 cm (h/R=0.357).

The main conclusion that can be drawn from the previous results is that rotor spacing has a limited effect on the coaxial rotor performance and is not a critical parameter that has a dramatic effect on performance. Only at small vertical separations, thrust reductions of about 5% occur. In order to maximize the performance of a coaxial system at the scale and thrust coefficients investigated, rotor separations should be equal or larger than h/R= 0.357 (4 cm). The following bullet list summarizes the trends observed:

- Reduced rotor spacing affects the coaxial rotor performance by reducing coaxial thrust.
- Percentile coaxial thrust reduction increases with disk loading.

- Beyond a certain rotor spacing coaxial thrust reduction stabilizes becoming independent of rotor separation.

6.4.2 Rotor Interaction

Now that the effects of rotor spacing have been quantified the interaction between rotors can be explored. Using the coaxial setup with separate transmissions shown in Figure 6.1(b) the variation in thrust and torque of the upper rotor (rotor attached to the test stand) as function of the lower rotor's operating conditions was measured. Rotational speeds were set based on tests performed on the single coaxial transmission and corresponded to a zero torque condition at a rotor separation of h/r=0.4464 (5cm). It was found that lower rotor had a negligible effect on the upper rotor. At the rotor separation studied changes in thrust and torque with respect to the single isolated rotor case were within the range of the experimental error (variations $< 2\%$). Hence it can assumed that the induced flow produced by the lower rotor at the upper rotor plane is not strong enough to produce measurable changes in the upper rotor performance. This is an important result that can be used to simplify the experimental characterization and design of coaxial rotors.

- Rotor design is simplified since upper rotors can be designed independently of lower rotors. A good performing single rotor will perform equally well in a coaxial setup.
- Experimentation is simplified since all the relevant upper and lower rotor parameters (thrust, power and efficiency) can be obtained by combining the information provided by single isolated rotor tests with tests on the coaxial transmission (Fig. 6.1(a)). Lower rotor thrust is obtained by subtracting the thrust of the isolated upper rotor to the total coaxial thrust, and lower rotor torque is equal in both rotors (zero torque condition).

The only obvious requirement to implement this approach is that operating conditions (collective, rotational speed) of the upper rotor in the isolated and coaxial tests

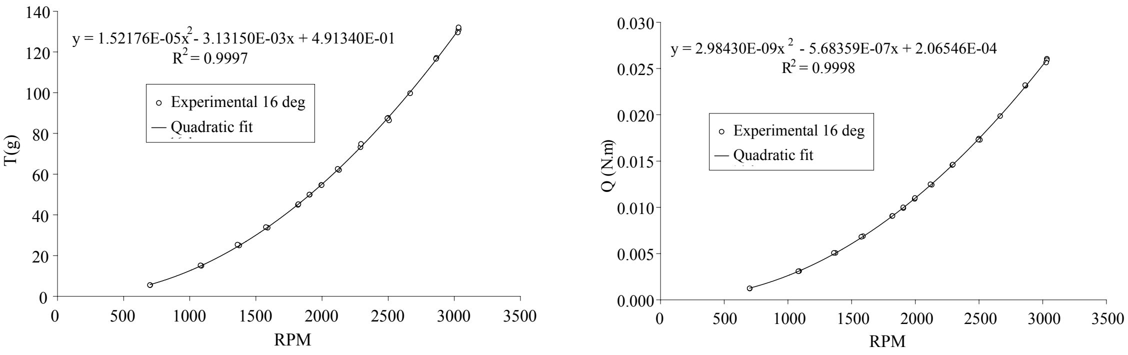

(a) Trust vs. RPM

(b) Torque vs RPM

Figure 6.4: Experimental thrust and torque vs. RPM of single rotor with rectangular blades and 6% camber airfoil with at 16 deg collective. Equations of best quadratic fit shown.

have to be identical. For a few cases this is not a problem, however if a coaxial rotor is to be characterized over a range of rotational speeds and collectives, the testing of the upper rotor becomes a very time consuming task. However, this can be avoided. For any rotor configuration thrust and torque are proportional to the square of the rotational speed (at a fixed collective). Hence, if at least three measurements of thrust and torque are available over a rotational speed range, a quadratic fit can be used to interpolate intermediate values with a very small margin of error. The coaxial tests performed covered rotational speeds roughly between 2000 and 3000 RPM, so single rotor tests at 2000 RPM, 2500 RPM, and 3000 RPM are sufficient to implement the proposed approach.

Figure 6.4 shows the experimental thrust and torque of a rotor with rectangular blades having 6% camber airfoils at a collective of 16 deg. Rotational speed was varied from 700 to 3000 RPM dividing the range in 30 intervals. The best quadratic fits are also plotted. The quadratic equations obtained were used for the calculations of lower rotor thrust and torque.

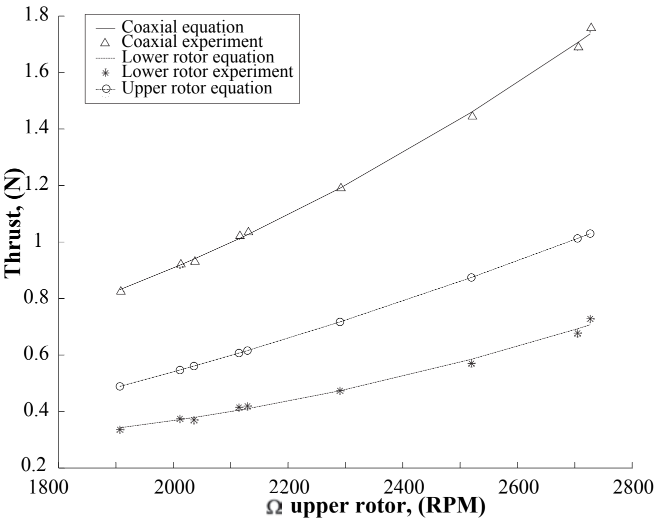

Figure 6.5: Thrust vs. Upper rotor rotational speed. Total, upper and lower rotor contributions shown. 6% camber airfoils, rectangular blades.

6.4.3 Rotor Load Sharing

Rotor load sharing as function of rotational speed can now be determined following the approach described in the previous section. Figure 6.5 shows the total coaxial thrust and the thrust components as function of the upper rotor's rotational speed. Collectives were set at 16 deg. The lower rotor thrust prediction can be obtained in two ways, as mentioned before by taking the difference of the coaxial and upper rotor fits (lines in the plot) or by directly subtracting the upper rotor lift prediction to the experimental coaxial thrust values, these are the asterisks in the plot.

It was found that over the entire range of rotational speeds and disk loadings, the upper rotor produced between 59% and 60% of the total thrust, this is shown in Figure 6.6. This result is consistent with full-scale helicopter characteristics where a load distribution of about 60% - 40% also occurs. For the other collective combinations tested (Table 6.1) similar results were obtained, upper rotor thrust contributions was consistently bounded between 59% and 61%.

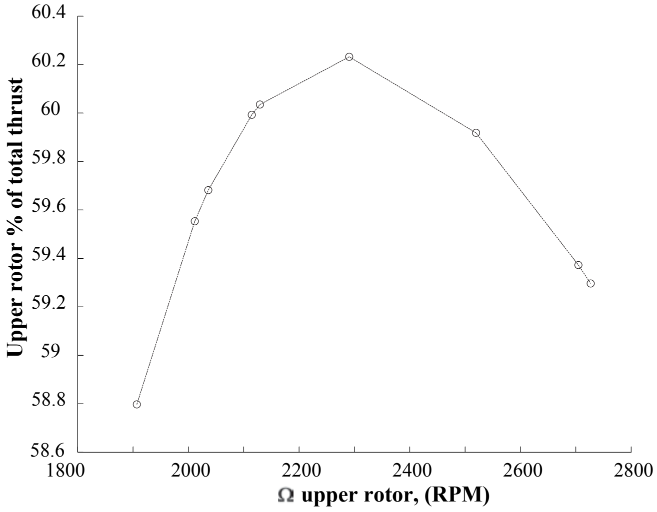

Figure 6.6: Upper rotor percentile contribution to total thrust. Collectives set at 16 deg.

6.5 Maximization of Power Loading in a Coaxial Rotor

The next question to address is the optimal collective setting that a coaxial rotor should have in order to maximize its power loading. Sunada in Ref. [44] addressed that problem and found that the thrust-torque ratio of a coaxial rotor at zero torque condition is maximized when both upper and lower rotors have the same rotational speed. Sunada performed his experiments at a fixed thrust, and his experimental variables were upper and lower collective pitch and rotational speeds. The experiments used small-scale rotors larger than the ones used in this investigation; however, Reynolds numbers were comparable. Sunada's conclusion was drawn at very specific operating conditions and with limited experimental data.

The experiments performed in the current investigation were used to verify how robust was Sunada's conclusion. Figure 6.7(a) shows the power loading vs. coaxial thrust for the different collective combinations of Table 6.1, and Figure 6.7(b) shows the percentile rotational speed difference between upper and lower rotor vs. coaxial thrust. The average rotational speed difference is a quantity that shows how dissimilar are the rotational speeds of upper an lower rotor. It is defined as the difference in rotational speeds ($\Omega_u - \Omega_l$) divided by the average rotational speed ($0.5(\Omega_u + \Omega_l)$) multiplied by 100 to obtain a percentage.

The results of Figure 6.7 show that the rotational speed difference is a function of the collective settings. When the upper rotor collective is the highest between the two rotors, the percentile rotational speed difference is negative ($\Omega_L > \Omega_U$), and when the lower rotor has the highest collective the situation reverses ($\Omega_L < \Omega_U$). When the two collectives are equal the differences in rotational speed are very small, changing signs depending on the thrust produced.

Power loading is also dependent on the collective settings and disk loadings. Figure 6.7(b) shows that the lowest power loadings occur when lower rotor collectives are smaller than the upper ones. In the coaxial thrust range of 1 N and 1.55 N, the configuration with upper 16 deg pitch and lower 18 deg pitch offers the best performance. For this case the percentile rotational speed differences are on the order of 8%, contradicting Sunada's conclusion. The results obtained showed that equal rotational speeds at a zero torque condition do not guarantee a maximization of the power loading. Differences in blade and airfoil geometries, rotational speed, Reynold number, and disk loadings affect the inflow distribution and wake structures, making very difficult to draw a general conclusion about the operating conditions that maximize the performance of a generic coaxial rotor.

The available experimental data can be used to answer a fundamental question: What is the penalty in terms of power of using a coaxial configuration instead of two side-by-side (tandem) rotors. The power loading of a coaxial rotor with upper and lower collectives set at 16 deg was compared to the power loading of a tandem system with identical rotor configuration. The tandem system is idealized as two isolated rotors not interacting with each other; hence its performance in terms of power loading vs. disk loading is the one of a single rotor. The results obtained are shown in Figure 6.8. Over the range of DL considered, the coaxial rotor has a power loading about 20% lower than the tandem system. Experimentally it was found that the upper rotor can be treated independently, hence the drop in PL is explained by the interaction of the lower rotor and the upper rotor's slipstream. The experiments were all performed at a zero torque condition, hence the drop in performance has to be linked to a reduction in thrust per unit power of the lower rotor. The next section addresses the use of momentum theory and BEMT applied to coaxial rotor systems.

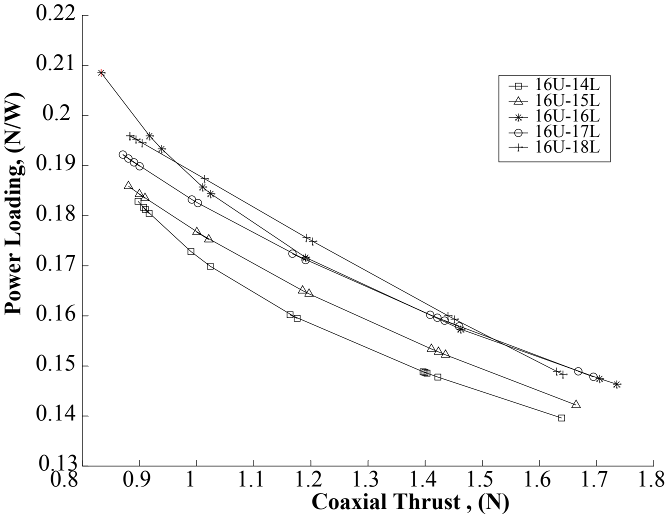

(a) Power loading vs. coaxial thrust.

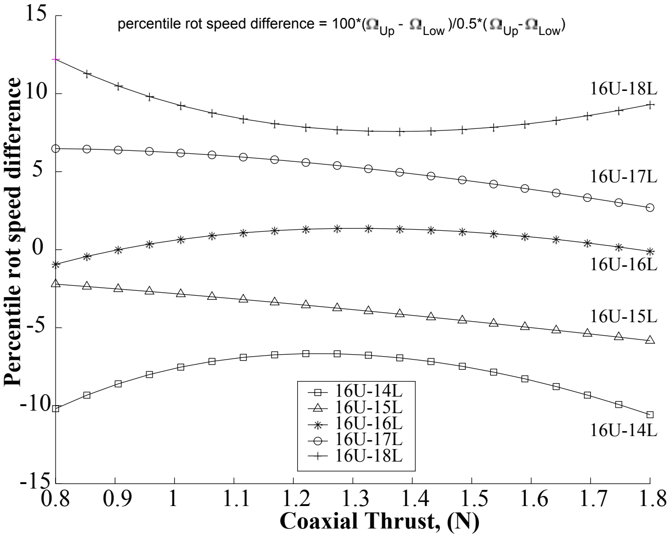

(b) Percentile rotational speed difference vs. coaxial thrust.

Figure 6.7: Power loading vs. coaxial thrust and percentile rotational speed difference vs. coaxial thrust, for the collective settings of Table 6.1

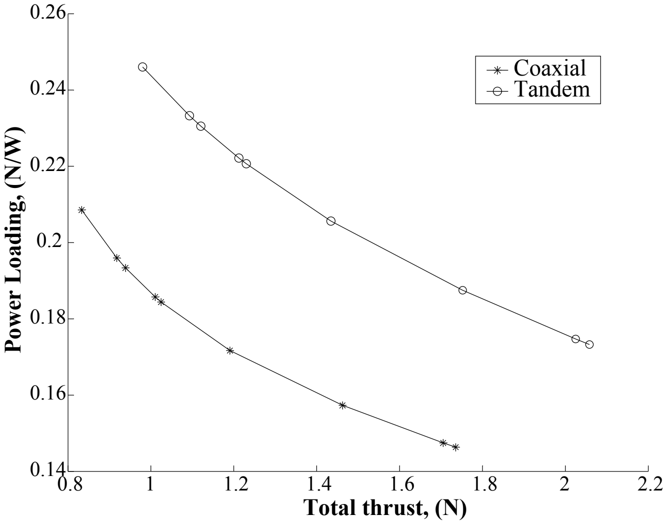

Figure 6.8: Power loading vs. thrust for coaxial and tandem systems

6.6 Modeling of a Coaxial Rotor

Momentum theory can be used to predict the performance of coaxial rotors using the flow model of Figure 6.9. In the diagram it is assumed that the rotor's vertical separation is large enough for the lower rotor to operate in the fully developed wake of the upper rotor. Under ideal flow conditions this would make the inner half area of the lower rotor to perceive an induced climb velocity.
Two cases can be considered in the analysis:

1. Load sharing of the rotors is equal i.e $T_{up} = T_{Low}$
2. Zero torque condition exists i.e. $Q_{up} = Q_{Low}$

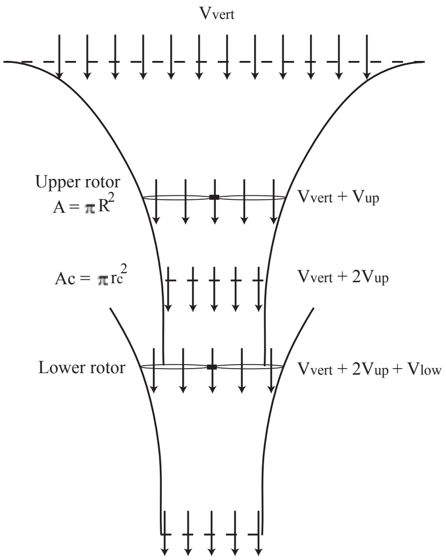

Figure 6.9: Flow model of a coaxial rotor operating in the fully developed wake of the upper rotor.

For case (1) momentum theory estimates an increase in induced power of 28%, while for the most realistic case (2) an increase of 22% is predicted. The interference-induced power factor k_{int} is defined as the ratio of the induced coaxial power by twice the induced power of a single isolated rotor:

$$K_{int} = \frac{(P_i)_{coax}}{(2P_i)_{isolated}} \tag{6.1}$$

Hence,for equally loaded rotors $k_{int} = 1.28$ and for balanced torque condition $k_{int} = 1.22$. This type of analysis assumes that the coaxial rotor operate as two isolated rotors with a mutually induced interference effect. Derivations of the previous results can be found in Ref. [49].

6.6.1 Blade Element Momentum Theory for a Coaxial Rotor

Momentum theory gives acceptable predictions for single and coaxial rotors at full-scale where profile power is obtained by using the airfoil's zero lift drag coefficient (C_{do}) and the induced power is calculated using induced power coefficients (κ=1.15 and $\kappa_{int} = 1.22 - 1.28$). However, as discussed in section 3.2.2, momentum theory is difficult to use for the types of rotors studied in the current research. Profile power calculations need to include the change in sectional drag coefficient with angle of attack, and induced power factors are highly dependent on rotor design.

The BEMT model presented in Chapter 5 can be extended to be used in coaxial systems. The upper rotor system is treated as a single isolated rotor, while the upper rotor's wake can be modeled as an apparent climb speed acting on the inner regions of the lower rotor. In order for the BEMT model to incorporate a climb or descent speed the discretized inflow equation (3.6) was re-derived from basic blade element (BET) and momentum theories as follows. The incremental thrust from momentum theory is given by:

$$dC_T = 4F\lambda(\lambda - \lambda_c)\, r\, dr. \tag{6.2}$$

Where F is Prandtl's tip loss factor, λ the inflow produced by the rotor, and λ_c is the inflow due to the climb speed. The incremental thrust from BET is given by:

$$dC_T = \frac{1}{2}\sigma\, C_l\, r^2\, dr \;=\; \frac{\sigma\, C_{l_\alpha}}{2}(\theta\, r^2 - \lambda r)\, dr. \tag{6.3}$$

Where σ is the solidity, C_l and C_{l_α} are respectively the lift coefficient and lift coefficient slope, θ is the collective, and r is the non-dimensionalized radial station.

Equating the incremental thrust coefficients from momentum and blade element theories:

$$\frac{\sigma\, C_{l_\alpha}}{2}(\theta\, r^2 - \lambda r)\, dr \;=\; 4F\lambda(\lambda - \lambda_c)\, r\, dr. \tag{6.4}$$

$$\lambda^2 \,+\, \left(\frac{\sigma C_{l_\alpha}}{8} \,-\, \lambda_c,\right)\lambda \,-\, \frac{\sigma C_{l_\alpha}}{8}\theta r \;=\; 0. \tag{6.5}$$

This is a quadratic equation in λ:

$$\lambda^2 \,+\, \left(\frac{\sigma C_{l_\alpha}}{8F} \,-\, \lambda_c,\right)\lambda \,-\, \frac{\sigma C_{l_\alpha}}{8F}\theta r \;=\; 0. \tag{6.6}$$

Solving for λ:

$$\lambda(r,\,\lambda_c) \;=\; \sqrt{\left(\frac{\sigma C_{l_\alpha}}{16F} \,-\, \frac{\lambda_c}{2}\right) \,+\, \frac{\sigma C_{l_\alpha}}{8F}\theta r} \,-\, \left(\frac{\sigma C_{l_\alpha}}{16F} \,-\, \frac{\lambda_c}{2}\right). \tag{6.7}$$

By solving Equation 6.7 the discrete inflow distribution along the span of a climbing rotor can be found. The lower rotor of a coaxial system is a special case since in hover it will perceive an apparent climb speed only in the region determined by the contraction ratio of the upper rotor's slipstream. Ideally a wake contraction $A/A_c = 2$ occurs (see Figure 6.9). In that case the average climb speed is two times the induced velocity at the upper rotor's plane (ν_{up}). However, in reality lower wake contractions are to be expected. For a general case the average speed in the streamtube can be defined as:

$$V_{up} = (A/Ac)\nu_{up} \;=\; (A/Ac)\sqrt{\frac{C_{Tup}}{2}}\,\Omega_{up}R. \tag{6.8}$$

For the hovering case λ_c is assumed equal to zero in the regions outside the upper rotor's streamtube. If that is not the case and the coaxial rotor has a vertical velocity, the climb velocity will have two components V_{vert} and V_{up}. In that case λ_c is calculated using simple superposition where necessary.

Since BEMT only provides the inflow at the rotor planes, the radial velocity distribution of the fully developed upper rotor's wake has to be prescribed. The simplest case is to assume a uniform distribution with a given contraction ratio based on the upper rotor's C_T. For the case studied the radius of the fully contracted upper rotor wake was set at 0.8R (A/Ac=1.56) instead of the ideal 0.707. This value was determined based on a simple wake characterization experiments were the vertical component of the velocity field of an isolated rotor was measured using a Pitot tube. Figure 6.10 shows a contour plot of a cross section of the velocity field below the rotor, and Figure 6.11 shows the normalized wake speed at two vertical locations. Both figures show that the wake boundary is in the vicinity of r=0.8.

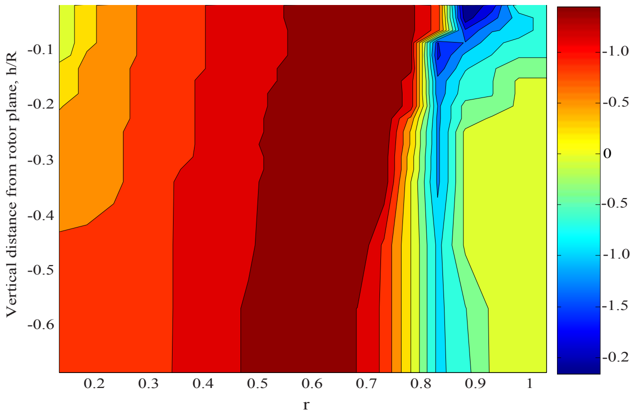

Figure 6.10: Contour plot of normalized wake velocities with respect to tip speed below single rotor plane. Collective at 16 deg, 2500 RPM.

The coaxial BEMT model was implemented and validated with the experimental data for a coaxial rotor with both upper and lower rotor collectives set at 16 deg. The BEMT calculations were run at five different trim conditions. For each case upper rotor speed was set to match experimental conditions, and the lower rotor speed was found by the code to obtain torque equilibrium. Upper and lower rotor calculations are shown in Figure 6.12. The predictions for the upper rotor thrust have and excellent agreement with the experiments. This is no surprise since it is treated in the model as an isolated rotor, a case already validated in Chapter 5. Lower rotor thrust and rotational speed predictions have larger margins of error but are still very good considering the simplicity of the approach. Figure 6.13 shows the percentile errors with respect to the experimental measurements of the lower rotor

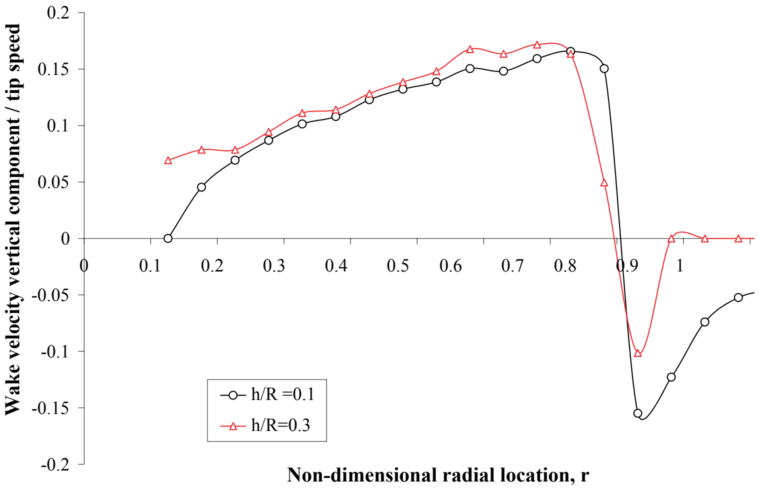

Figure 6.11: Radial position vs. normalized downwash velocities at two vertical locations.

thrust and rotational speed, and the total coaxial thrust. For the three parameters errors are below 5%. Lower rotor thrust was lower than the experimental values while its rotational speed was over predicted as a result of the under-estimation of the rotor torque. Lower power values are obtained for three main reasons:

- The airfoil characteristics from CFD under-predict the drag coefficients at the lower angles of attack. Since the interaction with the upper wake lowers the induced angles of attack over large regions of the lower rotor's blades, profile power will have a larger margin of error than for the isolated rotor case.
- Prandtl's tip loss function is used to account for the tip and root induced losses. However, there is no equivalent function to model the additional losses produced by the sudden change in inflow at the boundary of the upper rotor's wake on the lower rotor, hence induced losses are underestimated in that region.
- Lower rotor model predictions are dependent on the choice of the upper wake's velocity profile and contraction ratio. For the validation cases the assumption of a uniform wake velocity profile produced good results; however, contraction ratio had to be determined empirically. In order to completely eliminate

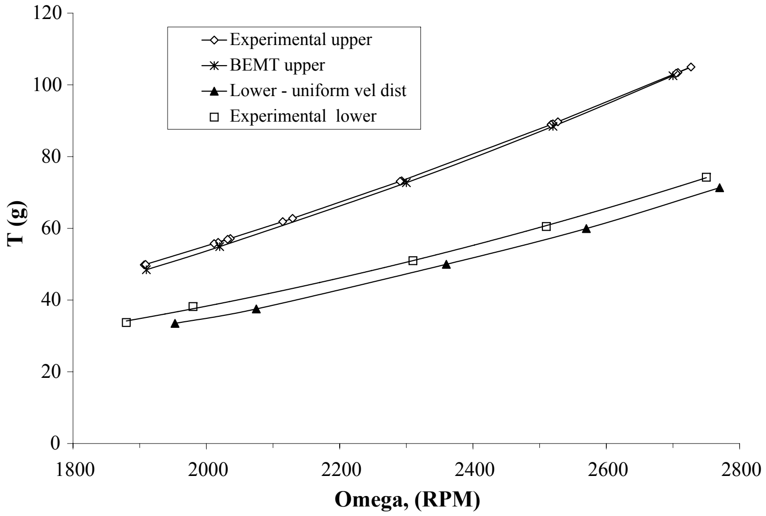

Figure 6.12: Thrust vs. rotational speed for upper and lower rotors. Experimental and BEMT results compared.

> the need of some type of wake characterization or visualization experiment higher order analytical tools such as free vortex modeling can be used as long as experimental validation is successful. Unfortunately, those tools were not available for the current research.

Figure 6.14 shows the non-dimensional inflow, thrust, and torque distribution in the spanwise direction for the upper and lower rotors. In the case shown, the balanced torque conditions was achieved with both rotors running at very similar speeds (2520 RPM upper, 2570 RPM lower), however the differences in thrust resulted in operating thrust coefficients of $C_{Tup} = 0.0205$ and $C_{Tlo} = 0.0134$. The effects of the upper wake and lower rotor interaction are evident from the spanwise thrust and power distributions (Fig 6.14(d) and 6.14(f)). At the boundary of the wake (r=0.8) a dramatic loss of lift and an increase in power occur. The relatively high upper rotor C_T, results in flow velocities large enough to produce negative induced angles of attack at the inner most lower rotor regions. Over the regions were negative lift is produced the inflow produced by the blades opposes the general flow direction, trying to increase the induced angles of attack. This explains the change of slope at r=0.45 of the lower rotor's inflow distribution in Figure 6.14(b).

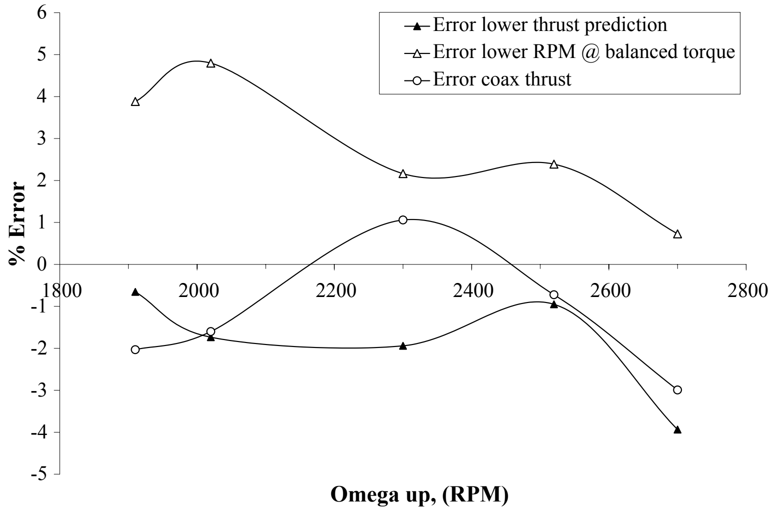

Figure 6.13: Percentile error vs upper rotor rotational speed for: lower rotor thrust,lower rotor rotational speed, and coaxial thrust.

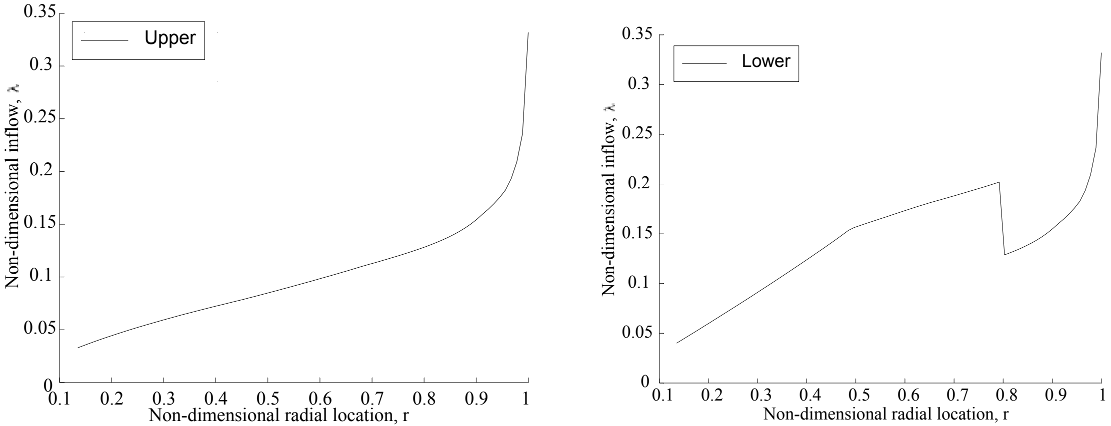

(a) Upper rotor - spanwise variation in inflow (b) Lower rotor - spanwise variation in inflow

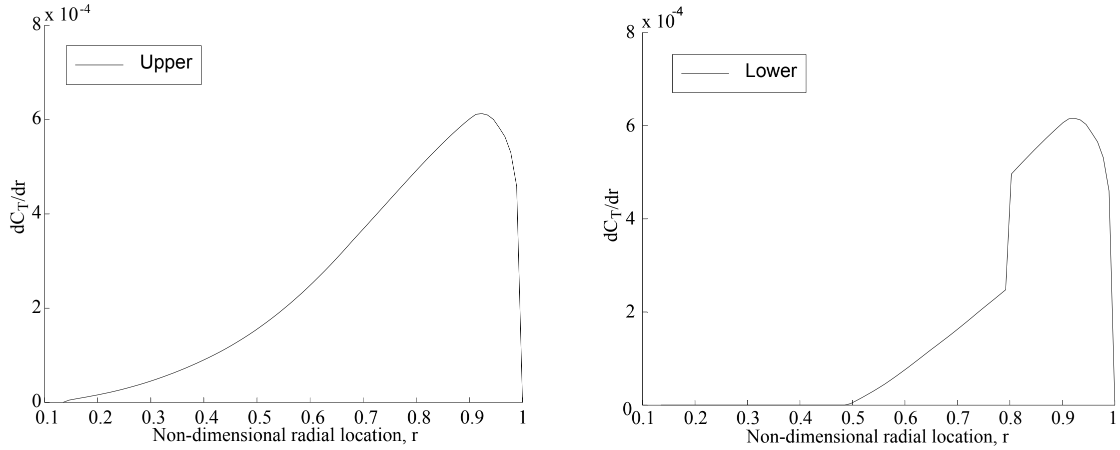

(c) Upper rotor - spanwise variation in thrust. (d) Lower rotor - spanwise variation in thrust.

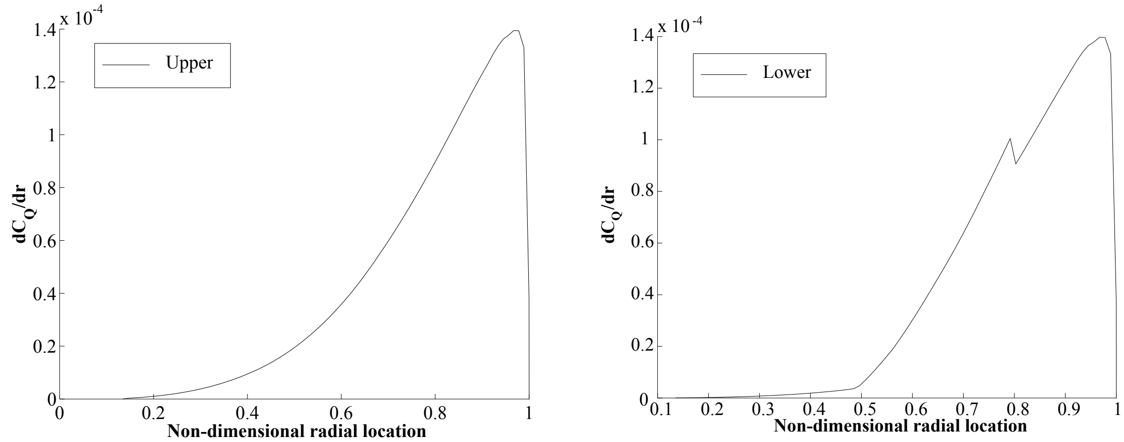

(e) Upper rotor - spanwise variation in torque. (f) Lower rotor - spanwise variation in torque.

Figure 6.14: BEMT predictions for spanwise variation in inflow and thrust for upper and lower rotors.

Considering the low computational cost and the simplifications employed, the results obtained are very encouraging and show that at least for rectangular bladed rotors thrust and power predictions are sufficiently accurate for the model to be used as a design tool. Lower rotor design is an aspect that can potentially benefit the overall system efficiency. This is a problem that has been largely overlooked for the longest time, and in general experimental and analytical coaxial studies have been consistently performed using identical upper and lower blade designs. Only over the last few years this problem has been addressed in Refs. [86] and [49]. Both publications use BEMT to show that lower rotor twist distribution can be tailored to improve its efficiency. Reference [49] goes a step beyond and under idealized flow conditions solves the BEMT equations to design the optimal twist distribution that satisfies the requirements for minimum induced and profile power (uniform inflow and all blade sections operating at maximum L/D ratio). At low Reynolds numbers the highly viscous flows and very non-linear airfoil behavior is expected to have a noticeable effect on an optimal twist distribution. Even tough the same fundamental principles apply, a particular solution will be a function of the sectional airfoil characteristics and upper wake topology.

A possible approach to find an improved lower rotor design for coaxial MAVs is to perform a parametric blade planform study similar to the one used on the single isolated rotor of section 5.6. Arbitrary twist distributions can be easily specified and root blade can be tapered in order to introduce positive twist to reduce the losses at the inner rotor regions. The results obtained need to be experimentally validated to assess the need of higher order wake modeling tools considering the uncertainty in the upper rotor wake characteristics.

6.7 Vehicle Design and Integration

This section presents the design process an issues considered in the development of fully functional rotary wing MAV.

6.7.1 Design Requirements

At the time the work that led to the results presented in this dissertation was initiated back in 1999, MAVs were a fairly new concept which design requirements were set arbitrarily by DARPA. The size, weight and functionality that were sought required a leap in the understanding of the physics involved and large improvements in the performance of all the vehicle's subsystems. Basic DARPA design requirements addressed mainly the vehicle dimensions, weight, and endurance; however, only vague mission scenarios were specified and there were no restrictions on vehicle configurations. The unique characteristics of a rotary wing vehicles seemed like a good match for a wide variety of missions. Rotary wing vehicles are currently the only configuration that can takeoff and land vertically, fly indoors and outdoors, hover and navigate in cluttered spaces at low forward speeds. Research in flapping-wing configuration has been motivated by the idea of matching these strengths without sacrificing good forward flight performance. Progress in that area has been slow due to the difficult aerodynamics and the high mechanical complexity. Rotary wing vehicle's poor forward flight performance limits its use to missions where hover and slow forward flight account for most of the mission duration It was anticipated that, in a situation where the target is far from the point of origin, an external delivery method (e.g. a mothership UAV or large scale munition) might be employed to transport the MAV. In order to facilitate delivery, the vehicle must be compactly packaged and able to withstand high g-loading.

6.7.2 Concept Selection

In order to select a configuration for the vehicle, different concepts were systematically compared. Selection was made based on the criteria listed below:

- Hover efficiency
- Compactness of stored/transported vehicle
- Ease of payload packaging

- Simplicity of structure
- Controllability
- Maneuverability

The configurations considered can be broken into four categories: single rotor, twin rotor, multi-rotor, and hybrid helicopter.

Single rotor configurations. These are conventional main rotor/tail rotor, rotors with vanes in the slipstream for providing anti-torque, and tip-jet driven rotors. The first two of these configurations have been successfully tested for UAVs and MAVs. The conventional main rotor/tail rotor design provides good aerodynamic efficiency and has good controllability and maneuverability. However, compactness in folding is adversely affected by the tail boom and comparatively a large rotor size is required. The tail rotor introduces additional power requirements that can be avoided using other designs. Vanes in the wake of the rotor working as antitorque devices are an aerodynamically clean option that offers an excellent hover performance (Ref. [36]). The use of vanes as antitorque devices can be complemented with a duct to have a further improvement in hover performance; however, forward flight characteristics and compactness are adversely affected by the large wetted area of the vanes and duct. Structural weight is also a concern since the vanes and/or duct have to be stiff enough to avoid any dynamic instabilities which may lead to overly heavy system, negating the aerodynamic gains achieved. Finally, tip-jets are attractive for their simplicity and ease of payload packaging as a result of the absence of a powerplant inside the fuselage. However, they have the drawback of poor controllability due to the high blade inertia.

Twin rotor configurations. Three twin rotor configurations were considered: coaxials, tandems and ducted coaxial configurations. The coaxial design is favored by most of the key design criteria: compactness of folding, simplicity of structure and ease of packaging. Tandem configurations have a hover efficiency higher than that of a coaxial design because of the the smaller interference effects between rotors. However, compactness and the difficulty of folding are among their key drawbacks.

Ducted coaxial designs are well suited for MAVs, but have significant compactness problems since shrouds and ducts cannot be stored efficiently. A ducted coaxial configuration has been widely used for UAV design, for which Sikorsky's Cypher and Cypher II are good examples (Ref. [87]).

Multi-rotor configurations. Recently, there has been an interest in the rotorcraft industry in designing rotorcraft with four or more lifting rotors. Such configurations could be controlled by varying the RPM of different rotors to change the direction of the thrust vector. Some small scale examples include the Mesicopter (Ref. [31]), the Gyronsaucer and the Roswell Flyer. The last two are commercially available RC helicopters and are reported to have very good controllability. The Mesicopter, a meso-scale flying machine which is no larger than a penny, is still in the development stage. A quad rotor design can have good hover efficiency as well as good handling and control characteristics. However motor efficiency can be an issue. In order to avoid a complex transmission instead of having a single power plant each rotor is driven independently by a motor. Higher percentile power plant weight and lower motor efficiency levels are to be expected, adding this to the obvious compactness problems makes the multi-rotor configurations a non-ideal choice.

Hybrid helicopter configurations. The candidates in the compound helicopter category are rotor-wing or stopped rotor, tilt-rotor, tilt-wing. All these designs prove difficult to achieve a compact stored/transported state because of the large size of their lifting surfaces. And require complex mechanical and electronic systems to coordinate the transition between hover and forward flight. They are all well suited for payload packaging and also very effective in high-speed forward flight. However, since high speed forward flight is not a design priority these configurations are not suitable options.

From this qualitative assessment it can be concluded that the conventional single rotor/tail rotor configuration, the single rotor with vanes, and the coaxial design, are the best candidates for the present design problem. The coaxial configuration has the advantages of compactness of folding and ease of deployment while the conventional configurations is superior from a controllability view point. However, given the relative strength of the compactness requirement, the folding problems associated with the tail boom preclude its use. Hence, the final configuration chosen is that of a coaxial rotorcraft.

6.7.3 Vehicle Configuration

Several iterations were necessary until all issues of the vehicle design were properly solved. Vehicle configuration and performance evolved and improved as the aerodynamic research presented in the previous chapters provided the answers to basic design questions. Rotor and swashplate design were the subsystems that underwent the most radical changes; however, general vehicle configuration and operation did not go through a fundamental transformation.

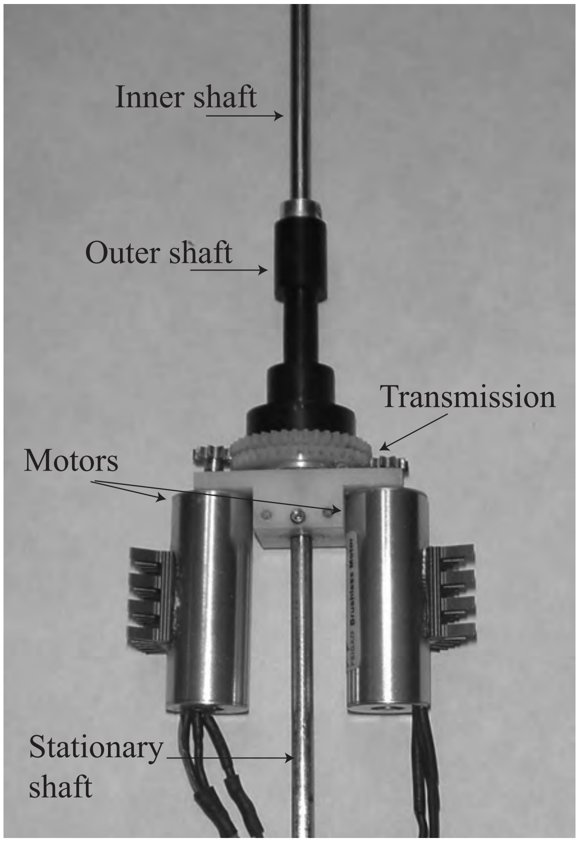

Figure 6.15: Current generation coaxial vehicle transmission design.

The basic core structure of the vehicle is a central stationary shaft from which transmission, motors, electronics, and battery packs are attached. Figure 6.15 shows a picture of the current generation design. Structure was kept at minimum and light materials such as plastic and carbon fiber composites were used where possible. Each rotor is driven by an independent motor, and a simple one-stage gear reduction is used as transmission. Each gear is attached to one of the coaxial shafts that drive the rotors. Friction is minimized by using small ball bearings. Batteries and electronics are at the bottom of the central shaft in order to have a center of gravity below the lower rotor. This is a key factor that largely determines the handling characteristics of the vehicle. Landing gear was manufactured out of carbon composite rods and served as support structure while protecting the rotors from collisions. Figure 6.16 shows a picture of the working prototype. Rotor diameter was set at 22 cm which corresponds to the third generation rotors studied in Chapter 2. The blades have a 6% baseline camber with a 2:1 linear asymmetric taper starting at 80% of the span. With a 22 cm rotor diameter vehicle hover endurance is about 10 min with a payload of 10 additional grams. Rotor diameter was set arbitrarily and can be easily changed without any hardware modifications to improve payload and endurance.

Five main subsystems were considered in the implementation of the coaxial vehicle:

- Propulsion
- Motor/transmission
- Lateral control system
- Electronics
- Power source

The total weight of the vehicle without batteries is 115 g, and depending on their capacity batteries add between 25g and 45g. Table 6.3 shows the vehicle's weight break down. Only propulsion and lateral control systems were designed from scratch, the other subsystems were carefully selected off-the-shelf products. The following sections discuss in more detail some of the vehicle's subsystems.

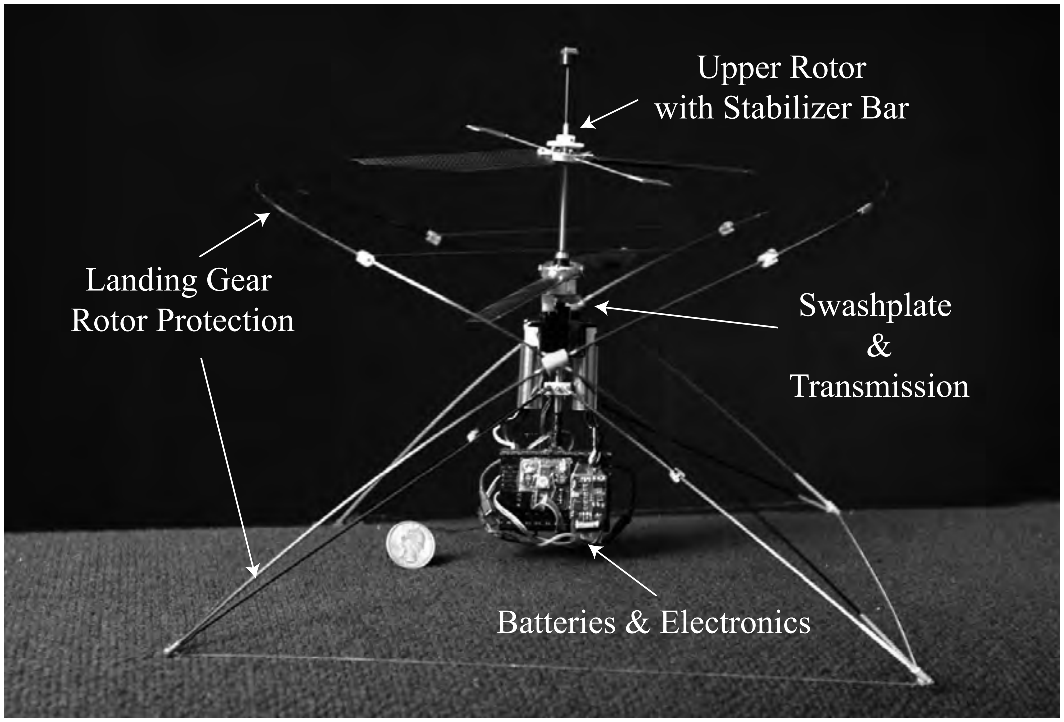

Figure 6.16: Coaxial MAV prototype.

6.7.4 Vehicle Control

A practical MAV must to be controlled in the three dimensional space without couplings that limit its functionality. This means that pitch, roll, altitude, and yaw have to be independent from each other. In order to achieve this the following configuration was used:

- Altitude is controlled by simultaneously increasing the rotational speed of the two rotors without affecting the heading. Hence there is no need to have collective pitch control in the rotors, which would have a huge weight and complexity penalty.
- Yaw is controlled by changing simultaneously the rotational speed of the two rotors. A torque imbalance in both directions can be achieved without a change in altitude if one rotor speeds up while the other slows down keeping total thrust constant.
- Pitch and roll are controlled by tilting the tip path plane of the lower rotor. A

Element	Mass (g)
Structure	34
Electronics	20
Motors	34
Stabilizer bar	4
Blades	4
Landing gear	9
Batteries 2 or 3 cell	24 - 36
Total Weight	129 - 141

Table 6.3: Coaxial vehicle weight breakdown.

swashplate that introduces a cyclic pitch input was custom designed for this purpose.

At the early stages of the project different control schemes were considered for the implementation of lateral control in the prototype. Some of the options considered were flaps in the downwash, a gimbaled transmission, thrust vectoring (using a ducted fan at the base of the vehicle), and a swashplate. At first the swashplate seemed prohibitive because of the mechanical complexity involved, especially considering the vehicles first generation had a three bladed rotors. Only after experimental studies identified the manufacturing and aerodynamic advantages of using two bladed rotors the vehicle design was changed; and two bladed rotors were adopted. With this new configuration the use of a swashplate became plausible.

Swashplate Configuration

The main advantage of having a two bladed rotor is that the cyclic pitch input of one bladed is exactly the opposite of the other. In addition, if a teetering two bladed rotor is considered rotor response will lag the cyclic pitch inputs by exactly 90 degrees. These two facts allow for great mechanical simplification. The swashplate was conceived keeping in mind three main considerations: weight, complexity and

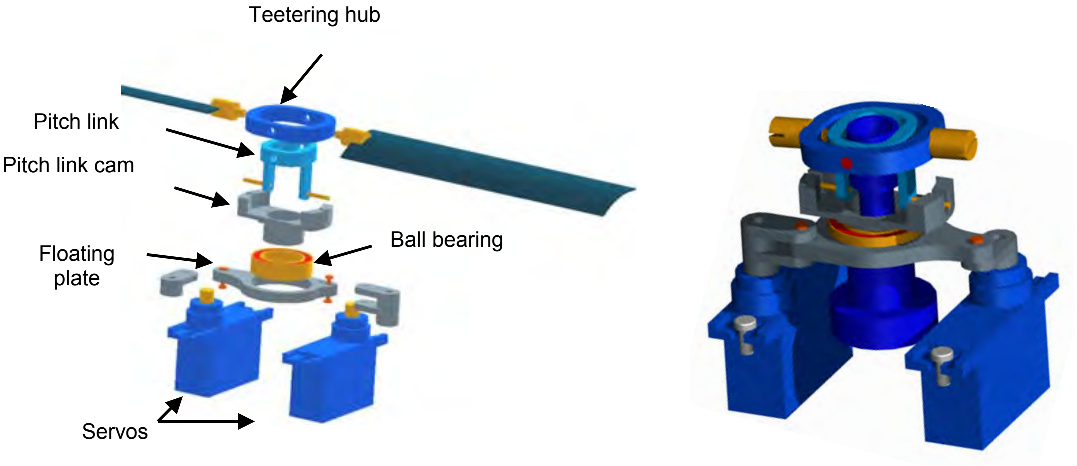

(a) Exploded view of the swashplate (b) Assembled swashplate

Figure 6.17: Exploded and assembled views of the custom designed swashplate.

robustness. Figure 6.17 shows an exploded view of the design, and Figure 6.19 shows a picture of the first working prototype manufactured. The swashplate controls only the lower rotor, and can introduce only a cyclic input to the blades. The design was inspired by the spider system shown in Figure 6.18 from Ref. [88]. The leading edges of the blades are connected to the legs of a "spider", which is connected in turn to the cyclic pitch control axle. This can be tilted about a central universal joint through the inputs of the stick in the cockpit. When the spider is tilted, the lower spider arm gives a minimum pitch to its blade, while a maximum pitch is given to the position diametrically opposite.

The swashplate consists of five main elements: a teetering hub that holds the blades, a pitch link, a pitch link cam, two servos, and a "floating plate" that holds a ball bearing. Since the vehicle is coaxial, the inner space of the mast is already being filled by the upper rotor shaft so only exterior components can be used. The U shaped part labeled *pitch link* in Figure 6.17(a) is hinged to the main shaft. The hub that holds the blades is hinged at 90 deg to the pitch link creating a universal joint. The pitch link arms have a steel pin that protrudes at the bottom on each side. These pins fit two slots in the pitch link cam. This assembly of elements is equivalent to the spider system shown above.

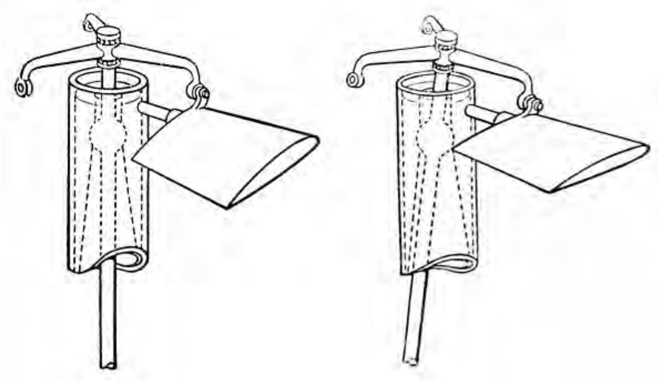

Figure 6.18: Spider system fir changing cyclic pitch from Ref. [88].

In this design, pitch inputs are not given with a vertical displacement as in a conventional swashplate. Instead, the servos move the floating plate that holds the ball bearing in the horizontal plane around the mast of the helicopter. Cyclic pitch input is given to the blades through the pitch link cam and is dependent on its azimuth angle and offset position with respect to the rotational axis of the rotors. Each of the two servos moves the floating plate in orthogonal axis on a plane perpendicular to the main shaft, giving almost uncoupled longitudinal and lateral cyclic inputs.

Swashplate Kinematics

The input to the swashplate is an angular deflection of the servos that will move the floating plate around the rotor mast. In order to have accurate control of the rotor response, it is required that the angular deflection of the servos for a given pitch input is as large as possible. In the current prototype maximum servo angular deflections are of the order of ± 5 deg, producing floating plate displacements of ± 1.5 mm on each axis.

Displacement of the floating plate will be translated in a displacement of the pitch link cam, which will drive back and forth (in the horizontal plane) the pitch link. The distance between the pitch link axis and the pins that fit in the pitch link cam is 8.5 mm. This yields a maximum pitch input of ± 10 deg. Maximum cyclic inputs are necessary only when aggressive maneuvering is required. In a conservative maneuver only half the cyclic input is used.

Design Considerations

The tip path plane of the lower rotor tilts 6 deg when a maximum cyclic input is given. This produces a lateral force at the hub of about 10% the lower rotor thrust. In order for the vehicle to pitch or roll in the direction the tip path plane tilts, the Center of Gravity (CG) of the vehicle has to be below the lower rotor. The side force rotor component multiplied by the hub-CG separation gives the total pitching/rolling moment. Location of the CG is about 10 mm below the lower hub when no batteries are on the vehicle. and with batteries depending on their capacity CG location ranges from 25 mm to 35 mm below the lower rotor hub. The moments produced are more than sufficient to control the vehicle in hover and in slow forward flight.

As was shown in a previous section rotor spacing has a very small influence on the aerodynamic efficiency of the coaxial rotor, however it needs to be carefully specified in order to avoid in-flight rotor collisions. The prototype has a teetering upper rotor that incorporates a Bell-type stabilizer bar that works as a flywheel. The stabilizer bar isolates the upper rotor from the fuselage motion, making the helicopter passively stable in hover. The pitch and roll stability of the helicopter depend in large part in the characteristics of the stabilizer bar. The two important parameters are the paddle's weight and their radial spacing. Increasing any of those two variables increases the vehicle's stability and reduces its maneuverability. No formal mathematical study was performed for the dynamic modeling of the rotor system and the stabilizer bar parameters were chosen based on flight testing in order to achieve a balance between stability and maneuverability. Reference [89] addresses the modeling form first principles and basic aerodynamics of a model helicopter that has a Bell-Hiller type stabilizer bar. The approach followed in that work can be used as a guide for the eventual dynamic modeling of the coaxial prototype.

Figure 6.19: Swashplate prototype.

6.7.5 Electronics

The vehicle used the following off-the-shelf electronics:

- A four channel RF receiver
- Two brushless speed controllers
- A rate gyro
- Two micro servos
- 2 or 3 cell LI-PO batteries

The four available receiver channels were used to control the two speed controllers and the two swashplate servos. In order to allow a pilot to fly the helicopter a programmable radio controller (Futaba 8UA) was used to mix the motor signals. In the controller the throttle stick changed simultaneously the rotational speed of both rotors keeping the vehicle in a trimmed zero torque condition. The yaw input differentially changed the speed of the rotors (increasing speed of one and reducing speed of the other) such that only a small variation in total thrust occurred. The rate gyro was used to stabilize yaw and was connected in line to the upper rotor control signal. The vehicle does not have a high-level control or stabilization system, and the pilot is in charge of manually compensating for perturbations. However, the vehicle has extremely good handling stability characteristics, which makes it easier to fly than a conventional RC helicopter. These characteristics are very desirable specially for the development and implementation of a control or stability augmentation system. The prototype is a very forgiving testbed for algorithms and hardware, which require extensive testing and fine tuning before they can be integrated to the vehicle.

Earlier prototypes used Lithium Ion batteries; however, their discharge rate was not large enough to efficiently power the vehicle. The commercialization of Lithium Polymer batteries with higher energy densities and much better discharge rates (up to 13C continuous) provided an energy source that is a better match for hovering MAVs. The vehicle can operate using a two cell or three cell battery packs providing respectively 7.4 V and 11.1 V. Batteries used had a nominal capacity of 560 mAh and weighted 12g per cell.

6.7.6 Powertrain - Rotor Matching

An important consideration in the design of any aerial vehicle is the choice and characteristics of the power plant. From airliners to MAVs not only the aerodynamic efficiency of the design determines its range payload and endurance, the motor/turbine/engine efficiency plays also a major role. For a rotor the relationship between thrust and power can be easily derived from momentum theory to explore the effects of aerodynamic and mechanical efficiency of the system. Starting from the definition of thrust and power:

$$T = C_T \, \rho \, A \, (\Omega \, R)^2 \qquad P = C_P \, \rho \, A \, (\Omega \, R)^3. \tag{6.9}$$

taking the ratio of

$$\frac{T^3}{P^2} = \frac{C_T^3\,\rho^3\,A^3\,(\Omega\,R)^6}{C_P^3\,\rho^2\,A^2\,(\Omega\,R)^6} = \frac{C_T^3}{C_P^2}\,\rho\,A. \tag{6.10}$$

Solving for the power

$$P = \frac{T^{3/2}}{\sqrt{\frac{C_T^3}{C_P^2}\,\rho\,\pi R^2}} = \frac{T^{3/2}}{R\,\sqrt{\rho\pi}\frac{C_T^{3/2}}{C_P}} \tag{6.11}$$

The inflow ratio λ_h is related to the thrust coefficient in hover by

$$\lambda_h = \frac{\nu_i}{\Omega R} = \sqrt{\frac{T}{2\,\rho\,A\,(\Omega R)^2}} = \sqrt{\frac{C_T}{2}}. \tag{6.12}$$

And the relationship between FM,λ_h, C_T, and C_P gives

$$FM = \frac{\lambda_h\,C_T}{C_P} = \frac{C_T^{3/2}}{\sqrt{2}C_P}. \tag{6.13}$$

Replacing Eq.6.13 into Eq.6.11

$$P = \frac{T^{3/2}}{R\sqrt{2\rho\pi}\,FM} \tag{6.14}$$

The compound powerplant-transmission efficiency η can be introduced in the equation

$$P = \frac{1}{\eta}\frac{T^{3/2}}{R\sqrt{2\rho\pi}\,FM} \tag{6.15}$$

Or solving for the thrust

$$T = (\eta P\,R\,\sqrt{2\rho\pi}\,FM)^{2/3} \tag{6.16}$$

Using these simple equations the effects of the mechanical and aerodynamic efficiencies as well as rotor diameter on various vehicle characteristics can be plotted. Figures 6.20(a) and 6.20(b) show respectively the effect of FM and motor-transmission efficiency (η) on the Maximum Take Off Weight (MTOW) of the vehicle. A fixed maximum shaft power of 10W and no powertrain losses were assumed in Figure 6.20(a), and a fixed FM of 0.6 was assumed in Figure 6.20(b). From the plots it is clear that mechanical and aerodynamic efficiencies are equally important for the

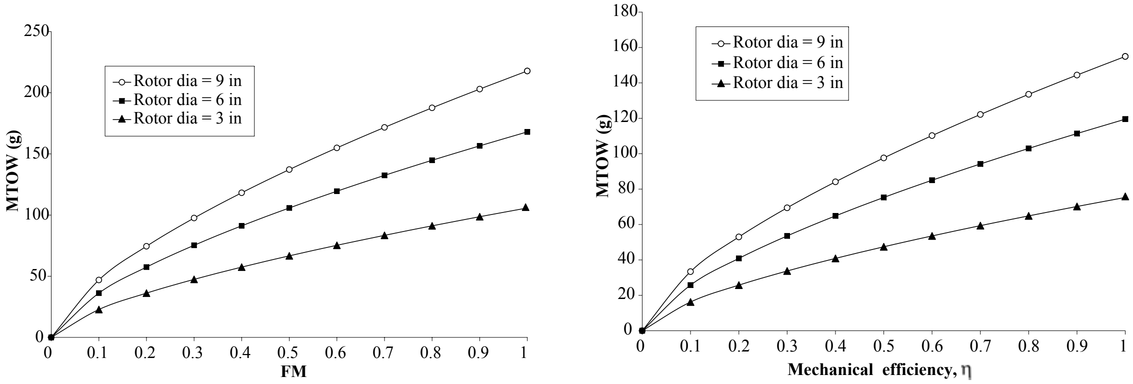

(a) MTOW vs. FM @ $\eta = 1$.

(b) MTOW vs. η @ FM=0.6.

Figure 6.20: MTOW vs. FM and MTOW vs. η for various rotor diameters.

performance of any rotary wing vehicle. Low levels of mechanical efficiency result in a large power requirements regardless of how optimized the aerodynamics are. This is why it is key for the implementation of any vehicle to simultaneously achieve the highest possible level of mechanical and aerodynamic efficiency.

Motor Characterization

In order to match the operational conditions for a good mechanical and aerodynamic performance the behavior of the powerplant over a wide range of operational conditions is required. Manufacturers rarely provide the rotor performance curves and if they do, overly optimistic results are usually given. This is why an electric motor characterization procedure was developed. The same hover test stand used for rotor testing (see section 2.2) was used for measuring current, voltage, torque and rotational speed at various motor loads. The rotor is replaced by a solid aluminum cylinder, and a no-contact symmetric load is applied to the system through and array of strong neodymium magnets. The Eddie currents induced by the magnets result in a torque that opposed the motion of the cylinder. magnitude of the torque is a function of the rotational speed and the strength of the magnetic field. The magnet array was mounted on a height gage such that vertical spacing between the magnet array and the spinning cylinder could be accurately controlled. Figure 6.21 shows a picture of the setup.

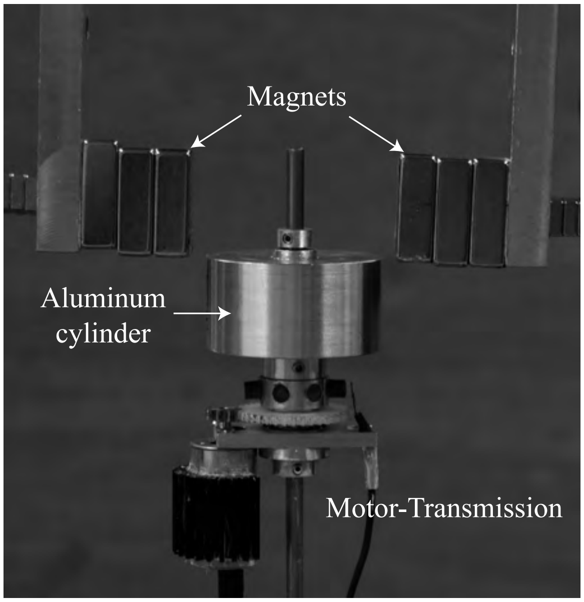

Figure 6.21: Motor characterization test stand showing Eddie-current break.

The vehicle prototype currently uses brushless motors manufactured by Feigao (ref 1208436L). Brushless motors are triphasic and require an electronic speed controller that supplies the commutated current to the motor windings. The current and voltage required by the system were measured before the speed controller (Castle Creations Phoenix 10), hence the experiments provide the compound efficiency of controller, motor and transmission. Experiments were performed at two fixed nominal voltages of 7.4V and 11.1V. These are the voltages provided by two and three lithium polymer cells (LI-PO) connected in series which are the batteries used in the prototype. Figure 6.22 shows the results obtained.

System efficiency improved monotonically with rotational speed. The highest efficiency value measured was 65% at 24,000 RPM using a nominal voltage of 7.4 V. The use of higher voltage to drive the system increased maximum output power at all rotational speeds, however efficiency values were about 5% lower. For a coaxial vehicle weighting 140g, an efficient rotor design needs to operate in the vicinity of 2750 RPM. Hence, in order to maximize mechanical efficiency an optimal transmission reduction ratio of 9 to 1 is desired. Before the motor characterization tests were performed the vehicle's transmission had a reduction ratio of 4 to 1. The mechanical power required by each rotor is about 4 W in hover; hence, from Figure 6.22(a) the system efficiency can be estimated to be ≈43%. This means that a simple change in the reduction ratio can potentially offer power savings in excess of 30% with respect to the original vehicle power consumption.

The prototype's transmission was upgraded to a reduction ratio of 6 to 1 such that the motors were operating in hover at about 16500 RPM. This improved the system efficiency up to ≈ 50%. Unfortunately, before larger reduction ratios can be implemented, swashplate design needs to be modified such that the servos do not interfere with the larger gears needed. The improvements in motor efficiency translated into a noticeable increase in vehicle's endurance.

6.8 Summary

This chapter explored the effects of basic coaxial rotor parameters on the system's performance. An experimental setup that allowed to measure the thrust and rotational speed of a upper and lower rotors at a zero torque condition was developed. The following conclusions were obtained from the tests:

- Rotor spacing does not have a large effect on coaxial rotor performance. At vertical separations larger than h/R=0.4 system thrust does not undergo measurable changes.

- At a trimmed zero torque condition the upper rotor carries ≈60% of the total thrust when identical blades are used. Load distribution is barely affected by disk loading or by collective pitch settings as long as torque between rotors is balanced.

- For the cases studied, the upper rotor is practically unaffected by the lower rotor. Induced aerodynamic effects produced by the lower rotor at the upper rotor plane are negligible.

- Power loading of the coaxial rotor was found not to be maximized when both rotors were operating at the same rotational speed, contradicting Sunada's

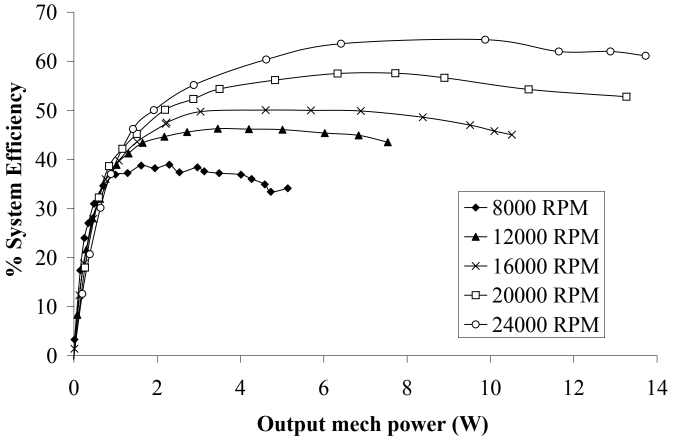

(a) System efficiency at 7.4V.

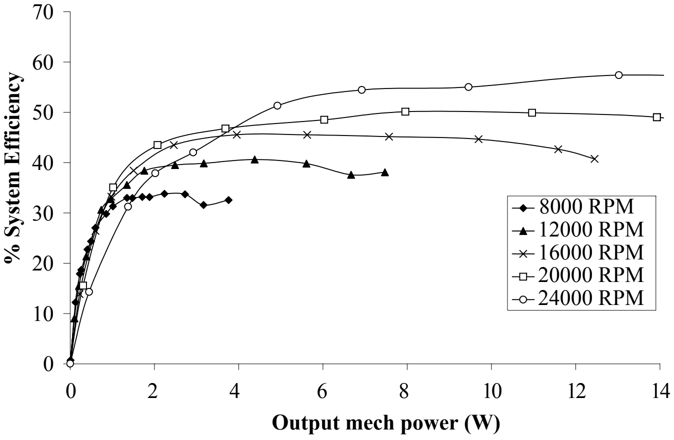

(b) System efficiency at 11.1V.

Figure 6.22: Efficiency vs. shaft power of controller-motors-transmission system at various rotational speeds.

conclusion from Ref. [44]. Sunada's draw his conclusion using a limited amount of experimental data and considered only a very specific case. The current research covered a wider test space, finding that optimal rotor operating conditions are a function of disk loading and that PL of a coaxial is maximized in some cases when rotors operate at very different rotational speeds.

The first two bulleted results are consistent with the interaction of the lower rotor with a fully developed wake. A rudimentary single rotor wake characterization experiment using a Pitot tube supported this result. The experiments showed that the wake of an isolated rotor was fully contracted at a vertical spacing h/R≈0.2.

Basic blade element momentum theory equations were rederived to include climb speed and were used to predict the performance of coaxial rotors. The upper rotor was treated as a single rotor and the interaction between lower rotor and upper rotor's slipstream was modeled as an apparent climb speed that extended over a fraction of the rotor area. Lower rotor predictions are a function of the upper's wake radial velocity profile and its contraction ratio. From wake characterization experiments upper rotor's wake boundary was set at 0.8R and upper rotor's inflow was scaled according to the assumed contraction. Validation with experiments showed that good thrust prediction were obtained (≈ 5% error), however lower rotor torque was largely under-predicted because of two main factors:

- Sectional drag coefficient from CFD are under-predicted at the lower angles of attack at which large sections of the lower rotor blades operate.
- Induced power at the boundary of the upper rotor slipstream is under-predicted since the sudden inflow change does not include a loss function.

A fully functional coaxial MAV was implemented and designed based on the aerodynamic coaxial studies performed. Vehicle configuration, rotors and swashplate were designed from scratch, while batteries, motors and electronics were carefully selected off-the-shelf components. A motor characterization test procedure was developed and used to determine the most efficient working regime for the prototype's motors and an optimal transmission reduction ratio. The prototype's stability and handling characteristics were superior to those of conventional RC helicopters, making it a very forgiving platform for the development of control systems or stability augmentations algorithms.

Chapter 7

Concluding Remarks

Micro air vehicles are an emerging technology that can potentially transform the way a wide array of law enforcement, military, and civilian missions are approached. The possibility of having small flying vehicles sending video or sensor data from remote locations where it is either too dangerous, time consuming, or simply impossible for a human to be has been the main motivation for this area of research. However, before MAVs can be used as intended, two main aspects of the technology have to be resolved: platform development and control system implementation.

Efficient vehicle configurations with enough endurance, range, and good maneuverability have to be developed. Yet, this is just half the problem. What will make MAVs practical is the integration of a good performing platform with the necessary electronics to minimize or eliminate altogether human intervention. This dissertation focused on the understanding of the aerodynamic issues related to rotary wing MAVs, and on the development of a stable platform that can be used for the testing and implementation of control systems.

7.1 Summary of Contribution and Results

Most of the experimental research performed addressed the effects on hover performance of geometric and operational parameters of single isolated rotors. The following are the most important results and contributions that relate to this aspect of the investigation.

1. A computerized hover stand that directly measured thrust, torque, rotational speed and electric power of small-scale rotors was developed. Hardware and

software were customized to achieve excellent levels of accuracy, minimizing testing time and assuring repeatability of the results.

2. Systematic hover testing of single isolated rotors was performed. Experiments can be divided into two main categories: tests with rectangular blades, where the effects of airfoil where isolated. And tests with non-rectangular blades, where geometric blade and airfoil parameters were coupled. From the rectangular blade tests the following conclusions and results were obtained:

    - The use of conventional streamlined airfoils historically used in full-scale vehicles, results in extremely poor performance at MAV scale. The low Reynolds number regime at which the blades operate has large adverse effect on sectional airfoil characteristics.
    - Thin cambered plates which are able to achieve higher lift coefficients and lift-to-drag ratios are a better choice for small-scale rotor implementation.
    - Having more than two blades in an MAV rotor is not a good design choice. Even though theory predicts a reduction in tip losses as the number of blades increase, other more significant aerodynamic and structural advantages are achieved with two bladed rotors. For a given solidity a fewer number of blades translates into wider chords, which at a fixed rotational speed will have higher Reynolds numbers. Additionally, for a fixed blade thickness wider chords results in curved plates with a lower thickness ratios. Higher Reynolds numbers and low thickness ratios are factors that benefit the aerodynamic airfoil performance, resulting in higher rotor efficiency.
    - The effect of Reynolds number on airfoil performance also influences the choice of rotor solidity. As opposed to full-scale helicopters where rotors having the highest C_T/σ usually achieve the highest FMs, at MAV scale low solidity translates into low chord-based Reynolds numbers and non-optimal rotor performance. The lower blade area does not compensate for the added viscous losses increasing the optimal chord width. Additionally,

similar structural limitations as for the choice of number of blades also apply in this case.

- Rotor efficiency at MAV scale is largely determined by the airfoil characteristic. The most relevant thin curved airfoil parameters are: camber amount, camber location, thickness ratio, and leading edge shape.
- Circular arcs are outperformed by thin curved plates with a maximum camber location shifted toward the leading edge. However, the ease of manufacture and simple parameterization made circular arcs the airfoil of choice in this dissertation.
- Experimentally the highest FMs were achieved with airfoil cambers ranging from 6% to 9%.
- Measurement of the zero-lift drag on rotors with flat plate blades showed that over the tip Reynolds numbers range covered (25,000<Re<65,000), the flow in the rotor blades cannot be assumed laminar. Most likely the flow is transitional and is separating at various at different regions of the blade surface.
- Leading edge shape had a large influence on the zero-lift drag coefficient of flat plates, the use of sharp symmetric leading edges resulted in the lowest drag values. For the various leading edge shapes considered zero-lift drag coefficients were adversely affected by a reduction in Reynolds number and an increase in thickness ratio.
- Leading edge shape also played an important role in hover performance. Maximum FMs were increased and rotor stall was delayed by the use of sharp asymmetric leading edges.

Non rectangular blades were used to study the coupled airfoil and blade parameters on rotor hover performance. The tapered geometries were manufactured by removing material from baseline rectangular blades. This resulted in a coupling between blade planform, twist distribution and spanwise airfoil geometries. From the experiments with non-rectangular blades the following conclusions and results were obtained:

- when using flat plate airfoils, blade planform only matters to the extend it affects solidity distribution. As long as the thrust weighted solidity is kept constant, the effects on rotor performance will be minimal.
- Large improvements in hover rotor performance were achieved by tapering blades with 6% and 9% airfoil cambers. Negative twist and gradual camber reduction were introduced at the tapered sections resulting in the simultaneous reduction of induced and profile power.
- The highest maximum FM achieved was 0.65 by rotors with 6% and 9% baseline camber blades with asymmetric 2:1 linear taper starting at 80% span. Maximum FM reached the same nominal value; however, they occurred at different disk loadings.

3. Rotational speed at MAV scale, as opposed to full scale-helicopters, is a parameter that can be chosen over a wide range. Lower rotational speeds translate into lower FM but higher PL. Since the final objective is to minimize the power consumption, maximization of the power loading and not the FM should be the design driver.

4. A Blade element momentum theory model was implemented and an algorithm to calculate the equivalent sectional airfoil characteristics from hover rotor tests was developed. This approach was used to compare the characteristics of various airfoils, and to determine the relative contributions of induced and viscous losses to the total power of some sample rotors. It was found that viscous losses accounted for 40% of the total power on a representative rotor with rectangular untwisted blades. This is larger than the 30% profile power contribution typical of full-scale rotors. In order for MAV rotors to achieve high levels of efficiency both induced and viscous losses have to be as low as possible. This is achieved by having a good blade design coupled with well

performing airfoils.

5. CFD was used in a parametric study of a family of circular arc airfoils. The effects on lift, drag and moment coefficients of a series of geometric parameters was explored over a range of Reynolds numbers. The CFD solvers TURNS, Fluent and INS2d were evaluated, validating the results with published wind-tunnel experiments of a circular arc airfoil at a Reynolds number of 60,000. Validation showed that TURNS produced the best lift coefficient predictions followed by INS2d which under-predicted lift at the higher angles of attack. Fluent was unable to capture the non-linearities of the lift measurements. All three codes under-predicted drag; however, TURNS and INS2d qualitatively captured the trends in L/D ratio. The solver INS2d was chosen over TURNS for its ease of convergence at low Re and lower computational cost. The parametric study produced a multidimensional airfoil database.

6. The CFD generated airfoil database was integrated to a BEMT rotor model. A blade-airfoil parameterization was defined coupling blade planform with twist distribution and airfoil shape. The algorithm interpolated the database to obtain the spanwise airfoil characteristics. Prediction were validated with some of the measurement for rectangular and non rectangular blades. Thrust and maximum FM predictions were satisfactory for blades with maximum cambers of 6% and below. For blades with higher cambers the early stall predictions of the CFD solver resulted in lower thrust values than experimentally measured. Similarly, power predictions at the lower collectives were underestimated because of the limited accuracy of the CFD drag coefficients at low angles of attack. Nevertheless, the approach can be efficiently used in the preliminary design of MAV rotors. Thrust and power calculations for a wide variety of geometries and operational conditions are obtained in just a few minutes with similar or even better precision than with the much more computationally expensive three dimensional CFD simulations. A parametric grid search was used to find the optimal tip geometry within a defined design space.

7. Experimental characterization of a representative coaxial rotor was performed at a zero torque condition over a range of rotational speeds. The hover test stand was used to measure the coaxial thrust,rotational speeds, and electric power of each rotor. The following conclusions were obtained by exploring the coaxial rotor configuration:

    - Rotor spacing does not have a large effect on coaxial rotor performance. At vertical separations larger than h/R=0.35 system thrust does not undergo measurable changes.
    - At a trimmed zero torque condition the upper rotor produces approximately 60% of the total thrust when identical blades are used. Load distribution is barely affected by disk loading or by collective pitch settings as long as torque between rotors is balanced.
    - Power loading of the coaxial rotor was found not to be maximized when both rotors were operating at the same rotational speed. The current research covered a wider test space, finding that optimal rotor operating conditions are a function of disk loading and that PL of a coaxial is maximized in some cases when rotors operate at very different rotational speeds.

8. BEMT equations were derived to include a climb speed. The interaction of the lower rotor with the fully contracted upper rotor slipstream was modeled as an apparent climb speed over the inner regions of the rotor disk. Lower rotor predictions are a function of the upper's wake radial velocity profile and its contraction ratio. From wake characterization experiments upper rotor's wake boundary was set at 0.8R and a uniform wake velocity distribution was assumed. At fixed collectives of 16 degs, for a range of operating conditions, the model was used to predict coaxial thrust and lower rotor rotational speed to achieve torque equilibrium. Results were validated with experiments obtaining satisfactory levels of accuracy in both thrust and power calculations ($\leq 5\%$ error). The model tends to under-predict the power of the lower rotor because

of the following reasons:

- Sectional drag coefficient from CFD are under-predicted at the lower angles of attack at which large sections of the lower rotor blades operate.
- Induced power at the boundary of the upper rotor slipstream is under-predicted since the sudden inflow change does not include a loss function.
- Model calculations are a function of the assumed contraction ratio and upper wake's velocity profile. contraction ratio was empirically estimated, and a uniform velocity profile was assumed.

9. A fully functional coaxial MAV was implemented and designed based on the aerodynamic coaxial studies performed. Vehicle configuration, rotors and swashplate were designed from scratch, while batteries, motors and electronics were carefully selected off-the-shelf components.

10. A motor characterization test procedure was developed and used to determine the most efficient working regime for the prototype's motors. It was found that motor efficiency and proper rotor-motor matching is as important as having good aerodynamic performance.

11. The coaxial configuration chosen for the implementation of the prototype proved to have large advantages in terms of compactness and stability. In fact, the prototypes stability and handling characteristics are superior to those of conventional RC helicopters, making it a very forgiving platform for the development of control systems or stability augmentations algorithms.

7.2 Recommendations for Future Work

The experimental aspects of this dissertation established a solid foundation for the characterization of small-scale rotors. The methods, software, and hardware used, provide repeatable results within the margins of experimental error and can be used with confidence in the future. However, some of the computational and analytical aspects of this research need to be refined. Most of the inaccuracies in the rotor thrust and power calculations can be linked to the early lift stall and the underprediction of drag coefficients from INS2d solutions. The use of a different CFD solver with better predictive capabilities at the Reynolds numbers considered, or empirical corrections to the database are possible approaches. Blade element momentum theory (BEMT) is an extremely inexpensive approach that coupled with good sectional airfoil characteristics can be used as a powerful rotor design tool. Based on the results obtained in this dissertation, it can be concluded that BEMT capabilities are adequate for preliminary MAV-scale rotor design and basic rotor optimization. The main appeal of the method implemented in this dissertation, is that once the airfoil database has been calculated it can be used to predict the performance of a wide variety of blade geometries and rotor configurations with a minimum of additional effort. This is not the case for higher order aerodynamic modeling tools such as Free Vortex Modeling (FVM), or three-dimensional CFD. This is specially true for CFD simulations that require vasts amounts of computing power. Higher order modeling tools might be used in the refinement of a previously optimized design with the approach implemented in this research.

This dissertation focused on the use of circular arc airfoils for MAV rotor implementation. Circular arcs offered unique advantages in terms of manufacturing ease and blade-airfoil parameterization. However, better aerodynamic performance can be achieved with thin curved plates having different camber lines. Detailed experimental and computational parametric studies should be carried out to identify an airfoil family with optimized sectional characteristics for the use in rotary wing MAVs.

The coaxial MAV prototype developed through the course of the research can undergo large performance and functionality gains with some basic component redesign. First of all, the transmission reduction ratio is currently 6:1 and needs to be increased to the optimal 9:1. Only then, motors will be able to work at their most efficient rotational speed.

Outdoor vehicle maneuverability and control authority in the current prototype need to be improved. When facing wind gusts the lower rotor swashplate is not able to produce large enough moments to fly into the wind. This can be solved by introducing a cyclic input to the paddles of the upper rotor's stabilizer bar, increasing the vehicle's control authority without sacrificing stability. The existing swashplate can be modified to do this without a large weight penalty.

Appendix A

Low Reynolds Number Flow Physics and Basic Rotor Aerodynamics

A.1 Flow Regimes, Reynolds and Mach Numbers

The nondimensional parameter known as the Reynolds number was introduced by Irish engineer Osborne Reynolds in 1883. The Reynolds number is defined as the ratio of inertial forces (ρV_∞) to viscous forces (μ/c) in the fluid, and it provides a criterion for dynamic similitude. The Reynolds number of an airfoil with chord c and free stream velocity V_∞ is given by Eq. A.1.

$$Re = \frac{\rho_\infty V_\infty c}{\mu}. \tag{A.1}$$

Where ρ_∞ is the fluid density and μ the dynamic viscosity of the fluid. As Reynolds number is reduced viscous forces become dominant and boundary layer behavior becomes more complex. Phenomena such as transition separation and reattachment can occur within a short chordwise distance having a large effect on pressure distribution and airfoil performance.

Mach number is another key non-dimensional parameter used to characterize aerodynamics flows. Free stream Mach Number is defined as the ratio of the free stream convection velocity V_∞ and the local speed of the sound a_∞ as shown in Eq.A.2.

$$M_\infty = \frac{V_\infty}{a_\infty}. \tag{A.2}$$

Mach number can be understood as the ratio of inertial forces in the flow to forces resulting from compressibility effects. Three different aerodynamic regimes are de-

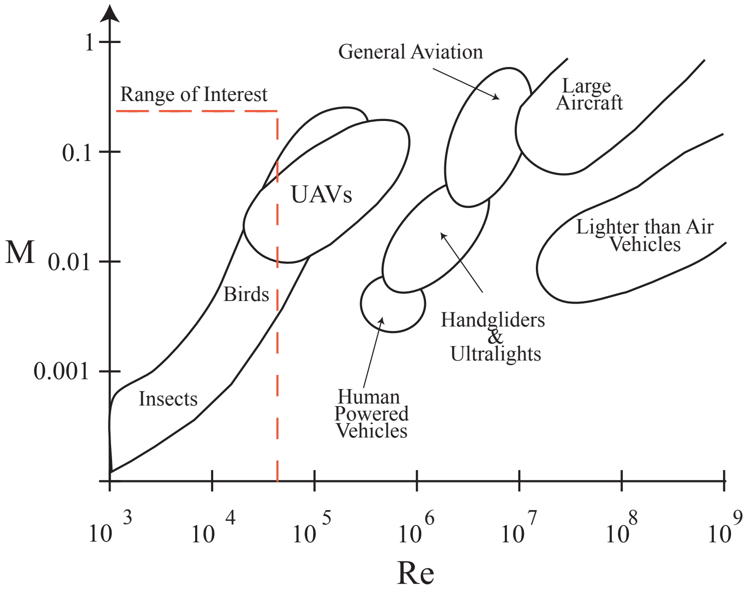

Figure A.1: Reynolds Vs. Mach number for various types of vehicles

fined based on Mach number. When $M < 1$ the flow is subsonic, if M = 1 the flow is sonic and if $M > 1$ the flow is supersonic.

Figure A.1 shows Reynolds number vs. Mach number for various types of vehicles and animals. The dashed rectangle defines the range of interest for MAV development. Micro Air Vehicles fly in the lower subsonic range at Reynolds numbers below 70,000. This is the regime where most birds and insects are also encountered. For the rotors studied in this dissertation a maximum Mach number of approximately 0.14 at the blade's tips was attained, making compressibility effects negligible.

A.2 Boundary layer Behavior

The boundary layer concept was introduced by Prandtl in 1904 and was used to explain the differences between the observed fluid behavior and inviscid flow theory. This was a problem that could not be solved in the 19th Century and was known as d'Alembert's paradox. When there is relative motion between a solid body and fluid, the fluid adheres to the surface, creating a thin region where the flow velocity will increase from zero up to the free stream velocity. This region is known as the boundary layer, and it is responsible for the frictional drag forces on an airfoil. The flow within the boundary layer can be either laminar or turbulent. A laminar flow is characterized by being organized and uniform, while a turbulent flow is disorganized and has abundant mixing between the fluid layers.

Boundary Layer thickness is defined as the distance from the body surface up to where 99% of the free stream velocity is recovered. Due to the momentum transfer within the turbulent boundary layers, these have fuller velocity profiles, and are thicker than laminar ones. When laminar flow is disturbed and changes into turbulent,the boundary layer undergoes what is known as transition.

The drag produced by the two types of boundary layer varies with the inverse of the Reynolds number. However laminar flow produces lower values of drag. For flows over a flat plate, Blasius found the expressions for the laminar boundary layer thickness (δ) and the skin friction coefficient (c_f) given by Eq.A.3 and Eq.A.4 respectively.

$$\delta = \frac{5.2x}{\sqrt{Re_x}}. \tag{A.3}$$

$$c_f = \frac{0.664}{\sqrt{Re_x}}. \tag{A.4}$$

There is no exact analytical solutions for the turbulent boundary layer over a flat plate. However, numerical solutions have been found using empirical models of turbulent diffusion. The approximate thickness is given by Eq.A.5.

$$\delta = \frac{0.37x}{Re_x^{0.2}}. \tag{A.5}$$

Where Re_x is the Reynolds number based on the distance from the leading edge of the plate. The total shear stress drag can be obtained by integrating the skin friction drag coefficient along the surface, as shown in Eq.A.6

$$C_d = \frac{1}{c}\int_0^c c_f \, dx \tag{A.6}$$

By replacing the skin friction coefficient in the previous expression with Eq.A.4 the laminar shear drag coefficient can be obtained as shown in Eq.A.7.

$$C_{d\,lam} = 1.328\, Re_x^{-0.5}. \tag{A.7}$$

Since no exact solution for the turbulent boundary layer has been obtained, there are various proposed models for the turbulent shear drag coefficient. Two of the most widely used are presented in Eqs. A.8 and A.9 from Refs. [72] and [73] respectively.

$$C_{d\,tur} = 0.074\, Re_x^{-0.2}. \tag{A.8}$$

$$C_{d\,tur} = 0.455\, (\log Re_x)^{-0.258}. \tag{A.9}$$

These expressions can be used to check experimental data. For example, the laminar shear drag coefficient can be considered an absolute lower bound for the minimum drag coefficient of an airfoil, while turbulent drag coefficient are usually close to the minimum drag coefficients of airfoils at Reynolds number of one million and above.

The variation of pressure in the direction of the flow, or pressure gradient, has a large influence over the boundary layer. The well known Bernoulli's principle, which states that an increase in velocity occurs simultaneously with decrease in pressure (with various assumptions), can be used to give a simple explanation of the boundary layer's velocity profile behavior.

When the pressure decreases in the direction of the flow, a favorable pressure gradient exists. The boundary layer's velocity profile becomes fuller as energy is gained, this corresponds to case (a) of Figure A.2. When pressure increases in the direction of the flow an adverse pressure gradient is obtained, gradually distorting the boundary layer's velocity profile As shown in case (b) of Figure A.2. Since the boundary layer has limited energy, if the adverse gradient is sustained long enough, the flow will eventually reverse its direction. When this occurs the external flow pattern breaks down and the flow separates from the surface forming a turbulent

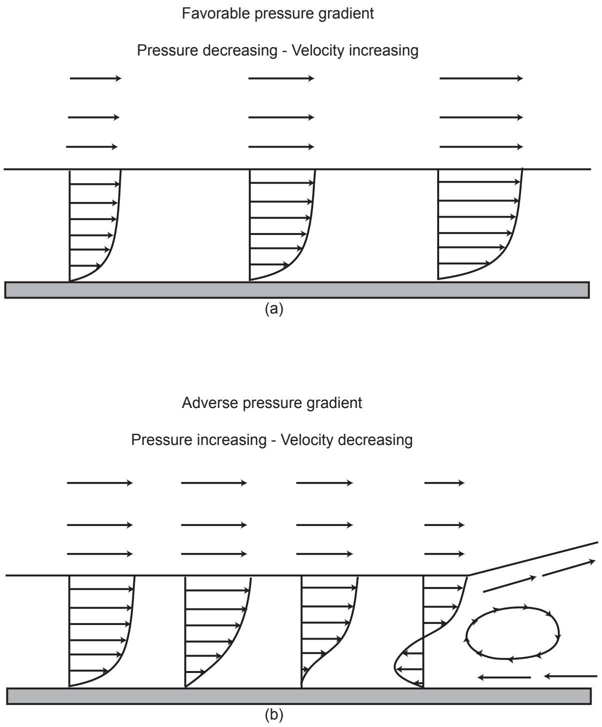

Figure A.2: Effect on boundary layer of favorable and adverse pressure gradients.

wake. The difference in pressure between the front and back of a body produced by separation introduces another source of drag, known as form drag.

The lower shear drag forces produced by laminar boundary layers come at a price. There is a trade-off between lower drag and boundary layer stability. Laminar boundary layer are comparatively unstable, being very sensitive to flow disturbances and able to withstand only small adverse pressure gradients. However stability tends to increase as Reynolds number is reduced.

When a laminar Boundary layer faces an adverse pressure gradient there are three possible outcomes. It can separate stalling the airfoil, it can separate and eventually reattach as a turbulent boundary layer, or it can transition into a turbulent boundary layer without the occurrence of separation. What exactly occurs depends on a series factors, such as the intensity of the adverse pressure gradients, surface roughness, surface curvature, freestream turbulence and of course, Reynolds number.

A.3 Lift Generation and Boundary Layers

An airfoil generates lift by producing a pressure difference between the upper and lower surfaces. This can be achieved by having low pressure in the upper surface, high pressure in the lower surface or a combination of the two. As discussed in section A.2, if pressure increases in the direction of the flow, the boundary layer faces an adverse pressure gradient, this means that no matter how lift is generated adverse pressure gradients have to occur. Figure A.3 shows the velocity distributions assuming inviscid flow for three different airfoils at 3 degrees angle of attack. Airfoil **a)** is a NACA 0012, it is a symmetric airfoil that relies mostly on accelerating the flow over the upper surface producing a strong suction peak. Airfoil **b)** is a 5 digit NACA 88012. In this case, both a positive pressure in the lower surface and a negative pressure in the upper surface are used. Finally, airfoil **c)** is a 4 digit NACA 6406, its key characteristics are a relatively small thickness and a concave lower surface. This airfoil relies largely on producing a positive pressure in the lower surface, such that if a laminar separation bubble or catastrophic separation occurs in the upper surface, a considerable amount of lift can still be generated.

A.4 Low Reynolds Numbers Sub-Regimes

Reynolds number is a dominant factor that dictates airfoil performance and vehicle design. Carmichael in his 1981 survey (Ref. [5]) divided the Reynolds number realm into twelve segments covering ten orders of magnitude. For each range, basic flow characteristics and main aerodynamic issues were explained. Four of these regimes are of interest for the current research. Some of Carmichael's comments complemented with additional information are presented here.

The first interval covers Reynolds numbers between 1,000 and 10,000. About 30% of the inner blade segments of propellers and rotors of existing MAVs are in this range. However, its relevance is expected to grow as the next generation of smaller vehicles is developed. The flow in this regime is characterized for being laminar with a tendency to separate before undergoing transition. The research performed

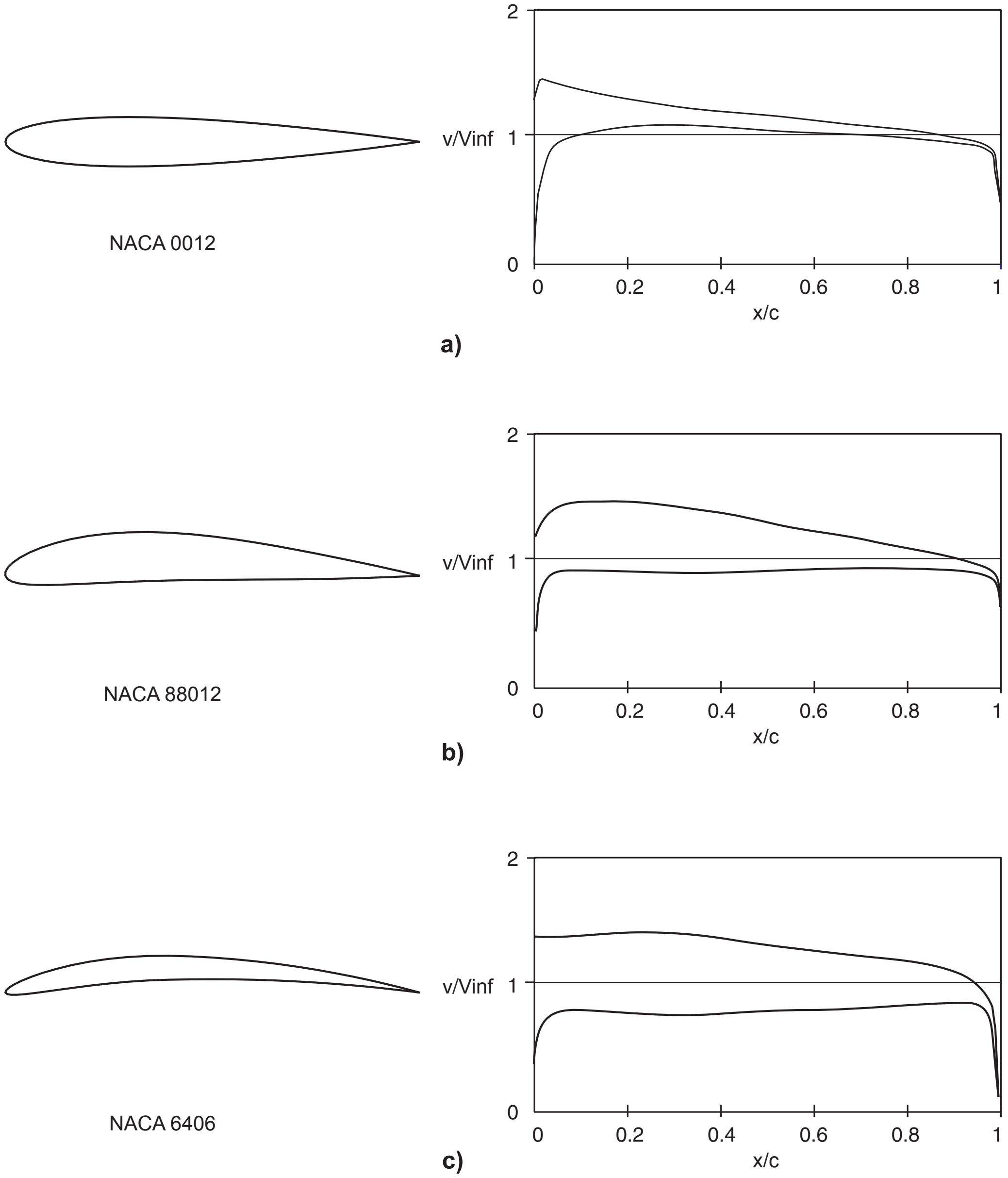

Figure A.3: Velocity distribution for three different types or airfoils at 3 deg aoa.

on the Mesicopter (Refs. [31, 52, 53, 54]) is in this range. Computational results showed how airfoil design, specially camber distribution, still is an important factor that affects airfoil performance.

The next interval defined by Carmichael covers Reynolds numbers between 10,000 and 30,000. Here the flow exhibits a similar behavior than in the immediately lower range, being laminar with a tendency to separate before transitioning into turbulent. Very limited research has been performed in this regime. One of the few sources, as reported by Carmichael, is an obscure report by Bauer (Ref. [70]) that claims the existence of 100% laminar-flow hand-launched gliders. Bauer determined experimentally that the drag coefficient of the model tested matched closely what the laminar boundary layer theory predicts. However, this was only achieved at low lift coefficents of the order of 0.5. When angles of attack were increased separation without reattachment occured and the airplanes stalled. The lack of reliable experimental data on this Reynolds number range makes difficult to ascertain general flow characteristics and behavior.

The third interval covers the Reynolds numbers between 30,000 and 70,000. This is where most of the fixed-wing MAVs and the outer sections of MAV rotors operate. Flow in this regime is characterized by the occurrence of laminar separation bubbles that introduce hysteresis in the experimental measurements. Below a Reynolds number of about 50,000 the chordwise distance is generally not sufficient for reattachment to occur; however, experiments have shown that the use of boundary layer trips or turbulators to reduce the critical Reynolds number (Reynolds number at which transition occurs) has been successful near the upper bound of this range.

Finally the interval that covers Reynolds numbers between 70,000 and 200,000 is characterized by the ease to obtain extensive laminar flow that is able to transition to turbulent without catastrophic separation. Turbulators can still be useful to reduce the size of the separation bubbles, but only in the vicinity of the lower bound of the interval. Most of the low Reynolds number experimental research covers this regime, which is typical of fixed-wing radio control models, and small UAVs.

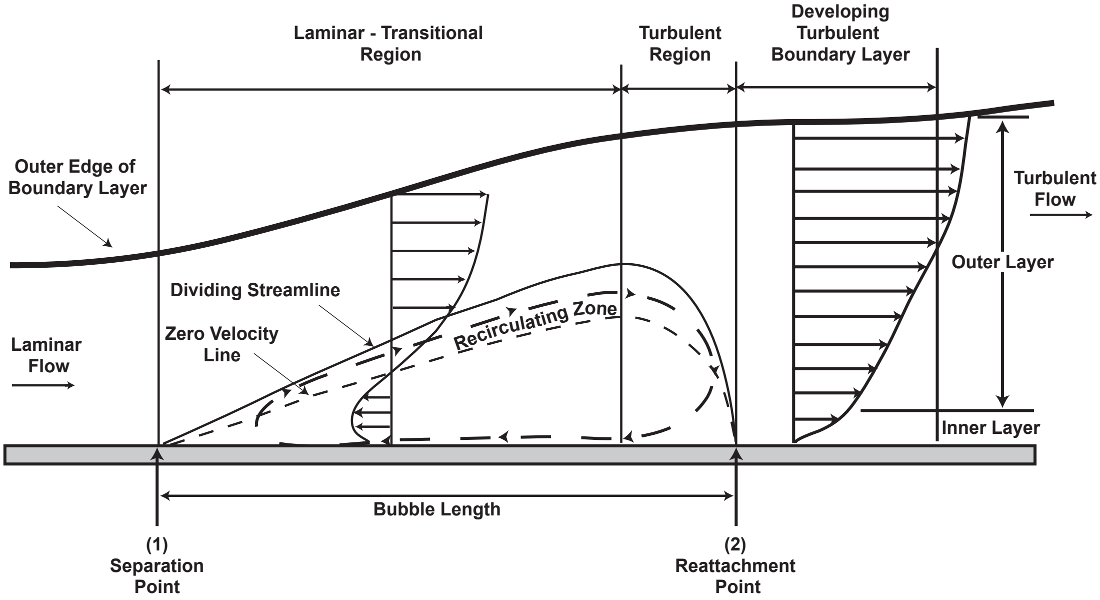

Figure A.4: Sketch of laminar separation bubble.

A.5 Laminar Separation Bubble

In this section a description of the laminar separation bubble, conditions for its formation and its effects on airfoil performance are presented.

Figure A.4 shows a diagram of a laminar separation bubble superimposed to the expected boundary layer velocity profile. As previously discussed, when a laminar boundary layer faces an adverse pressure gradient separation occurs as soon as there is a change in sign along the velocity profile, this corresponds to point 1 in the diagram. The bubble is contained within the outer edge of the boundary layer, and has recirculating flow, easily identifiable in the pressure distribution plots as a segment of constant pressure. The recirculating region is divided in two distinct zones, one with laminar-transitional flow and another with turbulent flow. Reattachment occurs at point 2 in the diagram. The attached boundary layer is now turbulent and exhibits its typical fuller velocity profile.

From the discussion in section A.4 it is clear that laminar separation bubbles are constrained to a Reynolds number range. However, this range varies with airfoil shape and environmental conditions. Carmichael (Ref. [5]) proposed a rule of

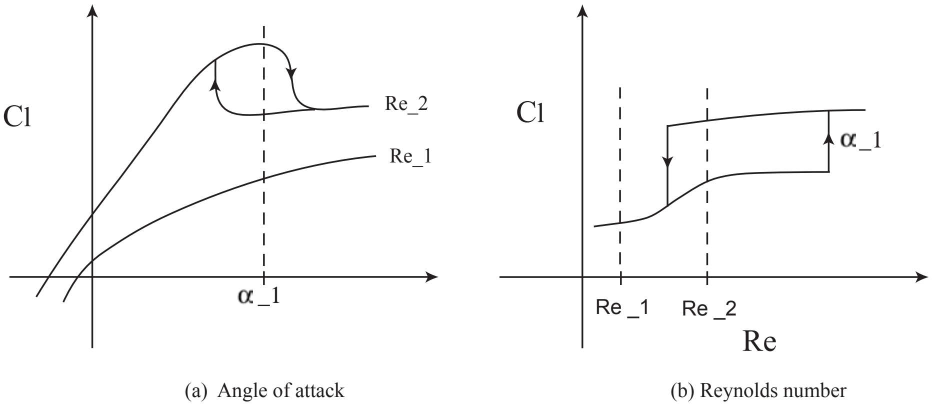

(a) Angle of attack (b) Reynolds number

Figure A.5: Schematic of hysteresis in lift coefficient with variations in a) angle of attack, and b) Reynolds number from data in (Ref. [1])

thumb that gives a rough estimate of the chances of a bubble to form. Considering the chordwise distance from the point of separation to the point of reattachment, the Reynolds number using the freestream velocity is approximately 50,000. This means that airfoils with chord Reynolds numbers below 50,000 will undergo laminar separation without bubble formation. At the lower Reynolds numbers, bubbles will be long, extending for a substantial fraction of the chord and having a marked effect on the airfoil's pressure distribution. A smaller suction peak reduces the lift coefficient slope while increasing pressure drag. Bubble length shortens as Reynolds number increases, gradually reducing its adverse effects over the airfoil performance. Laminar separation bubbles can occur at much higher Reynolds number -of about one million- in those cases bubble length is very small extending just for a few percent of the total chord length. Short bubbles do not have a noticeable effect on the pressure distribution or on the airfoil performance, they just work as a tripping mechanism that facilitates the transition of the boundary layer. Figure A.6 obtained from Ref. [71] illustrates the previous point, showing how dramatic the influence of a large bubble can be as opposed to the minute influence of a short one.

Long bubbles explain the airfoil behavior first identified by Schmitz (Ref. [1]). In his wind tunnel experiments he documented hysteresis in both lift and drag when angle of attack and Reynolds numbers were cycled, as shown in Figure A.5. When

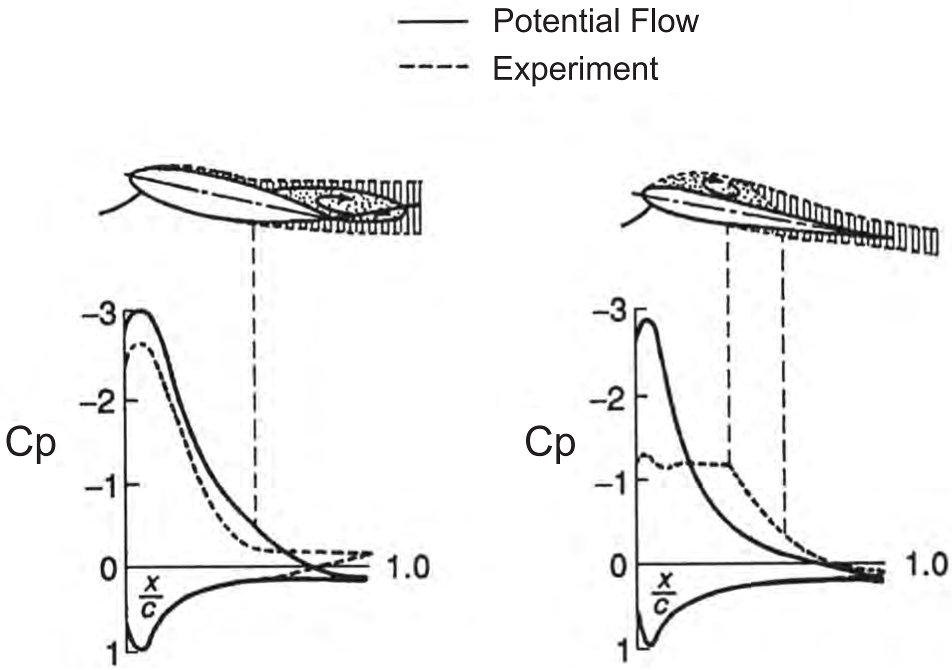

Figure A.6: Long and short bubble effect on pressure distribution (Ref. [71])

increasing angle of attack there is a point where turbulent reattachment does not occur and the bubble bursts, producing thin airfoil stall. In order to reattach the flow, it is not sufficient to go back to an angle immediately below to where stall occurred. It is necessary to reduced it by several degrees more until a bubble forms again as illustrated in Figure A.5 (a). A similar hysteresis loop is observed when cycling the Reynolds number while keeping a fixed angle of attack. To reattach the flow, Reynolds number has to be increased well beyond the point were stall initially occurred as shown in Figure A.5 (b). This behavior needs to be considered when performing rotor testing, care must be taken to avoid misleading measurements when acquiring data for a given collective. If a hysteresis loop is identified, a consistent experimental procedure needs to be followed to avoid erroneous measurements, this issue is addressed with more detail in Section 2.2.3.

A.6 Reynolds Number Effects on Aerodynamic Airfoil Characteristics

One of the most relevant wind tunnel experimental investigations at low Reynolds numbers was performed by Schmitz (Ref. [1]). He compared the characteristic of five different airfoils over a Reynolds number range of 42,000 up to 420,000. Three thick streamlined airfoils, a flat plate and a thin cambered plate were studied, these are shown in Figure A.7.

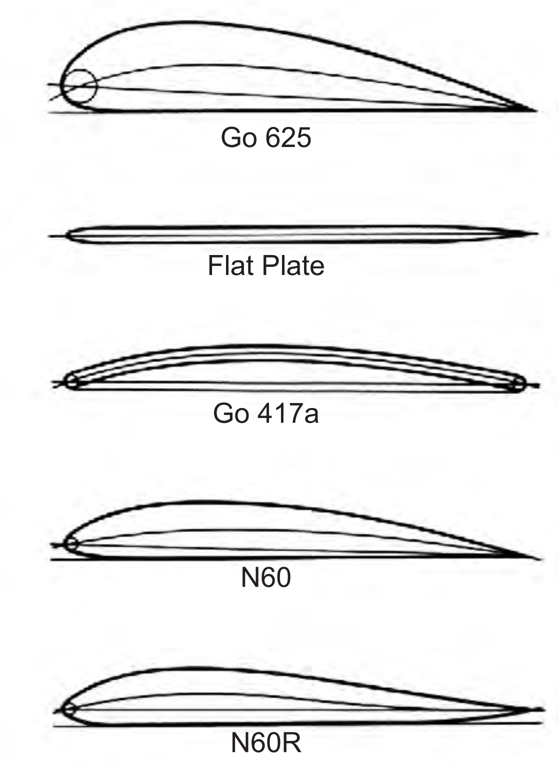

Figure A.7: Airfoils studied by Schmitz in Ref. [1] .

Schmitz results showed how airfoil behavior undergoes radical changes when tested below and above their critical Reynolds number, this is the Reynolds number at which transition occurs. He also identified some distinct characteristics of thin flat and curved plates.

Figure A.8 shows the polar plots at different Reynolds numbers for each of the airfoils Schmitz investigated. The first striking difference are the large hysteresis loops present at the higher Reynolds numbers for the streamlined airfoil. These loops are a consequence of the formation of long laminar separation bubbles. This does not occur for the flat or the cambered plates. For all cases, as Reynolds number is reduced, drag and lift undergo large variations, adversely affecting the lift to drag ratio of the profiles.

The effect of Reynolds number over maximum lift coefficient is shown in Figure A.9. For the thin plates there is a gradual reduction in C_{Lmax} with no change is slope, as opposed to the streamlined airfoils that below the critical Reynolds number go through a dramatic and sudden drop in maximum lift. Minimum drag coefficients have a similar behavior, linearly reducing as Reynolds number increases - for the thin plates - and suddenly dropping - for the streamlined airfoils - as the critical Reynolds numbers are reached, this is shown in Figure A.10.

If now the lift coefficient slope is considered, it can be observed in Figure A.11 that the streamlined, airfoils such as the N60, N60R and Go625, undergo a large reduction in $C_{L\alpha}$ as Reynolds number is reduced. These airfoils achieve a maximum $C_{l\alpha}$ of 1.8π at a Re=420,000. At Re=42,000 there is no linear section in the lift coefficient curve, and $C_{l\alpha}$ cannot be defined. On the other hand the effect of Reynolds number on thin plates is more subtle. The flat plate is practically not affected, keeping an ideal lift coefficient slope of 2π over the whole Reynolds number range. The Go417A airfoil achieves surprisingly a lift coefficient slope of 2.8π at Re=420,000, having a slight reduction down to $C_{l\alpha} = 2.77\pi$ at Re=42,000.

A.6.1 Thin Cambered Airfoil Characteristics

Schmitz results suggest that if an airfoil is required to work below their critical Reynolds number, thin cambered airfoils have desirable aerodynamic characteristics that are not present in conventional thick streamlined airfoils in this regime.

Laitone, following on Schmitz work, focused his investigation (Refs. [16, 17, 18]) on explaining the superior aerodynamic performance of a sharp-nosed thin plate over any known round nosed airfoil at low Reynolds numbers. He performed wind-tunnel force measurements as well as pressure distribution and flow visualization experiments. Laitone's result showed that sharp leading edges continually shed

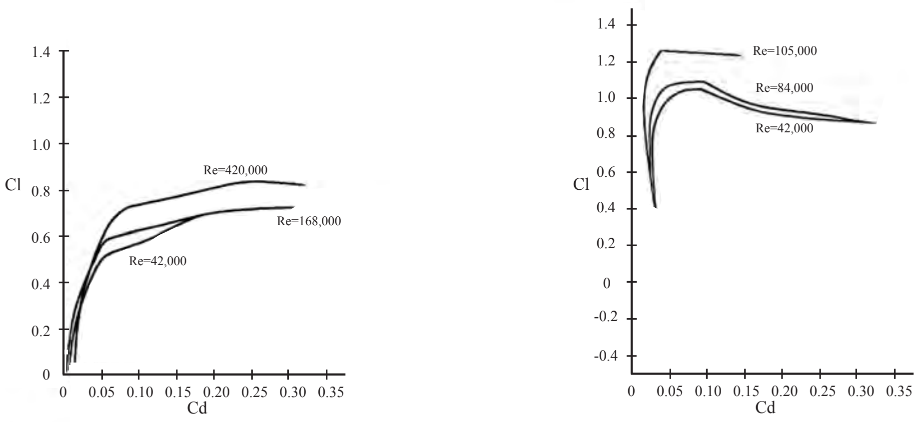

Flat plate

Go 417a

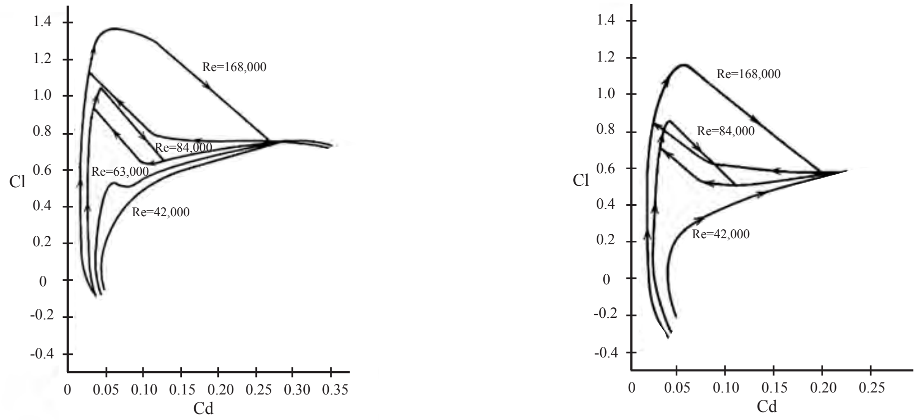

N60

N60R

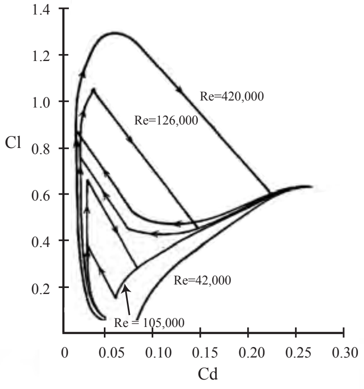

Go 625

Figure A.8: Drag polars for the airfoils studied by Schmitz from data in Ref. [1] .

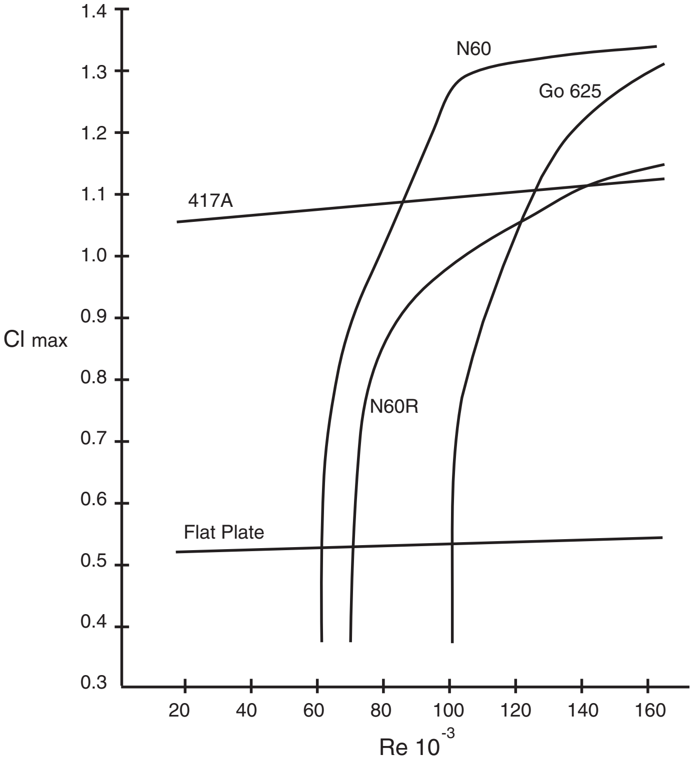

Figure A.9: Reynolds number vs. maximum lift coefficient for the airfoils studied by Schmitz from data in Ref. [1] .

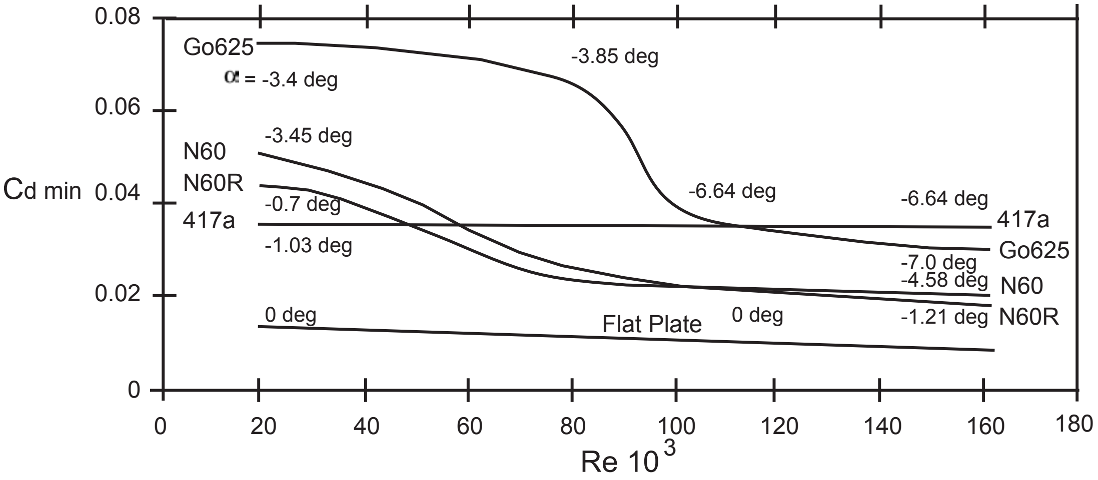

Figure A.10: Reynolds number vs. minimum drag coefficient for the airfoils studied by Schmitz from data in Ref. [1] .

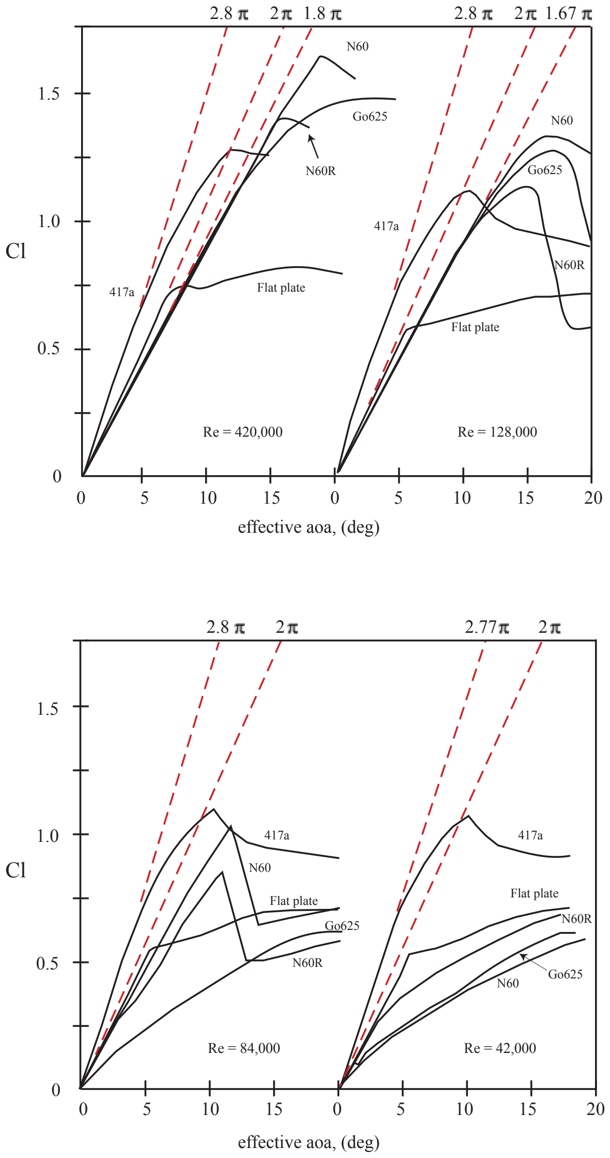

Figure A.11: Effective AoA vs. lift coefficient at different Reynolds numbers for airfoils studied by Schmitz,(Eff. aoa=0 at $C_l = 0$), from data in Ref. [1].

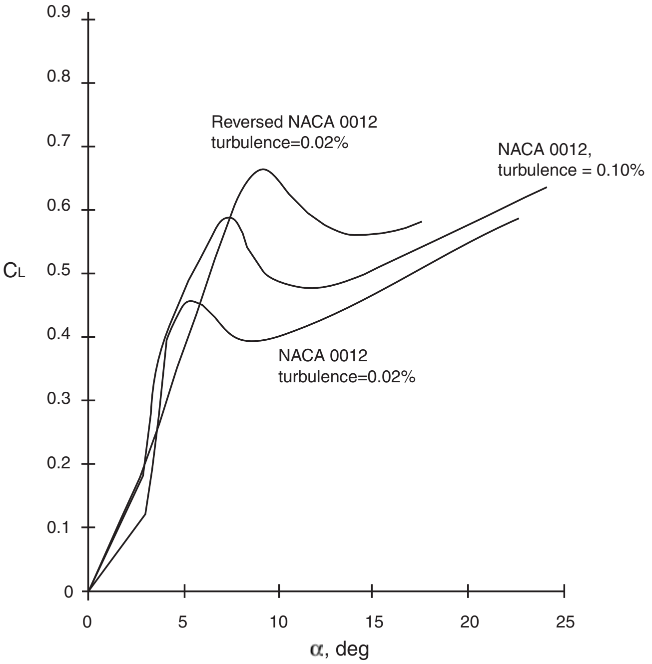

Figure A.12: Angle of attack vs. lift coefficient for rectangular wings of AR 6 at two different turbulence levels and Re=20,700 Ref. [17]

small vortices that rolled along the upper surface preventing flow separation over a range of angles of attack. He also explored the effects of turbulence in the force measurements, showing how it had a strong effect on the NACA 0012 airfoil (cf. Fig. A.12) while thin plates were practically unaffected. Higher turbulence levels improve NACA 0012 lift generation characteristic by lowering the critical Reynolds number, and thus delaying separation.

These findings complement Schmitz results that attributed the good airfoil performance to the large adverse pressure gradients produced by the sharp leading edges at a very short chordwise distance. These work as boundary layer trips that induce early transition, making the upper surface boundary layer more resilient to perturbances.

Laitone also proved experimentally how at low Reynolds numbers, lift generation does not depend on the Kutta trailing edge condition. By testing a reversed NACA 0012 (trailing edge working as leading edge) he showed that considerably

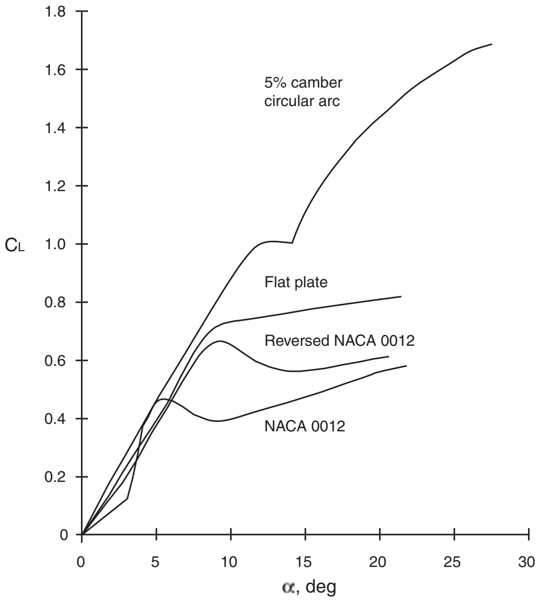

Figure A.13: Angle of attack vs. lift coefficient for AR=6 rectangular wings at Re=20,700, Ref [16]

.

higher lift coefficients could be achieved as shown in Figure A.13. Lift generation was improved, however maximum lift-to-drag ratio was reduced from 7.45 to 6.7 due to the additional drag produced by the separated flow at the thicker region of the airfoil.

Thin cambered airfoils not only have desirable aerodynamic characteristics at low Reynolds numbers but are also easily manufactured. Since they have a uniform thickness except at leading and trailing edges, mold design and manufacturing techniques are simpler than for a streamlined airfoil. This is specially true when considering circular arcs, which can be easily molded from tubes and cylinders. An advantage unique to circular arcs is that when they are cut, the resultant segments are still circular arcs. This unique feature is extensively used in the research presented in Chapters 4 and 5. As a Summary, the characteristics that make thin plates preferable to streamlined airfoils at Reynolds numbers below 70,000 are:

- Higher maximum lift coefficients than conventional airfoils

- Lower minimum drag coefficients than conventional airfoils
- Linear behavior of lift and drag coefficients with Reynolds number, without abrupt changes
- Independence of lift coefficient slope with Reynolds number
- Lack of hysteresis loops when cycling Reynolds numbers or angle of attack
- Low sensitivity to ambient turbulence
- Ease of manufacture

These characteristic make thin circular arc airfoils ideal for the systematic study and implementation of rotary wing MAVs.

A.7 Fundamental Rotor Aerodynamics

Until this point issues related exclusively to low Reynolds number airfoil aerodynamics have been addressed. This section introduces fundamental rotary-wing aerodynamic concepts.

A.7.1 Momentum Theory for a Hovering Rotor

The simplest analysis that can be performed on a hovering rotor involves the use of the classic momentum theory developed by Rankine in the nineteen century. The well known equations of conservation of mass, momentum and energy can be applied to the hovering rotor problem using the flow model shown in Figure A.14. It is assumed that thrust loading is uniform over an infinitely thin propeller disk (infinite number of blades), and that the flow is quasi-steady, irrotational, inviscid and incompressible (ideal fluid). Applying conservation of mass on the control volume the mass flow rate $\dot{m}$ is given as

$$\dot{m} = \rho A_{\infty} \omega = \rho A_2 v_i = \rho A v_i. \tag{A.10}$$

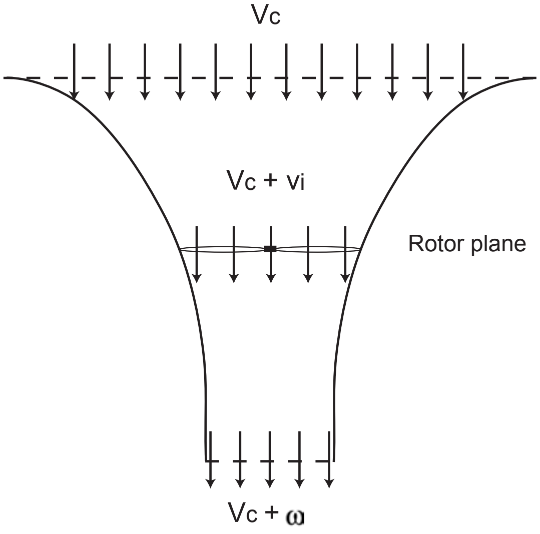

Figure A.14: Flow model used by momentum theory for a single rotor in axial flight.

Where ρ is the fluid density, A is the actuator disk area and v_i is the induced velocity in the plane of the rotor. By applying the conservation of momentum equation the expression for the rotor thrust T as function of the induced velocity v_i is found

$$T = \iint_{\infty} \rho(\overrightarrow{V} \cdot d\overrightarrow{S})\overrightarrow{V} = \dot{m}\omega. \tag{A.11}$$

Now applying the conservation of energy concept, the power P consumed by the hovering rotor is given by

$$P = Tv_i = \iint_{\infty} \frac{1}{2}\rho(\overrightarrow{V} \cdot d\overrightarrow{S})\overrightarrow{V}^2 = \frac{1}{2}\dot{m}\omega^2. \tag{A.12}$$

From equations A.11 and A.12 the relationship between the flow velocities at the rotor plane and at the far wake is easily obtained

$$v_i = \frac{1}{2}\omega. \tag{A.13}$$

This means, following the conservation of mass principle, that the area of the slipstream at infinity is half the area of the rotor disk. From equations A.10, A.11 and A.13 the expression for the induced velocity as function of the thrust can be obtained.

$$v_i = \sqrt{\frac{T}{2\rho A}} = \sqrt{\left(\frac{T}{A}\right)\frac{1}{2\rho}}. \tag{A.14}$$

Where T/A is the disk loading, an important rotor operational parameter also denoted as DL. The disk loading has units of force per unit area, and it will be discussed in more detail in the following section. Using equation A.14 the power required by a hovering rotor as a function of its thrust is given by

$$P = Tv_i = T\sqrt{\frac{T}{2\rho A}} = \frac{T^{3/2}}{\sqrt{2\rho A}}. \tag{A.15}$$

Considering that for this derivation it was assumed that the rotor was working in an ideal fluid with potential flow, the power calculated does not include any viscous loses. In fact this is known as *ideal power*, since it is the theoretical minimum that the rotor will require for a given thrust.

A.7.2 Thrust and Power Coefficients

As it is common in engineering, non-dimensional coefficients are defined to facilitated the analysis of the problems. In rotor analysis rotor thrust and power are non-dimensionalised as follows

$$C_T = \frac{T}{\rho A \Omega^2 R^2}. \tag{A.16}$$

$$C_P = \frac{P}{\rho A \Omega^3 R^3}. \tag{A.17}$$

Where A is the rotor disk area, R is the rotor radius and Ω is the rotational speed of the rotor in rad/s. Another common nondimensional quantity, the inflow ratio λ, can be defined now in function of the thrust coefficient.

$$\lambda_i = \frac{v_i}{\Omega R} = \frac{1}{\Omega R}\sqrt{\frac{T}{2\rho A}} = \sqrt{\frac{T}{2\rho A(\Omega R)^2}} = \sqrt{\frac{C_T}{2}}. \tag{A.18}$$

The power coefficient con now be expressed as

$$C_P = C_T \lambda_i = \frac{C_T^{3/2}}{\sqrt{2}}. \tag{A.19}$$

A.7.3 Rotor Hover Efficiency Metrics

There are two main rotor efficiency metrics that are used in helicopter analysis, these are the figure of merit or FM and the power loading or PL. The figure of merit has the advantage of being a nondimensional quantity that has a clear theoretical background, as opposed the power loading that has unit of thrust per unit power.

A.7.4 Figure of Merit

The figure of merit is defined as the ratio of the ideal induced power, as obtained in equation A.19, by the actual power that the rotor is consuming (cf. Eq A.20). The actual power can be experimentally measured to obtain a given rotor's FM. Since in most cases that is not an option, a standard approach has been adopted to analytically calculate the power required for a given rotor.

$$FM = \frac{Ideal\, power}{Actual\, power} = \frac{Ideal\, power}{Induced\, Power + Profile\, Power}. \tag{A.20}$$

The power required to hover has two main components, induced and profile power. Induced power is related to the acceleration of the fluid necessary to generate thrust, and it also includes losses product of physical phenomena ignored by the assumptions made in momentum theory and the actuator disk model. These are tip losses, nonuniform inflow, slipstream rotation and finite number of blades. The ideal induced power can be corrected to include all the non-ideal effect by multiplying the induced power coefficient by a constant, known as the *induced power factor* and denoted by κ. The induced power factor needs to be empirically determined for each rotor; however, a value of 1.15 gives in most cases a good approximation for full-scale helicopters.

Profile power includes all the viscous effects that influence the blades performance. Viscous effects on an airfoil section such as separation, pressure drag and skin friction are modeled through the drag coefficient. Drag coefficient is a function of angle of attack, Reynolds and Mach numbers. Since these parameters change along the blade, profile power should be obtained on a blade element basis and integrated along the span. For full-scale helicopters Reynolds numbers are high enough such that it can be assumed that the coefficient is constant and equal to the zero lift drag coefficient C_{d_0} of the airfoil at 75% of the span. Assuming this, profile power for a rotor of diameter R with N_b rectangular blades of chord c and a drag force per unit span D is given by

$$P_0 = \Omega\, N_b \int_0^R D\, y\, dy = \frac{1}{8}\,\rho\, N_b\, \Omega^3\, c\, C_{d_0} R^4. \tag{A.21}$$

Dividing by $\rho A(\Omega R)^3$ the profile power coefficient is obtained

$$C_{P_0} = \frac{1}{8}\left(\frac{N_b\, c\, R}{A}\right) C_{d_0} = \frac{1}{8}\left(\frac{N_b\, c\, R}{\pi\, R}\right) C_{d_0} = \frac{1}{8}\sigma\, C_{d_0}. \tag{A.22}$$

Where the solidity σ is the ratio of the blade by the rotor areas. The figure of merit can now be expressed as function of the thrust and power coefficients, the induced power factor, the zero lift drag coefficient and the rotor solidity.

$$FM = \frac{Ideal\, power}{Induced\, Power + Profile\, Power} = \frac{\frac{C_T^{3/2}}{\sqrt{2}}}{\kappa\frac{C_T^{3/2}}{\sqrt{2}} + \frac{\sigma\, C_{d_0}}{8}}. \tag{A.23}$$

In order to have the highest possible figure of merit it is necessary to simultaneously minimize the profile and induced losses. The minimum induced power is achieved when the inflow ratio over the rotor disk is uniform. The inflow radio distribution along the blade span in hover is defined as

$$\lambda_h(r) = \frac{v_i(r)}{\Omega\, R}. \tag{A.24}$$

Where $v_i(r)$ is the induced velocity at a radial position r. Gessow in his classic book (Ref. [76]) shows that a parabolic twist distribution, known as *ideal twist* results in a theoretical uniform inflow. However, such a geometry cannot be physically implemented. The minimum theoretical profile power is achieved when each blade station is operating at its maximum lift to drag ratio (L/D). This is a simple concept very difficult to implement considering that the angle of attack for maximum L/D is not only a function of the airfoil shape but also depends on Reynolds number and Mach number. In actual helicopter rotors a combination of twist and taper is generally used to reduce the induced and profile powers to acceptable levels. References [77] and [78] give an excellent overview of the theory.

In order to have a valid comparison of the hover efficiency of two rotors, it is necessary for both rotors to have the same disk loading, if this is not the case, the comparison is meaningless since the ideal power for the two rotors will be different. As mentioned before, this expression for figure of merit makes the assumption that the profile losses are accurately obtained by assuming that the drag coefficient is constant along the blade span and equal to the zero-lift drag coefficient C_{d_0}. This is a reasonable approximation at Reynolds numbers of more than one million, where the average drag coefficient at the operating collective angles is close to C_{d_0}, but as it is shown in Chapter 3, for low Reynolds numbers flows, this assumption introduces large inaccuracies. For acceptable predictions, other values of the average drag coefficient should be used.

A.7.5 Power Loading

Power loading is defined for a rotor as the ratio of the thrust produced by the power required. It has units of thrust per unit power. When designing a vehicle it is wanted to maximize the power loading such that energy requirements are minimized. This will give the vehicle the best endurance or payload capabilities possible. Power loading comparisons are not affected by operating conditions or vehicle configurations, being always valid and able to clearly show which rotor is requiring less energy for a given thrust.

A relationship between figure of merit and power loading can be obtained by combining the figure of merit equation and the expression for induced velocity from equation A.14

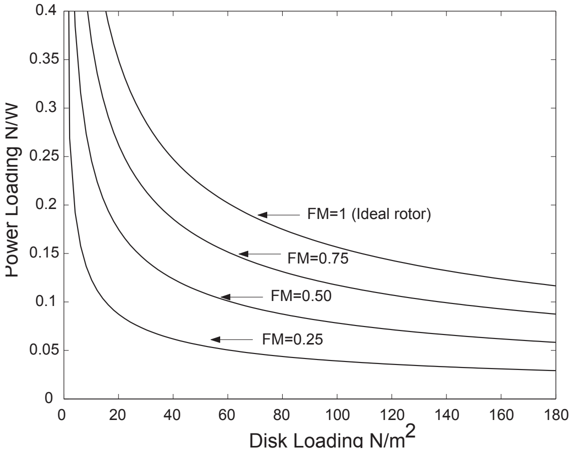

Figure A.15: Disk Loading vs. Power Loading for various Figures of Merit at sea level ($\rho = 1.225kg/m^3$).

$$FM = \frac{T\,v_i}{P_{Act}} = \frac{T}{P_{Act}}\sqrt{\left(\frac{T}{A}\right)\frac{1}{2\rho}} = PL\,\frac{\sqrt{DL}}{\sqrt{2\rho}}. \tag{A.25}$$

This equation can be used to plot the disk loading vs. power loading for different figures of merit. Figure A.15 shows how PL varies with FM and DL. It is clear that power loading increases as FM approaches the ideal value of 1, and as disk loading is reduced. Full-scale helicopters have disk loadings that range from 185 $N.m^{-2}$, for small vehicle such as the Bell 206, up to 720 $N.m^{-2}$ for the Sikorsky CH-53E. Over that range the power loading curves have very shallow slopes, being almost independent of the disk loading. This is not the case for MAVs, that may have disk loadings that are in the region where larger effects on the power loading are present. This is illustrated with experimental data in Chapter 2.

BIBLIOGRAPHY

[1] Schmitz, F. W., “Aerodynamics of Model Aircraft wing Measurements I”, R.T.P. Translation No 2460. Issued by Ministry of Aircraft Production. 1983.

[2] Miley, S.J.,“A Catalog of Low Reynolds Number Airfoil Data for Wind Turbine Applications”. RFP-3387 VC-60, Rockwell International Feb. 1982. Us Dept. of Energy, Wind Energy Technology Division, Federal Wind Energy Program.

[3] Bruining, A., “Aerodynamic Characteristics of a Curved Plate Airfoil Section at Reynolds Numbers 60,000 and 100,000 and Angles of Attack from -10 to +90 Degrees,” Technische Hogeschool, Delft, Netherlands, Dept. of Aerospace Engineering,Report Number VTHLR-281, May, 1979.

[4] Althaus, D., “ProfilePolaren Fur den Modellflug,” Institut Fur Aerodynamik u. Gasdynamik der Universitat Stuttgart Neckar-Verlag, Postfach 1820, 7730 Villingen-Schwenningen, Germany, 1980.

[5] Carmichael, B.H., “Low Reynolds Number Airfoil Survey,” Volume I, NASA Contractor Report 165803, November, 1981.

[6] Arena, A.V., and Mueller, T.J., “Laminar Separation, Transition and Turbulent Reattachment Near the Leading Edge of Airfoils,” *AIAA Journal*, Vol. 18, No. 7, pp. 747-753, July 1980.

[7] Mueller, T.J., and Batill, S.M., “Experimental Studies of Separation on a Two-Dimensional Airfoil at Low Reynolds Numbers,” AIAA Journal, Vol. 20, No. 4 pp. 456-463, April 1982.

[8] Mueller, T.J., “The Influence of Laminar Separation and Transition on Low Reynolds Number Airfoil Hysteresis,” *Journal of Aircraft*, Vol. 22, No. 9, pp. 763-770, September 1985.

[9] Brendel, M., and Mueller, T.J., “Boundary Layer Measurements on an Airfoil at Low Reynolds Numbers,” *Journal of Aircraft*, Vol. 25, No. 7, pp. 612-617, July 1988

[10] Mueller, T.J.,"Aerodynamic Measurements at Low Reynolds Numbers for Fixed Wing Micro-Air Vehicles," presented at the RTO AVT Course on Development and Operation of UAVs for Military and Civil Applications, Rhode-Saint-Genese, Belgium, September 13-17, 1999.

[11] Pelletier, A. and Mueller, T.J., "Low Reynolds Number Aerodynamics of Low-Aspect-Ratio, Thin/Flat/Cambered-Plate Wings," *Journal of Aircraft*, Vol. 37, No. 5, pp. 825-832, September-October 2000.

[12] Selig M.S., Donovan J.F., Fraser DB. Airfoils at Low Speeds, Soar Tech Publ., Virginia Beach, VA, 1989.

[13] Selig M.S., Donovan J.F., Fraser DB. Summary of Low Speed Airfoil Data, Vol.1 Vol. 2 Vol.3 Vol.4, Soar Tech Publications, Virginia Beach, VA, 1989-2004.

[14] Selig M.S. and Maughmer, M.D. "A Multi-Point Inverse Airfoil Design Method Based on Conformal Mapping," *AIAA Journal*, Vol.30, No.5, May 1992, pp 1162-1170.

[15] Selig M.S. and Maughmer, M.D. "Generalized Multipoint Inverse Airfoil Design," *AIAA Journal*, Vol.30, No.11, Nov 1992, pp. 2618-2625.

[16] Laitone, E.V., "Aerodynamic Lift at Reynolds Numbers Below 70,000," *AIAA Journal*, Vol. 34, No. 9, pp 1941-1942.

[17] Laitone, E.V.,"Aerodynamic Lift at Reynolds Numbers Below 70,000," AIAA, Aerospace Sciences Meeting and Exhibit, 33rd, Reno, NV; UNITED STATES; 9-12 Jan. 1995. AIAA paper 1995-0434.

[18] Laitone, E.V., "Wind Tunnel Tests of Wings at Reynolds Numbers Below 70000," Experiments in Fluids Vol. 23, 1997, pp 405-409.

[19] Lowson, M.V., "Aerodynamics of Aerofoils at Low Reynolds Numbers," UAVs - 14th Unmanned Air Vehicle Systems International Conference, United Kingdom, April, 1999.

[20] Sunada, S., Sakaguchi, A., and Kawachi, K., "Airfoil Section Characteristics at Low Reynolds Numbers," *Journal of Fluid Engineering*, Vol. 119, March 1997, pp. 129-135.

[21] Sunada, S., Yasuda, T., Yasuda, K., Kawachi, K., "Comparison of Wing Characteristics at an Ultralow Reynolds Number," *Journal of Aircraft*, Vol. 39, no. 2, pp. 331-338. Mar.-Apr. 2002.

[22] Sunada, S., Kawachi, K., "Effects of Reynolds Number on Characteristics of Fixed and Rotary Wings," *Journal of Aircraft*, Vol. 41, no. 1, pp. 189-192. Jan.-Feb. 2004

[23] Okamoto, M., Azuma, A., "Experimental Study on Aerodynamic Characteristics of Unsteady Wings at Low Reynolds Number" *AIAA Journal*, Vol. 43, no. 12, pp. 2526-2536. Dec. 2005.

[24] Van den Berg, C. and Ellington, C.P., "The Three-Dimensional Leading-Edge Vortex of a 'Hovering' Model Hawkmoth," Phil. Trans. R. Soc. Lond. B, 352, 329-340. 1997

[25] Ellington, C.P. and Usherwood, J.R. (2001). Lift and Drag Characteristics of Rotary and Flapping wings. In Fixed and Flapping Wing Aerodynamics for Micro Air Vehicle Applications (ed. T.J. Mueller), pp. 231-248. Progress in Astronautics and Aeronautics, vol. 195. Reston: AIAA.

[26] Dickinson, M. H., F. O. Lehmann, and Sane, S., "Wing rotation and the aerodynamic basis of insect flight," *Science* 284(5422): 1954-1960, 2001.

[27] Dickinson, M.H., "Unsteady Mechanisms of Force Generation in Aquatic and Aerial Locomotion," *Am. Zool.* 36(6): 537-554. 1996.

[28] Samuel, P., Sirohi, J., Rudd, L., Pines, D., and Perel, R., "Design and Development of a Micro Coaxial Rotorcraft," Proceedings of the AHS Vertical Lift Aircraft Design Conference,American Helicopter Society, Alexandria, VA, Jan. 2000.

[29] Lipera, L.,et al., “The Micro Craft iSTAR Micro Air Vehicle: Control System Design and Testing,” Proceedings of the AHS 57th Annual Forum, Washington, DC, May 9-11 2001.

[30] Grasmeyer, J., and Keenon, M., “Development of the Black Widow Micro Air Vehicle,” AIAA Paper 2001-0127, Jan. 2001.

[31] Kroo, I., and Kunz, P., “Meso-Scale Flight and Miniature Rotorcraft Development,” Fixed and Flapping Wing Aerodynamics for Micro Air Vehicle Applications, edited by T. J. Mueller, Progress in Astronautics and Aeronautics, AIAA, Reston, VA, 2001, pp. 503517.

[32] Morris, S. J., “Design and Flight Test Results for Micro-Sized Fixed- Wing and VTOL Aircraft,” 1st International Conference on Emerging Technologies for Micro Air Vehicles, 1997, pp. 117131.

[33] Pornsin-Sirirak, T. N., Lee, S. W., Nassef, H., Grasmeye, J., Tai, Y. C., Ho, C.M., and Keennon, M., “MEMS Wing Technology for a Battery-Powered Ornithopter,” Proceedings of the 13th IEEE Annual International Conference on MEMS 2000, pp. 779804.

[34] Kornbluh, R., “Project Mentor: Biologically Inspired Platform,” Keynote Presentation at the 8th AIAA/CEAS Aeroacoustics Conference, 1719 June 2002, Breckenridge, Colorado

[35] Young, L. A., Aiken, E.W., Johnson, J. L., Demblewski, R., Andrews, J., and Klem, J., “New Concepts and Perspectives on Micro-Rotorcraft and Small Autonomous Rotary Wing Vehicles,” Proceedings of the 20th AIAA Applied Aerodynamics Conference, AIAA, Reston, VA; also AIAA Paper 2002-2816, June 2002.

[36] Sirohi, J., Tishchenko M., Chopra I., “ Design and Testing of a Micro-Aerial Vehicle with a Single Rotor and Turning Vanes,” Proceedings of the AHS 61th Annual Forum, Grapevine TX, 1-3 June 2005.

[37] Woods, M.I., Henderson, J.F., and Lock G.D.. "Energy requirements for the flight of Micro Air Vehicles," *Aeronautical Journal*, Vol. 105, pp. 135-149, 2001.

[38] Baxter, D.R.J., East, R.A., "A Survey of Some Fundamental Issues in Micro-Air-Vehicle Design," Proceedings 14th UAVs - Unmanned Air Vehicle Systems International Conference, United Kingdom; 12-14 Apr. 1999. pp. 34.1-34.13. 1999

[39] Lambermont, P.; and Pirie, A., *Helicopters and Autogyros of the World,* Cassell and Company Ltd., 1970.

[40] Coleman, C.P., "A Survey of Theoretical and Experimental Coaxial Rotor Aerodynamic Research," Proceedings of the 19th European Rotorcraft Forum, Cernobbio, Italy, Sept. 14-16, 1993.

[41] Harrington, R. D."Full-Scale-Tunnel Investigation of the Static-Thrust Performance of a Coaxial Helicopter Rotor," NACA TN-2318, Mar. 1951.

[42] Dingledein, R. C. "Wind-Tunnel Studies of the Performance of Multirotor Configurations," NACA TN-3236, Aug. 1954.

[43] Nagashima, T., and Nakanishi, K., "Optimum Performance and Wake Geometry of Coaxial Rotor in Hover," Proceedings of the 7th European Rotorcraft and Powered Lift Forum, Paper No. 41, Sept. 1981.

[44] Sunada, S.,Tanaka, K., Kawashima, K., "Maximization of Thrust-Torque Ratio of a Coaxial Rotor," *"Journal of Aircraft,"* Vol.42 no.2 pp. 570-572, 2005.

[45] Saito, S.; and Azuma, A., "A Numerical Approach to Coaxial Rotor Aerodynamics." Proceedings of the 7th European Rotorcraft and Powered Lift Forum, Paper No. 42, Sept. 1981.

[46] Andrew, M. J., "Coaxial Rotor Aerodynamics in Hover." Vertica, vol. 5, 1981, pp. 163172.

[47] Zimmer, H., “The Aerodynamic Calculation of Counter Rotating Coaxial Rotors,” Proceedings of the 11th European Rotorcraft and Powered Lift Forum, Paper No. 27, Sept. 1985.

[48] Bagai, A., and Leishman J. G.,”Free-Wake Analysis of Tandem, Tilt-Rotor and Coaxial Rotor Configurations,” *Journal of the American Helicopter Society,*” Vol. 41, (3), 1996, pp. 196-207.

[49] Leishman, J.G., Ananthan, S., “Aerodynamic Optimization of a Coaxial Proprotor,” Proceeding AHS 62th Annual Forum,Phoenix, AZ, May 9-11, 2006.

[50] Rogers,S. E. and Kwak,D., “An Upwind Differencing Scheme for the Steady-State Incompressible Navier-Stokes Equations,” NASA TM 101051, November 1988.

[51] Rogers,S. E. and Kwak,D., “An Upwind Differencing Scheme for the Time accurate Incompressible Navier-Stokes Equations,” AIAA Journal, Vol. 28, No.2, 1990, pp. 253-262.

[52] Kunz., P.J., “Aerodynamics and Design for Ultra-Low Reynolds Number Flight” Ph.D. Dissertation, Department of Aeronautics and Astronautics, Stanford University, CA, June 2003.

[53] Kroo, I., and Kunz, P., “Analysis and Design of Airfoils for use at Ultra-Low Reynolds Numbers,” Fixed and Flapping Wing Aerodynamics for Micro Air Vehicle Applications, edited by T. J. Mueller, Progress in Astronautics and Aeronautics, AIAA, Reston, VA, 2001, pp. 503517.

[54] Kroo, I., and Kunz, P., “Meso-Scale Flight and Miniature Rotorcraft Development,” Fixed and Flapping Wing Aerodynamics for Micro Air Vehicle Applications, edited by T. J. Mueller, Progress in Astronautics and Aeronautics, AIAA, Reston, VA, 2001, pp. 503517.

[55] Singh, A.P., “A Computational Study on Airfoils at Low Reynolds Numbers,” Proceedings of the ASME Fluids Engineering Division, FED-253, ASME, 2000, pp 405-411.

[56] Kellogg, M.I., and Bowman, W.J., Parametric Design Study of the Thickness of Airfoils at Reynolds Numbers from 60,000-150,000, 42nd AIAA Aerospace Sciences and Exhibit, Reno, Nevada, January, 2004.

[57] Drela, M., “XFOIL: An Analysis and Design System for Low Reynolds Number Airfoils,” Conference on Low Reynolds Number Airfoil Aerodynamics, University of Notre Dame, June 1989.

[58] Ramamurti, R, Sandberg, W., Loehner, R., “Simulation of the dynamics of Micro Air Vehicles,” AIAA Paper 2000-896, Jan. 2000.

[59] Shum, Y.K., Marsden, D.J., “Separation Bubble Model for Low Reynolds Number Airfoil Applications,” Journal of Aircraft, Vol. 31, No. 4., July, 1994, pp. 761-766.

[60] Bohorquez, F., Rankins, F., Baeder, J.D., and Pines, D.J., “Hover Performance of Rotor Blades at Low Reynolds Numbers for Rotary Wing Micro Air Vehicles. An Experimental and CFD Study,” 21st AIAA Applied Aerodynamics Conference, Orlando, FL, June 2003.

[61] Corfeld, K. J., Strawn, R. C., and Long, L. N., “Computational Analysis of a Prototype Martian Rotorcraft Experiment,” 20th AIAA Applied Aerodynamics Conference, Saint Louis, MO, June 2002,AIAA Paper 2002-2815.

[62] Bohorquez F., Samuel, P.,Sirohi, J., Pines, D., Rudd, L., Perel. R. , ”Design Analysis and Hover Performance of a Rotary Wing Micro Air Vehicle”, AHS Journal, Vol. 48, (2), April 2003, p. 80.

[63] Meakin, B., and Potsdam, M., “Reference Guide for Scalable OVERFLOW-D v1.5e,” NASA Ames Research Center, Moffett Field, CA, June 2002.

[64] Gupta, V., Baeder, J.D., “Low Mach Number Preconditioning for Tiltrotor Rotor-Wing Interaction,” AHS 4th Decennial Specialists Conference on Aeromechanics, San Francisco, CA, January, 2004.

[65] Gupta, V., Ph.D. Dissertation, University of Maryland, College Park, 2005.

[66] Schroeder, E., Baeder, J., “using Computational Fluid Dynamics for Micro Air Vehicle Airfoil Validation and Prediction,” 23rd AIAA Applied Aerodynamics Conference, Toronto, Ontario, June 6-9, 2005, AIAA paper 2005-4841.

[67] Schroeder, E., “Low Reynolds Number Flow Validation using Computational Fluid Dynamics with Applications to Micro Air Vehicles,”. Master’s Thesis, Department of Aerospace Engineering, University of Maryland at College Park, 2005.

[68] Lakshminarayan, V., Bush B., Duraisamy K., and Baeder J., “Computational Investigation of Micro Hovering Rotor Aerodynamics,” 24th AIAA Applied Aerodynamics Conference, San Francisco, California, June 5-8, 2006. AIAA paper 2006-2819.

[69] Hein, B.R., “Hover Performance of a Micro Air Vehicle: Rotors at Low Reynolds Number,” 2005 AHS Lichten Award Competition.

[70] Bauer, Andrew B., “The Laminar Airfoil Problem,” National Free Flight Society Symposium Report 1975. available at http://www.freeflight.org/store/sympoCD.htm

[71] Gad-El-Hak, M.,*Flow Control: Passive, Active, And Reactive Flow Management* Cambridge University Press, Cambridge, UK, 2000.

[72] Anderson J. D., *Fundamental of Aerodynamics* McGraw-Hill, 3 ed., New York NY, 2001.

[73] McCormick, B. W., *Aerodynamics Aeronautics and Flight Mechanics* John Wiley & Sons Inc., 2 ed., New York NY, 1995.

[74] Kline, S. J., and F. A. McClintock, “Describing Uncertainties in Single-Sample Experiments,” *Mech. Eng.*,75, p. 3-8, January 1953.

[75] Samuel, P., Sirohi, J., Rudd, L., Pines, D., and Perel, R., Design and Development of a Micro Coaxial Rotorcraft, Proceedings of the AHS Vertical Lift Aircraft Design Conference, American Helicopter Society, Alexandria, VA, Jan. 2000.

[76] Gessow, A., Myers, G., *Aerodynamics of the Helicopter* Frederick Ungar Publishing, 8 ed., New York NY, 1985.

[77] Prouty, R.W., *Helicopter Performance, Stability, and Control* PWS Publishers, Boston, Massachusetts, 1986.

[78] Leishman, *J.G., Principles of Helicopters Aerodynamics*, Cambridge University Press, 1 ed., New York, NY, 2000.

[79] Spalart, P., and Allmaras, S., “A One Equation Turbulence Model for Aerodynamic Flows,” 30th Aerospace Sciences Meeting and Exhibit, AIAA, Reno, NV, January, 1992.

[80] G. R. Srinivasan and J.D. Baeder. “TURNS: A Free-Wake Euler/Navier-Stokes Numerical Method for Helicopter Rotors” AIAA Journal, Vol. 31, No.5, 1993, pp. 959-952.

[81] T. J., Barber, “An Investigation of Strut-Wall Intersection Losses.” Journal of Aircraft, Vol. 15 No. 10, 1978, pp. 676-681.

[82] T. J., Mueller, B. J. Jansen, Jr. “Aerodynamic Measurements at Low Reynolds Numbers.” AIAA Paper 82-0598, March 1982.

[83] Spalart, P. R., “Trends in Turbulence Treatments,” AIAA Paper 00-2306, 2000.

[84] Akima Hiroshi, ”A Method of Univariate Interpolation that Has the Accuracy of a Third-Degree Polynomial,” ACM Transactions on Mathematical Software, Vol.17, No 3, 1991, pp. 341-366.

[85] Dingeldein, R. C. “Wind Tunnel Studies of the Performance of Multirotor Configurations,” NACA Technical Note 3236.

[86] Bohorquez, F. and Pines, D., “Hover Performance and Swashplate Design of a Coaxial Rotary Wing Micro Air Vehicle,” Proceedings of the AHS 60th Forum, Baltimore, MD, June 7-10, 2004.

[87] Zorpette, G., “Spying Saucer-Cypher,” *Scientific American*, Vol. 276 June 1997, p. 40.

[88] Fay, John Foster, *The helicopter: history, piloting and how it flies*, Newton Abbot: David and Charles, 4th ed. 1987, c1954.

[89] Kim, S. K., Tibury, D. M., “Mathematical Modeling and Experimental Identification of an Unmanned Helicopter Robot with Flybar Dynamics.” *Journal of Robotic Systems*, Vol. 21, March 2004, pp 95-116.